REPORT DOCUMENTATION PAGE

AFRL-SR-BL-TR-02-

0090

1. REPORT DATE (DD-MM-YYYY)	2. REPORT TYPE	3. DATES COVERED (From - To)
15-11-2001	Final Technical	01-04-1999 – 30-09-2001

4. TITLE AND SUBTITLE	5a. CONTRACT NUMBER
(U) Drop/Gas Interactions of Dense Sprays	
	5b. GRANT NUMBER
	F49620-99-1-0083
	5c. PROGRAM ELEMENT NUMBER
	61102F

6. AUTHOR(S)	5d. PROJECT NUMBER
	2308
G. M. Faeth	5e. TASK NUMBER
	BX
	5f. WORK UNIT NUMBER

7. PERFORMING ORGANIZATION NAME(S) AND ADDRESS(ES)	8. PERFORMING ORGANIZATION REPORT NUMBER
The University of Michigan Ann Arbor MI 48109-2140	GDL/GMF-01/01

9. SPONSORING / MONITORING AGENCY NAME(S) AND ADDRESS(ES)	10. SPONSOR/MONITOR'S ACRONYM(S)
AFOSR/NA 801 North Randolph Street Room 732 Arlington VA 22203-1977	AFOSR
	11. SPONSOR/MONITOR'S REPORT NUMBER(S)

12. DISTRIBUTION / AVAILABILITY STATEMENT

Approved for public release; distribution is unlimited

13. SUPPLEMENTARY NOTES

20020315 039

14. ABSTRACT

Turbulence generation and secondary drop breakup were studied. Turbulence generation is due to the motion of high-speed dispersed phases through continuous phases. Secondary drop breakup intrinsically follows primary liquid breakup in sprays. Measurements showed that flows caused by turbulence generation consisted of dispersed phase wakes (involving laminar-like turbulent wakes) surrounded by a turbulent interwake region involving isotropic turbulence in the final decay region. These measurements provided information about the properties of both of these regions. Measurements also provided the temporal properties of secondary drop deformation and breakup for shock wave disturbances at large liquid-gas density ratios. Numerical simulations yielded corresponding information at conditions more representative of practical combustion chambers that would be difficult to address with physical experiments.

15. SUBJECT TERMS

Multiphase flow, homogeneous turbulence, drop breakup, sphere wakes, turbulence generation

16. SECURITY CLASSIFICATION OF:			17. LIMITATION OF ABSTRACT	18. NUMBER OF PAGES	19a. NAME OF RESPONSIBLE PERSON
a. REPORT	b. ABSTRACT	c. THIS PAGE			Julian M. Tishkoff
Unclassified	Unclassified	Unclassified	UL	155	19b. TELEPHONE NUMBER (include area code) (703) 696-8478

Standard Form 298 (Rev. 8-98)
Prescribed by ANSI Std. Z39.18

Drop/Gas Interactions of Dense Sprays

C. Aalburg, J.-H. Chen, Z. Dai, K. Lee, J. Mazallon, K.A. Sallam and G.M. Faeth
Department of Aerospace Engineering
The University of Michigan
Ann Arbor, Michigan 48109-2140, U.S.A.

Final Report

1 April 1999 - 30 September 2001

15 November 2001

ACKNOWLEDGMENTS

Table of Contents

Table of Contents (continued)

List of Tables

List of Figures

Nomenclature: Liquid Breakup

Symbol	Description
a	rate of drop acceleration
C_D	drag coefficient
d	drop diameter
d_p	particle diameter
L	wake length
MMD	mass median drop diameter
Oh	Ohnesorge number, $\mu_L/(\rho_L d_o \sigma)^{1/2}$
r	drop radius
Re	Reynolds number, $d_o u_o/\nu_G$
S	drop displacement
SMD	Sauter mean diameter
t	time
t^*	characteristic breakup time, $d_o(\rho_L/\rho_G)^{1/2}/u_o$
u	streamwise velocity
u_b	streamwise velocity after breakup
U_p	relative streamwise particle velocity
We	Weber number, $\rho_G d_o u_o^2/\sigma$
μ	viscosity
ν	kinematic viscosity
ρ	density
σ	surface tension

Subscripts

f	liquid phase property
g	gas phase property
G	gas phase property
L	liquid phase property
o	initial condition

Nomenclature: Turbulence Generation

Symbol	Description
A	dimensionless integral scale, $\varepsilon L_u/(\bar{u}')^3$
C_d	particle drag coefficient
D	dissipation factor, $(\theta/\ell_p)^3 = \varepsilon d_p(C_d/8)^{1/2}/(\pi U_p^2(U_p-\bar{u}))$
D_p	Parthesarathy dissipation factor, $\varepsilon d_p(C_d/8)^{1/3}/U_p^3$
d_p	particle diameter
L_u	streamwise integral length scale
ℓ_K	Kolmogorov length scale, $(v^3/\varepsilon)^{1/4}$
ℓ_p	mean particle spacing, $((U_p-\bar{u})/n'')^{1/3}$
M	mesh size of a grid
n	power in turbulence decay law
n''	particle number flux
Re	particle Reynolds number, $d_p U_p/v$
Re_λ	turbulence Reynolds number, $\lambda \bar{u}'/v$
t_K	Kolmogorov time scale, $(v/\varepsilon)^{1/2}$
U_p	mean streamwise relative velocity of a particle
u	streamwise gas velocity
u_K	Kolmogorov velocity scale, $(\varepsilon v)^{1/4}$
v	cross-stream gas velocity
x	streamwise distance
x_o	streamwise virtual origin location
β	empirical factor, Eq. (4)
ε	rate of dissipation of turbulence kinetic energy
θ	wake momentum diameter, $(C_d d_p^2/8)^{1/2}$
λ	Taylor length scale $(15v\bar{u}'^2/\varepsilon)^{1/2}$
v	molecular kinematic viscosity of gas

Superscripts

$\bar{(\;)}$	mean value
$\bar{(\;)}'$	rms fluctuating value
$\bar{(\;)}'^2$	mean-square fluctuating value

Drop/Gas Interactions of Dense Sprays

1. Introduction

Sprays and spray processes have been studied extensively due to their many applications; see Faeth (1990,1996) and Faeth et al. (1995) and references cited therein. Unfortunately, sprays are complex multiphase turbulent flows and fundamental understanding of their properties is not well developed — particularly those processes relating to the near-injector dense portion of the flow. This is a serious deficiency because the dense-spray region involves the breakup of the liquid to form a dispersed phase, which is crucial to the mixing properties of sprays, and also generates the initial conditions required to analyze the structure of the better understood dilute portion of sprays. Thus, the objective of the present investigation was to study two aspects of dense sprays that involve drop/gas interactions, namely: (1) secondary drop breakup (which is the most significant rate process of dense sprays) and the related problem of primary breakup of nonturbulent liquid jets in crossflow (which is an important spray breakup process for many propulsion systems); and (2) turbulence generation by dispersed phases, which is the most significant source of turbulence production within dense sprays. The research has relevance to air-breathing propulsion systems, liquid rocket engines and internal combustion engines, among others.

The following description of the research is brief. Additional details may be found in the articles, papers and theses resulting from the investigation that are summarized in Table 1. The table also provides a summary of the participants in the investigation, oral presentations of research results and a summary of honors/awards obtained during the grant period. Finally, for convenience, several articles resulting from the research are reproduced in appendices, as follows: Aalburg et al. (2002a), Chen et al. (2000), Chen and Faeth (2000), Chen and Faeth (2001), Chou and Faeth (1998), Dai and Faeth (2001) and Mazallon et al. (1999).

The following report considers secondary breakup and turbulence generation, in turn. Each part is written to stand alone so that readers can skip to portions of the report of interest to them.

Table 1. Summary of Investigation*

_____

Articles, Papers, Theses and Reports:

Aalburg, C. (2002) *Deformation and Breakup of Round Drops and Nonturbulent Liquid Jets in Uniform Crossflows.* Ph.D. Thesis, The University of Michigan, Ann Arbor, MI.

Aalburg, C. Faeth, G.M. and van Leer, B. (2000) Deformation and Drag Properties of Nonturbulent Round Liquid Jets in Uniform Crossflows. *Bull. Amer. Phys. Soc.* 45, 176-177 (abstract only).

Aalburg, C. Faeth, G.M. and van Leer, B. (2001) Deformation and Drop Properties of Drops Subjected to Shock Wave and Steady Disturbances. . *Bull. Amer. Phys. Soc.*, abstract only.

Aalburg, C., van Leer, B. and Faeth, G. M. (2002) Deformation of Laminar Round Liquid Jets in Uniform Gaseous Crossflows. *Int. J. Multiphase Flow*, submitted.

Aalburg, C., Faeth, G.M. and van Leer, B. (2002) Deformation and Drop Properties of Round Drops Subjected to Shock Wave Disturbances. *40th Aerospace Sciences Meeting*, Reno, NV, AIAA Paper No. 2002-0341.

Chen, J.-H. (1999) *Turbulence Generation in Homogeneous Dilute Particle-Laden Flows.* Ph.D. Thesis, The University of Michigan, Ann Arbor, Michigan.

Chen, J.-H. and Faeth, G.M. (1999) Inter-Wake Turbulence Properties in Homogeneous Particle-Laden Flows. *30th AIAA Fluid Dynamics Conference*, Norfolk, VA, AIAA Paper No. 99-3758.

Chen, J.-H. and Faeth, G.M. (2000) Inter-Wake Turbulence Properties of Homogeneous Particle-Laden Flows. *AIAA J.* 38:995-1001.

Chen, J.-H. and Faeth, G.M. (2000) Measurements and Predictions of Turbulence Generation in Homogeneous Particle-Laden Flows. *38th Aerospace Sciences Meeting,* Reno, NV, AIAA Paper No. 2000-0182.

Chen, J.-H. and Faeth, G.M. (2001) Continuous-Phase Properties of Homogeneous Particle-Laden Turbulent Flows. *AIAA J.* 39, 180-183.

Chen, J.-H., Chou, W.-H., Dai, Z., Wu, J.-S., and Faeth, G.M. (1998) Secondary Breakup and Turbulence Interactions of Drops. Report GDL/GMF-98-01, Department of Aerospace Engineering, The University of Michigan, Ann Arbor, MI.

Chen, J.-H., Lee, K. and Faeth, G.M. (1999) Structure of the Interwake Region of Dilute Turbulent Dispersed Flows. *Bull. Amer. Phys. Soc.* 44, 81 (abstract only).

Chen, J.-H., Wu, J.-S. and Faeth, G.M. (2000) Turbulence Generation in Homogeneous Particle-Laden Flows. *AIAA J.* 38:636-642.

Chou, W.-H. and Faeth, G.M. (1998) Temporal Properties of Secondary Drop Breakup in the Bag Breakup Regime. *Int. J. Multiphase Flow*, 24, 889-912.

Dai, Z. and Faeth, G.M. (1999) Temporal Properties of Multimode Secondary Breakup. *37th Aerospace Sciences Meeting*, Reno, NV, AIAA Paper No. 99-0333.

Dai, Z. and Faeth, G.M. (2001) Temporal Properties of Secondary Breakup in the Multimode Breakup Regime. *Int. J. Multiphase Flow* 27:217-236.

Dai, Z., Sallam, K.A. and Faeth, G.M. (1999) Turbulent Primary Breakup of Plane Free Bow Sheets. *Proc. 22nd Symp, Naval Hydro.*, National Academy Press, Washington, D.C., 568-581.

Faeth, G.M. (1999) Liquid Atomization in Multiphase Flows: A Review. *30th AIAA Fluid Dynamics Conference*, Norfolk, VA, AIAA Paper No. 99-3639.

Lee, K., Chen, J.-H. and Faeth, G.M. (2001) Turbulence Generation in Homogeneous Polydisperse Particle-Laden Flows. *Bull. Amer. Phys. Soc.*, abstract only.

Mazallon, J., Dai, Z. and Faeth, G.M. (1999) Primary Breakup of Nonturbulent Round Liquid Jets in Gas Crossflows. *Atom. Sprays*, 9, 291-312.

Sallam, K.A. (2002) *Properties of Spray Formation by Turbulent Primary Breakup*. Ph.D. Thesis, Aerospace Engineering Department, The University of Michigan, Ann Arbor, MI.

Sallam, K.A. and Faeth, G.M. (2001) Surface Properties of Turbulent Liquid Jets in Still Air. *Bull. Amer. Phys. Soc.*, abstract only.

Sallam, K.A., Dai, Z. and Faeth, G.M. (1999) Drop Formation at the Surface of Plane Tubulent Liquid Jets in Still Gases. *Int. J. Multiphase Flow* 25, 1161-1180.

Sallam, K.A., Dai, Z. and Faeth, G.M. (1999) Breakup of Turbulent Liquid Jets in Still Gases. *30th AIAA Fluid Dynamics Conference*, Norfolk, VA, AIAA Paper No. 39-3759.

Sallam, K.A., Faeth, G.M. and Dai, Z. (2000) Primary Breakup of Round and Plane Liquid Jets. *Bull. Amer. Phys. Soc.*, 45, 15 (abstract only).

Sallam, K.A., Dai, Z. and Faeth, G.M. (2002) Liquid Breakup at the Surface of Turbulent Round Liquid Jets in Still Gases. *Int. J. Multiphase Flow*, in press.

Sallam, K.A., Dai, Z. and Faeth, G.M. (2002) Turbulent Primary Breakup of Round and Plane Liquid Jets in Still Air. *40th Aerospace Sciences Meeting*, Reno, NV, AIAA Paper No. 2002-1115.

Participants:

Aalburg, C., Graduate Student Research Assistant and Doctoral Candidate, The University of Michigan

Chen, J.-H., Graduate Student Research Assistant and Doctoral Candidate, The University of Michigan

Dai, Z., Postdoctoral Research Fellow, The University of Michigan

Faeth, G.M., Principal Investigator and Professor, The University of Michigan

Lee, K., Graduate Student Research Assistant and Doctoral Candidate, The University of Michigan

Mazallon, J., Graduate Student Research Assistant, The University of Michigan

Sallam, K.A., Graduate Student Research Assistant and Doctoral Candidate, The University of Michigan

Oral Presentations:

Faeth, G.M. (1999) Temporal Properties of Secondary Breakup. *37th Aerospace Sciences Meeting*, Reno, NV, contributed.

Faeth, G.M. (1999) Search for the Turbulent Mixing Mechanism of Combusting Sprays in Propulsion and Power Systems. Mechanical Engineering Seminar, Texas A&M University, College Station, TX, invited.

Faeth, G.M. (1999) Search for the Turbulent Mixing Mechanism of Combusting Sprays for Propulsion Applications, Zucrow Memorial Lecture, Purdue University, West Lafayette, IN, invited.

Faeth, G.M. (1999) Liquid Atomization in Multiphase Flows: A Review. *30th AIAA Fluid Dynamics Conference*, Norfolk, VA, invited.

Faeth, G.M. (1999) Inter-Wake Turbulence Properties in Homogeneous Particle-Laden Flows. *30th AIAA Fluid Dynamics Conference*, Norfolk, VA, contributed.

Faeth, G.M. (1999) Breakup of Turbulent Liquid Jets in Still Gases. *30th AIAA Fluid Dynamics Conference*, Norfolk, VA, contributed.

Faeth, G.M. (2000) Rates and Outcomes of Secondary Drop Breakup. Wright Aeronautical Laboratory, Wright-Patterson Air Force Base, Ohio, invited.

Faeth, G.M. (2000) Drop/Gas Interactions in Dense Sprays. ARO/AFOSR Contractors' Meeting, Chemical Propulsion, Sante Fe, NM, invited.

Faeth, G.M. (2000) Measurements and Predictions of Turbulence Generation in Homogeneous Particle-Laden Flows. *38th Aerospace Sciences Meeting*, Reno, NV, contributed.

Faeth, G.M. (2000) Turbulent Primary Breakup of Round and Plane Free Liquid Jets in Still Gases. ONR 2000 Free Surface Turbulence and Bubbly Flows Workshop, California Institute of Technology, Pasadena, CA, contributed.

Faeth, G.M. (2001) Search for the Turbulent Mixing Mechanism Within Combusting Sprays. Mechanical and Aerospace Engineering Seminar, University of Missouri-Rolla, Rolla, MO, invited.

Faeth, G.M. (2001) Turbulent Mixing in Dispersed Multiphase Flows. Mechanical and Aerospace Engineering Seminar, Arizona State University, Tempe, AZ, invited.

Faeth, G.M. (2001) Search for the Turbulent Mixing Mechanism Within Sprays. Mechanical Engineering Seminar, Michigan State University, East Lansing, MI, invited.

Faeth, G.M. (2001) Surface Properties of Turbulent Liquid Jets in Still Air. 54th Annual Meeting, American Physical Society, Division of Fluid Dynamics, San Diego, CA, contributed.

Faeth, G.M. (2001) Primary Breakup of Turbulent Liquids. Spray, Spume and Foam Workshop, University of Marseille, Marseille, France, invited.

Faeth, G.M. (2001) Deformation and Drag Properties of Drops Subjected to Shock-Wave and Steady Disturbances. 54th Annual Meeting, American Physical Society, Division of Fluid Dynamics, San Diego, CA, contributed.

Faeth, G.M. (2001) Turbulence Generation in Homogeneous Polydisperse Particle-Laden Flows. 54th Annual Meeting, American Physical Society, Division of Fluid Dynamics, San Diego, CA, contributed.

Honors/Awards

Mazallon,J. Dai, Z. and Faeth, G.M. (1999) Best Propellants and Combustion Paper presented at the AIAA 37th Aerospace Sciences Meeting: "Aerodynamic Primary Breakup at the Surface of Round Nonturbulent Liquid Jets in Crossflow," Reno, NV.

Faeth, G.M. (1999) Invited Plenary Lecture, 5th ASME/JSME Joint Thermal Engineering Conference, San Diego, CA.

Faeth, G.M. (1999) Invited Plenary Lecture, 30th AIAA Fluid Dynamics Conference, Norfolk, VA.

Faeth, G.M. (1999) Invited Plenary Lecture, 52nd Annual Meeting of Division of Fluid Dynamics, American Physical Society, New Orleans, LA.

Faeth, G.M. (1999) Invited Zucrow Memorial Lecture, Purdue University, West Lafayette, IN.

Faeth, G.M. (1999) Invited Distinguished Lecture, Texas A&M University, College Station, TX.

Faeth, G.M. (1999) NASA, Public Service Medal, Washington, D.C.

Faeth, G.M. (2000) Highly-Cited Researcher Certificate, Institute for Scientific Information, Philadelphia, PA.

Faeth, G.M. (2001) Invited Plenary Lecture, 6th Intl. Conf. on Tech. and Combust. for a Clean Environment, Porto, Portugal

2. Secondary Breakup

2.1 Introduction

Secondary breakup of drops is an important fundamental process of multi-phase flows with applications to liquid atomization, dispersed multiphase flow, spray drying, combustion instability, heterogeneous detonations, the properties of rain and interactions between high-speed vehicles and rain, among others. In particular, recent studies of the structure of dense sprays confirm the conventional view of liquid atomization that primary breakup of the liquid surface yields drops that intrinsically are unstable to secondary breakup and that secondary breakup tends to control mixing rates in dense sprays in much the same way that drop vaporization tends to control mixing rates in dilute sprays, see Faeth (1990,1996), Faeth et al. (1995) and references cited therein. Motivated by these observations, the objectives of the present investigation were to study drop deformation and breakup for well-defined shock-wave disturbances.

A problem that is closely related to the secondary breakup of drops when exposed to shock-wave disturbances is the primary breakup of round nonturbulent liquid jets subjected to uniform crossflows. In particular, a recent experimental study of the breakup of round nonturbulent liquid jets in uniform crossflows due to Mazallon et al. (1999) found both qualitative and quantitative similarities between the primary breakup of liquid jets in crossflow and the secondary breakup of drops to shock-wave disturbances. In addition, the primary breakup of nonturbulent liquid jets in uniform crossflows is of practical interest due to the use of injectors involving flows of this type for both the primary combustors and the afterburners of high-performance aircraft. Motivated by these observations, the primary breakup of nonturbulent liquid jets was considered during the present investigation using computational methods similar to those considered during the present secondary breakup studies. The main focus of the present report, however, involves the secondary breakup properties of dispersed phases such as drops. Thus, findings concerning liquid jet breakup will not be considered any

further here, although the article describing the experimental jet study of Mazallon et al. (1999) can be found in Appendix E, and the computational aspects of the work are described by Aalburg et al. (2002b).

Reviews of past work on secondary breakup are reported by Faeth (1990,1996), Faeth et al. (1995), Hinze (1995), Hsiang and Faeth (1992,1993,1995) and references cited therein. These reviews indicate that regimes of drop deformation and breakup, and that the outcomes of breakup (i.e., drop size and velocity distributions after breakup) when liquid/gas density ratios are large and effects of liquid viscosity are small (small Ohnesorge number conditions), are known reasonably well. On the other hand, earlier work has shown the drop breakup processes can extend over significant distances and times compared to characteristic distances and times of the dense spray region. This observation motivated experimental studies of the temporal properties of secondary breakup in the bag and shear breakup regimes at large liquid/gas density ratios during prior experimental work in this laboratory due to Chou et al. (1997) and Chou and Faeth (1998). An objective of the present investigation was to extend these studies by completing a similar experimental study of multimode breakup at large liquid/gas density ratios. The following discussion of this study is brief, more details can be found in Dai and Faeth (2001). Finally, the articles by Chou and Faeth (1998) and Dai and Faeth (2001), both of which appeared during the present report period, can be found in Appendices E and F, respectively.

Another limitation of earlier studies of secondary drop breakup is that they generally have been limited to experimental studies carried out at large liquid/gas density ratios that can be readily provided by experiments carried out at atmospheric pressure. In order to avoid the problems of experimentation at elevated pressures required to examine secondary drop breakup at the small liquid/gas density ratios of many practical applications, these conditions were studied during the present investigation using computational methods. The following discussion of this study also is brief and more details can be found in Aalburg et al. (2002a) which can be found in Appendix A.

2.2 Experimental Methods

Apparatus. A shock tube with the driven section open to the atmosphere was used to generate shock-wave disturbances. The driven section was rectangular (38×64 mm) with a length of 6.7 m to provide 17-24 ms of uniform flow behind the shock wave. Shock strengths were weak (shock Mach numbers of 1.01-1.15); therefore, gas properties behind the shock waves approximated air at normal temperature and pressure. A vibrating capillary drop generator, with electrostatic selection to control the drop spacing, was used to provide a continuous drop stream to interact with the shock wave at the test location.

Instrumentation. Drops were observed in two ways: pulsed shadowgraph photographs to visualize the breakup process, and single- and double-pulsed holography to observe the outcome of breakup. See Hsiang and Faeth (1992,1993,1995), Chou et al. (1997) and Chou and Faeth (1998) for the details and experimental uncertainties of these measurements.

Test Conditions. Test conditions can be summarized most easily using the drop deformation and breakup regime map of Fig. 1. This map shows the various deformation and breakup regimes as a function of Weber and Ohnesorge numbers, as suggested by Hinze (1955). Only one region was considered during the present experimental study secondary breakup, namely, multimode breakup with We of 15-140, Oh less than 0.1, and liquid/gas density ratios greater than 500.

2.3 Computational Methods

The time-dependent, incompressible and axisymmetric Navier-Stokes equations were solved using the projection methods of Chorin (1968) with a multigrid Poisson solver for the pressure equation. The discretization in space was carried out on a staggered grid according to the marker and cell (MAC) method of Harlow and Welch (1965). The level set method of Sussman et al. (1994) was used to capture the liquid/gas interface and yielded the local fluid properties of each cell with a smooth transition between the gas and the liquid phases near the interface. A redistancing algorithm according to Sussman and Fatemi (1999) was used to maintain the level set as an accurate distance function at all times. The interface calculations allowed for effects of surface tension, pressure and shear forces, with surface tension represented as a body force distributed over an interface having finite thickness, following Brackbill et al. (1991). The discretization in both space and time were second-order accurate.

The domain size was typically $7.5\ r_o \times 15\ r_o$ and was covered with a moving grid having 192×384 cells. The boundary conditions were symmetric along the sides, with a fixed velocity across the inlet and a fixed pressure along the outlet. Tests of various-sized solution regions and finer grids caused less than a 3% change near breakup conditions in the results reported during this study. The simulations were started with an initially motionless radial plane of the drop being subjected to a sudden divergence-free velocity field. Except for the evaluation of the drop deformation for a constant body force, buoyancy was neglected. The flow was assumed to be isothermal with constant liquid and gas phase properties.

2.4 Results and Discussion

The multimode breakup regime is characterized by a wide variety of breakup topographies, which makes it a difficult regime to quantify, see Dai and Faeth (2001) for
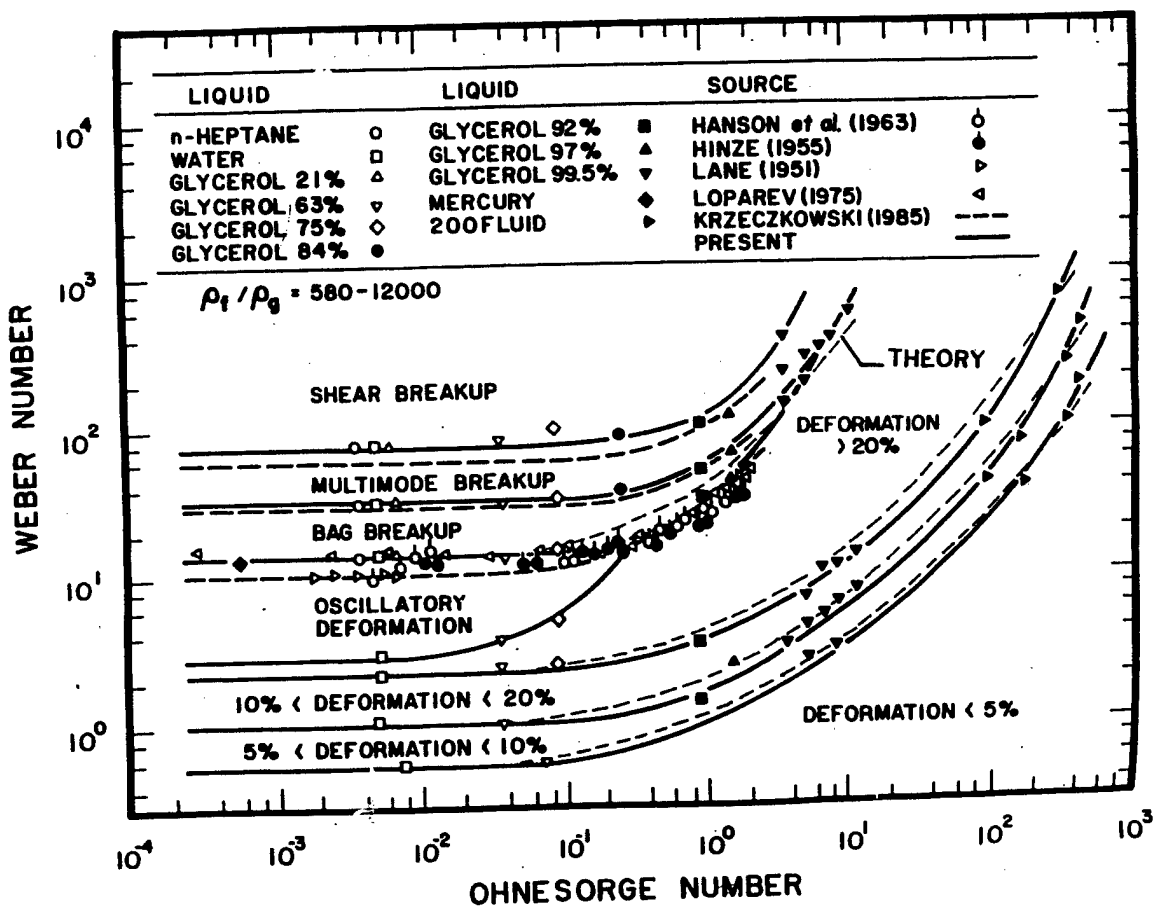
Figure 1 Drop deformation and breakup regime map for shock wave disturbances. Measurements of Hanson et al. (1963), Hinze (1955), Lane (1951), Loparev (1975), Kreczkowski (1985) and Hsiang and Faeth (1995).

extensive photographs of multimode breakup at various Weber numbers (We = 15, 20, 25, 32, 40, 50 and 81) and Chou et al. (1997) and Chou and Faeth (1998) for companion visualizations of the secondary breakup of drops in the bag and shear breakup regimes that bound the multimode breakup regime.

Important variables needed to treat the transient properties of secondary breakup in the multimode breakup regime are the times required for the onset and end of breakup. Measurements of these properties are plotted as a function of We, for $\rho_L/\rho_G > 500$ and $Oh < 0.1$, in Fig. 2. Results appearing in the figure include measurements of Hsiang and Faeth (1992), Chou et al. (1997), Chou and Faeth (1998) and the present investigation for We of 15-150, which spans the range from bag to well into the shear breakup regime (note that the ranges of the various breakup regimes are marked on the plot). The onset of breakup gradually decreases from $t/t^* = 3$ to 2 as We increases in the multimode breakup regime. In contrast, the end of breakup is at $t/t^* = 4$ for bag breakup increasing to $t/t^* = 7.5$ at We = 40 and then decreasing once again to $t/t^* = 5$ at We = 80, which is the start of shear breakup. For larger We, it is well known that t/t^* at the end of breakup remains relatively constant up to the largest values of We where breakup has been observed (Faeth 1996). The rather different behavior in the multimode breakup regime involves the development of a plume-like drop structure as We increases from the bag breakup regime, with this structure dominating the breakup process at We = 40, to finally an evolution from the plume breakup process to shear breakup as We increases in the range 40-80, see Dai and Faeth (2001) for a complete discussion of these transitions.

Within the multimode breakup regime, there are four kinds of drops that are formed: small drops formed from breakup of the bag associated with bag breakup, large drops formed from breakup of the ring structure at the base of the bag, relatively large drops formed by breakup of the plume structure mentioned in connection with Fig. 2, and finally, drops of various sizes formed from the core (parent or drop-forming) drop that dominates the shear breakup process.

The volume fractions of drops formed from these four drop breakup structures in the multimode breakup regime are plotted as a function of the Weber number in Fig. 3. At the start of the multimode breakup regime, We = 15, 75% of the drop volume comes from the ring and the rest, 25%, from the bag. The volume of drops coming from the bag and ring progressively decreases with increasing Weber number, with drops from bag and ring disappearing at We = 30 and 40, respectively. The volume of drops formed from the plume reaches a maximum of roughly 25% at We = 30, whereas the volume of drops formed from the core drop begins to increase at We = 18 and becomes 100% at We = 40.
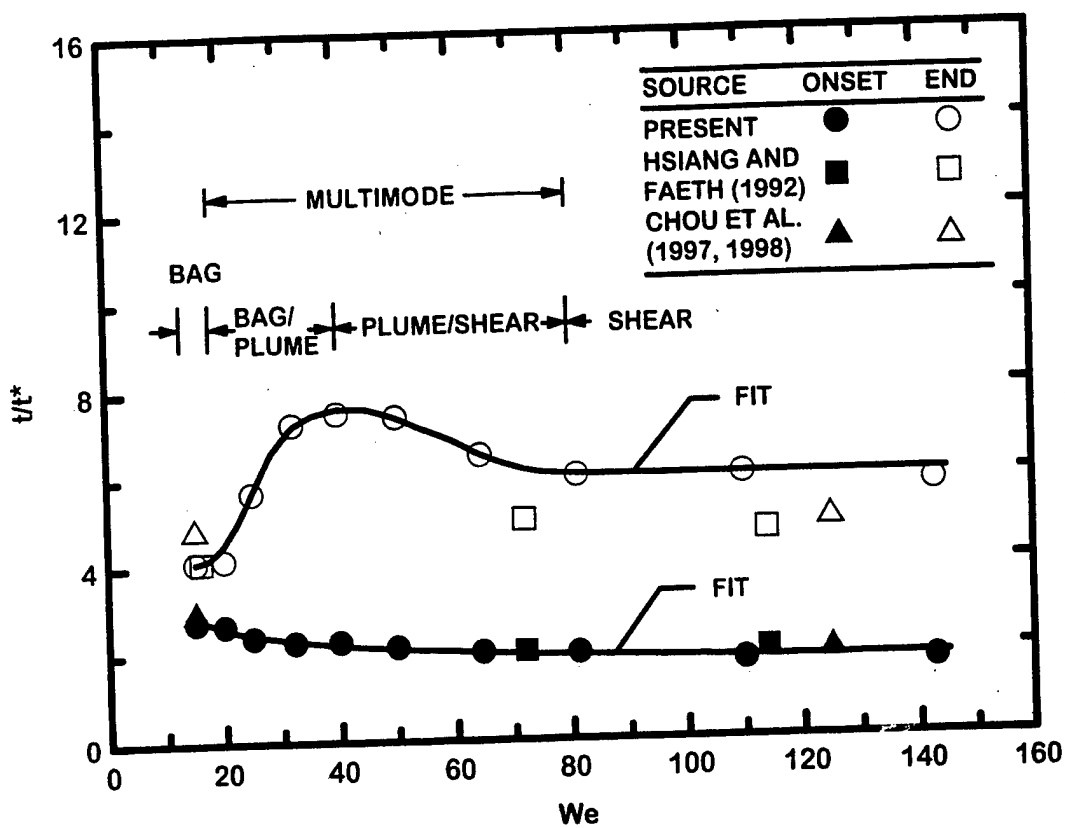
Figure 2 Measurements of times of onset and end of breakup as a function of Weber number for shock wave disturbances. Measurements of Hsiang and Faeth (1992), Chou et al. (1998) and Dai et al. (2001). From Dai et al. (2001).
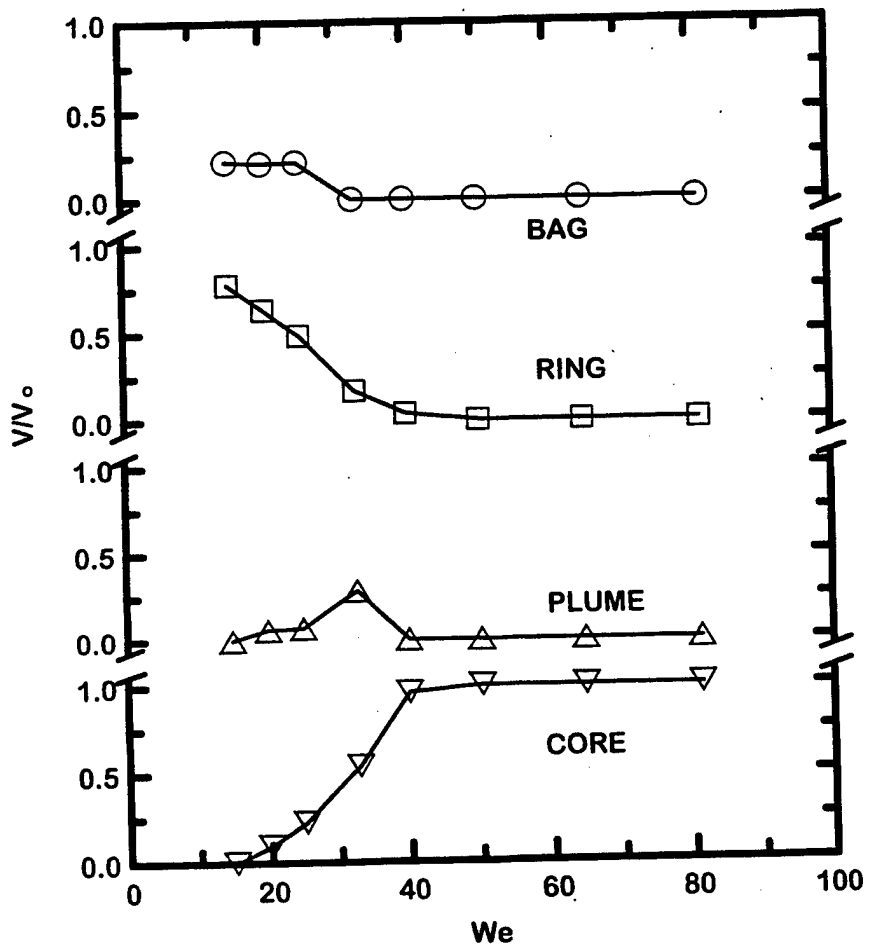
Figure 3 Volumes of bag, ring, plume and core drops as a function of Weber number for shock wave disturbances in the multimode regime. From Dai et al. (2001).

The sizes of the ring, plume and core drops during multimode breakup are plotted as a function of We in Fig. 4; the sizes of the bag drops were too small to be resolved during the measurements. The sizes are given in Fig. 4 as SMD/d_0 for each regime, with each drop group being approximately monodisperse. As in Fig. 3, the drops formed from the core drop dominate properties for We > 40; in this region, the complete size distribution is reasonably approximated by the root normal distribution if the core drop is not included, as discussed by Chou et al. (1997).

The velocities of the parent (core or drop-forming) and post-breakup drops are plotted as a function of time during breakup in Fig. 5. Chou and Faeth (1998) present a simplified analysis that is to be helpful for correlating these drop velocities. The parent drop exhibits considerable acceleration during the pre-breakup period, caused by growth of its cross-stream dimension due to drop deformation which increases its drag (somewhat like opening an umbrella on a windy day). Near the onset of breakup, the velocities of post-breakup drops are larger than the parent drop because these drops are small and tend to accommodate to the gas velocity faster than the relatively large parent drop. Finally, similar to bag breakup, see Chou and Faeth (1998), final values of u_p and u_s-u_p tend to be comparable, which implies a reduction of the relative velocity of the parent drop by roughly 50% during the time of breakup. This is substantial and highlights the importance of treating secondary breakup as a rate process rather than by jump conditions.

Finally, the rate of removal of drop liquid from the parent drop is plotted as a function of time during breakup in Fig. 6, for the relatively simple case of near-bag breakup conditions, where theory has been reasonably successful in describing breakup events, see Dai and Faeth (2001) for discussion of the more complex multimode regime. For bag breakup, the breakup of bag and the ring occurs relatively rapidly as singular events; these become smoothed out during the more complex multimode regime.

Given the results of Chou et al. (1997), Chou and Faeth (1998) and Dai and Faeth (2001), a reasonable beginning has been made in defining the temporal properties of secondary drop breakup at the large liquid/gas density ratios and small Ohnesorge number conditions representative of conditions in sprays at atmospheric pressure. Thus, the next, or computational, phase of the study, was undertaken in order to begin to gain a better understanding of secondary breakup at the small liquid/gas density ratio and large Ohnesorge number conditions encountered in the spray combustion processes of practical propulsion systems. These results will be considered next.
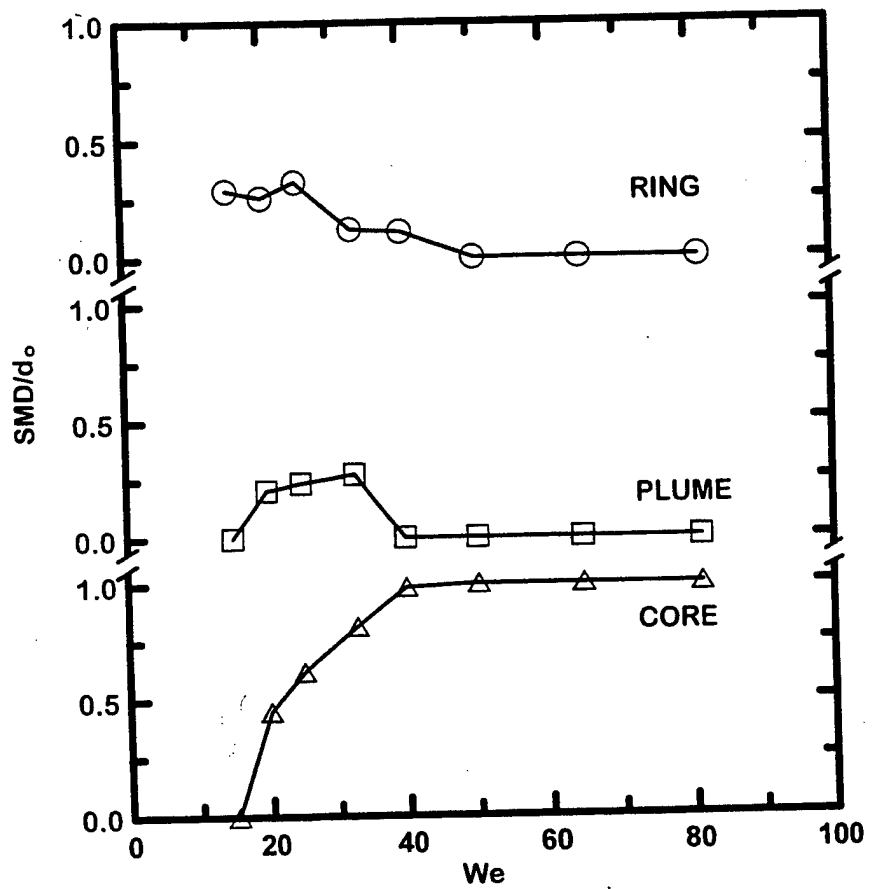
Figure 4 SMD of the ring, plume and core drops as a function
of Weber number for shock wave disturbances in the multi-
mode regime. From Dai et al. (2001).
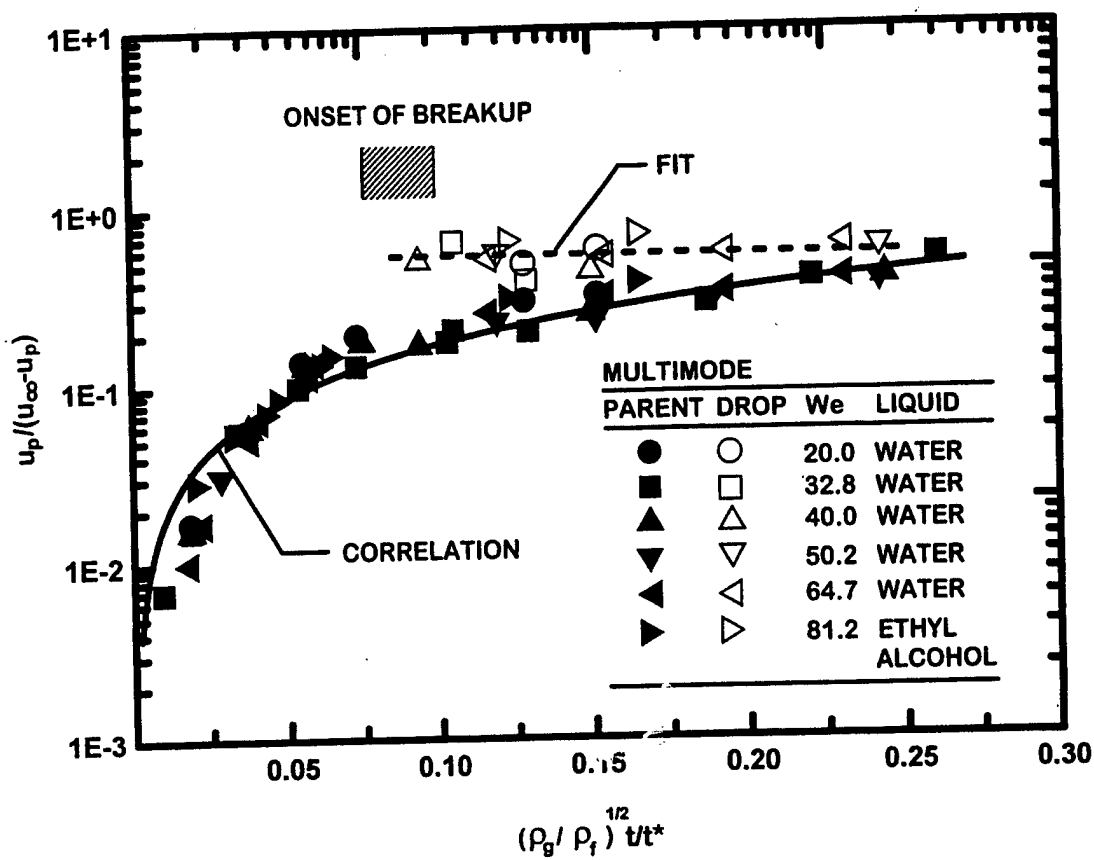
Figure 5 Velocities of parent and post drop breakup drops as a function of time during breakup for shock wave disturbances in the multimode regime. From Dai et al. (2001).
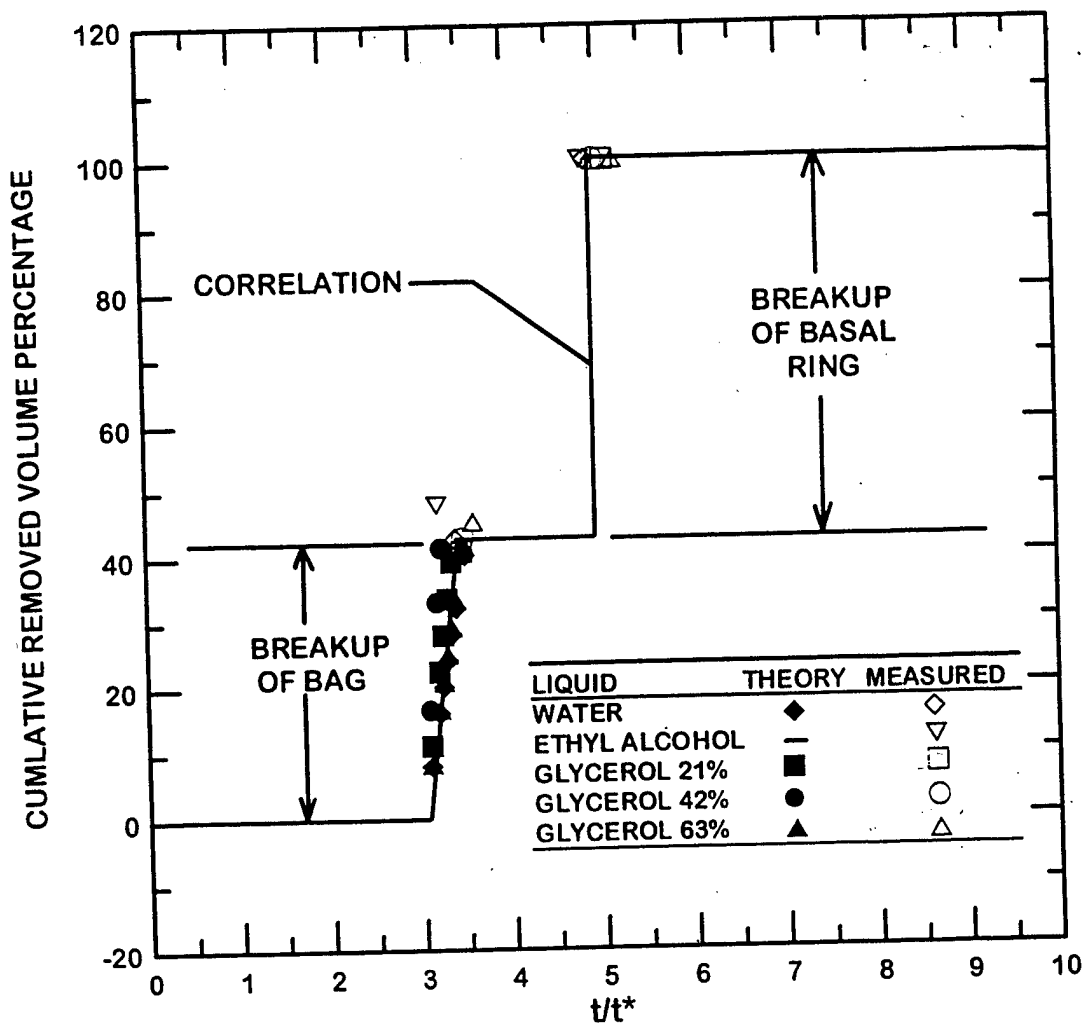
Figure 6 Cumulative removed volume percentage of liquid from the parent drop as a function of time during bag breakup. From Chou and Faeth (1998).

2.5 Computational Results and Discussion

Prior to considering the deformation and breakup properties of drops subjected to shock-wave disturbances, the numerical predictions were evaluated using earlier measurements and computations of the properties of solid spheres and deforming drops. This included both steady wake lengths and the drag coefficients of solid spheres as a function of Reynolds number (but limited to conditions prior to transition to oscillating wakes at Re = 130).

The wake length, L, measured from the downstream stagnation point on the drop to the point where the flow reattaches at the axis, normalized by the drop diameter is plotted as a function of Reynolds number in Fig. 7. The steady wake length progressively increases with increasing Reynolds number and present predictions are in good agreement with existing measurements and earlier predictions.

Figure 8 is an illustration of the drag coefficient calculated from the momentum loss in the gas phase across the drop plotted as a function of the Reynolds number; the agreement between measurements and current predictions is excellent. Although C_D is relatively constant for large Re, it exhibits a large increase as the Re approaches the Stokes range; this behavior will be shown to have a large impact on drop deformation and breakup that was not recognized earlier due to limitations of experiments.

Past measurements at large liquid/gas density ratios have shown that drop breakup is associated with drop deformation levels $((d_c-d_o)/d_o)$ exceeding 60% (Hsiang and Faeth 1992,1993,1995). Thus, this criterion was adopted to provide estimates of drop breakup conditions, thereby avoiding the intractability of complete numerical simulations of breakup which would involve large numbers of spatial and temporal grid points due to large range of spatial and temporal scales and three-dimensional nature of actual drop breakup processes (see Chou et al. 1997; Chou and Faeth 1998; Dai and Faeth 2001).

Exploiting the deformation threshold for breakup just mentioned, breakup regime boundaries for liquid drops subjected to shock-wave disturbances were found in terms of the classical We-Oh coordinates first proposed by Hinze (1955). The resulting plot is illustrated in Fig. 9. Parametric conditions shown on the plot include predicted breakup boundaries for Re = 25 and ρ_L/ρ_G = 2, Re = 50 and ρ_L/ρ_G = 2, 8, 32 and ∞, and Re = 100 and ρ_L/ρ_G = 2. The measured breakup regime boundary of Hsiang and Faeth (1995) is also shown on the plot. First of all, it should be noted that predicted variations of the breakup regime boundary are not large for variations of ρ_L/ρ_G in the range 2-∞; therefore, it appears that the liquid/gas density ratio does not have a large effect on the fundamental secondary breakup properties of drops. Finally, the
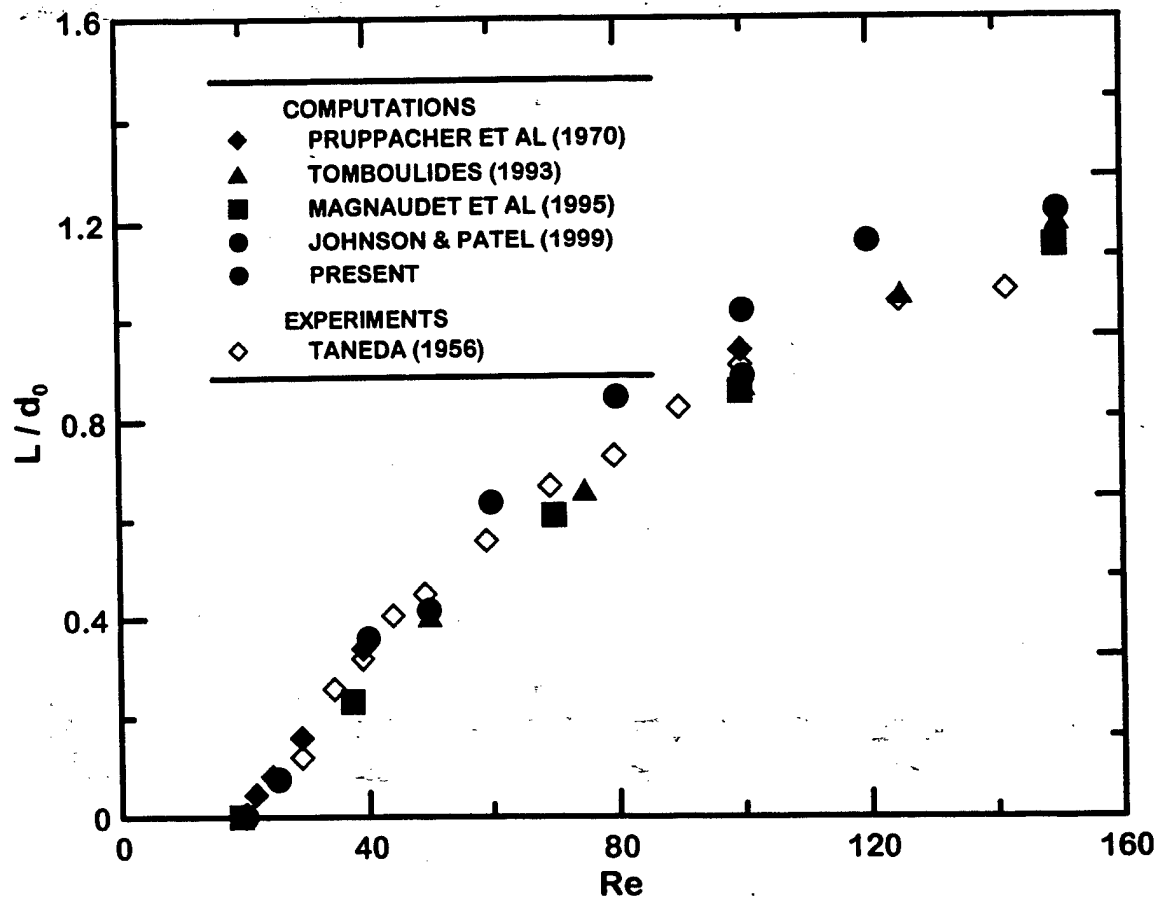
Figure 7 Measured and predicted steady wakelength behind a sphere as a function of Reynolds number for values smaller than the onset of instabilities (Re < 130). Measurements from Taneda (1956); predictions from Pruppacker et al. (1970), Tomboulidis (1993), Magnaudet et al. (1995), Johnson and Patel (1999) and the present investigation. From Aalburg et al. (2002a).
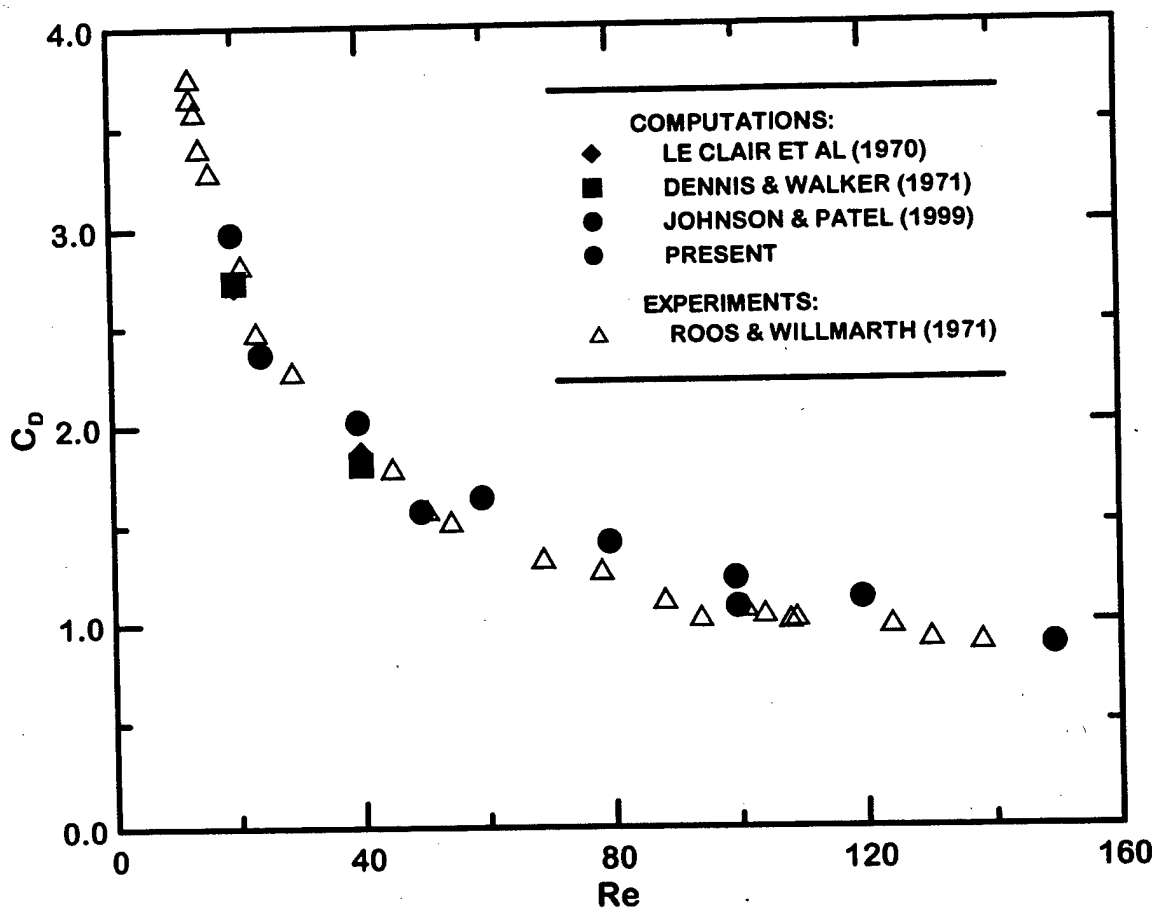
Figure 8 Measured and predicted drag coefficients as a function of Reynolds number for spheres. Measurements from Roos and Willmarth (1971); predictions from LeClair et al. (1970), Johnson and Patel (1999)) and the present investigation.From Aalburg et al. (2002a).

extrapolated breakup line for $\rho_L/\rho_G = \infty$ agrees quite well with the large ρ_L/ρ_G measurements of Hsiang and Faeth (1995), even for large Oh conditions, which helps justify the present deformation threshold for breakup.

The influence of the Reynolds number on drop breakup for $\rho_L/\rho_G = 2$ is seen to be small for Re > 50. But results at Re = 25 indicate significantly increased resistance to breakup as Re becomes small — toward the Stokes regime. Studying present computed results shows that this behavior comes about due to the effect of Reynolds number on drag, shown in Fig. 8. For Re < 50, drag coefficients increase appreciably as the Stokes range is approached. This increases the rate of acceleration of the drop toward the ambient velocity so that the velocity defect (and thus the local Weber number) at the maximum deformation condition is reduced. As a result, larger initial Weber numbers are needed for breakup. This effect was not observed for past measurements of drop breakup because test conditions generally did not consider Re < 50 where variations of C_D with the Reynolds number become important.

Somewhat analogous to the effect of Re to increase the drop drag coefficient, thus causing droop acceleration to reduce relative drop/gas velocities when maximum deformation conditions are reached, is the effect of increasing Ohnesorge number on the Weber number needed for breakup. The results illustrated in Fig. 9 show that for small Ohnesorge numbers (Oh < 0.1), liquid breakup is relatively independent of the Ohnesorge number and is first observed for Weber numbers on the order of 10; whereas for large Ohnesorge number (Oh > 1), Weber numbers at the onset of breakup progressively increase and become proportional to the square of the Ohnesorge number, or:

$$\log(\mathrm{We}) \approx 2 \cdot \log(\mathrm{Oh}) \tag{1}$$

which implies

$$\sqrt{\mathrm{We}}\,/\mathrm{Oh} \approx \mathrm{const} \tag{2}$$

This behavior can be explained based on effects of liquid viscosity slowing the rate of deformation of the drop as the Ohnesorge number increases; as a result, the velocity difference between the drop and the ambient gas (for the corresponding local Weber number) is reduced compared to small Ohnesorge number conditions. As a result, larger initial Weber numbers are needed for breakup (Hsiang and Faeth 1995).

On the other hand, the computations also revealed an effect of liquid/gas viscosity ratio at large Oh, this was not observed during the experiments due to problems of experimentally
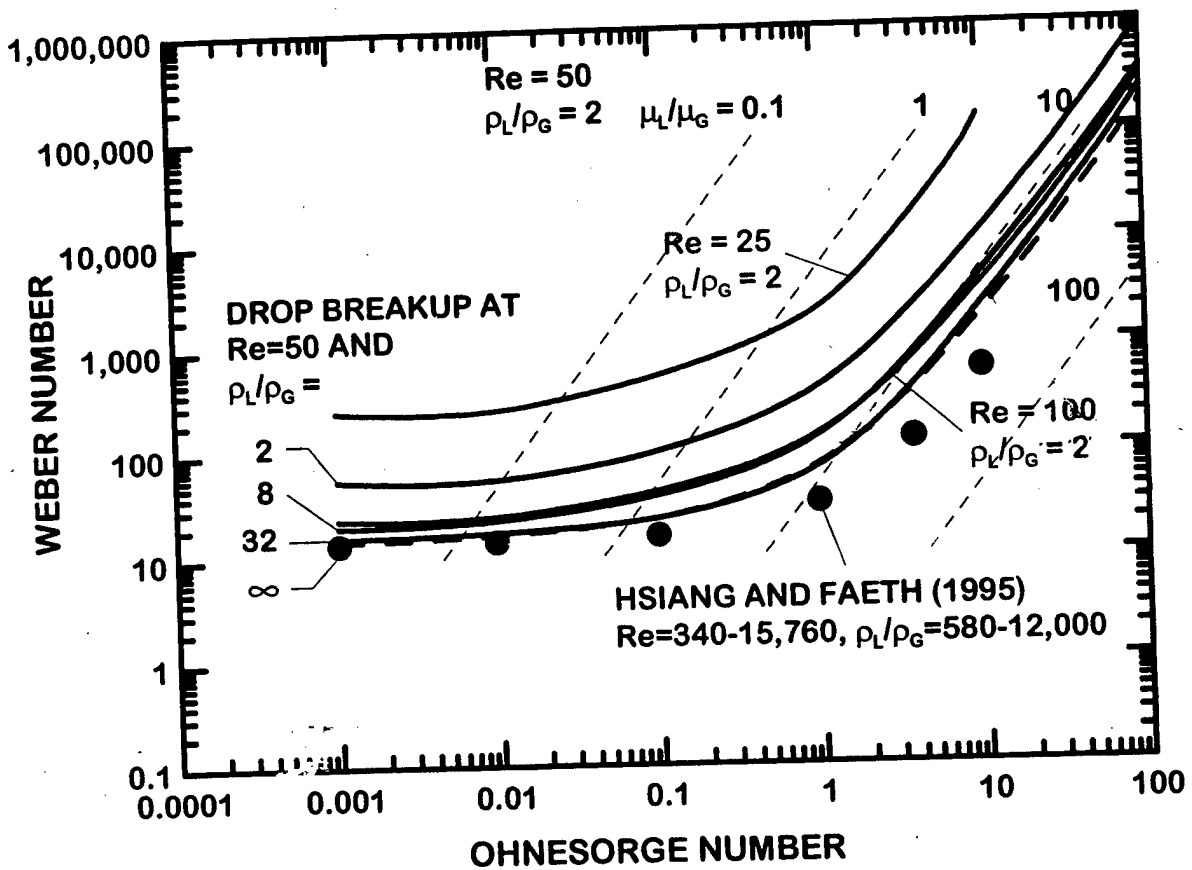
Figure 9   Measured and predicted breakup regime map in the classical drag-force/surface-tension-force (We) and viscous-force/surface-tension force (Oh) coordinates of Hinze (1975). Measurements from Hsiang and Faeth (1995), predictions from the present investigation. From Aalburg et al. (2002a).

reaching these conditions. This behavior is illustrated by the lines of constant viscosity ratio μ_L/μ_G, which are specified completely by the values of We and Oh for given values of Re and ρ_L/ρ_G, and which have been drawn for $\mu_L/\mu_G = 0.1$, 1, 10 and 100 for $\rho_L/\rho_G = 2$ and Re = 50 in Fig. 9. It is evident that while for small Ohnesorge numbers, where the surface-tension-forces dominate over liquid viscous forces, the ratio of drag-forces/surface-tension-forces (the We number) is the governing breakup parameter, conditions at large Ohnesorge numbers, where liquid viscous forces dominate over surface-tension-forces, involve a rather restricted range of μ_L/μ_G for a given Reynolds number and liquid/gas density ratio.

The large effect of liquid/gas density ratio on the Hinze form of the secondary breakup map regime is not desirable and alternative plots were sought. A better approach for representing conditions where effects of liquid viscosity were large, large Oh, was to account for liquid viscous effects directly by plotting the ratio of drag to liquid viscous forces instead of the ratio of drag to surface-tension forces, as follows:

$$\frac{\text{drag forces}}{\text{liquid viscous forces}} = Re \sqrt{\frac{\rho_L}{\rho_G}} \frac{\mu_G}{\mu_L} = \frac{\sqrt{We}}{Oh} \qquad (3)$$

This turns out to be precisely what the analysis of the slopes of the breakup lines at large Oh yielded in Eq. 2. Figure 10 is an illustration of the breakup regime map in the new coordinates, plotting the ratio of drag to liquid viscous forces, $We^{1/2}/Oh$, as a function of the ratio of surface tension to liquid viscous forces, $1/Oh$. This approach yields secondary drop deformation and breakup regime boundaries that are relatively independent of both liquid/gas density and viscosity ratios and are in excellent agreement with existing measurements of these properties at small Oh.

2.6 Conclusions

There were two phases to this portion of the investigation: (1) an experimental study of the secondary breakup properties of drops in the multimode breakup regime, and (2) a computational study of the deformation and breakup properties of round liquid drops subjected to shock-wave disturbances. The experimental study of drop breakup in the multimode breakup regime involved Oh > 0.1 where effects of liquid viscosity are small, and yielded the following major conclusions:

1. With increasing Weber numbers, the multimode breakup regime begins at the end of the bag breakup regime at We = 18 and ends at the start of the shear breakup regime at We = 80. The multimode breakup regime can be subdivided into a bag/plume breakup regime for We
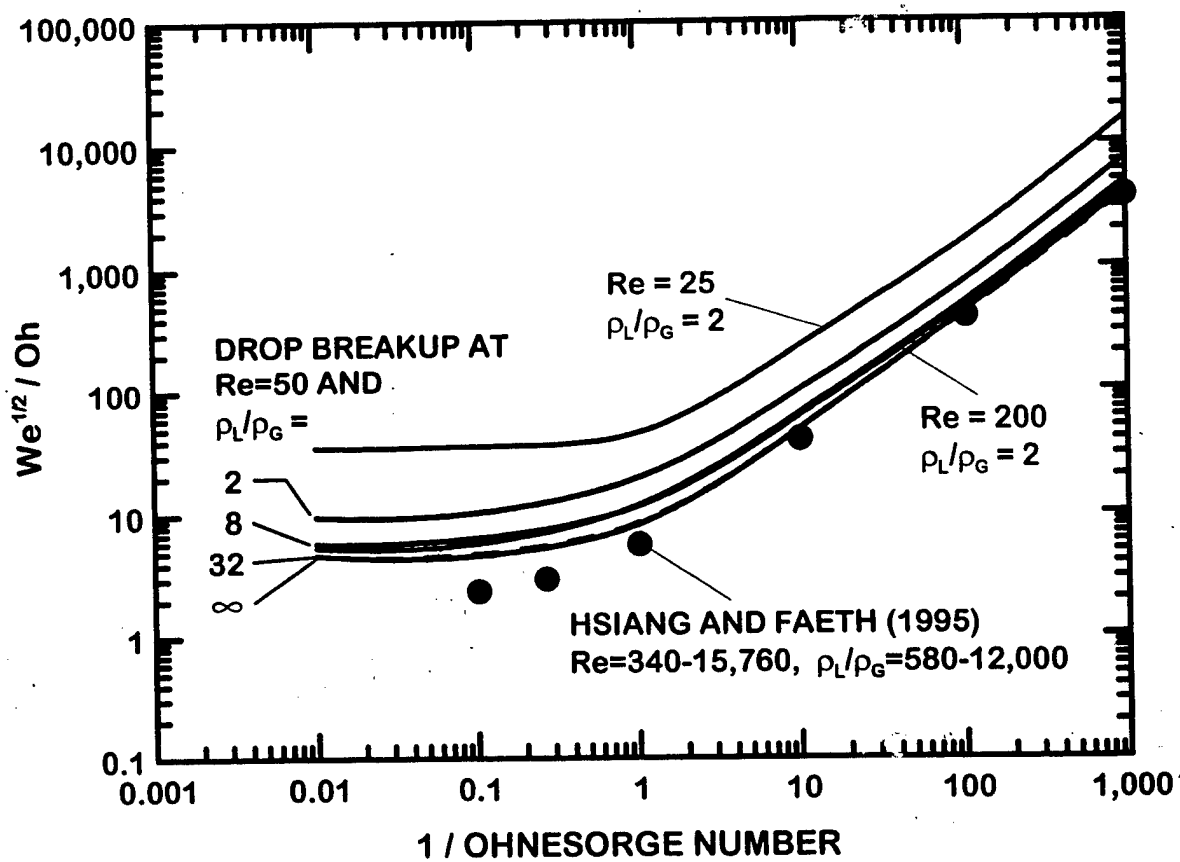
Figure 10 Measured and predicted breakup regime map in the revised drag-force/liquid-viscous-force ($We^{1/2}/Oh$) and surface-tension/liquid-viscous-force force ($1/Oh$) coordinates. Measurements from Hsiang and Faeth (1995), predictions from the present investigation. From Aalburg et al. (2002a).

= 18-40 and a plume/shear breakup regime for We = 40-80 with the transition between these regimes fixed by the disappearance of bag and ring structures and the attainment of a maximum breakup time.

2. With increasing We in the range 18-80, $t/t*$ at the onset of breakup decreases from a value of 3.0 to a value of 2.0 at the onset of shear breakup. The end of breakup has values of $t/t*$ = 4.0 and 5.0 at the end of bag breakup and the beginning of shear breakup but reaches a maximum value of $t/t*$ of 7.5 at the transition between the bag/plume and plume/shear regimes at We = 40 because Rayleigh breakup of the plume is slow.

3. Drop deformation and drag properties prior to the onset of breakup appear to be relatively universal for We of 13-150. The drop/drag coefficient transitions from values similar to spheres to values similar to thin disks as the cross-stream dimension of the drop D_{Lmax}/d_o varies in the range 1.0-2.0 and the onset of breakup is approached. These two effects cause drop/drag forces to increase 16:1 in the deformation period for present test conditions, with associated drop accelerations leading to breakup onset.

4. Liquid volume fractions associated with the bag, ring, plume and core drops have been found for We of 18-80, and the sizes of ring, plume and core drops have been found for the same range of conditions. The sizes of drops formed by breakup of the bag and the core drops were not found but should approximate the known behavior in the bag and shear breakup regimes until specific information becomes available. The velocities of the parent drop were similar to behavior observed by Chou and Faeth (1998) for bag breakup, whereas the velocities of post-breakup drops exhibited continuous variations with increasing $t/t*$ and did not indicate any sudden changes at transitions to new breakup regimes.

5. The mass removal rates of liquid from the parent drop resembles behavior in the bag breakup regime at small We and behavior in the shear breakup regime at large We. The differences between these behaviors are not large compared to experimental uncertainties, however, yielding a reasonable correlation of liquid removal rates for spray modeling purposes.

The conclusions of the present computational study of the deformation and breakup properties of round liquid drops subjected to shock-wave disturbances are as follows:

1. Predictions and measurements of wake and drag properties of spheres, and the deformation and breakup properties of drops subjected to steady and shock-wave disturbances are in good agreement.

2. The liquid/gas density ratio has only a small effect on the the deformation and breakup properties of drops.

3. The effects of Re number are small for large Re. However, as Re approaches the Stokes range, the We required for breakup increases significantly with decreasing Re due to corresponding increases of the drag coefficient.

4. At large Oh, surface tension has a negligible influence on breakup. Then plotting the ratio of drag to liquid viscous forces, $We^{1/2}/Oh$, as a function of surface tension to liquid viscous forces, $1/Oh$, yields breakup regime boundaries that are constant for large Oh, however, and are relatively independent of the liquid/gas density ratio.

3. Turbulence Generation

3.1 Introduction

Turbulence generation by drops controls the turbulence properties, and thus the mixing properties, within dense sprays (Faeth et al. 1990, 1996; Faeth et al. 1995). This behavior follows because velocities are relatively uniform in dense sprays, inhibiting the conventional production of turbulence, whereas the relative velocities of drops are large, which implies significant flow disturbances from drop wakes within dense sprays.

Drop-generated turbulence differs from grid-generated turbulence because drops are present throughout the flow, and their arrival at any point is random, yielding a truly stationary turbulent field. In contrast, grids generate turbulence at a plane of the flow yielding an unsteady flow field that subsequently decays. Thus, drop-generated turbulence is unique compared to conventional turbulence and has been studied very little in spite of its importance to practical spray processes. Motivated by these observations, turbulence generation was studied during this phase of the present investigation.

Past studies of turbulence generation have mainly considered homogeneous dilute dispersed flows (Lance and Bataille 1982, 1991; Parthasarathy and Faeth 1990; Mizukami et al. 1992). Lance and Bataille (1982,1991) studied homogeneous air/water bubbly flows downstream of a turbulence-generating grid. Effects of turbulence generation were observed as progressive increases of turbulence levels with increasing void fractions. Unfortunately, these results are difficult to interpret due to combined effects of turbulence generation and grid-generated turbulence.

Initial work in this laboratory on turbulence generation is described by Parthasarathy and Faeth (1987, 1990) and Mizukami et al. (1992). Aside from qualitative observations of turbulence generation in bubbly jets (Parthasarathy and Faeth 1987) experimental conditions consisted of uniform fluxes of nearly monodisperse spherical glass beads falling at roughly constant speeds in stagnant (in the mean) air and water. Measurements included phase velocities and turbulence properties of the continuous phase. Turbulence properties were analyzed using a stochastic method based on Campbell's theorem (Rice 1954) that involved synthesis of randomly-arriving particle wakes. The measurements showed that particle-generated turbulence had rather different properties from conventional turbulence. The theory helped explain this behavior as a result of the random arrival of particle wakes so that *mean* wake properties contribute to the apparent turbulence field. However, although the stochastic theory assisted data interpretation, quantitative predictions were not very satisfactory because particle wake properties at intermediate Reynolds numbers (typical of drops in sprays) in turbulent environments were unknown and had to be extrapolated from results at large Reynolds number turbulent wakes in nonturbulent environments. These studies were also problematical because the nearly stagnant (in the mean) continuous phases caused significant experimental uncertainties due to the resulting large turbulence intensities (up to 1000%) along with problems of buoyant disturbances.

Subsequent work sought to resolve the properties of wakes at intermediate Reynolds numbers in turbulent (roughly isotopic) environments (Wu and Faeth 1993,1994,1995). It was found that these wakes scaled in the same manner as self-preserving laminar wakes (Schlichting 1975) but with enhanced viscosities due to the presence of turbulence. Thus, the wakes were termed "laminar-like turbulent wakes." Naturally, the properties of laminar-like turbulent wakes differed considerably from the wake properties assumed by Parthasarathy and Faeth (1990) and Mizukami et al. (1992). These results also suggested that turbulence generation dominated flows are likely to consist of laminar-like turbulent wakes embedded in relatively large inter-wake turbulent regions. Nevertheless, differences between the ambient turbulence properties of the wake studies and actual flows dominated by turbulence generation are a concern.

Based on this status, the specific objectives of the present study were as follows: (1) to complete new measurements of flow properties resulting from turbulence generation with reduced experimental uncertainties, (2) to use the measurements to determine the nature of the wake disturbances and the potential for wake-to-wake interactions during turbulence generation, and (3) to use the measurements to highlight differences between turbulence fields associated with turbulence generation and more conventional turbulence. The present discussion of the study is brief, see Chen et al. (2000) and Chen and Faeth (2000,2001) for more details.

3.2 Experimental Methods

Apparatus. A sketch of the test apparatus appears in Fig. 11. The arrangement consists of a vertical counterflow wind tunnel with upflowing air and freely-falling particles. The air flow system consisted of a rounded inlet, a flow straightener and a contraction with air flow supplied by a variable-speed blower at the top of the tunnel. The particle flow was provided by a variable-speed screw feeder with the particles dispersed by an array of screens and finally aligned to the vertical direction using a flow straightener. The test section has a 305 × 305 mm crossection with glass side walls to provide optical access.

Instrumentation. Particle number fluxes were measured by collecting particles in a thin-walled cylindrical container that could be traversed across the test section.

Gas and particle velocities were measured using a traversible laser velocimetry (LV) system. A single-channel dual-beam, forward-scatter, frequency-shifted LV was used, finding streamwise and crosstream velocities by rotating the optics accordingly. The air flow was seeded with oil particles for gas velocity measurements but was not seeded for particle velocity measurements. Particle velocity signals were readily determined due to their large signal amplitudes and nearly constant velocities. Wake discrimination measurements were also made, allowing the properties of the interwake region to be measured as described by Chen and Faeth (2001).

Test Conditions. The experiments involved nearly monodisperse spherical glass particles having nominal diameters of 0.5, 1.1 and 2.2 mm. These particles yielded Reynolds numbers in the range 106-990. Turbulence intensities relative to the mean gas velocity (1.1 m/s) were less than 25%. The flows were dominated by turbulence generation with direct dissipation of turbulence due to particles less than 2%. Particle volume fractions were less than 0.003% so the flows were very dilute. The resulting relative turbulence intensities due to turbulence generation were in the range 0.2-5.0%.

Recent experiments have considered polydisperse (bimodal) particle flows, provided by a second particle feeder. The particles for these experiments consist of binary pairs of the monodisperse particle populations considered during the first phase of the study. Study of the polydisperse flows is still in progress and information about these flows is not yet complete; therefore, the following discussion will be limited to the monodisperse flows where test results and analysis are relatively complete.
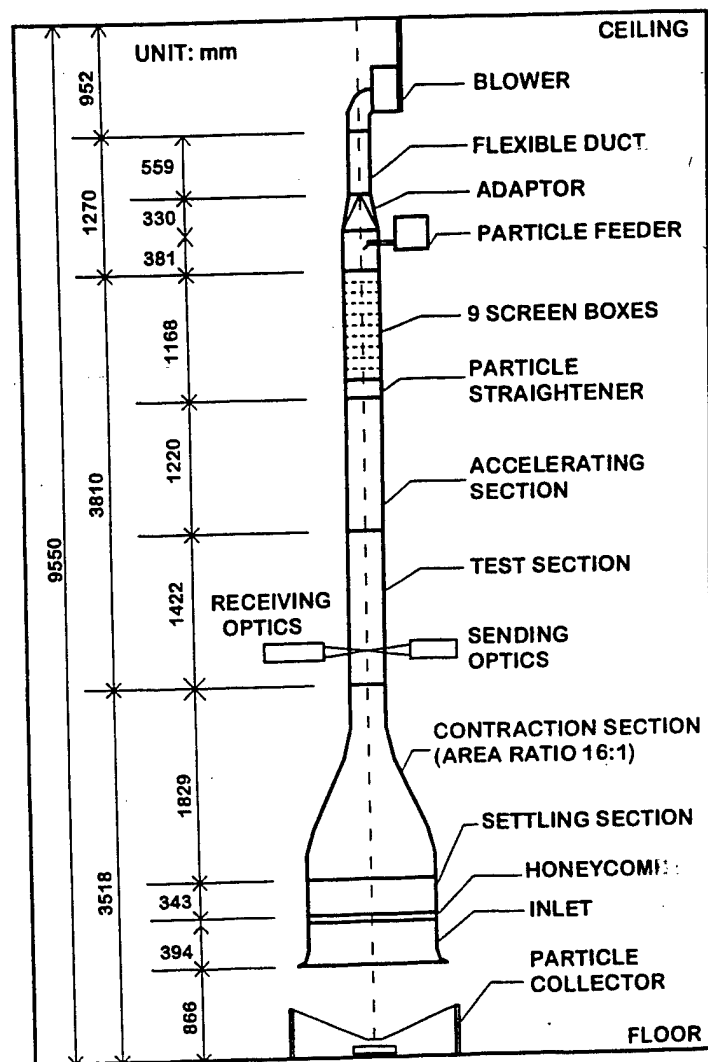
Figure 11 Sketch of the counterflow particle/air wind tunnel. From Chen et al. (2000).

3.3 Results and Discussion

Apparatus Evaluation. Sampling measurements showed that particle fluxes varied less than 10% over the central 205×205 mm cross-section of the flow where velocity measurements were made. Mean and fluctuating particle and gas velocities were uniform over the same cross-section for positions ± 100 mm from the normal measuring plane.

Particle Wake Properties. Direct temporal records of streamwise and crosstream velocities properly indicated wake disturbances that increased in frequency with increasing particle fluxes. Typical records indicating effects of particle Reynolds numbers for mid-range particle loadings are illustrated in Fig. 12 (Note that u and v records were not obtained at the same time). Relatively large negative spikes are observed on the streamwise velocity records indicating wake disturbances. Corresponding disturbances on the crosstream velocity records are absent for the 0.5 mm particles and have both negative and positive (or both) values for the larger particles. This behavior is expected based on the known properties of laminar-like turbulent wakes (Wu and Faeth 1994, 1995). In particular, mean crosstream velocities in these wakes are always small whereas the crosstream turbulence contribution is small for the 0.5 mm particles whose Re are below the onset of eddy shedding into the wake. In contrast, laminar-like turbulent wakes properties of the 1.1 and 2.2 mm particles have significant crosstream velocity fluctuations which explains the crosstream wake disturbances seen for these conditions. Thus, the results of Fig. 12 are strongly supportive of laminar-like turbulent wake behavior for the present test flows.

A further evaluation of particle wake properties is illustrated in Fig. 13. These results involve measurements of mean velocities in particle wakes for various particle sizes. Measurements were obtained for various maximum velocity defects which represent results for paths of the LV measuring volume at various radial distances from the wake axis. Effects of turbulence were handled by averaging several velocity records. Predictions for the same mean velocity defects, particle sizes and ambient turbulence intensities were obtained from the laminar-like turbulent wake properties reported by Wu and Faeth (1994, 1995). The agreement between measurements and predictions is excellent, supporting the presence of laminar-like turbulent wake properties for turbulence generation processes typical of sprays.

The proportions of wake and inter-wake regions were estimated based on the laminar-like turbulent wake properties combined with stochastic simulations to find realizations of particle positions. Laminar-like turbulent wakes were associated with each particle conservatively assuming that wake radii were equal to twice the characteristic wake radii and extended in the streamwise direction until the maximum mean velocity defect equaled the ambient rms turbulent fluctuations. These results indicated that wake cross-sectional areas generally were less than 30%
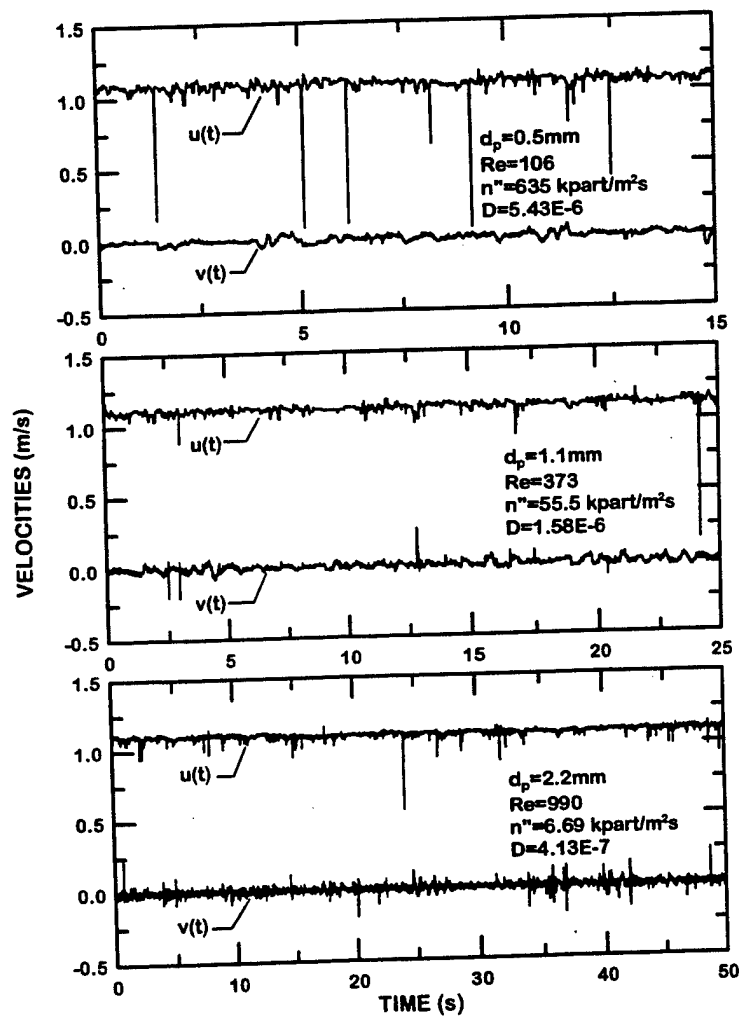
Figure 12 Effects of particle loading and size on streamwise and cross-stream velocity records. From Chen et al. (2000).
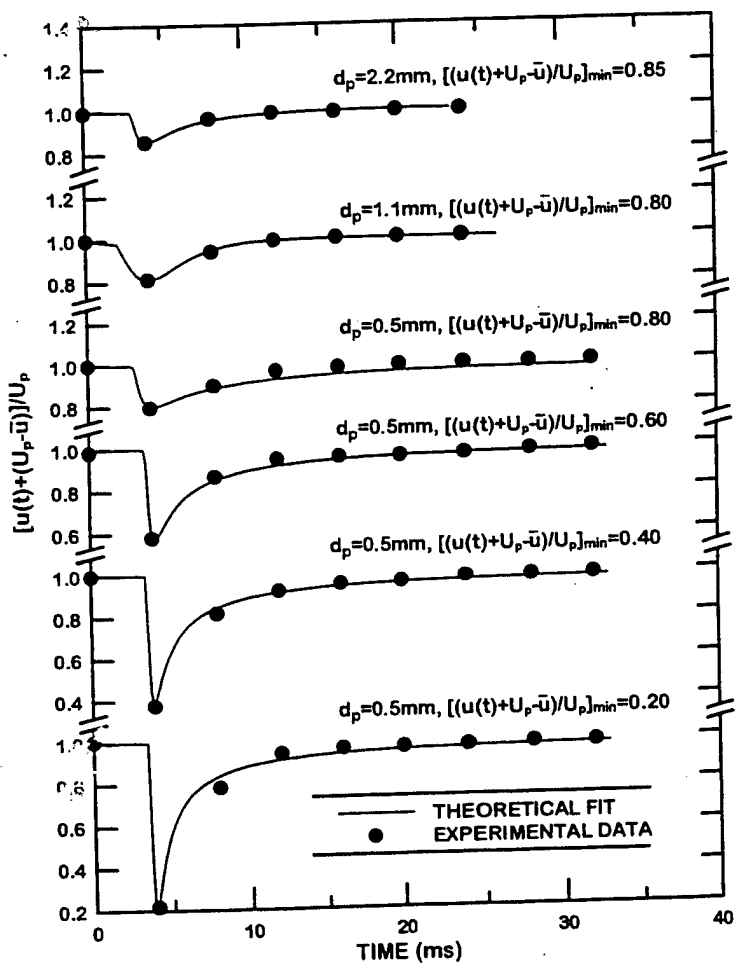
Figure 13 Measured and predicted streamwise velocities in particle wakes as a function of time for various velocity defects and particle sizes. From Chen et al. (2000).

of the available cross-sectional area and that less than 25% of the wakes experienced direct wake/wake interactions (mainly weak interactions far from both particles). Thus, the present test flows involve laminar-like turbulent wakes surrounded by relatively large inter-wake regions with occasional strong wake/wake interactions: actual dense sprays should be similar (Chen et al. 2000).

Interwake Properties (Relative Turbulence Intensities). Correlations of the properties of the turbulent interwake region were sought by drawing analogies between the turbulent interwake region and grid-generated turbulence. Past experimental observations show that turbulence downstream of grids can be divided into three regions: (1) a developing region near the grids, where the wakes from grid elements are merging and the turbulence flow is inhomogeneous and anisotropic; (2) an initial-decay region where the turbulent flow is nearly homogeneous and is locally isotropic; and (3) a final decay region, where viscous effects dominate, regions containing vorticity become sparse (giving the appearance of isolated turbulent spots from single-point measurements), and the turbulence decays more rapidly than in the initial decay region. Thus, comparing the turbulent interwake region with grid-generated turbulence suggests that the wake disturbances of turbulence generation correspond to the developing region of grid-generated turbulence and that the turbulent interwake region of turbulence generation corresponds to either the initial- or final-decay regions of grid-generated turbulence. Batchelor and Townsend (1948a,b) suggest a value of $Re_\lambda \approx 5$ as the condition for the onset of the final-decay region for grid-generated turbulence; therefore, the present turbulent interwake regions involving $Re_\lambda \approx 0.4$-3.5 have significant potential for behavior analogous to the final decay region.

The analogy between the present turbulent interwake region and grid-generated turbulence was based on an expression for grid-generated turbulence from Batchelor and Townsend (1948a,b), as follows:

$$(\bar{u}' \text{ or } \bar{v}')/ \bar{u} = \beta[C_D M/(x-x_o)]^n \tag{4}$$

where β is an empirical factor and they propose n = 1/2 and 5/4 in the initial- and final-decay periods, respectively. For present conditions the turbulent interwake region was homogeneous; therefore, a reasonable analogy to the distance from the grid for grid-generated turbulence is a distance on the order of the mean particle spacing. The length corresponding to the product of mesh size and drag coefficient for grid-generated turbulence was taken to be the particle wake momentum diameter θ, which similarly involves the product of the particle diameter and drag coefficient. Given these analogies, the expression corresponding to Eq. (4) for the turbulent interwake region becomes

$$(\bar{u}' \text{ or } \bar{v}')/U_p = \beta(\theta/C_p)^n \tag{5}$$

where β may not necessarily be the same for $\bar{u}'$ and $\bar{v}'$. Introducing expressions for θ in terms of C_d, d_p and ℓ, and eliminating n'' from the resulting expression using the formula for ε yields the following potential correlation for the relative turbulence intensities of the turbulent interwake region

$$(\bar{u}' \text{ or } \bar{v}')/U_p = \beta D^{n/3} \tag{6}$$

where D is a dimensionless dissipation factor defined as follows:

$$D = (\theta/\ell_p)^3 = \frac{\varepsilon d_p(C_d/8)^{1/2}}{\pi U_p^2(U_p - \bar{u})} \tag{7}$$

During the earlier turbulence generation studies of Parthesarathy and Faeth (1990) and Mizukami et al. (1992), expressions very similar to Eqs. (6) and (7) were developed that proved to be reasonably effective for correlating their relative turbulence intensity measurements. Their expressions were developed using a simple stochastic analysis to synthesize the properties of particle wake disturbances alone (with no consideration of a turbulent interwake region) based on Campbell's theorem, similar to the analysis of electrical noise from Rice (1954). The resulting correlation was identical to Eq. (6) except that D was replaced by an alternative dimensionless dissipation factor D_p, defined as follows:

$$D_p = \varepsilon d_p(C_d/8)^{1/3}/U_p^3 \tag{8}$$

The dimensionless dissipation factors D and D_p are closely related for the stagnant flow conditions considered in by Parthesarathy and Faeth (1990) and Mizukami et al. (1992) where $\bar{u}$ = 0, noting that the effect of the different powers of C_d in Eq. (7) and (8) is small because C_d is on the order of unity for the conditions of all of these experiments. Based on the measurements of Parthesarathy and Faeth (1990) and Mizukami et al. (1992), this correspondence between the two correlations suggests that n = 3/2. This estimate is reasonably close to the value n = 5/4 suggested by Batchelor and Townsend (1948a,b) where Eq. (4) is used to correlate turbulence intensities in the final-decay period of grid-generated turbulence, which is also consistent with the present relatively small values of Re_λ noted earlier.

Present measurements of streamwise and cross-stream relative turbulence intensities, within the turbulent interwake region for all three particle sizes, are plotted in Fig. 14 as a
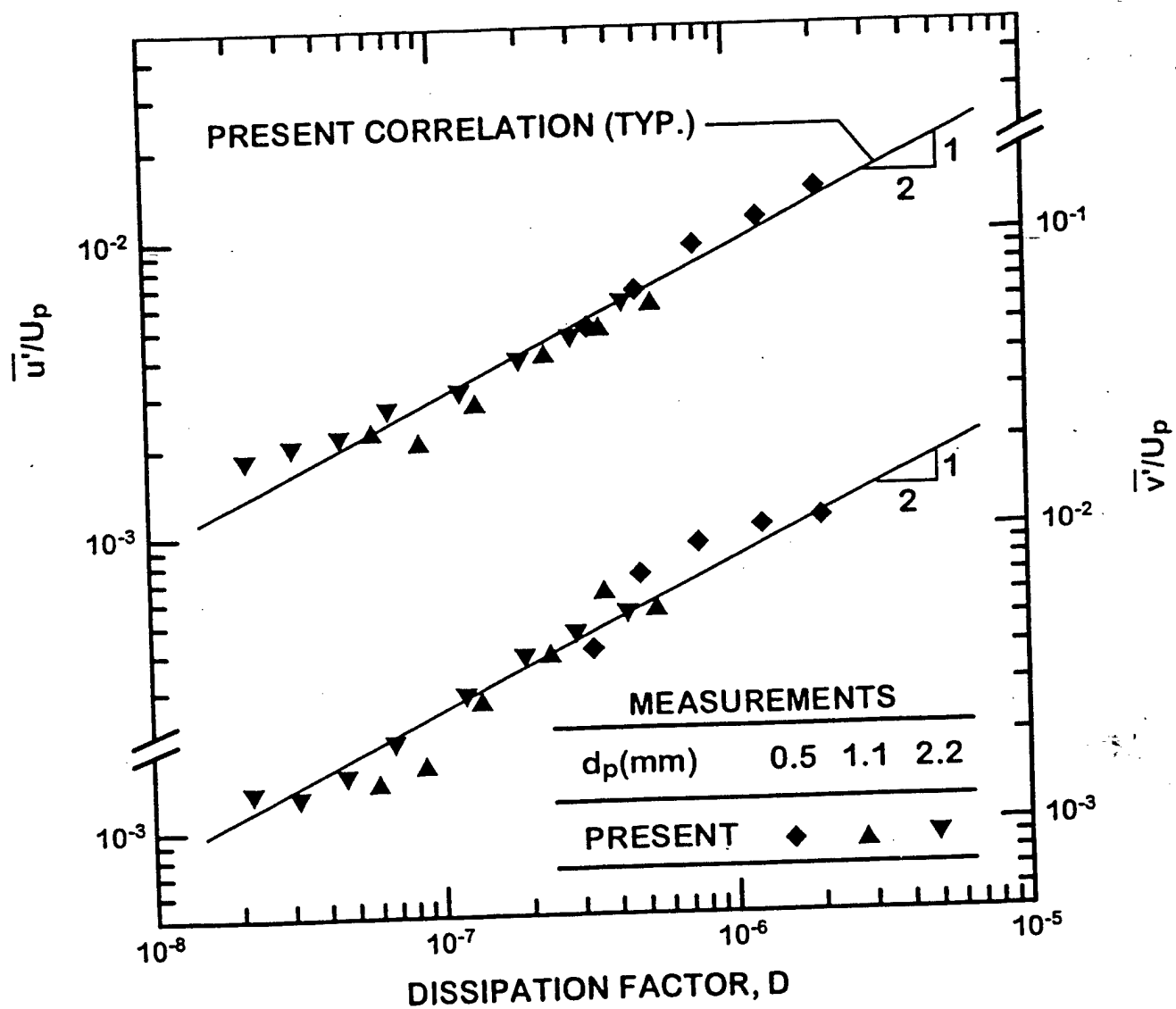
Figure 14 Streamwise and cross-stream relative turbulence intensities in the interwake region as a function of the dissipation factor for various particle sizes. From Chen and Faeth (2000).

function of D according to Eq. (6). The correlation is seen to be remarkably good, over the two-order-of-magnitude range of D considered during the present experiments. Best-fit correlations of the measurements found by linear regression had powers of 0.48 and 0.56 (with standard deviations of both these powers of 0.03) for streamwise and cross-stream relative turbulence intensities, respectively. As a result, there is no statistical significance for the differences between the powers of these fits and the value of n = 3/2 found by Parthesarathy and Faeth (1990) and Mizukami et al. (1992). Thus, for consistency with this earlier work, the measurements were correlated as shown in Fig. 14 using the earlier value of n to yield

$$\overline{u}'/U_p = 9.2D^{1/2}, \quad \overline{v}'/U_p = 7.9D^{1/2} \tag{9}$$

The standard deviation of the coefficients of Eqs. (9) are 1.5 and 1.6, respectively, and the correlation coefficients of both these fits are 0.98, which is excellent.

The difference between the coefficients of the streamwise and the cross-stream relative turbulence intensities is not statistically significant. Thus, the turbulent interwake region is isotropic within present capabilities to evaluate this behavior. Slight anisotropy favoring the streamwise direction, however, is not unexpected. In particular, the present wake discrimination system was not totally effective, which introduces some streamwise velocity bias because of uneliminated streamwise mean velocity disturbances from wakes. In addition, past studies of grid-generated turbulence at small turbulent Reynolds numbers (Re_λ of 36-72, which is somewhat larger than the present range) from Bennett and Corrsin (1978) yielded values of $\overline{u}'/\overline{v}'$ in the range 1.09-1.22, which is similar to the present mean value of $\overline{u}'/\overline{v}' = 1.16$ found from Eqs. (9). Thus, potential for a small fundamental level of anisotropy for the turbulent interwake region cannot be ruled out.

The correspondence between the correlations of Eq. (6) involving D, based on sole consideration of the turbulent interwake region, and involving D_p, based on sole consideration of wake disturbances helps explain the effectiveness of D_p for consideration of the relative turbulence intensities observed by Parthesarathy and Faeth (1990) and Mizukami et al. (1992), even though the wake disturbances did not contribute significantly to these measurements (i.e., wake disturbances were largely eliminated by their phase-discrimination systems). Thus, the nearly identical definitions of D and D_p suggest that either approach is fortuitously appropriate for both the turbulent interwake and wake disturbance regions of flows caused by turbulence generation (even though the detailed properties of these two flow regions differ considerably).

Interwake Properties (Probability Density Function). The probability density functions (PDF's) of the flow in the interwake region were measured, see Chen and Faeth (2000)

for the details. Within experimental uncertainties, the PDF's were Gaussian, as anticipated for the final-decay period of isotropic turbulence.

Interwake Properties (Energy Spectra). The energy spectra of the interwake region generally corresponded to the expectation of spectra for isotropic turbulence, see Chen and Faeth (2000). The spectra were independent of particle size and loading and approximate the spectra of simplified isotropic turbulence as discussed by Hinze (1975). A very interesting property of this turbulence was that it exhibited an extensive range of scales, roughly 1000:1, even though turbulence Reynolds numbers were small, e.g., less than 4. Consideration of length scales, taken up next, however, will show that this is a rational property of turbulence in the final-decay period which is surprising only because past measurements of the properties of turbulence in the final-decay period are relatively rare, and thus the properties of turbulence in this region are generally not well known.

Interwake Properties (Length Scales). Numerous studies of isotropic turbulence at large turbulence Reynolds numbers show that the rate of dissipation of turbulence kinetic energy can be estimated from values of velocity fluctuations and integral length scales using the following equation (Hinze 1975):

$$A = \epsilon L_u / (\overline{u}')^3 \qquad (10)$$

where A, the dimensionless integral length scale, is believed to be a constant on the order of unity. All properties on the right hand side of Eq. (10) have been measured during the present investigation so that values of A can be found at much smaller Re_λ than considered in the past.

The resulting values of A from the present investigation are plotted as a function of Re_λ in Fig. 15, providing results at small Reynolds numbers, $Re_\lambda = 0.4$-3.5. Results for isotropic turbulence from several past experiments, and from direct numerical simulations (DNS),[22-25] along with a DNS data fit due to Sreenivasan (1998), are plotted along with the present measurements. The earlier determinations of A involve relatively large turbulence Reynolds numbers, $20 \leq Re_\lambda \leq 800$, which places these flows in the initial decay period of isotropic turbulence where the turbulence is fully developed and acts over the entire flow region similar to conventional turbulence. In contrast, present measurements at small values of Re_λ exhibit very enhanced rates of dissipation, which is typical of behavior in the final decay period where the vorticity is sparse and turbulence appears to involve disconnected spots when single-point measurements are observed. This behavior is also consistent with previous indications that inter-wake turbulence was in the final decay period, based on relative turbulence intensities as discussed in connection with Fig. 14.
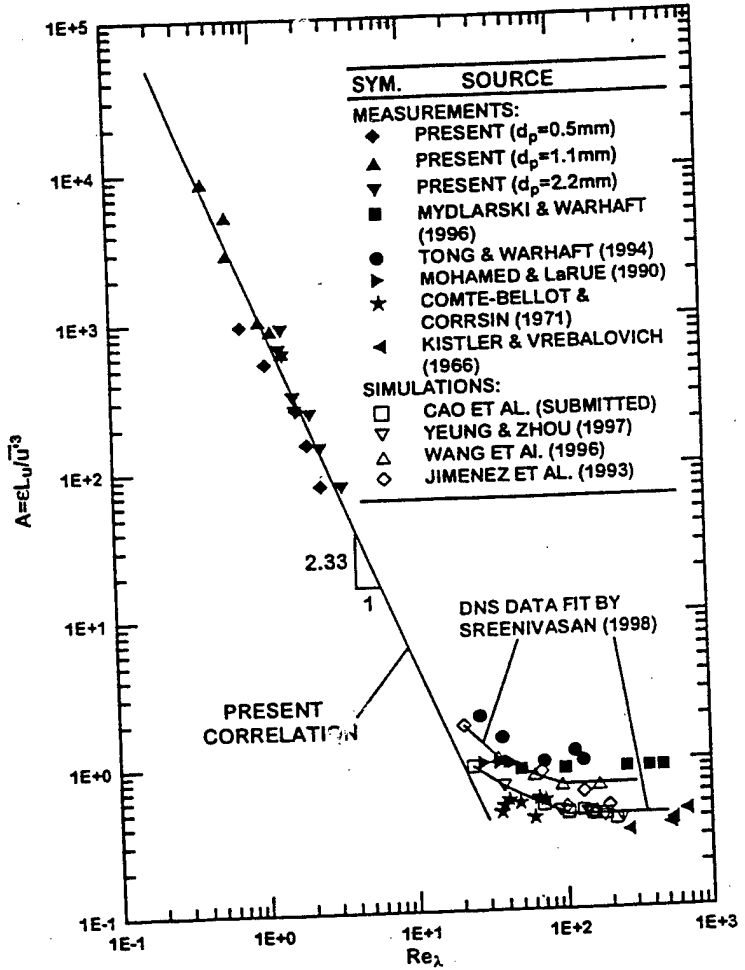
Figure 15 Normalized integral length scales as a function of the turbulence Reynolds number for grid-generated turbulence, numerical simulations of isotropic turbulence and measurements of turbulence in the interwake region of particle-generated turbulence. Measurements of Kistler and Vrebalovich (1966), Compte-Bellot and Corrsin (1971), Mohamed and LaRue (1990), Tong and Warhaft (1994), and Mydlarski and Warhaft (1996) for grid-generated turbulence; numerical simulations of Jiminez et al. (1993), Wang et al. (1996), Yeung and Zhou (1997), Cao et al. (1998) and Sreenivasan (1998) for isotropic turbulence; and measurements of the interwake region of particle-generated turbulence from the present investigation From Chen and Faeth (2000).

The measurement and predictions at large Re_λ yield scattered values of A in the range 0.3-2.0 which are on the order of unity and independent of Re_λ, as expected. Sreenivasan (1998) suggests that these variations of A are due to different initial conditions or grid geometries of the flows that were considered. In contrast, present values within the final decay period indicate strongly enhanced dissipation as Re_λ decreases (indicated by increasing values of A), analogous to strongly enhanced dissipation as Re_λ decreases (indicated by decreasing values of the turbulence intensity) along the axis of turbulent wakes in the final decay period, see Wu and Faeth (1993). The present measurements of A within the final decay period yield a best fit correlation as follows:

$$A = 1130\, Re_\lambda^{-2.33};\, 0.4 \le Re_\lambda \le 3.5 \tag{11}$$

where the experimental uncertainty of the power of Re_λ is 0.16 and the correlation coefficient of the fit is 0.96. Combining all the observations of A illustrated in Fig. 15, it is evident that A exhibits three regimes: (1) a large Re_λ regime (the initial-decay period) with $Re_\lambda > 100$, which corresponds to classical homogeneous isotropic turbulence at large Reynolds numbers; (2) a small Re_λ regime (the final-decay period) where $Re_\lambda < 10$, which corresponds to present turbulent inter-wake conditions; and (3) a transition regime with $10 < Re_\lambda < 100$, between the two outer limiting regimes.

It is interesting to consider the variation of the length scale ratio, L_u/λ, as a function of Re_λ, in the three regimes of A that were just defined. It is easy to show that this ratio assumes the following forms:

Final-decay period:
$$L_u/\lambda = 75\, Re_l^{-1.33};\, 0.4 \le Re_\lambda \le 3.5 \tag{12}$$

Initial-decay period:

$$L_u/\lambda = A\, Re_\lambda/15,\, 20 \le Re_\lambda \tag{13}$$

Transition period:

$$L_u/\lambda = 2.2,\quad 4 \le Re_\lambda \le 20 \tag{14}$$

The correlations of Eqs. (12)-(14) are illustrated in Fig. 16, along with results from available measurements and DNS simulations. Taken together, the various correlations provide reasonably good fits of results in the final-decay, transition and initial-decay periods.

The nature and location of transition to the final decay period seen in Fig. 16 seems quite reasonable. In particular, the variation of L_u/λ with decreasing Re_λ for fully-developed turbulent flows must change as Re_λ becomes small because realizable flow properties cannot involve a Taylor length scale (a microscale) larger than the integral scale (a macroscale), or conditions where $L_u/\lambda_\lambda < 1$. Thus, it is not surprising that the transition to the final-decay period, where L_u/λ_λ increases with decreasing Re_λ, occurs when L_u/λ reaches values on the order of unity.

Increasing values of L_u/λ with *increasing* Re_λ in the initial-decay period is well understood (Schlichting 1975; Tennekes and Lumley 1972), as a result of the relatively inviscid large-scale features (on the scale of integral scales) combined with progressively smaller microscales of turbulence as turbulence Reynolds numbers increases. The corresponding increasing values of L_u/λ with *decreasing* values of Re_λ in the final-decay period occurs for very different reasons. In this case, vortical regions are sparse although they still spread throughout the entire flow, yielding large integral scales in the presence of small dissipation scales; i.e., the dimensions of turbulent spots become small in comparison to the dimensions of the flow as a whole when the vortical regions of the flow become more sparse as turbulence decay proceeds.

3.4 Conclusions

This investigation considered the properties of turbulence generated by uniform fluxes of monodisperse spherical particles moving in air at normal pressure and temperature. Test conditions included monodisperse glass beads having diameters of 0.5-2.2 mm, , particle volume fractions less than 0.003%, particle Reynolds numbers of 106-990, turbulence generation rates of 0.2-5.0%. The major conclusions of the study are as follows:

1. Particle wake properties of the present turbulence-generated processes corresponded to the laminar-like turbulent wakes observed by Wu and Faeth (1994,1995) for spheres at intermediate Reynolds numbers in turbulent environments.

2. The turbulent interwake region is homogeneous and nearly isotropic with PDF's of streamwise and cross-stream velocities well approximated by Gaussian functions.

3. Relative turbulence intensities in the turbulent interwake region were correlated effectively by analogy to the known properties of isotropic grid-generated turbulence,
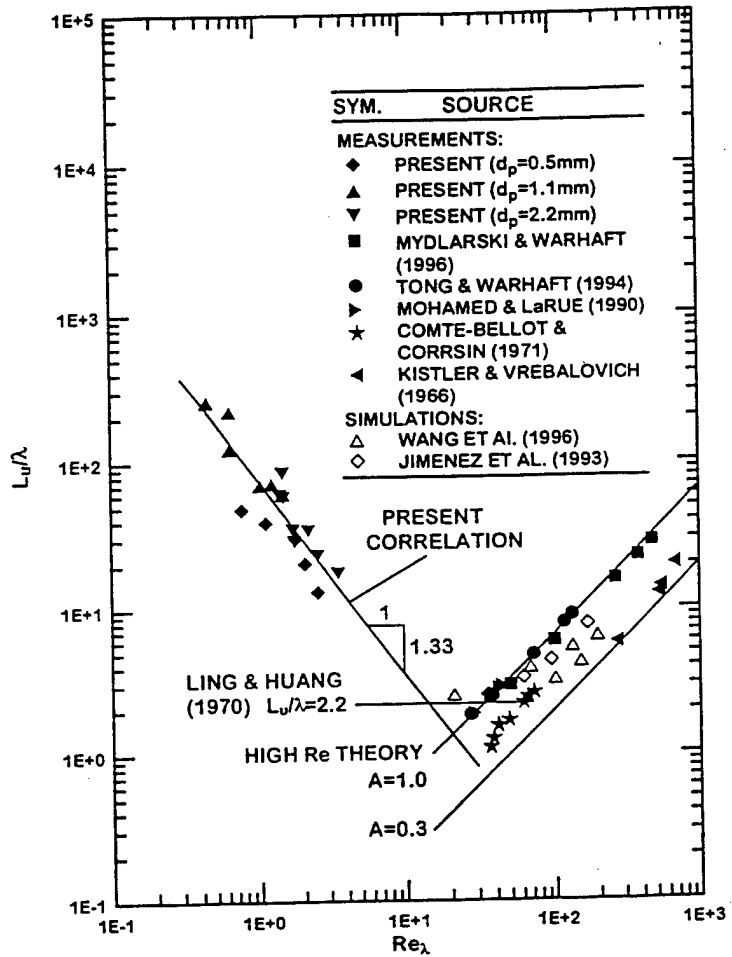
Figure 16 Ratios of integral and Taylor length scales as a function of the turbulence Reynolds number for grid-generated turbulence, numerical simulations of isotropic turbulence, and turbulence in the interwake region of particle-generated turbulence. Measurements of Kistler and Vrebalovich (1966), Compte-Bellot and Corrsin (1971), Mohamed and LaRue (1990), Tong and Warhaft (1994), and Mydlarski and Warhaft (1996) for grid-generated turbulence; numerical simulations of Jiminez et al. (1993) and Wang et al. (1996) for of isotropic turbulence; and measurements of the interwake region of particle-generated turbulence from the present investgigation. From Chen and Faeth (2000).

e.g., Batchelor and Townsend (1948a,b), by scaling these properties with the mean particle spacing normalized by the particle wake momentum diameter, to yield a dimensionless dissipation factor.

4.   The present dimensionless dissipation factor, based on consideration of inter-wake turbulence alone, is nearly identical to an earlier dimensionless dissipation factor found by Parthesarathy and Faeth (1990) and Mizukami et al. (1992). based on consideration of particle wake properties alone. This fortuitous agreement of correlations for the turbulent inter-wake region and for wake disturbances is no doubt responsible for the simple correlations of overall relative turbulence intensities (involving both regions) as a function of dimensionless dissipation factor observed during earlier work, by Parthesarathy and Faeth (1990) and Mizukami et al. (1992).

5.   For present turbulence generation conditions, and probably for most practical dispersed flows, the turbulent inter-wake region exhibited very small turbulence Reynolds numbers ($Re_\lambda < 4$) and was in the final decay period where vortical regions fill the entire inter-wake region but are sparse, i.e., where turbulence appears to involve disconnected turbulent spots when single-point measurements are observed.

6.   Within the final decay period, macroscale/microscale ratios (e.g., L_u/λ) decrease with increasing turbulence Reynolds numbers as opposed to increasing similar to fully-developed isotropic turbulence at large turbulence Reynolds numbers. Quite plausibly, the transition from the final decay region to the fully-developed turbulence region occurs when L_u/λ is on the order of unity; this condition corresponds to a turbulence Reynolds number on the order of ten which is similar to conditions at the transition of turbulent wakes in nonturbulent environments to the final decay period, see Wu and Faeth (1993).

7.   As a result of the behavior of length scale ratios in the final-decay period, illustrated in Fig. 16, and the fact that mean velocities in particle wakes contribute to turbulence properties (unless measured with wake discrimination systems), the range of length scales in flows resulting from turbulence generation is unusually large, as noted by past workers making measurements of the properties of turbulent flows resulting from turbulence generation, e.g., Parthesarathy and Faeth (1990) and Mizukami et al. (1992).

References

Aalburg, C., Faeth, G.M. and van Leer, B. (2002a) AIAA Paper No. 2002-0341.

Aalburg, C., van Leer, B. and Faeth, G. M. (2002b) *Int. J. Multiphase Flow*, submitted.

Batchelor, G.K. and Townsend, A.A. (1948a) *Proc. Roy. Soc. (London)* 193A, 539.

Batchelor, G.K. and Townsend, A.A. (1948b) *Proc. Roy. Soc. (London)* 194A, 527.

Bennett, J.C. and Corrsin, S. (1978) *Phys. Fluids* 21, 2129.

Berger, E. and Wille, R. (1972) *Ann. Rev. Fluid Mech.* 4, 313.

Brackbill, J.U., Kothe, D.B. and Zemach, C. (1991) *J. Comp. Phys.* 100, 335.

Cao, N., Chen, J. and Doolen, G.D. (1999) cited by Sreenivasan (1998).

Chen, J.-H. and Faeth, G.M. (2000) *AIAA J.* 38, 995.

Chen, J.-H. and Faeth, G.M. (2001) *AIAA J.* 39, 180.

Chen, J.-H., Wu, J.-S. and Faeth, G.M. (2000) *AIAA J.* 38, 636.

Chorin, A. J. (1968) *Math. Comp.* 22, 745.

Chou, W.-H.and Faeth, G.M. (1998) *Int. J. Multiphase Flow* 24, 889.

Chou, W.-H., Hsiang, L.-P. and Faeth, G.M. (1997) *Int. J. Multiphase Flow* 23, 651.

Compte-Bellot, G. and Corrsin, S. (1971) *J. Fluid Mech.* 48, 273.

Dai, Z. and Faeth, G.M. (2001) *Int. J. Multiphase Flow* 27, 217.

Dennis, J.C.R. and Chang, G.-Z. (1970) *J. Fluid Mech.* 42, 471.

Faeth, G.M. (1990) *Proc. Combust. Inst.* 23, 1345.

Faeth, G.M. (1996) *Proc. Combust. Inst.* 26, 1593.

Faeth, G.M., Hsiang, L.-P. and Wu, P.-K., (1995) *Int. J. Multiphase Flow* 21 (Suppl.), 99.

Hanson, A.R., Domich, E.G. and Adams, H.S. (1963) *Phys. Fluids* 6, 1070.

Harlow, F.H. and Welch, J.E. (1965) *Phys. Fluids* 8, 2182.

Hinze, J.O. (1955) *AIChE J.* 1, 289.

Hinze, J.O. (1975) *Turbulence*, 2nd Ed., McGraw-Hill, New York, p. 65ff.

Hsiang, L.-P. and Faeth, G.M. (1992) *Int. J. Multiphase Flow* 18, 635.

Hsiang, L.-P. and Faeth, G.M. (1993) *Int. J. Multiphase Flow* 19, 721.

Hsiang, L.-P. and Faeth, G.M. (1995) *Int. J. Multiphase Flow* 21, 545.

Jiminez, J., Wray, A. A., Saffman, P.G. and Rogallo, R. S. (1993) *J. Fluid Mech.* 255, 65.

Johnson, T.A. and Patel, V.C. (1999) *J. Fluid Mech.* 378, 19.

Kawaguti, P. and Jain, P. (1966) *J. Phys. Soc. Japan* 21:2055.

Kistler, A.L. and Vrebalovich, T. (1966) *J. Fluid Mech.* 26, 37.

Kovasznay, L.S.G. (1948) *Proc. Roy. Soc. (London)* 198(A), 174.

Krzeczkowski, S.A. (1980) *Int. J. Multiphase Flow* 6, 227.

Lance, M. and Bataille, J. (1982) *Adv. Two-Phase Flow & Heat Trans.* 1, Martinus Nijhoff, Amsterdam, 413.

Lance, M., and Bataille, J. (1991) *J. Fluid Mech.* 222, 95.

Lane, W.R. (1951) *Ind. Engr. Chem.* 43, 1312.

LeClair, B.P., Hamiliec, A.E. and Pruppacher, H.R. (1970) *J. Atmos. Sci.* 27, 308.

Loparev, V.P. (1975) *Izvestiya Akad. Nauk. SSR, Mech. Zhidhosti i Gaza* 3, 174.

Magnaudet, J., Rivero, M. and Fabre, J. (1995) *J. Fluid Mech.* 284, 97.

Mazallon, J., Dai, Z. and Faeth, G.M. (1999) *Atom. Sprays* 9, 291.

Mizukami, M., Parthasarathy, R.N. and Faeth, G.M. (1992) *Int. J. Multiphase Flow* 18, 397.

Mohamed, M.S. and LaRue, J.C. (1990) *J. Fluid Mech.* 219, 195.

Mydlarski, L. and Warhaft, Z. (1996) *J. Fluid Mech.* 320, 331.

Nishioka, M. and Sato, M. (1978) *J. Fluid Mech.* 89, 49.

Parthasarathy, R.N. and Faeth, G.M. (1987) *Int. J. Multiphase Flow* 13, 699.

Parthasarathy, R.N. and Faeth, G.M. (1990) *J. Fluid Mech.* 220, 485.

Pruppacher, H.R., LeClair, B.P. and Hamielec, A.E. (1970) *J. Fluid Mech.* 44, 781.

Ranger, A.A. and Nicholls, J.A. (1969) *AIAA J.* 7, 285.

Rice, S.O. (1954) *Noise and Stochastic Processes* (N. Wax, ed.), Dover Publications, New York, 133.

Roos, F.W. and Willmarth, W.W. (1971) *AIAA J.* 9, 285.

Roshko, A. (1954a) NACA Technical Report No. 1191.

Roshko, A. (1954b) NACA Technical Report No. 3169.

Sallam, K.A., Dai, Z. and Faeth, G.M. (1999) *Int. J. Multiphase Flow* 25, 1161.

Sallam, K.A., Dai, Z. and Faeth, G.M. (2002) *Int. J. Multiphase Flow*, in press.

Schlichting, H. (1975) *Boundary Layer Theory*, 7th ed., McGraw-Hill, New York, 234 & 599.

Sreenivassan, K.R. (1998) *Phys. Fluids* 10, 529.

Sussman, M. and Fatemi, E. (1999) *SIAM J. Sci. Comp.* 20, 1165.

Sussman, M., Smereka, P. and Osher, J. (1994) *J. Comp. Phys.* 114, 146.

Takami, H. and Keller, H.B. (1969) *Phys. Fluids* 12(II), 51.

Taneda, S. (1956) *J. Phys. Soc. Japan* 11, 1104.

Tennekes, H. and Lumley, J.L. (1972) *A First Course in Turbulence*, MIT Press, Cambridge, 275.

Thoman, D.C. and Szewczyk, A.A. (1969) *Phys. Fluids Suppl.* 12, II76.

Tomboulides, A., Orszag, S.A. and Karniadakis, G.E. (1993) AIAA Paper No. 93-0546.

Tong, C. and Warhaft, Z. (1994) *Phys. Fluids* 6, 2165.

Wang, L.-P., Chen, S., Brasseur, J.G. and Wynggaard, J.C. (1996) *J. Fluid Mech.* 309, 113.

Wu, J.-S. and Faeth, G.M. (1993) *AIAA J.* 31, 1448.

Wu, J.-S. and Faeth, G.M. (1994) *AIAA J.* 32, 535.

Wu, J.-S. and Faeth, G.M. (1995) *AIAA J.* 33, 171.

Wu, P.-K., Kirkendall, Fuller, R.F. and Nejad, A.S. (1997) *J. Prop. Power* 13, 64.

Yeung, P.K. and Zhou, Y. (1997) *Phys. Rev. E* 18, 1746.

Appendix A: Aalburg, C., Faeth, G.M. and van Leer, B. (2002) Deformation and Drop Properties of Round Drops Subjected to Shock Wave and Steady Disturbances. 40th Aerospace Sciences Meeting, AIAA Paper No. 2002-0341.

AIAA

AIAA 2002-0341
Deformation and Drag Properties of Round Drops Subjected to Shock Wave Disturbances

C. Aalburg, G.M. Faeth and B. van Leer
Department of Aerospace Engineering
The University of Michigan
Ann Arbor, MI 48109-2140

40th Aerospace Sciences Meeting & Exhibit
14-17 January 2002
Reno, Nevada

DEFORMATION AND DRAG PROPERTIES OF ROUND DROPS SUBJECTED TO SHOCK WAVE DISTURBANCES

C. Aalburg[*], G.M. Faeth[†] and B. van Leer[‡]
Department of Aerospace Engineering
The University of Michigan
Ann Arbor, Michigan 48109-2140, U.S.A.

ABSTRACT

A computational study is described that addresses the deformation and drag properties of round drops subjected to shock wave disturbances. The objective of the present study was to consider secondary breakup of drops at small liquid/gas density and viscosity ratios that are difficult to address by experiments but are more representative of conditions in practical sprays. The time-dependent, incompressible and axisymmetric Navier-Stokes equations were solved in conjunction with the level set method and the calculations were evaluated based on earlier results for wake and drag properties of solid spheres and deformation and secondary breakup properties of drops. The agreement between predictions and measurements was quite good. Similar to an early proposal by Hinze, the properties of breakup were mainly affected by the Weber number, We, and the Ohnesorge number, Oh. However, for large Oh, the computations revealed an effect of the liquid/gas viscosity ratio that was not observed during experiments. A better approach for representing these conditions was to account for liquid viscous effects directly by plotting the ratio of drag to liquid viscous forces, $We^{1/2}/Oh$, as a function of the ratio of surface tension to liquid viscous forces, $1/Oh$. Effects of the liquid/gas density ratio on drop breakup were found to be remarkably small. The Reynolds number, however, was found to have a considerable effect on drop breakup as the Stokes flow regime was approached. This behavior appears to be caused by the progressive increase of the drag coefficient as Reynolds numbers become small.

[*]Graduate Student Research Assistant, Department of Aerospace Engineering.
[†]A.B.M. Modine Professor, Department of Aerospace Engineering, Fellow AIAA, corresponding author, Tel.: +1-734-764-7202, Fax: +1-734-936-0106, E-mail: gmfaeth@umich.edu.
[‡]Professor, Department of Aerospace Engineering.

NOMENCLATURE

C_D = drag coefficient
d = drop diameter
L = wake length
Oh = initial Ohnesorge number, $\mu_L/\sqrt{\rho_L\sigma d_0}$
Re = Reynolds number, $\rho_G u d/\mu_G$
u = streamwise velocity
r = drop radius
t = time
t* = characteristic breakup time, $d_0/u_0\sqrt{\rho_L/\rho_G}$
We = initial Weber number, $\rho_G u_0^2 d_0/\sigma$
μ = molecular viscosity
ρ = density
σ = surface tension coefficient

Subscripts

0 = initial condition
c = cross stream dimension
G = gas phase property
L = liquid phase property

INTRODUCTION

The study of the deformation and drag properties of round drops subjected to shock wave disturbances is motivated by applications to the secondary breakup of drops within sprays found in power and propulsion systems. The current work is an extension of past studies of secondary drop breakup in this laboratory using experimental methods[1-6]. These studies established breakup regime transitions which were mainly affected by the Weber number, We, as a measure of the ratio between ambient drag to surface tension forces, and the Ohnesorge number, Oh, as a measure of the ratio between the liquid viscous to surface tension forces, similar to an early proposal of Hinze.[7] Due to experimental constraints, these results were limited to large liquid/gas density ratios, ρ_L/ρ_G=580-12,000, with the Reynolds number

varying in the range 300-16,000. Thus, the influence of the density ratio and the Reynolds number could not be investigated independently. Further, due to problems of experimentally reaching breakup conditions at large Oh, which are typical of practical high pressure combustion applications, the transition to breakup for Oh>10 remained unknown.

The objective of the present study was to consider the onset of secondary breakup of drops at the small liquid/gas density and viscosity ratios that are difficult to address by experiments but are more representative of conditions in practical sprays at the pressures typical of power and propulsion systems.

Since drop breakup is a complex, three-dimensional process, due to the formation of nodes, a detailed simulation would require, locally, a very fine grid and would have to be three-dimensional as well. Experimental results, however, have shown that breakup starts when the drop deformation, measured as the ratio between the cross-stream diameter, d_c, to the initial drop diameter, d_0, exceeds approximately 70%. By adopting these findings it is possible to estimate the onset of breakup without having to calculate the details of the breakup process itself, pending the future feasibility of such numerical calculations. The numerical computations were thus axisymmetric and allowed independent variation of all relevant parameters of drop breakup properties.

The calculations were evaluated based on earlier results for wake sizes and drag coefficients of solid spheres, steady drop deformation under a constant body force and the onset of breakup due to shock wave disturbances. Numerical simulations were carried out for a range of parameters to study the effects of Weber number, Ohnesorge number, Reynolds number, liquid/gas density ratio and liquid/gas viscosity ratio on the deformation and breakup of liquid drops.

COMPUTATIONAL METHODS

The time-dependent, incompressible and axisymmetric Navier-Stokes equations were solved using the projection method of Chorin[8] with a multigrid Poisson solver for the pressure equation. The discretization in space was carried out on a staggered grid according to the marker and cell (MAC) method of Harlow and Welch[9]. The level set method of Sussman et al.[10] was used to capture the liquid/gas interface and yielded the local fluid properties of each cell with a smooth transition between the gas and the liquid phases near the interface. A redistancing algorithm according to

Sussman and Fatemi[11] was used to maintain the level set as an accurate distance function at all times. The interface calculations allowed for effects of surface tension, pressure and shear forces, with surface tension represented as a body force distributed over an interface having finite thickness, following Brackbill et al.[12] The discretizations in both space and time were second-order accurate.

The domain size was typically 7.5 r_0 x 15 r_0 and was covered with a moving grid having 192 x 384 cells. The boundary conditions were symmetric along the sides, with a fixed velocity across the inlet and a fixed pressure along the outlet. Tests of various-sized solution regions and finer grids caused less than a 3% change near breakup conditions in the results reported in this study. The simulations were started with an initially motionless radial plane of the drop being subjected to a sudden divergence-free velocity field. Except for the evaluation of the drop deformation for a constant body force, buoyancy was neglected. The flow was assumed to be isothermal with constant liquid and gas phase properties.

RESULTS AND DISCUSSION

Computational evaluation

Prior to considering the breakup properties of drops subjected to shock wave disturbances, the numerical predictions were evaluated based on earlier measurements and computations of the properties of solid spheres and deforming drops. These included both the steady wake lengths and the drag coefficients behind solid spheres as a function of Reynolds number (limited to conditions prior to the transition to oscillating wakes at Re=130), and the deformation of drops subject to constant body forces.

The top illustration of Fig. 1 shows the streamline pattern behind an almost stationary and non-deforming drop, achieved by making the liquid/gas density ratio and the surface tension very large (ρ_L/ρ_G=1000, We=0.25, Oh=0.2). The wake length, L, measured from the downward stagnation point on the drop to the point where the flow reattaches at the axis, normalized by the drop diameter, is plotted as a function of Reynolds number in Fig. 2. The steady wake length progressively increases with increasing Reynolds number and present predictions are in good agreement with existing measurements.

Figure 3 is an illustration of the drag coefficient, calculated from the momentum loss in the gas phase across the drop, plotted as a function of the Reynolds number for Re=30-120. The agreement between past

measurements and current predictions is excellent. Although C_D is relatively constant for large Re, it exhibits a large increase as the Re approaches the Stokes range.

The bottom illustration of Fig. 1 is an illustration of the steady state streamlines and shape of a drop being accelerated by a constant body force (gravity). The calculations simulated an ethylene glycol drop dispersed in paraffin oil at three different Weber numbers, achieved by varying the diameter of the drop. The predicted deformation, measured in terms of the ratio of the maximum and minimum dimensions of the drop, is compared with measurements from Hsiang and Faeth[3] in Fig. 4, finding good agreement between predictions and measurements.

Drop deformation and breakup

The properties of drops subjected to shock wave disturbances for a given d_0 and given gas phase properties (ρ_0 and μ_0) are affected by the Weber number, the Ohnesorge number, the liquid/gas density ratio and the Reynolds number. In the following, the influence of the variation of each of these variables on the deformation and breakup of drops will be discussed, i.e. while one variable was being modified, the remaining three variables were held constant.

The deformation properties of liquid drops subjected to shock wave disturbances are illustrated by plots of normalized deformation, d_c/d_0, as a function of normalized time, t/t^*, in Fig. 5. The property d_c is the maximum cross stream dimension of the drop at any given time and t^* is the characteristic breakup time defined by Ranger and Nicholls.[13] The top illustration in Fig. 5 illustrates the effect of Weber number for constant Oh=0.01, ρ_L/ρ_G=2 and Re=50. The maximum degree of deformation progressively increases as the Weber number increases, eventually exceeding the breakup limit of approximately 60% deformation for We>64. For conditions prior to breakup, the drop shape oscillates during relaxation back to a round shape configuration.

The middle illustration of Fig. 5 illustrates the effect of varying the Ohnesorge number for We=32, ρ_L/ρ_G=2 and Re=50. For values of Oh≤0.01, varying Oh has almost no effect on either the amplitude or the frequency of deformation. Increasing the Ohnesorge number beyond 0.01, however, causes a progressive decrease of the maximum deformation, and eventually leads to a nonoscillatory relaxation process for Oh≥1.0.

The bottom illustration of Fig. 5 illustrates effects of varying the liquid/gas density ratio for We=16, Oh=0.01 and Re=50. Increasing the liquid/gas density ratio implies increasing the relaxation times. Normalizing the time by the characteristic Ranger and Nicholls breakup time, however, helps scale liquid/gas inertial effects correctly, so that the frequency of oscillation in terms of t/t^* tends to be relatively independent of the liquid/gas density ratios. Note, that while the characteristic time, t^*, scales with $(\rho_L/\rho_G)^{1/2}$, the acceleration of a drop with a constant drag coefficient is proportional to ρ_L/ρ_G. This means, that drops having large density ratios have a greater velocity defect with respect to the ambient velocity. Therefore, increasing the liquid/gas density ratio tends to increase maximum levels of deformation.

Plotting the maximum deformation as a function of gas/liquid density ratio reveals the limited influence of the density ratio on the overall deformation of drops. Figure 6 is an illustration of the Weber number at breakup, i.e. where deformation levels exceed 60%, as function of the gas/liquid density ratio for various Ohnesorge numbers at Re=50. The effect of the density ratio is nearly linear so that extrapolation to $\rho_G/\rho_L \to 0$ was not problematical.

Exploiting the extrapolation procedure and the deformation threshold for breakup, breakup regime boundaries for liquid drops subjected to shock wave disturbances were found in terms of the classical We-Oh coordinates first proposed by Hinze.[7] The resulting plot is illustrated in Fig. 7. Parametric conditions shown on the plot include predicted breakup boundaries for Re=25 and ρ_L/ρ_G=2; Re=50 and ρ_L/ρ_G=2, 8, 32 and ∞; and Re=100 and ρ_L/ρ_G=2. The measured breakup regime boundary of Hsiang and Faeth[3] is also shown on the plot. First of all, it should be noted that predicted variations of the breakup regime boundary are not large for variations of ρ_L/ρ_G in the range 2-∞. The extrapolated breakup line for ρ_L/ρ_G=∞ agrees quite well with the large ρ_L/ρ_G measurements of Hsiang and Faeth.[3]

The influence of the Reynolds number on drop breakup for ρ_L/ρ_G=2 is seen to be small for Re>50. But results at Re=25 indicate significantly increased resistance to breakup. Studying present computed results shows that this behavior comes about due to the effect of Reynolds number on drag, shown in Fig. 3. For Re<50, drag coefficients increase appreciably as the Stokes range is approached. This increases the rate of acceleration of the drop toward the ambient velocity so that the velocity defect (and thus the local

Weber number) at the maximum deformation condition is reduced. As a result, larger initial Weber numbers are needed for breakup. This effect was not observed for past measurements of drop breakup, because test conditions generally did not consider Re<50 where variations of C_D with the Reynolds number become important.

Somewhat analogous is the effect of increasing Ohnesorge number on the Weber number needed for breakup. The results show that for small Ohnesorge numbers (Oh<0.1), liquid breakup is relatively independent of the Ohnesorge number and is first observed for Weber numbers on the order of 10; whereas for large Ohnesorge numbers (Oh>1), Weber numbers at the onset of breakup progressively increase and become proportional to the Ohnesorge number:

$$\log(We) \approx 2 \cdot \log(Oh) \qquad (1)$$

which implies: $\quad \sqrt{We} / Oh \approx \text{const} \qquad (2)$

This behavior has been explained based on effects of liquid viscosity slowing the rate of deformation of the drop as the Ohnesorge number increases; as a result, the velocity difference between the drop and the ambient gas (or the corresponding local Weber number) is reduced compared to small Ohnesorge number conditions. Therefore, larger initial Weber numbers are needed for breakup.

On the other hand, the computations also revealed an effect of liquid/gas viscosity ratio at large Oh, that was not observed during the experiments due to problems of experimentally reaching these conditions. This behavior is illustrated by the lines of constant viscosity ratio μ_L/μ_G, which are specified completely by the values of We and Oh for given values of Re and ρ_L/ρ_G, and which have been drawn for μ_L/μ_G=0.1, 1, 10 and 100 for ρ_L/ρ_G=2 and Re=50 in Fig. 7. It is evident, that while for small Ohnesorge numbers, where the surface-tension-forces dominate over liquid viscous forces, the ratio of drag forces/surface-tension-forces (the We number) is the governing breakup parameter, conditions at large Ohnesorge numbers, where liquid viscous forces dominate over surface-tension-forces, involve a rather restricted range of μ_L/μ_G for a given Reynolds number and liquid/gas density ratio.

The large effect of liquid/gas viscosity ratio on the Hinze form of the secondary breakup regime map is not desirable and alternative plots were sought. A better approach for representing conditions where effects of liquid viscosity were large, large Oh, was

to account for liquid viscous effects directly by plotting the ratio of drag to liquid viscous forces, instead of the ratio of drag to surface tension forces, as follows

$$\frac{drag\ forces}{liquid\ viscous\ forces} \approx \text{Re} \sqrt{\frac{\rho_L}{\rho_G}} \frac{\mu_G}{\mu_L} = \frac{\sqrt{We}}{Oh} \qquad (3)$$

This turns out to be precisely what the analysis of the slopes of the breakup lines at large Oh yielded in Eq. 2. Figure 8 is an illustration of the breakup regime map in the new coordinates, plotting the ratio of drag to liquid viscous forces, $We^{1/2}/Oh$, as a function of the ratio of surface tension to liquid viscous forces, $1/Oh$. This approach yields secondary drop deformation and breakup regime boundaries that are relatively independent of both liquid/gas density and viscosity ratios and are in excellent agreement with existing measurements of these properties at small Oh.

CONCLUSIONS

The conclusions of the present study of the deformation and breakup properties of round liquid drops subjected to shock wave disturbances are as follows:

1. Predictions and measurements of wake and drag properties of spheres, and the deformation and breakup properties of drops subjected to steady and shock wave disturbances, are in good agreement.

2. The liquid/gas density ratio has only a small effect on the deformation and breakup properties of drops.

3. The effects of Re number are small for large Re. However, as Re approaches the Stokes range, the We required for breakup increases significantly with decreasing Re due to corresponding increases of the drag coefficient.

4. At large Oh, surface tension has a negligible influence on breakup. Then plotting the ratio of drag to liquid viscous forces, $We^{1/2}/Oh$, as a function of surface tension to liquid viscous forces, $1/Oh$, yields breakup regime boundaries that are constant for large Oh, however, and are relatively independent of the liquid/gas density ratio.

ACKNOWLEDGEMENTS

REFERENCES

1. Hsiang, L.-P., and Faeth, G.M., "Near-Limit Drop Deformation and Secondary Breakup", *Int. J. Multiphase Flow*, Vol. 18, No. 5, 1992, pp. 635-652.
2. Hsiang, L.-P., and Faeth, G.M., "Drop Properties After Secondary Breakup", *Int. J. Multiphase Flow*, Vol. 19, No. 5, 1993, pp. 721-735.
3. Hsiang, L.-P., and Faeth, G.M., "Drop Deformation and Breakup Due to Shock Wave and Steady Disturbances", *Int. J. Multiphase Flow*, Vol. 18, No. 4, 1995, pp. 545-560.
4. Chou, W.-H., Hsiang, L.-P., and Faeth, G.M., "Temporal Properties of Drop Breakup in the Shear Breakup Regime", *Int. J. Multiphase Flow*, Vol. 23, No. 4, 1997, pp. 651-669.
5. Chou, W.-H., Hsiang, L.-P., and Faeth, G.M., "Temporal Properties of Secondary Drop Breakup in the Bag Breakup Regime", *Int. J. Multiphase Flow*, Vol. 24, No. 6, 1998, pp. 889-912.
6. Dai, Z., and Faeth, G.M., "Temporal Properties of Secondary Drop Breakup in the Multimode Breakup Regime", *Int. J. Multiphase Flow*, Vol. 27, No. 2, 2001, pp. 217-236.
7. Hinze, J.O., "Fundamentals of the Hydrodynamic Mechanism of Splitting in Dispersion Processes", *AIChE J.*, Vol. 1, 1955, pp. 289-295.
8. Chorin, A.J., "Numerical Solution of the Navier-Stokes Equations", *Math. Comp.*, Vol. 22, No. 104, 1968, pp. 745-762.
9. Harlow, F.H., and Welch, J.E., "Numerical Calculation of Time-Dependent Viscous Incompressible Flow of Fluid with Free Surface", *Phys. Fluids*, Vol. 8, No. 12, 1965, pp. 2182-2189.
10. Sussman, M., Smereka, P., and Osher, S., "A Level Set Approach for Computing Solutions to Incompressible Two-Phase Flow", *J. Comp. Phys.*, Vol. 114, No. 1, 1994, pp. 146-159.
11. Sussman, M., and Fatemi, E., "An Efficient, Interface-Preserving Level Set Redistancing Algorithm and its Application to Interfacial Incompressible Flow", *SIAM J. Sci. Comp.*, Vol. 20, No. 4, 1999, pp. 1165-1191.
12. Brackbill, J.U., Kothe, D.B., and Zemach, C., "A Continuum Method for Modeling Surface Tension", *J. Comp. Phys.*, Vol. 100, 1991, pp. 335-354.
13. Ranger, A.A., and Nicholls, J.A., "The Aerodynamic Shattering of Liquid Drops", *AIAA J.*, Vol. 7, 1969, pp. 285-290.
14. Taneda, S., "Experimental Investigation of the Wake Behind a Sphere at Low Reynolds Numbers", *J. Phys. Soc. Japan*, Vol. 11, 1956, pp. 1104-1108.
15. Pruppacher, H.R., Le Clair, B.P., and Hamiliec, A.E., "Some Relations Between Drag and Flow Pattern of Viscous Flow Past a Sphere and a Cylinder at Low and Intermediate Reynolds Numbers", *J. Fluid Mech.*, Vol. 44, No. 4, 1970, pp. 781-790.
16. Tomboulides, A., Orszag, S.A., and Karniadakis, G.E., "Direct and Large-Eddy Simulation of Axisymmetric Wakes", *AIAA Paper* 93-0546, 1993.
17. Magnaudet, J., Rivero, M., and Fabre, J., "Accelerated Flows Past a Rigid Sphere or a Spherical Bubble. Part 1. Steady Straining Flow.", *J. Fluid Mech.*, Vol. 284, 1995, pp. 97-135.
18. Johnson, T.A., and Patel, V.C., "Flow Past a Sphere up to a Reynolds Number of 300", *J. Fluid Mech.*, Vol. 378, 1999, pp. 19-70.
19. Roos, F.W., and Willmarth, W.W., "Some Experimental Results on Sphere and Disk Drag", *AIAA J.*, Vol. 9, No. 2, 1971, pp. 285-291.
20. Le Clair, B.P., Hamiliec, A.E., and Pruppacher, H.R., "A Numerical Study of the Drag of a Sphere at Low and Intermediate Reynolds Numbers", *J. Atmos. Sci.*, Vol. 27, No. 2, 1970, pp. 308-315.
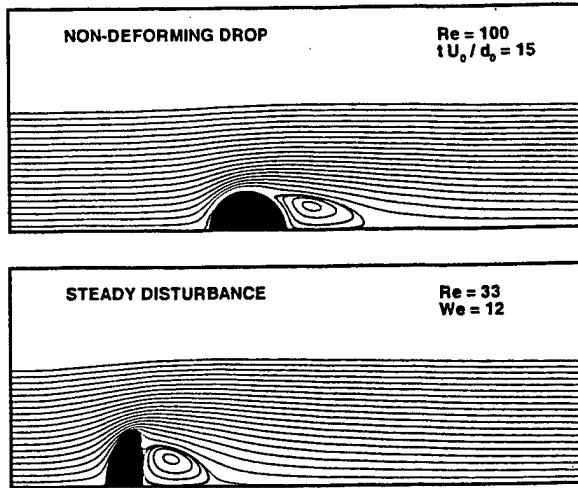
Fig. 1 Steady streamline patterns for the wake behind a non-deforming, stationary drop and behind a drop accelerated by a constant body force.

Fig. 3 Measured and predicted drag coefficients as a function of Reynolds number. Measurements from Roos and Willmarth,[19] predictions from Le Clair et al.,[20] Johnson and Patel,[18] and the present investigation.
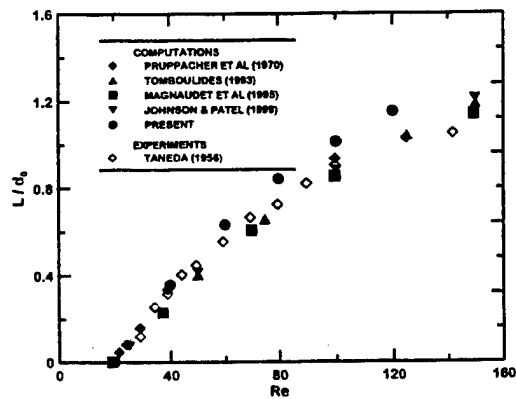
Fig. 2 Measured and predicted steady wakelength behind a drop as a function of Re for values smaller than the onset of instabilities (Re<130). Measurements from Taneda,[14] predictions from Pruppacher et al.,[15] Tomboulides,[16] Magnaudet et al.,[17] Johnson and Patel[18] and the present investigation.
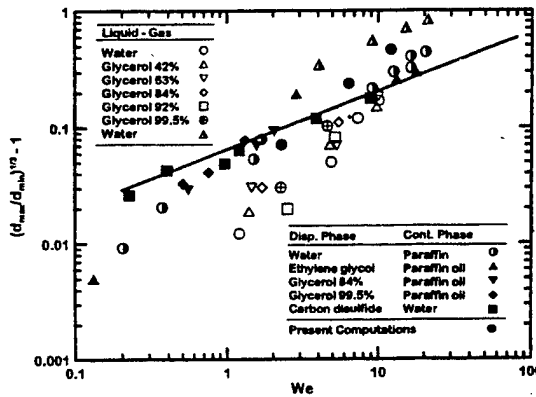
Fig. 4 Measured and predicted drop deformation due to a constant body force as a function of Weber number. Measurements of Hsiang and Faeth,[3] predictions from the present investigation.
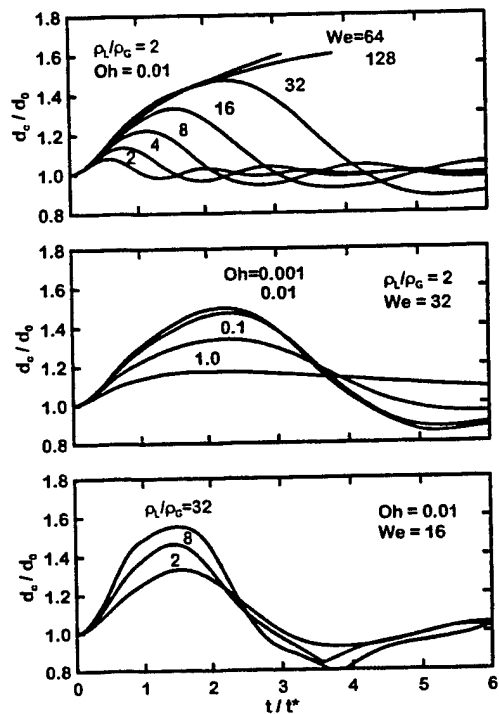
Fig. 5 Predicted drop deformation as a function of time for various Weber numbers, Ohnesorge numbers and density ratios at Re=50.
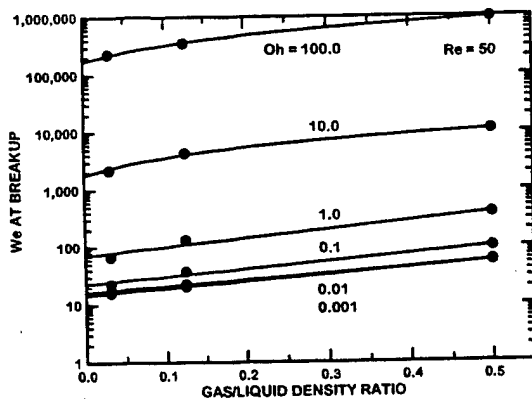
Fig. 6 Predicted Weber number at breakup as a function of gas/liquid density ratio for various Ohnesorge numbers.
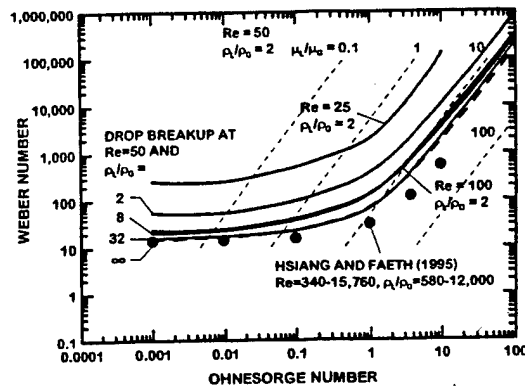
Fig. 7 Predicted and measured breakup regime map in the classical drag-force/surface-tension-force (We) and viscous-force/surface-tension-force (Oh) coordinates of Hinze.[7] Measurements from Hsiang and Faeth,[3] predictions from the present investigation.
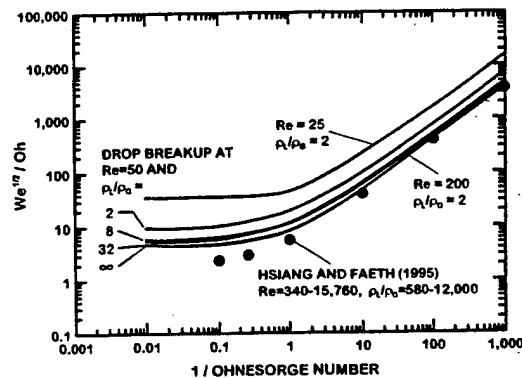
Fig. 8 Predicted and measured breakup regime map for drops in the revised drag-force/liquid viscous-force (We^{1/2}/Oh) and surface-tension-force/liquid-viscous-force (1/Oh) coordinates. Measurements from Hsiang and Faeth,[3] predictions from the present investigation.

Appendix B: Chen, J.-H. and Faeth, G.M. (2000) Inter-Wake Turbulence Properties of Homogeneous Particle-Laden Flows. *AIAA J.* 38, 995-1001.

Interwake Turbulence Properties of Homogeneous Dilute Particle-Laden Flows

J.-H. Chen* and G. M. Faeth[†]

University of Michigan, Ann Arbor, Michigan 48109-2140

The properties of turbulence generated by uniform fluxes of monodisperse spherical particles moving through a uniform flowing gas were studied experimentally, emphasizing the properties of the region surrounding individual wake disturbances, i.e., the turbulent interwake region. Mean and fluctuating values, probability density functions, and energy spectra of streamwise and cross-stream velocities were measured within a counterflowing particle/air wind tunnel using particle wake discriminating laser velocimetry. Test conditions included nearly monodisperse glass spheres having diameters of 0.5–2.2 mm, particle Reynolds numbers of 106–990, mean particle spacings of 13–208 mm, particle volume fractions less than 0.003%, direct rates of dissipation of turbulence by particles less than 4%, and turbulence generation rates sufficient to yield streamwise relative turbulence intensities in the range 0.2–1.5%. The turbulent interwake region was homogeneous and nearly isotropic with probability density functions that are well approximated by Gaussian functions. Relative turbulence intensities were correlated effectively based on an analogy to the properties of isotropic grid-generated turbulence by scaling with the mean particle spacing normalized by the particle wake momentum diameter. For present turbulence generation conditions the turbulent interwake region had turbulence Reynolds numbers of 0.4–3.5 and was in the final decay period where vortical regions fill the turbulent interwake region but are sparse. This implies enhanced rates of dissipation of turbulent kinetic energy and decreasing macroscale/microscale ratios of the turbulence with increasing Reynolds numbers, as opposed to increasing ratios with increasing Reynolds numbers typical of conventional fully developed isotropic turbulence.

Nomenclature

A = dimensionless integral length scale; Eq. (10)
C_d = particle drag coefficient
D = dissipation factor; Eq. (7)
D_P = Parthasarathy dissipation factor; Eq. (8)
d_p = particle diameter
$E_u(k)$ = streamwise energy spectrum
f = frequency
K = kurtosis of probability density function (PDF)
k = wave number, $2\pi/s$
L_u = streamwise integral length scale
ℓ_K = Kolmogorov length scale, $(\nu^3/\varepsilon)^{1/4}$
ℓ_p = mean particle spacing; Eq. (1)
M = mesh size of a grid
n = power in turbulence decay law; Eq. (4)
n'' = particle number flux
Re = particle Reynolds number, $d_p U_p/\nu$
Re_λ = turbulence Reynolds number, $Re_\lambda = \lambda \bar{u}'/\nu$
S = skewness of PDF
s = distance
t_K = Kolmogorov time scale, $(\nu/\varepsilon)^{1/2}$
U_p = mean streamwise relative velocity of a particle
u = streamwise gas velocity
u_K = Kolmogorov velocity scale, $(\varepsilon\nu)^{1/4}$
v = cross-stream gas velocity
x = streamwise distance
x_o = streamwise virtual origin location
β = empirical factor; Eqs. (4) and (5)
ε = rate of dissipation of turbulence kinetic energy
θ = wake momentum diameter, $(C_d d_p^2/8)^{1/2}$
λ = Taylor length scale; Eq. (3)
ν = molecular kinematic viscosity of air

Superscripts

$\overline{()}$ = mean value
$()'$ = rms fluctuating value
$\overline{()'^2}$ = mean-square fluctuating value

Introduction

TURBULENCE generation is the direct disturbance of the continuous-phase velocity field by the wakes of dispersed-phase objects in dispersed multiphase flows. Turbulence generation supplements the conventional production of turbulence caused by mean velocity gradients in the continuous phase. Turbulence generation is most important when the dispersed-phase objects have large relative velocities (large Reynolds numbers) and relatively large relaxation times compared to characteristic turbulence times. Such conditions are typical of many practical dispersed multiphase flows having significant separated-flow effects, e.g., sprays, particle-laden jets, bubbly jets, rainstorms, etc. In spite of its importance, however, turbulence generation has not received much attention so that current understanding and capabilities for predicting its properties are very limited. Motivated by these observations, the objective of the present investigation was to extend past studies of turbulence generation in this laboratory[1-3] to consider the properties of the continuous-phase region surrounding individual particle (drop) wake disturbances, i.e., the turbulent interwake region.

Earlier observations of flows resulting from turbulence generation in this laboratory have involved uniform fluxes of nearly monodisperse spherical particles moving at near terminal velocities in still water,[1] still air,[2] and upflowing air.[3] The resulting flows are homogeneous and stationary with turbulence production entirely caused by turbulence generation. An interesting feature of these flows is that the local rate of dissipation of turbulence kinetic energy mainly controls continuous-phase turbulence properties and that this parameter is readily found as the local rate of loss of particle mechanical energy per unit volume (the particle dissipation rate). All other continuous-phase properties of the flow [moments, probability density functions (PDFs), spectra, etc.], however, are not known and must be related to particle properties and particle dissipation rates.

The most recent study in this laboratory, involving particles in upflowing air,[3] avoided earlier problems of measurements in still environments that yielded flows having very large turbulence

58

intensities.[1,2] It was found that relative turbulence intensities were
proportional to the square root of the rate of dissipation in ac-
cord with a simplified stochastic theory of turbulence generation
described in Refs. 1 and 2. Other properties, however, were not ex-
plained by the simplified stochastic theory and exhibited features
not seen in conventional homogeneous turbulence: PDFs of stream-
wise velocities were not Gaussian, whereas PDFs of cross-stream
velocities were Gaussian, and the energy spectra of both velocity
components exhibited prominent -1 power decay regions in addi-
tion to the usual $-\frac{5}{3}$ power decay inertial region. These differences
from conventional turbulence properties were attributed to effects
of particle wakes that cannot be separated from other flow prop-
erties by conventional phase-discriminating velocity measurements
because the arrival of particle wakes in these flows is random. De-
tailed observations, however, showed that particle wake properties
approximated the properties of the laminarlike turbulent wakes ob-
served for particle wakes at intermediate Reynolds numbers in con-
ventional turbulent environments, described in Refs. 4–6, in spite of
the unusual features of continuous-phase turbulence resulting from
turbulence generation. Given estimates of the wake properties, it was
subsequently shown that most practical turbulence generation pro-
cesses involve particle wake disturbances surrounded by a relatively
large turbulent interwake region.[7]

Stochastic analysis to estimate the overall properties of flows
dominated by turbulence generation involves straightforward con-
ditional averaging of the properties of the wake disturbances and
the turbulent interwake region. At the present time information is
available concerning the laminarlike turbulent wake behavior of the
wake disturbances[5,6] and the overall properties of flows dominated
by turbulence generation.[1-3] The missing element for predictions
of the overall flow properties of turbulence generation involves in-
formation about the properties of the turbulent interwake region.
Thus, the objectives of the present investigation were to complete
conditional measurements of the properties of the turbulent inter-
wake region for the range of conditions considered in Ref. 3 and to
exploit existing methods in the turbulence literature to interpret and
correlate the measurements.

Present measurements were carried out in a counterflow parti-
cle/air wind tunnel considering nearly monodisperse glass spheres
having particle fluxes sufficient to yield relative turbulence inten-
sities of 0.2–1.5%. Measurements were made using particle wake
discriminating laser velocimetry to find moments and PDFs of veloc-
ities, energy spectra of streamwise velocity fluctuations, and char-
acteristic time and length scales. These results were interpreted and
correlated by studying potential analogies between the turbulent
interwake region of turbulence generation processes and homoge-
neous grid-generated turbulence, e.g., the studies of grid-generated
turbulence of Refs. 8–12 and references cited therein. The present
description of the study is brief; more details and a tabulation of the
data can be found in Chen et al.[3]

Experimental Methods

The apparatus consisted of a vertical counterflow wind tunnel
with upflowing air moving toward the suction side of the blower
and freely falling nearly monodisperse spherical glass particles that
were introduced at the top of the wind tunnel using a particle feeder
(see Ref. 3 for a complete description). The air flowpath consisted
of a rounded inlet, a flow straightener, and a 16:1 contraction ratio to
the 305×305 mm cross-section windowed test section. The particle
flowpath consisted of a variable-speed particle feeder, a screen array
particle dispersion section, a honeycomb particle flow straightener,
and a particle acceleration section to yield near terminal velocity
particles at the test section. The particles were collected in a flexible
plastic funnel below the air inlet.

Measurements included particle number fluxes by sampling and
particle and gas velocities by a traversible laser velocimetry (LV)
system. The particle measurements are described in Ref. 3; there-
fore, the following discussion will be limited to the gas veloc-
ity measurements. A single-channel, dual-beam, forward-scatter,
frequency-shifted LV was used, based on the 514.5-nm line of an
argon-ion laser. Streamwise and cross-stream velocities were found
by rotating the optics accordingly. A beam expander was used to
yield a measuring volume diameter and length of 55 and 425 μm,

respectively. The airflow entering the wind tunnel was seeded with
oil drops having a 1-μm nominal diameter for the air velocity mea-
surements. Velocities were found from the low-pass filtered analog
output of a burst counter signal processor. The combination of fre-
quency shifting plus a constant sampling rate of the analog output of
the signal processor eliminated effects of directional bias and am-
biguity and velocity bias. The glass particles were inspected with
a microscope after they were collected, which showed that the par-
ticles did not collect seeding particles and were not damaged dur-
ing passage through the test apparatus; therefore, they were reused.
Heavy seeding levels were used so that effects of LV step noise
were deferred to scales roughly an order of magnitude larger than
the Kolmogorov scales. In spite of the heavy seeding, however, ef-
fects of turbulence modulation by LV seeding particles were small.
For example, the seeding particles had good response for present
test conditions so that effects of slip were small. For such condi-
tions the locally homogeneous flow approximation is acceptable,
and effects of turbulence modulation by seeding particles are re-
flected by the increased apparent density of the continuous phase
caused by the presence of the seeding particles. With seeding par-
ticle volume fractions smaller than 2×10^{-7}, however, the density
increase was less than 0.02% with correspondingly small effects of
turbulence modulation.

Conditional sampling was carried out by installing a particle de-
tector so that disturbances from particle wakes could be deleted
from the velocity record. The particle detection system consisted of
a He–Ne laser sheet whose width was controlled by an adjustable
slot. The sheet was observed through a laser line filter from a direc-
tion nearly normal to the path of the sheet, using another adjustable
slot to control the length of the sheet that was observed. The LV
measuring volume was positioned just below the He–Ne laser sheet
at the center of the region observed. The required dimensions of the
region of the laser sheet that was observed were estimated according
to the laminarlike turbulent wake correlations of Refs. 5 and 6. The
region included had a radius larger than twice the characteristic lam-
inarlike wake radius (as defined in Refs. 5 and 6) from the particle
wake axis. When strong scattering from a glass sphere was detected,
velocity signals were not processed to contribute to the conditional
properties of the turbulent interwake region for the time required
for the particle wake to pass through the measuring plane. This time
was selected so that the maximum mean velocity defect of the wake
disturbance at the plane of the measurements was smaller than the
velocity fluctuation level of the turbulent interwake region. Satura-
tion of the particle detector occasionally allowed wake disturbances
from a nearby particle to be recorded; such conditions were treated
using velocity amplitude discrimination as discussed in Ref. 3. Fi-
nally, PDFs of streamwise and cross-stream velocities were used to
access the effectiveness of the particle wake discrimination system
as discussed later.

Velocity records having drop-out periods that resulted when dis-
turbances caused by particle wakes were removed were analyzed
directly by correcting the sampling time for most velocity statis-
tics, e.g., moments and other PDF properties. In contrast, obtaining
correct temporal power spectra in the presence of dropout periods re-
quires special treatment as described by Buchhave[13] and Buchhave
et al.[14] (see Ref. 3 for the present application of these methods).
Upflow velocities in the wind tunnel were set to provide absolute
turbulence intensities less than 15% so that LV measuring condi-
tions were excellent. Therefore, use of Taylor's hypothesis to convert
measured temporal power spectra and scales to spatial spectra and
scales is appropriate.[10] Sampling periods were adjusted to provide
experimental uncertainties (95% confidence) less than 5% for mean
velocities, less than 10% for rms velocity fluctuations, less than
10% for PDFs within one standard deviation of the most probable
velocity and less than 20% for temporal power spectra at frequen-
cies smaller than the reciprocal of the temporal integral scale with
uncertainties smaller elsewhere.

Test conditions are summarized in Table 1. Particle properties
were measured as described in Ref. 3. The particles were nearly
monodisperse with standard deviations of particle diameters less
than 10% of the mean particle diameters (Table 1). The parti-
cles approached terminal velocity conditions so that wake prop-
erties were quasisteady and the multiphase flow was approximately

Table 1 Summary of test conditions[a]

Parameter	Nominal particle diameter (mm)[b]		
	0.5 (0.047)	1.1 (0.109)	2.2 (0.126)
U_p, mm/s	3370	5530	7000
Re	106	373	990
C_d	1.22	0.79	0.54
$(dU_p/dx)/U_p$, %/m	2	11	14
θ, mm	0.183	0.299	0.519
n'', kpart/m²s	71–950	4–56	0.5–10
ℓ_p, mm	13–32	41–97	77–208
ε, m²/s³	0.088–1.17	0.041–0.54	0.012–2.3
ℓ_K, mm	0.2–0.5	0.3–0.6	0.4–0.7
t_K, ms	4–14	5–16	8–37
u_K, mm/s	34–60	31–54	21–44
$\bar{u}'/U_p$, %	0.5–1.5	0.2–0.6	0.2–0.6
λ, mm	0.7–0.9	0.6–0.8	1.2–1.8
Re_λ	0.7–2.5	0.4–1.5	1.4–3.5
L_u, mm	11–35	42–178	23–156

[a]Round glass beads (density of 2500 kg/m³) falling in upflowing air at standard temperature and pressure (air density of 1.16 kg/m³ and kinematic viscosity of 15.9 mm²/s) having a mean velocity of 1.1 m/s. Parameter ranges for each particle size given in order of lowest-highest particle number fluxes, respectively.
[b]Standard deviations given in parentheses.

homogeneous (e.g., rates of particle acceleration at the measuring location were in the range 2–14% of the mean particle velocity per meter); nevertheless, measured particle velocities at the measuring location were used to find other particle properties rather than assuming terminal velocity conditions. Assuming that the particles are falling randomly, the mean particle spacing is given by

$$\ell_p = [(U_p - \bar{u})/n'']^{\frac{1}{3}} \quad (1)$$

which yields values of 13–208 mm with corresponding particle volume fractions less than 0.003%.

The direct dissipation of turbulence kinetic energy (dissipation) by particles was less than 4%; see Chen[7] for a discussion of this estimate. In addition, dissipation within the wake disturbances was also small compared to the turbulent interwake region. This can be seen by noting that dissipation from mean velocities in the wake disturbances is small because of the small Mach numbers of these flows so that the ratio of the dissipation in the interwake region to that of the flow as a whole can be estimated by the corresponding estimate of the ratio of the turbulence kinetic energies of these two regions. This latter ratio is best estimated by the ratio of the square of the cross-stream velocities of these two regions (to avoid bias of the overall fluctuations by mean velocities in the wake disturbances) yielding a value of 88% (Ref. 7). This implies that dissipation within the wake disturbances is only roughly 12% of the total dissipation, which is smaller than the experimental uncertainties of turbulence kinetic energies (mean square velocity fluctuations); therefore, a reasonable approximation for the rate of dissipation in the turbulent interwake region can be found from the rate of turbulence generation by the particles, as follows:

$$\varepsilon = \pi n'' d_p^2 C_d U_p^3/8 \quad (2)$$

Given ε, the Kolmogorov scales can be computed from their definitions. For these dissipation rates relative turbulence intensities caused by turbulence generation were in the range 0.2–1.5%. Measurements to be discussed later will show that interwake turbulence is similar to homogeneous isotropic turbulence so that Taylor's dissipation length scale can be estimated from the following equation:

$$\lambda = (15\nu \bar{u}'^2/\varepsilon)^{\frac{1}{2}} \quad (3)$$

Present values of λ are somewhat larger but comparable to Kolmogorov length scales (i.e., $\lambda/\ell_K = 1.3$–3.5), which is not unexpected in view of the relatively small turbulence Reynolds numbers 0.4–3.5 of the present turbulent interwake regions. Finally, streamwise integral length scales were obtained from energy spectra as discussed later, yielding values comparable to mean particle spacings, i.e., 11–178 mm.

Evaluation of the apparatus is discussed by Chen et al.[3] and Chen.[7] Measurements of particle number fluxes and phase velocities showed that they varied less than experimental uncertainties

over the central 205 × 205 mm cross section of the flow, extending 200 mm in the streamwise direction, which surrounded the location where measurements were made. Similar measurements showed that flow properties varied less than experimental uncertainties as a function of time. Thus, present flows were properly homogeneous and stationary with turbulence within the turbulent interwake region produced by turbulence generation.

Results and Discussion

Relative Turbulence Intensities

Correlations of the properties of the turbulent interwake region were sought by drawing analogies between the turbulent interwake region and grid-generated turbulence. Past experimental observations show that turbulence downstream of grids can be divided into three regions: 1) a developing region near the grids, where the wakes from grid elements are merging and the turbulent flow is inhomogeneous and anisotropic; 2) an initial-decay region where the turbulent flow is nearly homogeneous and is locally isotropic; and 3) a final-decay region, where viscous effects dominate, regions containing vorticity become sparse (giving the appearance of isolated turbulent spots from single-point measurements), and the turbulence decays more rapidly than in the initial decay region. Thus, comparing the turbulent interwake region with grid-generated turbulence suggests that the wake disturbances of turbulence generation correspond to the developing region of grid-generated turbulence and that the turbulent interwake region of turbulence generation corresponds to either the initial- or final-decay regions of grid-generated turbulence. Batchelor and Townsend[11,12] suggest a value of $Re_\lambda \approx 5$ as the condition for the onset of the final-decay region for grid-generated turbulence; therefore, the present turbulent interwake regions involving $Re_\lambda \approx 0.4$–3.5 (see Table 1) have significant potential for behavior analogous to the final decay region.

The analogy between the present turbulent interwake region and grid-generated turbulence was based on an expression for grid-generated turbulence from Batchelor and Townsend,[11,12] as follows:

$$(\bar{u}' \text{ or } \bar{v}')/\bar{u} = \beta[C_d M/(x - x_0)]^n \quad (4)$$

where β is an empirical factor and they propose $n = \frac{1}{2}$ and $\frac{5}{4}$ in the initial- and final-decay periods, respectively. For present conditions the turbulent interwake region was homogeneous; therefore, a reasonable analogy to the distance from the grid for grid-generated turbulence is a distance on the order of the mean particle spacing. The length corresponding to the product of mesh size and drag coefficient for grid-generated turbulence was taken to be the particle wake momentum diameter θ, which similarly involves the product of the particle diameter and drag coefficient. Given these analogies, the expression corresponding to Eq. (4) for the turbulent interwake region becomes

$$(\bar{u}' \text{ or } \bar{v}')/U_p = \beta(\theta/\ell_p)^n \quad (5)$$

where β may not necessarily be the same for $\bar{u}'$ and $\bar{v}'$. Introducing expressions for θ in terms of C_d and d_p, Eq. (1) for ℓ_p, and eliminating n'' from the resulting expression using Eq. (2) yields the following potential correlation for the relative turbulence intensities of the turbulent interwake region:

$$(\bar{u}' \text{ or } \bar{v}')/U_p = \beta D^{n/3} \quad (6)$$

where D is a dimensionless dissipation factor defined as follows:

$$D = (\theta/\ell_p)^3 = \frac{\varepsilon d_p (C_d/8)^{\frac{1}{2}}}{\pi U_p^2(U_p - \bar{u})} \quad (7)$$

During the earlier turbulence generation studies of Refs. 1 and 2, expressions very similar to Eqs. (6) and (7) were developed that proved to be reasonably effective for correlating their relative turbulence intensity measurements. Their expression was developed using a simple stochastic analysis to synthesize the properties of particle wake disturbances alone (with no consideration of a turbulent interwake region) based on Campbell's theorem, similar to the analysis of electrical noise from Rice.[15] The resulting correlation was identical to Eq. (6) except that D was replaced by an alternative dimensionless dissipation factor D_p, defined as follows:

$$D_p = \varepsilon d_p (C_d/8)^{\frac{1}{2}}/U_p^3 \quad (8)$$

CHEN AND FAETH
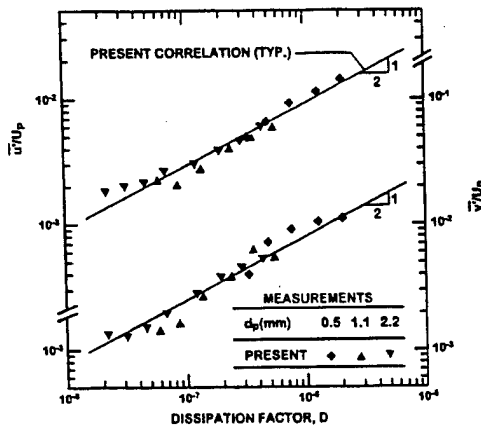
Fig. 1 Streamwise and cross-stream relative turbulence intensities as a function of the dissipation factor for various particle sizes.

The dimensionless dissipation factors D and D_P are closely related for the stagnant flow conditions considered in Refs. 1 and 2 where $\bar{u} = 0$, noting that the effect of the different powers of C_d in Eqs. (7) and (8) is small because C_d is on the order of unity for the conditions of all of these experiments (see Table 1). Based on the measurements of Refs. 1 and 2, this correspondence between the two correlations suggests that $n = \frac{3}{2}$. This estimate is reasonably close to the value $n = \frac{5}{4}$ suggested by Batchelor and Townsend,[11,12] where Eq. (4) is used to correlate turbulence intensities in the final-decay period of grid-generated turbulence, which is also consistent with the present relatively small values of Re_λ noted earlier.

Present measurements of streamwise and cross-stream relative turbulence intensities, within the turbulent interwake region for all three particle sizes, are plotted in Fig. 1 as a function of D according to Eq. (6). The correlation is seen to be remarkably good, over the two-order-of-magnitude range of D considered during the present experiments. Best-fit correlations of the measurements found by linear regression had powers of 0.48 and 0.56 (with standard deviations of both these powers of 0.03) for streamwise and cross-stream relative turbulence intensities, respectively. As a result, there is no statistical significance for the differences between the powers of these fits and the value of $n = \frac{3}{2}$ found in Refs. 1 and 2. Thus, for consistency with this earlier work, the measurements were correlated as shown in Fig. 1 using the earlier value of n to yield

$$\bar{u}'/U_p = 9.2D^{\frac{1}{2}}, \qquad \bar{v}'/U_p = 7.9D^{\frac{1}{2}} \qquad (9)$$

The standard deviation of the coefficients of Eqs. (9) are 1.5 and 1.6, respectively, and the correlation coefficients of both these fits are 0.98, which is excellent.

The difference between the coefficients of the streamwise and the cross-stream relative turbulence intensities is not statistically significant. Thus, the turbulent interwake region is isotropic within present capabilities to evaluate this behavior. Slight anisotropy favoring the streamwise direction, however, is not unexpected. In particular, the present wake discrimination system was not totally effective as discussed later, which introduces some streamwise velocity bias because of uneliminated streamwise mean velocity disturbances from wakes. In addition, past studies of grid-generated turbulence at small turbulence Reynolds numbers [Re_λ of 36–72, which is somewhat larger than the present range (see Table 1)] from Bennett and Corrsin[16] yielded values of $\bar{u}'/\bar{v}'$ in the range 1.09–1.22, which is similar to the present mean value of $\bar{u}'/\bar{v}' = 1.16$ found from Eqs. (9). Thus, potential for a small fundamental level of anisotropy for the turbulent interwake region cannot be ruled out.

The correspondence between the correlations of Eq. (6) involving D, based on sole consideration of the turbulent interwake region, and involving D_P, based on sole consideration of wake disturbances, helps explain the effectiveness of D_P for consideration the relative turbulence intensities observed in Refs. 1 and 2, even though the
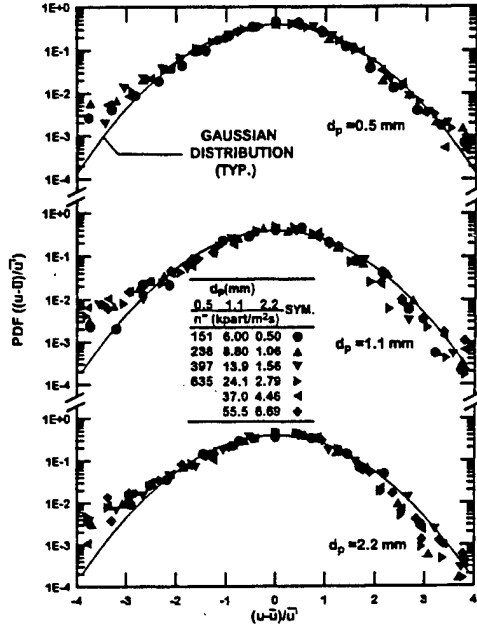
Fig. 2 Typical PDFs of streamwise velocities for various particle sizes and number fluxes.

wake disturbances did not contribute significantly to these measurements (i.e., wake disturbances were largely eliminated by their phase-discrimination systems). Thus, the nearly identical definitions of D and D_P suggest that either approach is fortuitously appropriate for both the turbulent interwake and wake disturbance regions of flows caused by turbulence generation (even though the detailed properties of these two flow regions differ considerably).

PDFs

Potential departures of the turbulent interwake region from the behavior of isotropic turbulence were studied further by considering the PDFs and the higher-order (skewness and kurtosis) statistical moments of streamwise and cross-stream velocities. Typical measured streamwise and cross-stream PDFs of velocities for various particle sizes and loadings are plotted in Figs. 2 and 3. Fits of the measurements are also shown on the plots, corresponding to best Gaussian fits based on rms velocity fluctuations. These PDFs are plotted using logarithmic scales to highlight potential effects of wake disturbances and the performance of the fits at the extremities of the distributions where the PDFs become small.

PDFs of cross-stream velocities illustrated in Fig. 3 are symmetric, which is consistent with absence of any preferred direction for cross-stream velocities because of contributions from either the turbulent interwake region or from wake disturbances that were not completely eliminated by the wake discrimination system of the LV. The cross-stream PDFs are also in generally good agreement with the Gaussian fits. The main exceptions are slight upward biases near both edges of the distributions, which are thought to be caused by increased experimental uncertainties near the extremities of the distributions because of sampling limitations (e.g., normalized PDFs at these locations are very small, on the order of 10^{-3}).

In contrast to the symmetric PDFs of cross-stream velocities, the PDFs of streamwise velocities illustrated in Fig. 2 exhibit a distinct asymmetry. This involves an upward bias of the measurements from the Gaussian distribution near -2.5 standard deviations, whereas the positive sides of the distributions agree quite well with Gaussian distributions. This behavior, however, no doubt results from small disturbances caused by mean streamwise velocities in the particle wakes that were not eliminated by the present particle wake discrimination system.
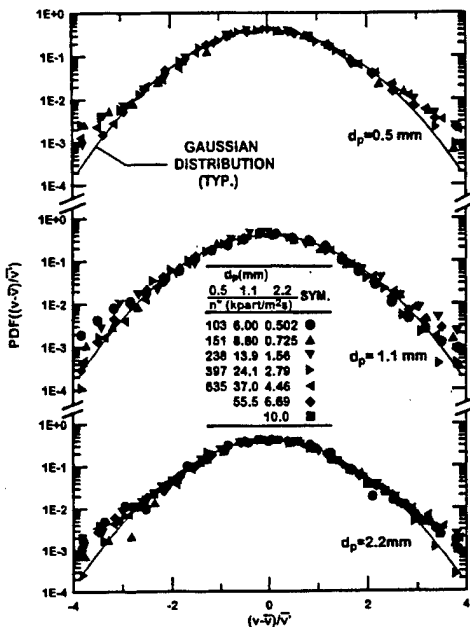
Fig. 3 Typical PDFs of cross-stream velocities for various particle sizes and number fluxes.

Fig. 4 Energy spectra of streamwise velocity fluctuations for various particle sizes and number fluxes.

Higher moments of the PDFs averaged over all of the measurements in the turbulent interwake region, can be summarized as follows: values of $S(u)$ and $S(v)$ are -0.5 and 0.0, with standard deviations of 0.4 and 0.1, respectively; and values of $K(u)$ and $K(v)$ are 7 and 8, both with standard deviations of 2. The departures of measured values of skewness from the Gaussian value of $S = 0$ are not statistically significant, although the measurements do suggest a contribution of wake disturbances to the somewhat larger negative skewness of the PDF of streamwise velocities. The departures of the measured values of kurtosis from the Gaussian value of $K = 3$ also borders on the limit of statistical significance, particularly in view of the larger experimental uncertainties of this high-order moment caused by sampling limitations. Thus, the present PDF measurements within the turbulent interwake region are adequately described by Gaussian functions, similar to conventional isotropic turbulence.

Energy Spectra

Streamwise energy spectra within the turbulent interwake region were obtained using Taylor's hypothesis to transform measured temporal spectra to spatial spectra as already described. The corresponding integral length scales were found by noting that the normalized amplitude of the energy spectra plots $2\pi E_u(k)/(\bar{u}'^2 L_u)$ approaches the value of four as the normalized wave number of these plots $kL_u/(2\pi)$ becomes small, analogous to temporal spectra as discussed by Hinze.[10] The resulting normalized energy spectra of streamwise velocity fluctuations are illustrated in Fig. 4 for various particle sizes and loadings. Correlations of energy spectra for approximate isotropic turbulence are also shown on the plot for comparison with the measurements. The approximate spectra represent the simplification of isotropic turbulence discussed by Hinze,[10] where correlations of velocity fluctuations are assumed to satisfy exponential functions. This simplification implies that the $-\frac{5}{3}$ power decay of the energy spectra within the inertial subrange of turbulence is approximated by a -2 power decay.

Although the energy spectra illustrated in Fig. 4 are separated by particle sizes to help readability, the spectra are independent of both particle size and loading and agree reasonably well with the isotropic turbulence approximation described by Hinze.[10] Thus, the prominent -1 power decay region of the spectra of the over-

all flow (wake disturbances plus the turbulent interwake region) of continuous-phase turbulence resulting from turbulence generation, seen in Refs. 1–3, disappears when the particle wake disturbances are removed. This finding implies that the -1 power decay region seen for the overall flow is caused by wake disturbances. Finally, the present spectra are truncated at large wave numbers to avoid step noise caused by sampling limitations, with full spectra expected to reach wave numbers characteristic of Kolmogorov scales at values of $kL_u/(2\pi)$ on the order of 100. Thus, the present interwake turbulence exhibits a substantial range of scales, roughly 1000:1, even though turbulence Reynolds numbers are small, less than 4. Consideration of length scales in the present turbulent interwake regions, however, will show that the present large range of scales represent reasonable behavior for turbulence in the final decay period, which is characteristic of the turbulent interwake region for present test conditions. These same considerations of length scales will also show that the present large range of scales appears for very different reasons than in high-Reynolds-number isotropic turbulence. This behavior will be discussed next.

Length Scales

Numerous studies of isotropic turbulence at large turbulence Reynolds numbers show that the rate of dissipation of turbulence kinetic energy can be estimated from values of velocity fluctuations and integral length scales using the following equation[10]:

$$A = \varepsilon L_u/(\bar{u}')^3 \qquad (10)$$

where A, the dimensionless integral length scale, is believed to be a constant on the order of unity. All properties on the right-hand side of Eq. (10) have been measured during the present investigation so that values of A can be found at much smaller Re_λ than considered in the past.

The resulting values of A from the present investigation are plotted as a function of Re_λ in Fig. 5, providing results at small Reynolds numbers $Re_\lambda = 0.4$–3.5. Results for isotropic turbulence from several past experiments,[17–21] from direct numerical simulations (DNS),[22–25] and from a DNS data fit from Sreenivasan[26] are plotted along with the present measurements. The earlier

1000
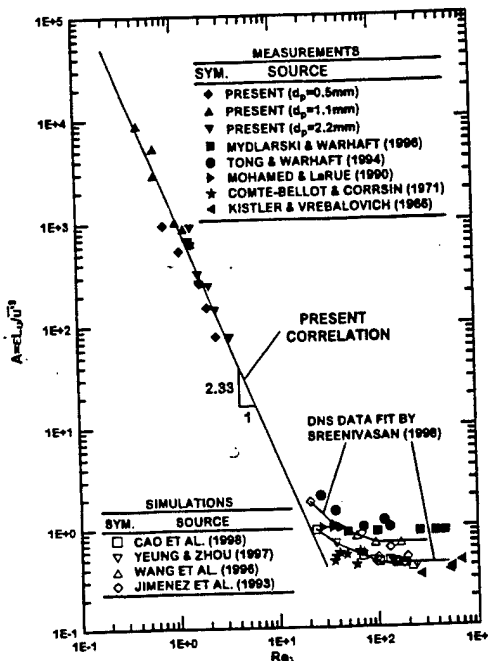
Fig. 5 Normalized integral length scales as a function of turbulence Reynolds number for both grid-generated and particle-generated turbulence. Measurements of Kistler and Vrebalovich,[17] Comte-Bellot and Corrsin,[18] Mohamed and LaRue,[19] Tong and Warhaft,[20] Mydlarski and Warhaft,[21] and the present investigation; predictions of Jiminez et al.,[22] Wang et al.,[23] Yeung and Zhou,[24] and Cao et al.[25]; DNS data fit of Sreenivasan.[26]

determinations of A involve relatively large turbulence Reynolds numbers, $20 \leq Re_\lambda \leq 800$, which places these flows in the initial decay period of isotropic turbulence where the turbulence is fully developed and acts over the entire flow region similar to conventional turbulence. In contrast, present measurements at small values of Re_λ exhibit very enhanced rates of dissipation, which is typical of behavior in the final-decay period where the vorticity is sparse and turbulence appears to involve disconnected spots when single-point measurements are observed.[4,11,12,27,28] This behavior is also consistent with earlier indications that interwake turbulence was in the final-decay period, based on relative turbulence intensities as discussed in connection with Fig. 1.

The measurement and predictions at large Re_λ yield scattered values of A in the range 0.3–2.0, which is on the order of unity and independent of Re_λ, as expected. Sreenivasan[26] suggests that these variations of A are caused by different initial conditions or grid geometries of the flows that were considered. In contrast, present values within the final-decay period indicate strongly enhanced dissipation as Re_λ decreases (indicated by increasing values of A), analogous to strongly enhanced dissipation as Re_λ decreases (indicated by decreasing values of the turbulence intensity) along the axis of turbulent wakes in the final-decay period (see Ref. 4). The present measurements of A within the final-decay period yield a best fit correlation as follows:

$$A = 1130 Re_\lambda^{-2.33}, \qquad 0.4 \leq Re_\lambda \leq 3.5 \qquad (11)$$

where the experimental uncertainty of the power of Re_λ is 0.16 and the correlation coefficient of the fit is 0.96. Combining all of the observations of A illustrated in Fig. 5, it is evident that A exhibits three regimes: 1) a large Re_λ regime (the initial-decay period) with $Re_\lambda > 100$, which corresponds to classical homogeneous isotropic turbulence at large Reynolds numbers; 2) a small Re_λ regime (the

final-decay period) where $Re_\lambda < 10$, which corresponds to present turbulent interwake conditions; and 3) a transition regime with $10 < Re_\lambda < 100$ between the two outer limiting regimes.

It is interesting to consider the variation of the length scale ratio L_u/λ as a function of Re_λ, in the three regimes of A that were just defined. This ratio assumes the following forms.

Final-decay period:

$$L_u/\lambda = 75 Re_\lambda^{-1.33}, \qquad 0.4 \leq Re_\lambda \leq 3.5 \qquad (12)$$

Initial-decay period:

$$L_u/\lambda = A Re_\lambda/15, \qquad 20 \leq Re_\lambda \qquad (13)$$

Finally, in the transition region, Ling and Huang[27] find $A \sim Re_\lambda^{-1}$, which implies the following.

Transition period:

$$L_u/\lambda = 2.2, \qquad 4 \leq Re_\lambda \leq 20 \qquad (14)$$

The correlations of Eqs. (12–14) are illustrated in Fig. 6, along with results from available measurements and DNS simulations. Taken together, the various correlations provide reasonably good fits of results in the final-decay, transition, and initial-decay periods.

The nature and location of transition to the final-decay period seen in Fig. 6 seems quite reasonable. In particular, the variation of L_u/λ with decreasing Re_λ for fully developed turbulent flows must change as Re_λ becomes small because realizable flow properties cannot involve a Taylor length scale (a microscale) larger than the integral scale (a macroscale), or conditions where $L_u/\lambda < 1$. Thus, it is not surprising that the transition to the final-decay period, where L_u/λ increases with decreasing Re_λ, occurs when L_u/λ reaches values on the order of unity.

Increasing values of L_u/λ with increasing Re_λ in the initial-decay period is well understood[8,10] as a result of the relatively inviscid large-scale features (on the scale of integral scales) combined
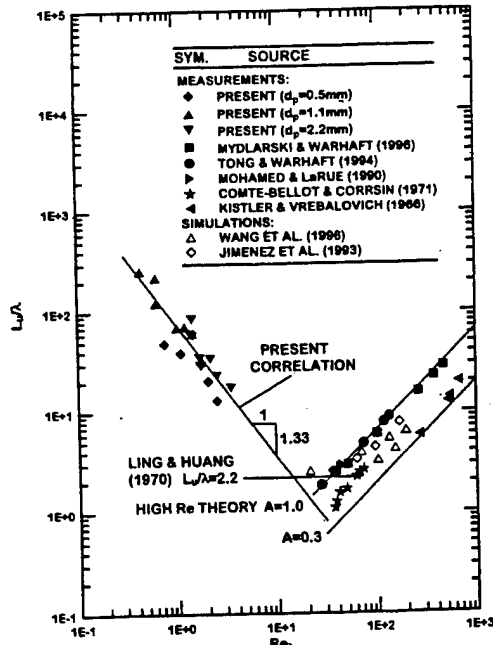
Fig. 6 Ratios of integral and Taylor length scales as a function of turbulence Reynolds number for both grid-generated and particle-generated turbulence. Measurements of Kistler and Vrebalovich,[17] Comte-Bellot and Corrsin,[18] Mohamed and LaRue,[19] Tong and Warhaft,[20] Mydlarski and Warhaft,[21] and the present investigation; predictions of Jiminez et al.[22] and Wang et al.[23]; correlation of Ling and Huang.[27]

with progressively smaller microscales of turbulence as turbulence Reynolds numbers increase. The corresponding increasing values of L_u/λ with decreasing values of Re_λ in in the final-decay period occurs for very different reasons. In this case vortical regions are sparse although they still spread throughout the entire flow, yielding large integral scales in the presence of small dissipation scales, i.e., the dimensions of turbulent spots become small in comparison to the dimensions of the flow as a whole when the vortical regions of the flow become more sparse as turbulence decay proceeds.

Conclusions

This investigation considered the properties of turbulence generated by uniform fluxes of monodisperse spherical particles moving through air at standard temperature and pressure, emphasizing the properties of the turbulent interwake region. Test conditions included nearly monodisperse glass beads having diameters of 0.5–2.2 mm, particle Reynolds numbers of 106–990, mean particle spacings of 13–208 mm, particle volume fractions less than 0.003%, direct rates of dissipation of turbulence by particles less than 4%, and turbulence generation rates sufficient to yield streamwise relative turbulence intensities of 0.2–1.5%. The major conclusions of the study are as follows:

1) The turbulent interwake region is homogeneous and nearly isotropic with PDFs of streamwise and cross-stream velocities well approximated by Gaussian functions.

2) Relative turbulence intensities in the turbulent interwake region were correlated effectively by analogy to the known properties of isotropic grid-generated turbulence, e.g., Batchelor and Townsend,[11,12] by scaling these properties with the mean particle spacing normalized by the particle wake momentum diameter to yield a dimensionless dissipation factor.

3) The present dimensionless dissipation factor, based on consideration of interwake turbulence alone, is nearly identical to an earlier dimensionless dissipation factor found in Refs. 1 and 2, based on consideration of particle wake properties alone. This fortuitous agreement of correlations for the turbulent interwake region and for wake disturbances is no doubt responsible for the simple correlations of overall relative turbulence intensities (involving both regions) as a function of dimensionless dissipation factor observed during earlier work.[1-3]

4) For present turbulence generation conditions and probably for most practical dispersed flows, the turbulent interwake region exhibited very small turbulence Reynolds numbers ($Re_\lambda < 4$) and was in the final-decay period where vortical regions fill the entire interwake region but are sparse, i.e., where turbulence appears to involve disconnected turbulent spots when single-point measurement are observed.

5) Within the final-decay period macroscale/microscale ratios (e.g., L_u/λ) decrease with increasing turbulence Reynolds numbers as opposed to increasing similar to fully developed isotropic turbulence at large turbulence Reynolds numbers. Quite plausibly, the transition from the final-decay region to the fully developed turbulence region occurs when L_u/λ is on the order of unity; this condition corresponds to a turbulence Reynolds number on the order of 10, which is similar to conditions at the transition of turbulent wakes in nonturbulent environments to the final decay period (see Ref. 4).

Acknowledgments

References

[1]Parthasarathy, R. N., and Faeth, G. M., "Turbulence Modulation in Homogeneous Dilute Particle-Laden Flows," *Journal of Fluid Mechanics,* Vol. 220, Pt. 2, 1990, pp. 485–514.

[2]Mizukami, M., Parthasarathy, R. N., and Faeth, G. M., "Particle-Generated Turbulence in Homogeneous Dilute Dispersed Flows," *International Journal of Multiphase Flow,* Vol. 18, No. 2, 1992, pp. 397–412.

[3]Chen, J.-H., Wu, J.-S., and Faeth, G. M., "Turbulence Generation in Homogeneous Particle-Laden Flows," *AIAA Journal,* Vol. 38, No. 4, 2000, pp. 636–642.

[4]Wu, J.-S., and Faeth, G. M., "Sphere Wakes in Still Surroundings at Intermediate Reynolds Numbers," *AIAA Journal,* Vol. 31, No. 8, 1993, pp. 1448–1455.

[5]Wu, J.-S., and Faeth, G. M., "Sphere Wakes at Moderate Reynolds Numbers in a Turbulent Environment," *AIAA Journal,* Vol. 32, No. 3, 1994, pp. 535–541.

[6]Wu, J.-S., and Faeth, G. M., "Effects of Ambient Turbulence Intensity on Sphere Wakes at Intermediate Reynolds Numbers," *AIAA Journal,* Vol. 33, No. 1, 1995, pp. 171–173.

[7]Chen, J.-H., "Turbulence Generation in Homogeneous Dilute Particle-Laden Flows," Ph.D. Dissertation, Dept. of Naval Architecture and Marine Engineering, Univ. of Michigan, Ann Arbor, MI, 1999.

[8]Schlichting, H., *Boundary Layer Theory,* 7th ed., McGraw-Hill, New York, 1979, pp. 234, 235, 599.

[9]Tennekes, H., and Lumley, J. L., *A First Course in Turbulence,* MIT Press, Cambridge, MA, 1972, pp. 113–124, 196–201.

[10]Hinze, J. O., *Turbulence,* 2nd ed., McGraw-Hill, New York, 1975, Chap. 3, pp. 65–67, 204, 496–519.

[11]Batchelor, G. K., and Townsend, A. A., "Decay of Isotropic Turbulence in the Initial Period," *Proceedings of the Royal Society of London,* Vol. A193A, No. 8, 1948, pp. 539–558.

[12]Batchelor, G. K., and Townsend, A. A., "Decay of Turbulence in the Final Period," *Proceedings of the Royal Society of London,* Vol. 194A, No. 8, 1948, pp. 527–543.

[13]Buchhave, P., "The Measurement of Turbulence with the Burst-Type Laser Doppler Anemometer—Errors and Correction Methods," Ph.D. Dissertation, Dept. of Mechanical and Aerospace Engineering, State Univ. of New York, Buffalo, NY, 1979.

[14]Buchhave, P., George, W. K., and Lumley, J. L., "The Measurement of Turbulence with the Laser-Doppler Anemometer," *Annual Review of Fluid Mechanics,* Vol. 11, 1979, pp. 443–504.

[15]Rice, S. O., "Mathematical Analysis of Random Noise," *Noise and Stochastic Processes,* edited by N. Wax, Dover, New York, 1954, pp. 133–294.

[16]Bennett, J. C., and Corrsin, S., "Small Reynolds Number Nearly Isotropic Turbulence in a Straight Duct and a Contraction," *Physics of Fluids,* Vol. 21, No. 12, 1978, pp. 2129–2140.

[17]Kistler, A. L., and Vrebalovich, T., "Grid Turbulence at Large Reynolds Numbers," *Journal of Fluid Mechanics,* Vol. 26, Pt. 1, 1966, pp. 37–47.

[18]Comte-Bellot, G., and Corrsin, S., "Simple Eulerian Time Correlation of Full- and Narrow-Band Velocity Signals in 'Grid-Generated', Isotropic Turbulence," *Journal of Fluid Mechanics,* Vol. 48, Pt. 2, 1971, pp. 273–337.

[19]Mohamed, M. S., and La Rue, J. C., "The Decay Power Law in Grid-Generated Turbulence," *Journal of Fluid Mechanics,* Vol. 219, Pt. 1, 1990, pp. 195–214.

[20]Tong, C., and Warhaft, Z., "On Passive Scalar Derivative Statistics in Grid Turbulence," *Physics of Fluids,* Vol. 6, No. 6, 1994, pp. 2165–2176.

[21]Mydlarski, L., and Warhaft, Z., "On the Onset of High-Reynolds-Number Grid-Generated Wind Tunnel Turbulence," *Journal of Fluid Mechanics,* Vol. 320, Pt. 2, 1996, pp. 331–368.

[22]Jiminez, J., Wray, A. A., Saffman, P. G., and Rogallo, R. S., "The Structure of Intense Vorticity in Isotropic Turbulence," *Journal of Fluid Mechanics,* Vol. 255, Pt. 1, 1993, pp. 65–90.

[23]Wang, L.-P., Chen, S., Brasseur, J. G., and Wyngaard, J. C., "Examination of Hypotheses in the Kolmogorov Refined Turbulence Theory Through High-Resolution Simulations, Part I Velocity Field," *Journal of Fluid Mechanics,* Vol. 309, Feb. 1996, pp. 113–156.

[24]Yeung, P. K., and Zhou, Y., "On the Universality of the Kolmogorov Constant in Numerical Simulation of Turbulence," *Physical Review E,* Vol. 18, No. 7, 1997, p. 1746.

[25]Cao, N., Chen, S., and Doolen, G. D., "Statistics and Structure of Pressure in Isotropic Turbulence," cited by Sreenivasan.[26]

[26]Sreenivasan, K. R., "An Update on the Energy Dissipation Rate in Isotropic Turbulence," *Physics of Fluids,* Vol. 10, No. 2, 1998, p. 529.

[27]Ling, S. C., and Huang, T. T., "Decay of Weak Turbulence," *Physics of Fluids,* Vol. 13, No. 12, 1970, pp. 2912–2924.

[28]Phillips, O. M., "The Final Period of Decay of Non-Homogeneous Turbulence," *Proceedings of the Cambridge Philosophical Society,* Vol. 52, Pt. 1, 1956, pp. 135–151.

R. M. C. So
Associate Editor

64

Appendix C: Chen, J.-H. and Faeth, G.M. (2001) Continuous-Phase Properties of Homogeneous
Particle-Laden Turbulent Flows. *AIAA J.* 39, 180-183.

65

Continuous-Phase Properties of Homogeneous Particle-Laden Turbulent Flows

J.-H. Chen* and G. M. Faeth[†]
University of Michigan,
Ann Arbor, Michigan 48109-2140

Nomenclature

C_D = particle drag coefficient
D = dissipation factor, Eq. (2)
d_p = particle diameter
f_i = volume fraction of region i
n'' = particle number flux
U_p = mean streamwise relative velocity of a particle
u, v = instantaneous streamwise and cross-stream gas velocity
$\bar{u}, \bar{v}$ = mean streamwise and cross-stream gas velocity
$\bar{u}', \bar{v}'$ = rms fluctuating streamwise and cross-stream velocity
ε = local rate of dissipation of turbulence kinetic energy
φ = average generic property of the overall flow
φ_i = average generic property of region i of the flow

Subscripts

i = turbulent interwake region
w = particle wake region

Introduction

TURBULENCE generation is defined as the direct disturbance of the continuous-phase velocity field by the wakes of dispersed-phase objects in dispersed multiphase flows. Turbulence generation supplements the conventional production of turbulence caused by mean velocity gradients in the continuous phase; it is most important when dispersed-phase objects have large relative velocities (large Reynolds numbers) and relatively large relaxation times compared to characteristic turbulence times. Such conditions are typical of many practical dispersed multiphase flows having significant separated-flow effects, e.g., sprays, particle-laden jets, bubbly jets, rainstorms, etc. Motivated by these observations, the present investigation sought to develop methods to predict the overall continuous-phase properties of homogeneous particle-laden turbulent flows dominated by turbulence generation and to evaluate the predictions based on earlier measurements from this laboratory.[1-5]

Initial observations of turbulence generation in this laboratory considered uniform fluxes of nearly monodisperse spherical particles in still water and air to yield homogeneous and stationary flows where turbulence production was caused entirely by turbulence generation.[1,2] The local rate of dissipation of turbulence kinetic energy ε mainly controls continuous-phase properties in these flows and can be found as the local rate of loss of particle mechanical energy per unit volume, as follows:

$$\varepsilon = \pi n'' d_p^2 C_D U_p^2 / 8 \qquad (1)$$

All other properties of these flows, however, are not known and must be related to dissipation rates and particle properties. Finally,

whereas simplified stochastic theories developed during these studies yielded encouraging correlations of turbulence intensities in terms of a dimensionless dissipation factor other properties were not predicted very well because of limited understanding about the particle wakes in these flows and their turbulent surroundings.[1,2]

Subsequent studies considered the properties of particle wakes at intermediate Reynolds numbers in turbulent environments typical of conditions for flows dominated by turbulence generation.[6,7] These wakes scaled similar to self-preserving laminar wakes but clearly were turbulent and mixed faster than laminar wakes as a result of the presence of turbulence in both the wakes and their surroundings; therefore, they were called laminarlike turbulent wakes. Recent observations of flows dominated by turbulence generation in upflowing air confirmed the presence of laminarlike turbulent wakes that were surrounded by a relatively large turbulent interwake region.[3-5] The turbulent interwake regions were found to be analogous to grid-generated isotropic turbulence in the final decay period, which are also widely recognized as being turbulent flows since the time of early observations of this flow by Batchelor and Townsend[8] more than 50 years ago, and yielded correlations of their properties [moments, probability density function (PDFs), etc.] in terms of the dimensionless dissipation factor and known properties of the dispersed phase.[4]

Motivated by these observations, the objective of the present investigation was to develop a way to predict the overall properties of the continuous phase of flows caused by turbulence generation, seeking to account for the random arrival of particle wakes and incorporating the known properties of laminarlike turbulent wakes and the turbulent interwake region. Information of this type would be measured in the continuous phase of flow dominated by turbulence generation and is of considerable importance as a result. The study was limited to homogeneous particle-laden turbulent flows involving uniform fluxes of nearly monodisperse spherical particles so that predictions could be evaluated based on the measurements of Refs. 1–3. The present description of the research is brief. (See Refs. 1–5 for additional details about the measurements and tabulations of data.)

Theoretical Methods

The present flows are assumed to consist of uniform fluxes of monodisperse spherical particles moving with known relative velocities (nearly equal to terminal velocities) within a homogeneous (nearly isotropic) and stationary turbulent continuous phase. A laminarlike turbulent wake is associated with each particle. The properties of the particle wakes must be considered to be part of the continuous-phase turbulence field because the arrival of particle wakes is random. Particle volume fractions were less than 0.003%, and their corresponding wake volume fractions were less than 2–30% so that effects of wake/wake interactions are small.[3] Then given particle properties, particle fluxes, and particle relative velocities, the dissipation factor of the flow D can be found from its definition, as follows[4]:

$$D = \frac{\varepsilon d_p (C_D/8)^{\frac{1}{2}}}{[\pi U_p^2 (U_p - \bar{u})]} \qquad (2)$$

as discussed in earlier work.[3-5] (See Ref. 4 for discussion of the relationship between D and the properties of the turbulent interwake region.) Then given D and the particle properties, the results of Chen and Faeth[4] provide the properties of the turbulent interwake region. Given this information and the known values of particle Reynolds numbers (having values of 1.06, 3.73, and 9.90×10^2 for the present test particles having nominal diameters of 0.5, 1.1, and 2.2 mm, respectively), the mean and fluctuating properties of the particle wakes can be obtained from the results of Wu and Faeth[6,7] for laminarlike turbulent wakes in a straightforward manner.

Given appropriate average properties of the laminarlike turbulent wakes and the turbulent interwake region, the corresponding overall property of the continuous phase was estimated using conditional averages, as follows:

$$\phi = f_w \phi_w + f_i \phi_i \qquad (3)$$

When computing the wake volume fraction, the small volume of the particle was ignored. Thus, the wake volumes included the region extending in the radial direction from the wake axis to the position where the mean streamwise velocity defect of the wake was $\exp(-2)$ of its value at the axis and for a streamwise distance extending to the point where the mean streamwise velocity defect at the axis was equal to the ambient r.m.s. velocity fluctuation level. Notably, doubling the size of this region had a negligible effect on the computed overall properties of the continuous phase.

Properties that will be considered in the following include $\phi = \bar{u}'^2, \bar{v}'^2$, PDF($u$), and PDF($v$). Corresponding values of ϕ_i for the turbulent interwake region for these properties could be obtained directly from the correlations of Chen and Faeth.[4] The analogous values of ϕ_w for the laminarlike turbulent wake region for these properties were obtained as averages over the volume used to find f_w. Distributions of mean streamwise velocities contribute along with streamwise velocity fluctuations when the laminarlike turbulent wake contribution to $\bar{u}'^2$ is found because the arrival of particle wakes is random. The corresponding mean cross-stream velocity contribution to $\bar{v}'^2$ was ignored, however, because this velocity is small compared to cross-stream velocity fluctuations.[6] Similarly, the PDF of streamwise velocities within the laminarlike turbulent wake region accounted for both mean and fluctuating velocities; in contrast, the PDF of cross-stream velocities within the laminarlike turbulent wake region only considered velocity fluctuations because the mean cross-stream velocity contribution to this velocity component is small.[6] The details of these computations are described by Chen.[5]

Results and Discussion

Earlier measurements suggested that streamwise and cross-stream relative turbulence intensities were mainly functions of the dissipation factor, relatively independent of particle Reynolds number.[1-3] Present predictions supported this behavior as illustrated in Fig. 1. Measurements shown on the figure include those
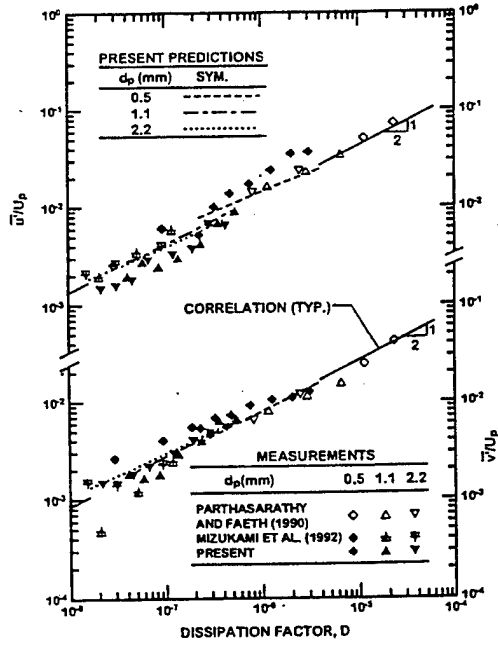

Fig. 1 Measurements and predictions of streamwise and cross-stream relative turbulence intensities of the overall flow as a function of dissipation factor: measurements of Parthasarathy and Faeth,[1] Mizukami et al.,[2] and Chen et al.[3]

of Parthasarathy and Faeth,[1] Mizukami et al.,[2] and Chen et al.[3] The corresponding predictions are limited to the last because of present limitations about the properties of laminarlike turbulent wakes.[6,7] The agreement between measurements and predictions is reasonably good. The predictions exhibit systematic effects of particle Reynolds number on relative turbulence intensities, but these effects are relatively small compared to experimental uncertainties over the available test range.[1-3] In addition, the measured variation of relative turbulence intensities as a function of the dissipation factor is seen to be predicted reasonably well.

The best-fit correlation of all the measurements illustrated in Fig. 1 yielded powers of D of 0.56 and 0.48 for the streamwise and cross-stream relative turbulence intensities with standard deviations of these powers of 0.03 and 0.02, respectively. As a result, there is no statistical significance between the powers of these fits and the power of $\frac{1}{2}$ suggested by the simplified theory of Parthasarathy and Faeth.[1] Thus, for consistency with the earlier work, the measurements were refitted by forcing the power to be $\frac{1}{2}$, yielding the correlations illustrated in Fig. 1 as follows:

$$\bar{u}'/U_p = 13.4D^{\frac{1}{2}}, \qquad \bar{v}'/U_p = 8.4D^{\frac{1}{2}} \qquad (4)$$

where the standard deviations of the coefficients of these expressions are both 1.5 and the correlation coefficients of these fits are both 0.96, which is quite good. The anisotropy of the overall flow is significantly larger than the turbulent interwake region, e.g., 1.59 for the overall flow from Eq. (4) compared to 1.16 from the turbulent interwake region alone from Chen and Faeth.[4] This behavior follows as a result of the relatively large contributions of the mean velocities in the particle wakes to the streamwise flow disturbance, which is absent from the cross-stream flow disturbance. Notably, this effect is represented quite accurately by the predictions.

The enhanced flow disturbance of the streamwise velocity component compared to the cross-stream velocity component caused by the properties of the particle wakes is also observed in the PDFs of streamwise and cross-stream velocities. Typical examples for the 0.5- and 2.2-mm-diam particles are illustrated in Figs. 2 and 3. Measured and predicted streamwise and cross-stream velocity components for two particle fluxes for each particle size are illustrated,
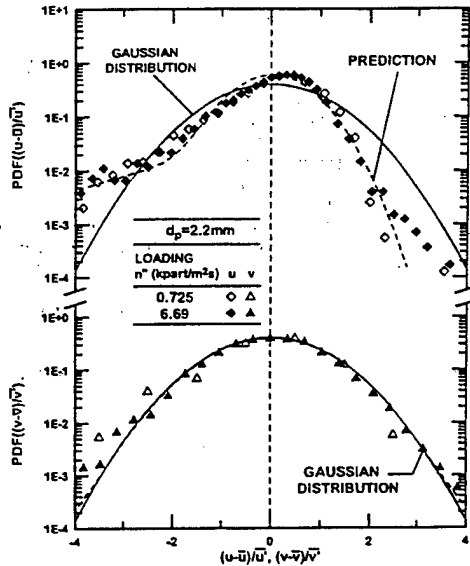
Fig. 3 Streamwise and cross-stream velocity PDFs (logarithmic scale) of the continuous phase for 2.2-mm-nominal-diameter particles: measurements of Chen et al.[3]

Fig. 2 Streamwise and cross-stream velocity PDFs (logarithmic scale) of the overall flow for 0.5-mm-nominal-diameter particles: measurements of Chen et al.[3]

along with standard Gaussian distributions for reference purposes. The figures employ logarithmic ordinates so that effects of wake disturbances that dominate regions where the PDFs are small can be seen.

Both predictions and measurements in Figs. 2 and 3 show that the PDF of gas velocities in the cross-stream direction is nearly Gaussian, whereas the PDF of gas velocities in the streamwise direction is not well approximated by a Gaussian distribution even though both velocity components satisfy Gaussian PDFs in the turbulent interwake region. (See Ref. 4 for a discussion of PDFs within the turbulent interwake region.) This behavior can be explained by noting that the PDF(v) is caused entirely by turbulence in the turbulent interwake region and in the particle wake disturbance, and because both these contributions are represented quite well by Gaussian distributions it is not surprising that their combined effect is adequately fitted by a Gaussian distribution as well. Naturally, the turbulence contributions to the PDF of gas velocities in the streamwise direction behave in the same way; therefore, effects of mean velocities in wake disturbances are mainly responsible for the departure of the PDF of gas velocities in the streamwise direction from a Gaussian distribution. First of all, the mean velocities in the laminarlike turbulent wake disturbances only contribute negative velocities compared to the mean velocities of the flow, and these velocities generally are rather large negative velocities compared to turbulence levels in the turbulent interwake region.[3] Thus, these contributions are responsible for the upward bias, compared to the Gaussian distribution, seen at large negative velocities in Figs. 2 and 3. This upward bias is compensated by the behavior of the PDF of gas velocities in the streamwise direction at positive velocities where the maximum PDF of gas velocities in the streamwise direction shifts slightly to positive velocities while the PDF of gas velocities in the streamwise direction at large positive velocities is biased downward from the Gaussian distribution. The narrower (or more peaked) PDF of gas velocities in the streamwise direction near the mean velocity condition as the particle size (or Reynolds number) decreases, then follows from the reduced levels of turbulence in the wake disturbances. Such reduced disturbances concentrate the effects of wake disturbances to the mean velocity distributions, which implies reduced velocity variations and thus a more peaked PDF of gas velocities in the streamwise direction. This behavior is
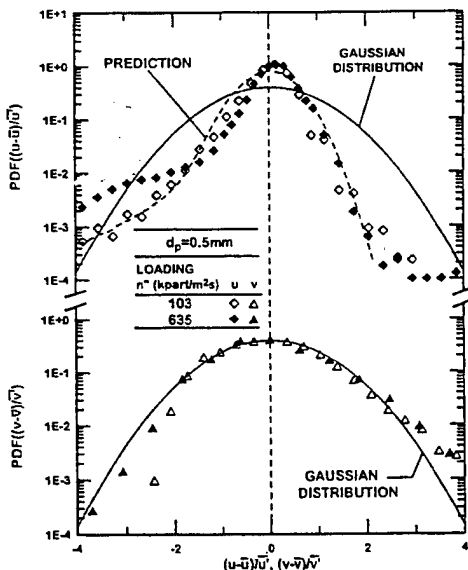
particularly promoted by laminarlike turbulent wake disturbances where streamwise turbulence intensities approach unity as a result of the unstable nature of wake flows.[6,7] Predictions and measurements also show that effects of particle fluxes on PDFs of u and v are small; this behavior generally agrees with numerous observations that the form of the PDFs of velocity fluctuations in turbulent flows is generally independent of the rate of dissipation of the turbulence. Finally, the agreement between measurements and predictions in Figs. 2 and 3 is reasonably good, with predictions correctly represecting the effect of particle sizes and fluxes on the PDFs of u and v, particularly in the region where the square of the arguments of the PDFs are smaller than four and present experimental uncertainties are small. The main discrepancies between predictions and measurements are observed in regions where velocities are significantly larger or smaller than the most probable values. These regions correspond to rather small values of the PDFs of u and v, however, and the discrepancies can be largely attributed to both the small values of the PDFs and the sampling limitations of the present measurements (unfeasible orders of magnitude increases in testing times would be required to avoid this limitation).

Summary

In summary, the overall properties of the continuous-phase turbulence generated by uniform fluxes of monodisperse spherical particles moving at near terminal velocities were studied. It was found that many properties of these flows—including relative turbulence intensities, anisotropies, and PDFs—could be predicted reasonably well based on volume-averaged contributions of the conditional averages of these properties within the laminarlike wake disturbance and turbulent interwake regions of the flows. The predictions show that most of the unusual properties of these flows, compared to conventional homogeneous turbulent flows,[4-8] come about as a result of effects of mean velocities in the particle wakes, which cannot be separated from the turbulence (barring some type of wake discrimination system) because the arrival of particle wakes is random.

Acknowledgments

References

[1]Parthasarathy, R. N., and Faeth, G. M., "Turbulence Modulation in Homogeneous Dilute Particle-Laden Flows," *Journal of Fluid Mechanics*, Vol. 220, Pt. 2, 1990, pp. 485–514.

[2]Mizukami, M., Parthasarathy, R. N., and Faeth, G. M., "Particle-Generated Turbulence in Homogeneous Dilute Dispersed Flows," *International Journal of Multiphase Flow*, Vol. 18, No. 2, 1992, pp. 397–412.

[3]Chen, J.-H., Wu, J.-S., and Faeth, G. M., "Turbulence Generation in Homogeneous Particle-Laden Flows," *AIAA Journal*, Vol. 38, No. 4, 2000, pp. 636–642.

[4]Chen, J.-H., and Faeth, G. M., "Inter-Wake Turbulence Properties of Homogeneous Particle-Laden Flows," *AIAA Journal*, Vol. 38, No. 6, 2000, pp. 995–1001.

[5]Chen, J.-H., "Turbulence Generation in Homogeneous Dilute Particle-Laden Flows," Ph.D. Dissertation, Dept. of Aerospace Engineering, Univ. of Michigan, Ann Arbor, MI, May 1999.

[6]Wu, J.-S., and Faeth, G. M., "Sphere Wakes at Moderate Reynolds Numbers in a Turbulent Environment," *AIAA Journal*, Vol. 32, No. 3, 1994, pp. 535–551.

[7]Wu, J.-S., and Faeth, G. M., "Effects of Ambient Turbulence Intensity on Sphere Wakes at Intermediate Reynolds Numbers," *AIAA Journal*, Vol. 33, No. 1, 1995, pp. 171–173.

[8]Batchelor, G. K., and Townsend, A. A., "Decay of Isotropic Turbulence in the Final Decay Period," *Proceedings of the Royal Society of London, Section A*, Vol. 194, No. 34, 1948, pp. 527–543.

M. Sichel
Associate Editor

Appendix D: Chen, J.-H., Wu, J.-S. and Faeth, G.M. (2000) Turbulence Generation in Homogeneous Particle-Laden Flows. *AIAA J.* 38, 636-642.

Turbulence Generation in Homogeneous Particle-Laden Flows

J.-H. Chen,* J.-S. Wu,† and G. M. Faeth‡
University of Michigan, Ann Arbor, Michigan 48109-2140

The generation of turbulence by uniform fluxes of monodisperse spherical particles moving through a uniform flowing gas was studied experimentally. Phase velocities, moments, probability density functions, and energy spectra were measured within a counterflowing particle/gas wind tunnel using phase-discriminating laser velocimetry. Test conditions included particle Reynolds numbers of 106–990, particle volume fractions less than 0.003%, direct rates of dissipation of turbulence by particles less than 4%, and turbulence generation rates sufficient to yield relative turbulence intensities in the range 0.2–5.0%. Velocity records showed that the flow consisted of randomly arriving wake disturbances within a turbulent interwake region and that the particle wake properties corresponded to recent observations of laminarlike turbulent wakes for spheres at intermediate Reynolds numbers in turbulent environments. Probability density functions of velocities were peaked for streamwise velocities due to contributions from mean streamwise velocities in particle wakes but were Gaussian for cross stream velocities that only involve contributions from the turbulence in the wakes. Relative intensities of streamwise and cross stream velocity fluctuations were roughly correlated in terms of a dimensionless rate of turbulence dissipation factor. Finally, energy spectra exhibited prominent -1 and $-\frac{5}{3}$ power decay regions associated with contributions from mean velocities in particle wakes and particle and interwake turbulence, respectively.

Nomenclature

C_D	= sphere drag coefficient
D	= dissipation factor, $\varepsilon d_p C_D^{1/3}/(2U_p^3)$
d_p	= sphere diameter
$E_u(k)$	= streamwise energy spectra
f	= frequency
k	= wave number, $2\pi f/\bar{u}$
L_u	= streamwise integral le..gth scale
ℓ_K	= Kolmogorov length scale
ℓ_p	= mean particle spacing
$\dot{n}''$	= particle number flux
Re	= particle Reynolds number, $d_p U_p/v$
t_K	= Kolmogorov timescale
U_p	= mean streamwise relative velocity of a particle
u	= streamwise gas velocity
u_K	= Kolmogorov velocity scale
v	= cross stream gas velocity
x	= distance in direction of particle motion
ε	= rate of dissipation of turbulence kinetic energy
v	= kinematic viscosity

Superscripts

$(\bar{\ })$	= mean value
$(\bar{\ })'$	= rms fluctuating value
$(\bar{\ })'^2$	= mean square fluctuating value

Introduction

A STUDY of the modification of continuous-phase turbulence properties due to the presence and motion of a dispersed phase is described. Hinze[1] identifies several turbulence modifica-

tion mechanisms that are observed in dispersed-multiphase flows. Of these, the least understood involve direct effects of dispersed phases on continuous-phase turbulence properties, as follows: the exchange of kinetic energy between the dispersed and continuous phases as the dispersed-phase motion accommodates to the continuous-phase motion, denoted turbulence modulation, which generally decreases turbulence fluctuations,[2-4] and the direct disturbance of the continuous-phase velocity field by particle wakes, denoted turbulence generation, which generally increases turbulence fluctuations.[3-7] Evaluating the relative magnitude of these two effects has been addressed by a number of investigators.[2,8-11] These studies show that turbulence generation (modulation) dominates turbulence modification, tending to increase (decrease) turbulence levels, when dispersed-phase elements have large (small) relaxation times compared to characteristic turbulence timescales. As a result, turbulence generation dominates turbulence modification in many practical dispersed-multiphase flows having significant separated-flow effects, for example, sprays, particle-laden jets, bubbly jets, rainstorms, etc.

Past studies of turbulence generation have considered dilute dispersed-multiphase flows in both shear[3-5,11] and homogeneous[6,7,12] flow configurations; however, the latter are preferred because they avoid problems of separating turbulence generation from conventional turbulence production in shear flows. Lance and Bataille[12] report an early study of homogeneous air/water bubbly flows downstream of a turbulence-generating grid. Effects of turbulence generation caused a progressive increase of continuous-phase turbulence levels with increasing void fractions; unfortunately, these results are difficult to interpret due to combined effects of bubble-and grid-generated turbulence.

Earlier studies of homogeneous flows where turbulence generation was the only mechanism of turbulence production involved uniform number fluxes of nearly monodisperse beads falling at their terminal velocities in nearly stagnant (in the mean) water and air.[6,7] Measurements included phase velocities and turbulence properties for various particle number fluxes and particle sizes corresponding to intermediate Reynolds number conditions ($Re = 100$–800) that are typical of practical sprays. The flows were analyzed using a simplified stochastic method involving superposition of randomly arriving particle velocity fields, by extending the method Rice[13] used to analyze noise. The stochastic approach provided some useful interpretations of flow properties, but was problematical because information about particle wakes at intermediate Reynolds numbers in turbulent environments typical of homogeneous dispersed flows was limited. Thus, wake properties were estimated by extrapolating available results at large Reynolds numbers in nonturbulent

environments, which is questionable and caused convergence problems for the Rice[13] approach similar to those encountered during stochastic analysis of sedimentation.[14] Other questions about the approximate analysis of Refs. 6 and 7 concerned the extent that particle wakes interacted with each other and the nature of the flowfield between wakes (the interwake region) if wake-to-wake interactions were small. These studies were also problematical because the nearly stagnant (in the mean) continuous phases caused large experimental uncertainties due to large turbulence intensities (up to 1000%).

Subsequent studies of sphere wakes at intermediate Reynolds numbers in both nonturbulent and turbulent environments provided information needed to understand turbulence generation better.[15–17] Wakes in nonturbulent environments yielded anticipated behavior for self-preserving turbulent and laminar wakes.[18,19] Findings more relevant to turbulence generation involved sphere wakes at intermediate Reynolds numbers in turbulent (roughly isotropic) environments that showed that these wakes scaled similar to self-preserving laminar wakes but with enhanced viscosities due to the presence of turbulence (termed laminarlike turbulent wakes).[16,17] Naturally, the laminarlike turbulent wakes differed considerably from the wakes assumed during the earlier turbulence-generation studies.[6,7] Estimates of flow properties also suggested that the probability of direct wake-to-wake interactions was small; instead, it was likely that wake disturbances were imbedded in relatively large turbulent interwake regions. Whether laminarlike turbulent wakes actually were observed during turbulence-generation processes was still an issue, however, because such turbulence fields differ from the conventional isotropic turbulence that was considered in Refs. 16 and 17.

Past studies raise several questions about turbulence generation: Were wake disturbances during turbulence generation equivalent to the laminarlike turbulent wakes observed in Refs. 16 and 17, does the flow involve wake disturbances imbedded in a turbulent interwake region or does it involve strongly interacting wakes, and can turbulence generation properties measured at large turbulence intensities be confirmed for moderate turbulence intensities where experimental uncertainties are much reduced? These issues were addressed during this investigation, which had the following specific objectives: 1) measure stationary homogeneous dispersed flows involving nearly monodisperse spherical solid (glass) particles at intermediate Reynolds numbers in air, using a counterflow particle/air wind tunnel, 2) use the measurements to determine the nature of wake disturbances and wake-to-wake interactions during turbulence generation, and 3) use the measurements to highlight differences between turbulence fields associated with turbulence generation and more conventional turbulence. The present description of the study is brief, see Ref. 20 for more details and a complete tabulation of data.

Experimental Methods

The apparatus consisted of a vertical counterflow wind tunnel with upflowing air moving toward the suction side of a blower and freely falling particles introduced at the top of the apparatus using a particle feeder (Fig. 1). The airflow system consisted of a rounded inlet, a honeycomb flow straightener (10-mm hexagonal cells, 76 mm long) and a 16:1 contraction ratio to the 305 × 305 mm cross section windowed test section. The particle dispersion section was located just above the test section. The upper part of the particle dispersion section involved nine equally spaced screens (square pattern with 0.9-mm-diam wires spaced 4.2 mm apart) to disperse the particles and to achieve a uniform particle flux. This was followed by a honeycomb flow straightener (10-mm hexagonal cells, 76 mm long) to remove lateral particle motion caused by the screens. The particle inlet section and the transition section to the blower were at the upper end of the wind tunnel. The wind-tunnel airflow was provided by a single inlet variable speed blower. The particle flow was provided by a variable-speed screw feeder (Accurate, Model 310/04). After passing through the wind tunnel, the particles impacted on a plastic sheet within a particle collector. Microscope inspection showed that the particles were not damaged by passing through the wind tunnel; therefore, they were reused.

Measurements included particle number fluxes and gas and particle velocities. Particle number fluxes were measured by collecting
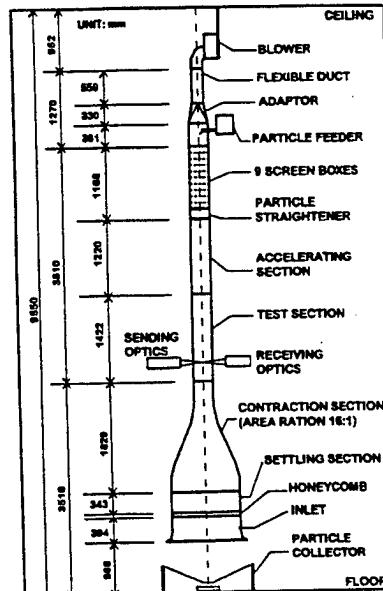
Fig. 1 Counterflow particle/air wind tunnel.

particles in a thin-walled cylindrical container having a 25-mm diameter that was closed at the bottom. The container was mounted on a rod so that it could be traversed across the test section. The accuracy of these measurements was dominated by finite sampling times that were selected to keep experimental uncertainties (95% confidence) less than 10%.

Gas and particle velocities were measured using a traversible (5-μm accuracy) laser velocimetry (LV) system. The LV was based on the 514.5-nm line of an argon-ion laser having an optical power of 1900 mW. A single-channel, dual-beam, forward- scatter, frequency-shifted LV arrangement was used, finding streamwise and cross stream velocities by rotating the optics accordingly. For gas velocities, the sending optics included a 3.75:1 beam expander to yield a measuring volume diameter and length of 55 and 425 μm, respectively. Because of the small measuring volume, the frequency of test particles passing through the measuring volume was small; the few that were observed were readily detected and eliminated from the sample due to their large signal amplitudes and relatively fixed velocities. The airflow entering the wind tunnel was seeded with oil drops having a 1-μm nominal diameter. Velocities were found from the low-pass filtered analog output of a burst-counter signal processor. The combination of frequency shifting plus a constant sampling rate of the analog output of the signal processor eliminated effects of directional bias and ambiguity as well as velocity bias. Temporal power spectra were obtained from the time series of velocities using the FFTRC fast Fourier transform routine.[21] Sampling periods were adjusted to provide the following experimental uncertainties (95% confidence): mean velocities less than 5%, rms velocity fluctuations less than 10%, probability density functions (PDFs) within one standard deviation of the most probable velocity less than 10%, and temporal power spectral densities less than 20% (at frequencies smaller than the reciprocal of the temporal integral scale with uncertainties smaller elsewhere).

Particle velocity measurements were made with the same LV arrangement as the gas velocities except that the optics were changed to provide a larger measuring volume having a diameter of 1.5 mm and a length of 10 mm. This provided a reasonable sampling rate of particle velocities. Optics were rotated to measure streamwise and cross stream velocities. The gas was not seeded for the particle velocity measurements, and the large-amplitude signals from particles were easily separated from background signals due to dust in the air. Sampling periods were adjusted to provide experimental

Table 1 Summary of test conditions[a]

Parameter	Nominal particle diameter, mm		
	0.5	1.1	2.2
U_p, mm/s	3370 (280)[b]	5530 (340)	7000 (200)
Re	106 (9)	373 (23)	990 (28)
C_D	1.22	0.79	0.54
$(dU_p/dx)/U_p$, %/m	2	11	14
$\dot{n}''$, kpart/m²s	71–950	4–56	0.5–10
ℓ_p, mm	32–13	97–41	208–77
L_u, mm	35–11	178–43	156–24
ε, m²/s³	0.088–1.17	0.041–0.54	0.012–0.23
ℓ_K, mm	0.5–0.2	0.6–0.3	0.7–0.4
t_K, ms	14–4	20–5	37–8
u_K, mm/s	34–66	28–54	21–44
$\bar{u}'/U_p$, %	0.5–5.0	0.2–0.9	0.2–0.8
$\bar{v}'/U_p$, %	0.5–1.3	0.2–1.2	0.2–0.9

[a]Round glass beads (density of 2500 kg/m³) falling in upflowing air at standard temperature and pressure (air density of 1.16 kg/m³ and kinematic viscosity of 15.9 mm²/s) having a mean velocity of 1.1 m/s. Parameter ranges for each particle size given in order of lowest–highest particle number fluxes, respectively.
[b]Standard deviations given in parentheses.

uncertainties less than 5% for streamwise mean velocities and less than 10% for rms streamwise and cross stream velocity fluctuations. Mean cross stream velocities were nearly zero and only were order of magnitude accurate due to their small magnitudes.

Test conditions are summarized in Table 1. The particles were nearly monodisperse with Reynolds numbers of 106–990, which is representative of the intermediate-Reynolds-number conditions of drops in sprays.[15] Terminal velocities and drag coefficients were measured, yielding values that agreed with the standard drag curve for spheres due to Putnam[22] within 15%. Test conditions were adjusted so that turbulence intensities relative to the mean gas velocity were less than 15% so that LV measuring conditions were excellent and the use of Taylor's hypothesis to convert temporal to spatial spectra and scales was justified.[23] The particles approached but did not reach terminal velocity conditions during the present turbulence generation measurements (e.g., rates of particle acceleration at the measuring location were in the range 2–14% of mean relative particle velocities per meter), whereas mean cross stream particle velocities were small. Particle velocity fluctuations were small due to their poor response to air motion and were mainly caused by variation of particle sizes.

Assuming that the particles are falling randomly, the mean particle spacing can be found from

$$\ell_p = [(U_p - \bar{u})/\dot{n}'']^{\frac{1}{3}} \tag{1}$$

which yields values of 13–208 mm and particle volume fractions less than 0.003 for the present experiments. Measured streamwise integral length scales had magnitudes comparable to mean particle spacings and were in the range 11–178 mm. The direct dissipation of turbulence kinetic energy (dissipation) by particles is less than 4% for present test conditions.[20] Thus, dissipation can be equated to the rate of turbulence generation by particles, which in turn is equal to the rate of transfer of mechanical energy to the gas as the particles move through the flow, that is,

$$\varepsilon = \pi \dot{n}'' d_p^2 C_D U_p^2 / 8 \tag{2}$$

Given ε, the Kolmogorov scales can be computed from their definitions,[19] yielding the ranges summarized in Table 1. Relative turbulence intensities due to turbulence generation were in the range 0.2–5.0%.

Results and Discussion

Apparatus Evaluation

The temporal and spatial uniformity of the particle flows were evaluated by collecting samples for various time periods and by traversing the sampling probe along the two perpendicular axes of symmetry at the lowest cross section, where measurements were made. These measurements were carried out for all three particle

sizes, spanning present ranges of particle fluxes for each size. Samples obtained from multiples of the shortest sampling period showed that the particle fluxes were statistically stationary with sampling times extending up to roughly 1000 times typical temporal integral scales of the present flows. Finally, the sampling measurements showed that mean particle fluxes varied less than 10% over the central 205 × 205 mm cross section of the flow, where velocity measurements were made. Mean and fluctuating particle velocities were also uniform within experimental uncertainties over the same region. The properties of the continuous (gas) phase were established by measurements of mean and fluctuating streamwise velocities at various times and over the central 205 × 205 mm cross section of the flow, considering streamwise distances up to ±100 mm from the normal cross section, where measurements were made. These results were not affected significantly for upflow velocities of 500–1300 mm/s. At these conditions, gas flow properties were statistically stationary and homogeneous within experimental uncertainties. See Ref. 20 for plots of all of the apparatus evaluation measurements.

Measurements of streamwise velocities for various particle sizes, particle fluxes, and upflow velocities were also used to establish minimum allowable particle fluxes. In particular, very low particle fluxes for a given upflow velocity yielded homogeneous flows having spurious turbulence intensities, amounting to relative turbulence intensities of 0.1–0.2% depending on particle size, due to inlet disturbances of the wind tunnel. Increasing the particle flux disrupted these disturbances and caused relative turbulence intensities to decrease for a time as particle fluxes increased before increasing once again in a manner similar to the behavior of turbulence generation seen in Refs. 6 and 7; therefore, present measurements were only undertaken for particle fluxes somewhat larger than the minimum relative turbulence intensity condition. Relative turbulence intensities at low particle fluxes were also affected by the upflow velocity. An upflow velocity of 1.1 m/s was finally selected to maximize the range of particle fluxes that could be considered while avoiding the excessive particle concentrations in the flow that are observed when upflow velocities approach the terminal velocity of the particles [see Eq. (1)]. For these conditions turbulence levels of the particle-laden flows ranged from twice to two orders of magnitude larger than the unladen flow, and it is unlikely that wind-tunnel disturbances affected the results reported here.

Particle Wake Properties

Typical temporal records of streamwise and cross stream gas velocities are illustrated in Fig. 2. When interpreting these data, it should be recalled that streamwise and cross stream velocities were observed at different times and there is no correlation between the two. In addition, the plots have low resolution to show the general appearance of the data over a sufficiently long period of time (50 s) so that several wake disturbances can be seen, even for the smallest particle number flux shown. Results are illustrated for all three particle sizes, characterized both by the particle number flux and the dimensionless dissipation factor of Refs. 6 and 7.

The most obvious features of the streamwise velocities illustrated in Fig. 2 is the appearance of relatively large negative velocity disturbances (negative velocity spikes) protruding from the smaller amplitude irregular turbulentlike background velocity signal. The frequency of appearance of these spikes is seen to increase as the particle number flux increases. Observations for long periods of time showed that the maximum velocity disturbances of these spikes were comparable to values expected based on the relative particle velocities for each particle size summarized in Table 1 (Note that the spikes illustrated in Fig. 2 have smaller magnitudes representative of far wake conditions that are most frequently observed; subsequent results will address near-wake conditions.) Thus, these spikes are associated with flow properties within particle wake disturbances.

Other properties of the velocity records illustrated in Fig. 2 suggest wake behavior similar to the laminarlike turbulent wakes observed in Refs. 16 and 17. For example, results for the 0.5-mm particles ($Re = 106$) exhibit negative spikes in the streamwise direction but no spikes in the cross stream direction. This behavior is consistent with laminarlike turbulent wake behavior at this value of Reynolds number, however, because mean cross stream velocities
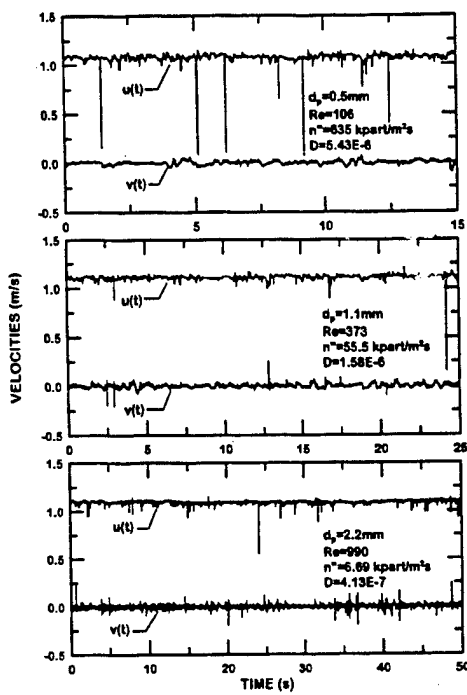
Fig. 2 Effect of particle loading and size on streamwise and cross stream velocity records.

Fig. 3 Measured and predicted streamwise velocities in particle wakes as a function of time for various velocity defects and particle sizes.

are small compared to both mean streamwise velocities and rms velocity fluctuations in laminarlike turbulent wakes and only the streamwise rms velocity fluctuations are observed before eddy shedding starts at $Re \approx 300$ (Refs. 16 and 17). In contrast, both large negative velocity spikes in the streamwise direction and spikes having both positive and negative velocity disturbances in the cross stream direction are observed for the 1.1- and 2.2-mm-diam particles that have $Re = 373$ and 990, respectively. This behavior is exactly what should be observed for laminarlike turbulent wakes, however, because cross stream turbulent velocity fluctuations are comparable to streamwise mean velocity defects when eddy shedding occurs for $Re > 300$ (Refs. 16 and 17).

The extended regions between wake disturbances in Fig. 2 exhibit turbulentlike behavior representative of the turbulent interwake region. The amplitudes of the velocity fluctuations in the turbulent interwake region do not vary significantly with time but tend to increase as the dissipation factor increases. The relationship between rms velocity fluctuations in the turbulent interwake region and the dissipation factor will be quantified later.

A final assessment of the similarities between the wake disturbances observed during the present turbulence generation studies and the laminarlike turbulent wakes observed in Refs. 16 and 17 involved direct comparison of mean streamwise velocities. This comparison was carried out for all three particle sizes at relatively large particle loadings so that representative samples of particle wakes could be observed in reasonable test times. Measurements were made for various maximum velocity defects, which represent results for paths of the LV measuring volume at various radial distances from the wake axis, because present particle paths were essentially vertical and the maximum mean velocity defect is a monotonic function of radial distance from the wake axis for laminarlike turbulent wakes.[16,17,20] Effects of turbulence were handled by averaging several velocity records (selected to have a maximum velocity defects within ±25% of the given maximum velocity defect) to obtain an estimate of mean streamwise wake velocities [the averaging criterion was an experimental uncertainty (95% confidence) of the maximum
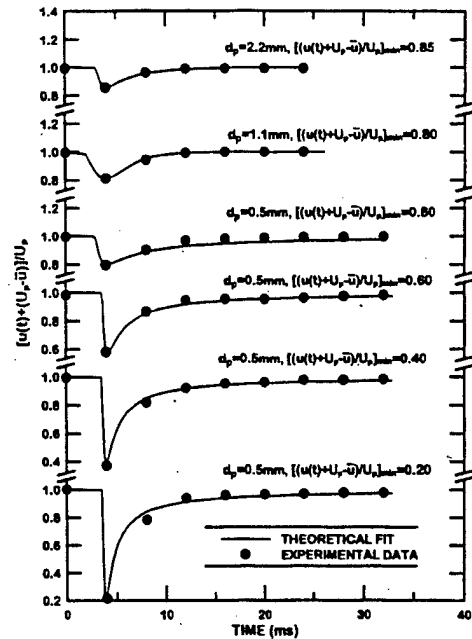
mean velocity defect less than 10%]. Predictions assuming vertical wake axes and having the same maximum mean velocity defects were obtained from the correlations for the mean properties of laminarlike turbulent wakes of Refs. 16 and 17 (at the same particle Reynolds number and relative turbulence intensity).

The resulting measured and predicted mean streamwise velocities in the particle wakes are illustrated in Fig. 3. These results involve plots of normalized streamwise velocities as a function of time for various particle diameters and maximum velocity defects. Note that the normalization of the ordinate of Fig. 3 implies that a value of 0 corresponds to the absolute (negative) particle velocity whereas a value of 1 corresponds to the absolute (positive) mean upflow velocity of the wind tunnel. Results for 0.5-mm particles are relatively comprehensive and involve dimensionless mean velocity defects in the range 0.20–0.80 because sampling rates were relatively large for these small particles. Results for particle diameters of 1.1 and 2.2 mm are limited to a single velocity defect (representative of the outer edge of the wakes) in order to obtain reasonable sampling rates for these small-particle flux conditions. It is evident that the agreement between measurements and predictions is excellent in Fig. 3, which supports the use of the laminarlike turbulent wake properties of Refs. 16 and 17 to help interpret present observations of turbulence generation.

Based on the reported findings, it seems reasonable to assume that the present wake disturbances are similar to the laminarlike turbulent wakes described in Refs. 16 and 17. This information was then used to estimate the proportions of the wake and interwake regions as well as the extent of direct wake/wake interactions. This was done by carrying out stochastic simulations to find realizations of particle positions in space for various particle fluxes and the three particle sizes. Random selections in three dimensions were made while accounting for the slight compression of particle spacing in the vertical direction due to gas upflow as discussed in connection with Eq. (1). Appropriate laminarlike turbulent wakes were then associated with each particle, assuming that wake radii were equal to twice the characteristic wake width at each streamwise distance behind the particle and that the wake extended in the streamwise direction until the maximum mean velocity defect was equal to the

ambient rms streamwise velocity fluctuations. These results indicated that wake cross-sectional areas generally were less than 30% of the available cross-sectional area and that less than 25% of the wakes experienced direct wake-to-wake interactions at any one time (with these interactions mainly confined to conditions far from both particles) over the present test range. Thus, the present flows involve laminarlike turbulent wakes surrounded by a relatively large turbulent interwake region, with occasional wake-to-wake interactions. This view agrees with the velocity traces of Figs. 2 if it is recognized that only a relatively small portion of each wake can generate the large velocity spikes seen on these plots. Further evidence of combined effects of the wake and interwake regions on overall flow properties will be sought from consideration of PDFs and spectra in the following.

PDF

More insight about the effect of particle wake disturbances on the total turbulence properties of homogeneous dispersed flows dominated by turbulence generation can be obtained from the PDFs of velocity fluctuations. Typical results along these lines are presented in Figs. 4 and 5 for 2.2- and 0.5-mm particles, respectively, which bound results for 1.1-mm particles. On each of these plots, PDFs are shown for streamwise and cross stream velocities at the low and high particle loadings specified by the dissipation factor values. Fits of the measurements are also shown on the plots, corresponding to least-squares sectional fits for the PDF(u) and best Gaussian fits for the PDF(v). The best Gaussian fits were established from the measured mean and rms fluctuating values obtained during the corresponding measurements.

The present PDFs plotted in Figs. 4 and 5 do not agree with earlier observations of Refs. 6 and 7 for dispersed flows in stagnant baths, which yielded Gaussian PDFs for both velocity components, with at most a slight upward bias (roughly 10% when averaged over all test conditions) of the PDF(u) near its most probable value. This behavior agrees with present behavior of PDF(v), which is nicely fitted by Gaussian PDFs for both loadings of all particle sizes. In contrast, the present PDF(u) are more peaked and somewhat skewed toward negative velocities compared to the mean velocity, that is, the PDF(u) exhibit greater kurtosis and skewness than the nearly Gaussian PDF(v) (Ref. 19). In addition, the PDF(u) for each
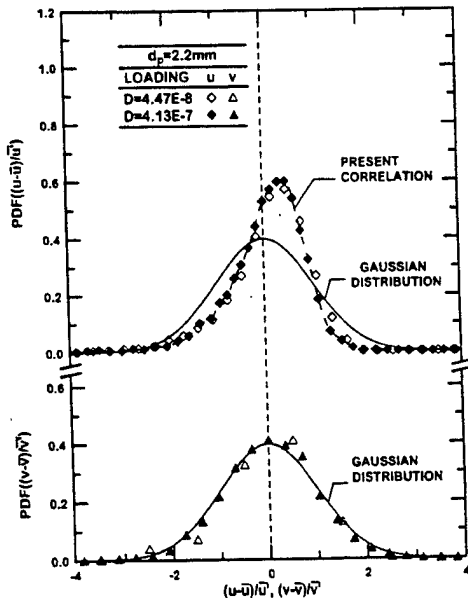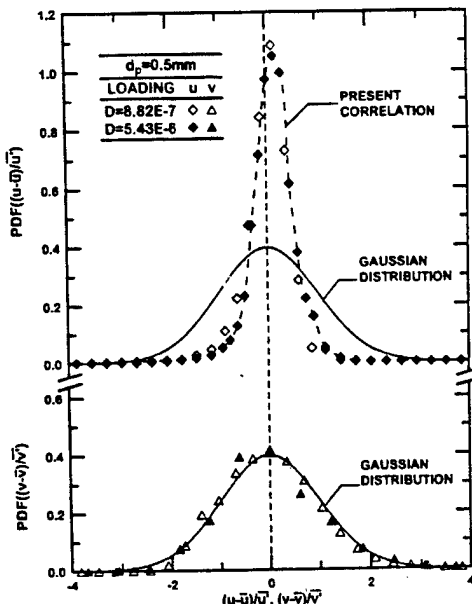
Fig. 5   Streamwise and cross stream velocity PDFs at various particle loadings for 0.5-mm particles.

particle size tends to be independent of particle loading, similar to PDF(v), but the PDF(u) becomes progressively more peaked (or has progressively increasing kurtosis) as the particle size (or Reynolds number) decreases. All of these characteristics can be explained from the properties of the streamwise and cross stream velocity records (and the spike disturbances due to particle wakes seen in the velocity records) of Figs. 2 and 3, as discussed next.

The main reason for the different PDF(u) of Refs. 6 and 7 and the present study follows from the much improved LV conditions of the present study that allowed the near-wake region of the spike disturbances due to particle wakes seen in Fig. 3 to be resolved for the streamwise velocity records. This point was easily demonstrated during the present experiments by reducing seeding levels so that the spikes seen in Fig. 2 were rarely resolved; the corresponding PDF(u) then became more Gaussian, similar to the results of Refs. 6 and 7. The other properties of PDF(u) in Figs. 4 and 5 then follow from the well-known effects of the properties of the velocity signal on the values of the skewness and kurtosis of the PDF(u). In particular, the spikes always contribute a streamwise negative velocity signal based on the results illustrated in Fig. 2; this implies a corresponding positive bias of the PDF(u), or negative skewness.[19] The more rapid reduction of streamwise velocities in the radial direction for small d_p (or Reynolds number) conditions (yielding narrower wake disturbances) implies a more peaked PDF(u), or a larger kurtosis of the PDF(u), for similar reasons.[19] In addition, the small effect of particle flux on the PDF(u) and the PDF(v) is consistent with the generally observed behavior of these functions, where the shape of the velocity signal as a function of time affects the skewness and kurtosis of the PDF but not the characteristic frequency of the signal,[19] for example, homogeneous, isotropic dispersed flows have Gaussian PDFs irrespective of their characteristic timescales or frequency scales. Finally, either the absence of discernible spikes for the cross stream velocity records for the 0.5-mm particles or the presence of both positive and negative spikes due to wake turbulence for the cross stream velocity records for the 2.2 mm particles is entirely consistent with the Gaussian behavior of the PDF(v) seen in Figs. 4 and 5. Taken together, the combined findings of Figs. 2–5 suggest that both particle wake disturbances and the interwake region provide significant contributions to the overall apparent turbulence properties of the present turbulence generated flows.


Fig. 4   Streamwise and cross stream velocity PDFs at various particle loadings for 2.2-mm particles.

CHEN, WU, AND FAETH
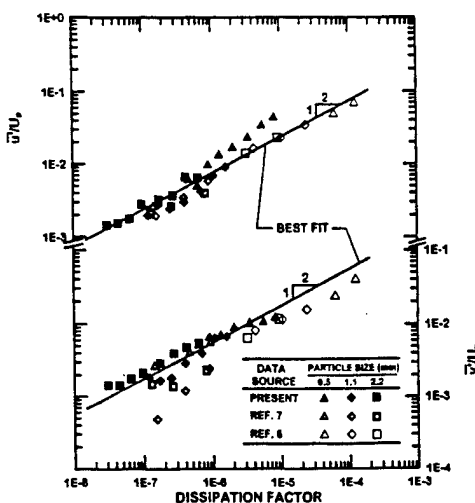
Fig. 6 Streamwise and cross stream rms velocity fluctuations as a function of particle dissipation factors and diameters: measurements of Parthasarathy and Faeth,[6] Mizukami et al.[7] and the present investigation.

Fig. 7 Energy spectra of streamwise velocity fluctuations for various particle loadings and sizes.

Velocity Fluctuations

The measurements of velocity fluctuations in Refs. 6 and 7 were correlated based on an approximate stochastic approach assuming that velocity fluctuations were entirely due to wake disturbances. This approach yielded reasonably effective correlations of relative turbulence intensities of streamwise and cross stream velocity fluctuation in terms of a dissipation factor D resulting from the approximate stochastic theory. This approach will be considered in the following due to its past success.

Measurements of streamwise and cross stream relative turbulence intensities are plotted as a function of the dissipation factor in Fig. 6. Measurements shown in Fig. 6 include results for particles in still (in the mean) water due to Parthasarathy and Faeth,[6] results for particles in still (in the mean) air due to Mizukami et al.,[7] and the present results for particles in counterflowing air. All three experiments used the same 0.5-, 1.1-, and 2.2-mm spherical glass particles. Correlations in terms of $D^{1/2}$, as suggested by the stochastic theory of Ref. 6, are fitted to the combined data sets for each velocity component. The correlations are seen to provide only fair agreement with the measurements. This is particularly true for the measurements of Mizukami et al.,[7] which exhibit significant scatter when plotted in the manner of Fig. 6. The results suggest some relationship between the properties of the wakes and the interwake region but clearly a correlation solely in terms of D cannot capture features such as the onset of cross stream wake disturbances for $Re > 300$ seen in Fig. 2. Thus, the correlations illustrated in Fig. 6 are only tentative pending more information about flow properties in the interwake region and the use of these results in a more rational conditional averaging procedure to summarize the properties of flows caused by turbulence generation.

Energy Spectra

Taylor's hypothesis could be used to convert measured temporal power spectra and temporal integral scales into energy spectra and spatial integral scales because present absolute turbulence intensities were small.[23] The resulting streamwise energy spectra are plotted as functions of normalized wave numbers in Fig. 7. Results are shown for various particle sizes and fluxes, with the latter represented by values of the dissipation factor. The LV conditions for these measurements were good so that effects of step noise were deferred until Kolmogorov wave numbers were approached. (This condition roughly corresponds to $kL_u = 100$.) The values of L_u for the measurements were found by setting $E_u(k)\bar{u}/(\overline{u'^2}L_u) = 4$ as kL_u
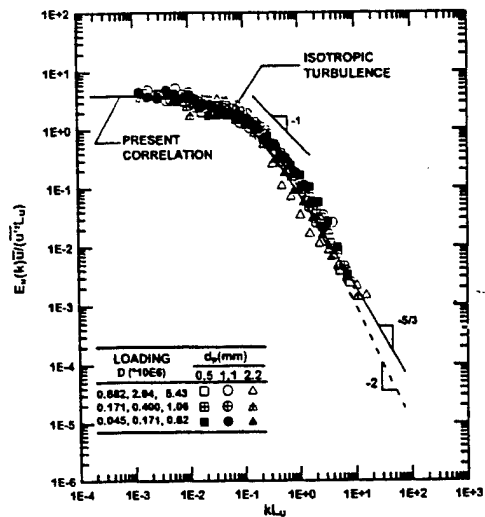
becomes small, as discussed by Hinze.[23] A correlation of the energy spectra for approximate isotropic turbulence is also shown on the plot, for comparison with the present measurements. This correlation represents a simplification of isotropic turbulence, where the $-\frac{5}{3}$ power decay of the inertial range is approximated by a -2 power decay that corresponds to an exponential temporal correlation of streamwise velocity fluctuations.[23] The energy spectra provide reasonably good correlations of present measurements as plotted in Fig. 7.

An interesting feature of the spectra of Fig. 7 is that they decay over a rather large range of kL_u (roughly four decades) even though present particle Reynolds numbers are not large (less than 1000). Much of this behavior is typical of other homogeneous turbulence fields where disturbances due to grids (having relatively small grid element Reynolds numbers) yield turbulent flows having extensive inertial ranges.[4,19,23] Another feature of the present flows enhances this behavior, however, as pointed out in earlier work.[6,7] In particular, the spectra of Fig. 7 include contributions from both particle wake disturbances and the turbulent interwake region. Then because the wake arrivals are random, mean velocities in the wakes contribute to the spectra increasing the range of scales that are present. Naturally, similar contributions are not present for grid-generated turbulence because measurements of these flows are made well downstream of the region of significant direct wake disturbances from the turbulence-generating grid.

The energy spectra of Fig. 7 also provide other evidence of direct contributions of mean velocities in wake disturbances. In particular, the spectra exhibit prominent -1 and $-\frac{5}{3}$ decay regions as kL_u increases. The -1 power decay region is not seen in conventional turbulent flows, but based on the approximate stochastic analysis of Ref. 6 such behavior is typical of the contribution of mean velocities in wake disturbances to temporal power spectra (and thus energy spectra under present approximations). Other evidence for this explanation is that the -1 decay region is associated with values of kL_u on the order of unity (which is roughly approximated by $k\ell_p$ in the order of unity; see Table 1) that is characteristic of wake dimensions. Larger wave numbers exhibit $-\frac{5}{3}$ power decay regions that are representative of conventional turbulence and probably involve contributions from both the wake disturbances and the turbulent interwake region as discussed earlier in connection with Fig. 2.

Conclusions

This investigation considered the properties of homogeneous turbulence generated by uniform fluxes of monodisperse spherical

particles moving through air at standard temperature and pressure. The experimental configuration consisted of particles falling in counterflowing air to supplement earlier measurements for particles falling in stagnant water (Ref. 6) and stagnant air (Ref. 7). Present test conditions included particle Reynolds numbers of 106–990, particle volume fractions less than 0.003% and direct rates of dissipation of turbulence by particles less than 4%, and particle number fluxes sufficient to yield relative turbulence intensities of 0.2–5%. The major conclusions of the study are as follows.

1) Measurements of gas velocities indicate that the particle wake properties of the present turbulence-generation processes correspond to the laminarlike turbulent wakes observed in Refs. 16 and 17 for spheres at intermediate Reynolds numbers in isotropic turbulence.

2) Estimates of the character of the present flows based on the properties of laminarlike turbulent wakes suggest that wake disturbances (generally involving cross-sectional areas less than 30% of the total available cross-sectional area) are embedded in a relatively large turbulent interwake region with relatively few (less than 25%) direct wake-to-wake interactions, with the latter dominated by portions of the wakes far from both particles.

3) Present measurements of relative turbulence intensities were in fair agreement with earlier measurements of turbulence generation in still liquids and gases from Refs. 6 and 7, and all of these measurements could be correlated in terms of the dissipation factor. These correlations are only considered tentative, however, pending development of a more rational approach that properly accounts for the relative contributions of wake disturbances and the turbulent interwake region, which fundamentally have very different flow properties.

4) Other properties measured during the present study, PDFs and spectra, were not in good agreement with the earlier observations of Refs. 6 and 7. In particular, present observations provided direct evidence of effects of both wake disturbances and interwake regions (as non-Gaussian PDFs and prominent -1 and $-\frac{5}{3}$ decay regions of energy spectra) that were either absent or less evident during the earlier studies. These differences were shown to result from the improved LV measuring conditions of the present study.

5) Contributions from both the wake disturbances and the turbulent interwake region also were responsible for the surprisingly large range of scales seen in the present flows in spite of relatively small particle Reynolds numbers. In particular, mean velocities in particle wake disturbances contribute to present apparent turbulence properties because wake arrivals are random and this contribution is generally not present in turbulence generated in other ways, for example, by grids or shear flows.

Acknowledgments

References

[1]Hinze, J. O., "Turbulent Fluid and Particle Interaction," *Progress in Heat and Mass Transfer*, Vol. 6, 1972, pp. 433–452.

[2]Hetsroni, G., "Particles-Turbulence Interaction," *International Journal of Multiphase Flow*, Vol. 15, No. 5, 1989, pp. 735–746.

[3]Squires, K. D., and Eaton, J. K., "Particle Response and Turbulence Modification in Isotropic Turbulence," *Physics of Fluids A*, Vol. 2, No. 6, 1990, pp. 1191–1203.

[4]Rogers, C. B., and Eaton, J. K., "The Effect of Small Particles on Fluid Turbulence in a Flat-Plate Turbulent Boundary Layer in Air," *Physics of Fluids A*, Vol. 3, No. 5, 1991, pp. 928–937.

[5]Parthasarathy, R. N., and Faeth, G. M., "Structure of Particle-Laden Turbulent Water Jets in Still Water," *International Journal of Multiphase Flow*, Vol. 13, No. 5, 1987, pp. 699–716.

[6]Parthasarathy, R. N., and Faeth, G. M., "Turbulence Modulation in Homogeneous Dilute Particle-Laden Flows," *Journal of Fluid Mechanics*, Vol. 220, Pt. 2, 1990, pp. 485–514.

[7]Mizukami, M., Parthasarathy, R. N., and Faeth, G. M., "Particle-Generated Turbulence in Homogeneous Dilute Dispersed Flows," *International Journal of Multiphase Flow*, Vol. 18, No. 2, 1992, pp. 397–412.

[8]Gore, R. A., and Crowe, C. T., "Effect of Particle Size on Modulating Turbulent Intensity," *International Journal of Multiphase Flow*, Vol. 15, No. 2, 1989, pp. 279–285.

[9]Kenning, V. M., and Crowe, C. T., "On the Effect of Particles on Carrier Phase Turbulence in Gas-Particle Flows," *International Journal of Multiphase Flow*, Vol. 23, No. 2, 1997, pp. 403–408.

[10]Yuan, Z., and Michaelides, E., "Turbulence Modulation in Particulate Flows—A Theoretical Approach," *International Journal of Multiphase Flow*, Vol. 18, No. 5, 1992, pp. 779–785.

[11]Rashidi, M., Hetsroni, G., and Banerjee, S., "Particle-Turbulence Interaction in a Boundary Layer," *International Journal of Multiphase Flow*, Vol. 16, No. 6, 1990, pp. 935–949.

[12]Lance, M., and Bataille, J., "Turbulence in the Liquid Phase of a Uniform Bubbly Air–Water Flow," *Journal of Fluid Mechanics*, Vol. 222, Pt. 1, 1991, pp. 95–119.

[13]Rice, S. O., "Mathematical Analysis of Random Noise," *Noise and Stochastic Processes*, edited by N. Wax, Dover, New York, 1954, pp. 133–294.

[14]Batchelor, G. K., "Sedimentation in a Dilute Dispersion of Spheres," *Journal of Fluid Mechanics*, Vol. 52, 1971, pp. 245–268.

[15]Wu, J.-S., and Faeth, G. M., "Sphere Wakes in Still Surroundings at Intermediate Reynolds Numbers," *AIAA Journal*, Vol. 31, No. 8, 1993, pp. 1448–1455.

[16]Wu, J.-S., and Faeth, G. M., "Sphere Wakes at Moderate Reynolds Numbers in a Turbulent Environment," *AIAA Journal*, Vol. 32, No. 3, 1994, pp. 535–541.

[17]Wu, J.-S., and Faeth, G. M., "Effects of Ambient Turbulence Intensity on Sphere Wakes at Intermediate Reynolds Numbers," *AIAA Journal*, Vol. 33, No. 1, 1995, pp. 171–173.

[18]Schlichting, H., *Boundary Layer Theory*, 7th ed., McGraw–Hill, New York, 1979, pp. 234, 235, 599.

[19]Tennekes, H., and Lumley, J. L., *A First Course in Turbulence*, MIT Press, Cambridge, MA, 1972, pp. 113–124, 196–201.

[20]Chen, J.-H., "Turbulence Generation in Homogeneous Dilute Particle-Laden Flows," Ph.D. Dissertation, Dept. of Aerospace Engineering, Univ. of Michigan, Ann Arbor, MI, May 1999.

[21]*IMSL Library Reference Manual*, 8th ed., IMSL, Inc., Houston, TX, 1980.

[22]Putnam, A., "Integrable Form of Droplet Drag Coefficient," *ARS Journal*, Vol. 31, No. 10, 1961, pp. 1467, 1468.

[23]Hinze, J. O., *Turbulence*, 2nd ed., McGraw–Hill, New York, 1975, Chap. 3, p. 204.

S. K. Aggarwal
Associate Editor

Appendix E: Chou, W.-H. and Faeth, G.M. (1998) Temporal Properties of Secondary Drop Breakup in the Bag Breakup Regime. *Int. J. Multiphase Flow* 24, 889-912.

Temporal properties of secondary drop breakup in the bag breakup regime

W.-H. Chou[1], G.M. Faeth*

Department of Aerospace Engineering, The University of Michigan, Ann Arbor, Michigan 48109-2140, U.S.A.

Abstract

The temporal properties of secondary drop breakup in the bag breakup regime were measured as a function of time for shock-wave-initiated disturbances in air at normal temperature and pressure. The test liquids included water, ethyl alcohol and various glycerol mixtures to yield liquid/gas density ratios of 633–893, Weber numbers of 13–20, Ohnesorge numbers of 0.0043–0.0427 and Reynolds numbers of 1550–2150. Single- and double-pulse shadowgraphy and holography were used to measure the structure, size and velocity of the parent drop, and the sizes and velocities of drops produced by secondary breakup. The parent drop undergoes significant deformation and lateral growth during breakup before forming a thin bag having a basal ring that is characteristic of the bag breakup regime. The basal ring contains roughly 56% of the initial drop volume (mass) and eventually yields drops having mean diameters of roughly 30% of the initial drop diameter by a Rayleigh breakup process; the size variations of drops formed from the basal ring increases with increasing Weber number due to the appearance of large 'node' drops that are characteristic of the onset of the multimode breakup regime. Breakup of the bag yields nearly monodisperse drops having diameters of roughly 4% of the initial drop diameter. The velocity distributions of the drops formed from breakup of the basal ring and the bag were individually independent of drop size but varied as a function of time and differed between the two groups. Many features of these phenomena were successfully correlated using phenomenological analyses. Finally, bag breakup requires considerable time (5–6 characteristic secondary drop breakup times) and extends over considerable streamwise distances (50–100 initial drop diameters) by the end of breakup, which suggests that bag breakup should be treated as a rate process, rather than by jump conditions, in some instances. © 1998 Elsevier Science Ltd. All rights reserved.

Keywords: Drop breakup; Drop dynamics; Pulsed holography; Sprays; Atomization

---

* Corresponding author.
[1] Currently with the Trane Corporation, LaCrosse, Wisconsin, U.S.A.

1. Introduction

The secondary breakup of drops is important because primary breakup yields drops that are intrinsically unstable to secondary breakup, while secondary breakup often is the rate controlling process within dense sprays in much the same way that drop vaporization often is the rate controlling process within dilute sprays (Faeth, 1997; Faeth et al., 1995; Wu et al., 1995). Motivated by these observations, the objective of the present investigation was to extend recent studies of the regimes and outcomes of secondary breakup caused by shock-wave disturbances due to Hsiang and Faeth (1992, 1993, 1995), and Chou et al. (1997), to consider the evolution of bag breakup as a function of time.

Several recent reviews of secondary breakup are available, see Faeth (1997), Faeth et al. (1995), Hsiang and Faeth (1992, 1993, 1995), Wu et al. (1995) and references cited therein; therefore, the following discussion of past work will be brief. Shock-wave disturbances were considered during most earlier studies, providing a step change of flow properties around the drop, similar to conditions experienced by drops at the end of primary breakup. Secondary breakup properties that have been considered include the conditions required for particular deformation and breakup regimes, the time required for the onset and end of breakup, the drag properties of deformed drops and the size and velocities of the drops produced by secondary breakup (i.e. the secondary breakup jump conditions). An interesting feature of these results is that secondary breakup extended over appreciable regions of time and space and was not properly described by jump conditions in some instances. For example, Liang et al. (1988) show that breakup times are equal to 5.5t^* for a wide range of breakup conditions, where t^* is the characteristic secondary breakup time for shear breakup defined by Ranger and Nicholls (1969) as follows:

$$t^* = d_0(\rho_L/\rho_G)^{1/2}/u_0. \tag{1}$$

In (1) d_0 and u_0 are the initial drop diameter and relative velocity, ρ denotes density and the subscripts L and G denote liquid and gas properties, respectively. Such times are comparable to flow residence times within the dense spray region where secondary breakup is a dominant process (Faeth, 1997; Faeth et al., 1995; Wu et al., 1995). Viewed another way, the original (or parent) drop moves roughly 50 initial drop diameters, while the smallest drops formed by secondary breakup move up to 100 initial drop diameters, during the period of breakup for typical shear breakup processes (Hsiang and Faeth, 1993, 1995). Such distances can represent a significant fraction of the length of the dense spray region. These observations suggest that the time-resolved features of secondary breakup eventually must be understood, i.e. the size and velocity distributions of the drops, and the rate at which liquid is removed from the parent drop, must be known as a function of time during secondary breakup. Motivated by this observation, the authors and their associates are concentrating on studies of the temporal properties (dynamics) of particular secondary breakup processes.

The first phase of the study of the temporal properties of secondary breakup considered the shear breakup regime where secondary breakup proceeds by the stripping of drop liquid from the periphery of the parent drop (Chou et al., 1997). Other conditions of the shear breakup study included $\rho_L/\rho_G > 680$, where gas-phase processes approximate quasi-steady behavior,

and small Ohnesorge numbers, $Oh = \mu_L/(\rho_L d_o \sigma)^{1/2} < 0.04$, where μ and σ denote viscosity and surface tension, respectively. It was found that the size distributions of drops produced by secondary breakup at each instant of time satisfied the universal root normal distribution function, with $MMD/SMD = 1.2$, due to Simmons (1977), where MMD and SMD denote the mass median and Sauter mean diameters of the drop size distributions, respectively. This behavior is very helpful because this two-parameter distribution function is fully defined by the SMD alone, given the MMD/SMD ratio. In contrast, the velocity distribution functions of drops produced by secondary breakup were uniform. Other measurements of shear breakup properties as a function of time included the size and velocities of the parent drop, the SMD and mean and fluctuating velocities of drops produced by secondary breakup, and the rate of liquid removal from the parent drop due to secondary breakup. All these properties were correlated and interpreted using phenomenological theories, providing the information needed to treat shear breakup as a rate process during computations of spray structure.

The present study seeks to extend information about the temporal properties of secondary breakup from the shear breakup regime to the bag breakup regime. Within the bag breakup regime, secondary breakup proceeds by deformation of the center of the drop into a thin balloon-like bag that extends in the downstream direction from a thicker ring-like structure of its base (the basal ring), with both the bag and the basal ring subsequently dividing into drops. An understanding of bag breakup is important for two reasons: (1) the bag breakup regime bounds the region where drops only deform and do not break up, which provides fundamental clues about the mechanism of the onset of secondary breakup, and (2) the complex multimode breakup regime is bounded by the bag- and shear-breakup regimes which clearly must be understood before addressing the important multimode breakup mechanism (Hsiang and Faeth, 1992, 1993, 1995). Similar to the earlier study of shear breakup, the present study emphasized new measurements of the temporal properties of bag breakup and used phenomenological theories to help interpret and correlate the measurements.

The present measurements were carried out using a shock tube facility, with the environment of the test drops during breakup roughly approximating air at normal temperature and pressure (NTP). Single- and double-pulse shadowgraphy and holography were used to find the properties of the parent drop, the size and velocity properties of drops produced by secondary breakup and the rate of liquid removal from the parent drop as a function of time during breakup. Test conditions were limited to relatively large liquid/gas density ratios ($\rho_L/\rho_G > 500$) and relatively small Ohnesorge numbers ($Oh < 0.1$), within the bag breakup regime where the Weber number, $We = \rho_G d_o u_o^2/\sigma$, is in the range 13–35 (Hsiang and Faeth, 1993). As a result, the present test conditions are most representative of bag breakup within sprays near atmospheric pressure. Drop liquids included water, ethyl alcohol and various glycerol mixtures, in order to provide information about effects of drop liquid properties.

The paper begins with a description of experimental methods. Results are then discussed considering the properties of the parent drop, the properties of the basal ring, the properties of drops formed from the bag itself and the overall properties of bag breakup, in turn. The following description of the study is brief, see Chou (1997) for more details and a complete tabulation of data.

2. Experimental methods

2.1. Apparatus and instrumentation

The test apparatus and instrumentation will be described only briefly because it was similar to earlier work (Hsiang and Faeth, 1992, 1993, 1995; Chou et al., 1997). The arrangement consisted of a rectangular shock tube with the driven section open to the atmosphere. The test location was windowed to allow observations of drop breakup. A vibrating capillary tube drop generator, combined with an electrostatic drop selection system, provided a stream of drops at the test location with sufficient spacing between drops to accommodate bag breakup with negligible drop/drop interactions.

Single- and double-pulsed shadowgraphy and holography were used to observe the properties of the parent drop and the size and velocity distribution functions of drops produced by secondary breakup. Laser pulse times were sufficiently short (7 ns) to stop the motion of drops on the film while using a weaker second laser pulse allowed directional ambiguity to be resolved for velocity measurements. The combined holocamera and reconstruction system allowed objects as small as 3 μm to be observed and as small as 5 μm to be measured with 5% accuracy. Results at each condition were summed over at least four realizations, considering 100–200 liquid elements, in order to obtain drop diameter and velocity correlations. Estimated experimental uncertainties (95% confidence) were less than 10% for drop diameters and less than 15% for streamwise drop velocities.

2.2. Test conditions

The test conditions are summarized in Table 1. The liquid properties were obtained from Lange (1952), except for the surface tensions of the glycerol mixtures which were measured in the same manner as Wu et al. (1991). The ranges of the test variables were as follows: $d_o = 0.62$–0.85 mm, $\rho_L/\rho_G = 633$–893, $Oh = 0.0043$–0.0427, $We = 13$–20 and $Re = 1550$–2150, where the Reynolds number, $Re = \rho_G d_o u_o / \mu_G$. The present We test range is narrow but this is consistent with the narrow We range of the bag breakup regime. The Re range of the present

Table 1
Summary of the test conditions for bag breakup[†]

Liquid[‡]	d_o (μm)	ρ_L (kg/m³)	ρ_L/ρ_G (–)	$\mu_L \times 10^4$ (kg/ms)	$\sigma \times 10^3$ (N/m)	$Oh \times 10^3$ (–)	Re (–)
Water	620	997	755	8.94	70.8	4.3	1670–1910
Ethyl alcohol	630	800	633	16.0	24.0	15.0	1830–2080
Glycerol (21%)	650	1050	806	16.0	67.3	7.5	1550–1660
Glycerol (42%)	650	1105	857	35.0	65.4	16.1	1550–1910
Glycerol (63%)	850	1162	893	108.0	64.8	42.7	1850–2150

†With We in the range 13–20 in air initially at 98.8 kPa and 298 ± 2 K in the driven section of the shock tube. Shock Mach numbers in the range of 1.01–1.04. Properties of air taken for conditions downstream of shock wave: with pressures of 119.7–129.8 kPa, ρ_G of 1.25–1.31 kg/m³ and μ_G of 18.5 × 10⁶ kg/ms.

‡Glycerol compositions given in parentheses are percent glycerin (by mass) in water.

experiments is higher than conditions where gas viscosity has a significant effect on drop drag properties, e.g. the drag coefficient, C_D, for spheres only varies in the range 0.4–0.5 for this Reynolds number range (White, 1974). Shock Mach numbers were relatively low, less than 1.04; therefore, the physical properties of the gas in the uniform flow region behind the shock wave were nearly the same as room air.

3. Results and discussion

3.1. Parent drop properties

3.1.1. Parent drop size

Fig. 1 is a composite illustration of several aspects of the temporal evolution of bag breakup. The illustration includes: measurements of the parent drop cross-stream diameter d_p, as a
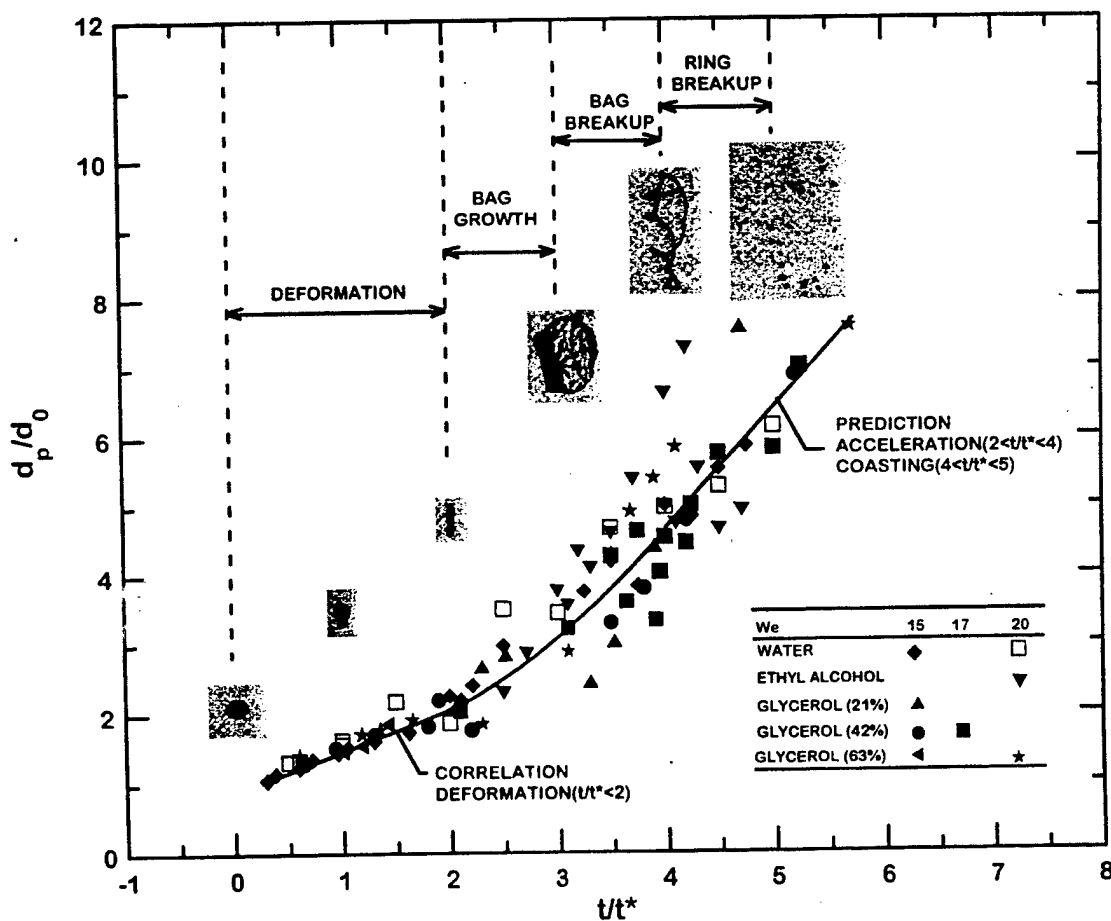

Fig. 1. Parent drop characteristic diameter as a function of time during bag breakup. Note that the shock wave has passed from left to right in the inset photographs.

function of time, t, for water, ethyl alcohol and glycerol drops having We of 13–20 and $Oh \leqslant 0.043$; delineation of the time periods of various portions of the bag breakup process; and inset photographs of the appearance of the parent drop at various times during breakup. The photographs are for a water drop in air subjected to a shock wave disturbance with $We = 20$ and $Oh = 0.0044$. Note that the shock wave passes from left to right in the inset photographs. The various positions of the bag breakup process are defined as follows: the deformation period where the drop deforms from a spherical to a disk-like shape for t/t^* of 0–2; the bag growth period where the center of the disk deforms into a thin membrane-like bag with a much thicker basal ring surrounding its open (upstream) end for t/t^* of 2–3; the bag breakup period where the bag progressively breaks up from its closed downstream end toward the basal ring for t/t^* of 3–4; and the ring breakup period where a series of relatively large node drops form along the ring followed by breakup of the ring into a circular array of relatively large drops to end the breakup process for t/t^* of 4–5. Note that the bag growth and ring breakup periods include a temporal range that is dominated by these processes. The actual time periods when bag and ring breakup occurs are contained in these periods, respectively, but are much shorter. The value of d_p is taken to be the cross-stream diameter of the disk before the basal ring forms $(0 \leqslant t/t^* \leqslant 2)$ and the outer diameter of the basal ring when it is present $(2 \leqslant t/t^* \leqslant 5)$.

The transition between a spherical drop and a relatively thin disk aligned normal to the flow direction occurs during the deformation period $(0 \leqslant t/t^* \leqslant 2)$ illustrated in Fig. 1. The deformation of the parent drop is caused by increased static pressures near the upstream and downstream stagnation points along the axis of the drop, combined with decreased static pressures near the drop periphery due to increased flow velocities in this region. This pressure distribution tends to squeeze the drop into a thin disk-like shape. A detailed analysis of this process was not undertaken; instead, it was found that the deformation process could be expressed reasonably well according to the following empirical correlation suitable for the present range of test conditions:

$$d_p/d_o = 1.0 + 0.5t/t^*, \quad 0 \leq t/t^* \leq 2. \tag{2}$$

Subsequent consideration of parent drop size parameters will focus on the properties of the basal ring. This interest is motivated by the fact that the size of the basal ring ultimately controls the size of the drops formed by basal ring breakup while these drops tend to dominate the size properties of drops formed by bag breakup because they are the largest drops in the size distribution. In addition, subsequent considerations will show that the basal ring, and thus the drops formed from the basal ring, comprise a major fraction of the original volume of liquid in the parent drop.

The results illustrated in Fig. 1 show that the rate of lateral acceleration of the basal ring diameters is largest in the period where the bag is present, with subsequent lateral acceleration progressively becoming small toward the end of the period where the bag itself breaks up. This behavior suggests that the higher pressure within the bag, caused by stagnation of the gas flow relative to the drop by the bag, is mainly responsible for the outward acceleration of the basal ring, as well as for the growth of the bag. This pressure difference progressively disappears as the breakup of the bag itself proceeds so that the basal ring simply continues to coast outward in the latter stages of the breakup process; this behavior is supported by the relatively constant

outward velocity of the basal ring diameter toward the end of the entire breakup process. These ideas are developed in the following to obtain the predicted variation of d_p/d_o as a function of t/t^* for the period $2 \leqslant t/t^* \leqslant 5$ that is illustrated in Fig. 1.

Analysis of basal ring growth was carried out ignoring acceleration of the parent drop, i.e. it was assumed that the relative velocity of the basal ring with respect to the gas is equal to the initial relative velocity, u_o; the variation of the diameter of the basal ring tube itself, d_r, was also neglected even though later considerations will show that this diameter decreases by almost a factor of two during the time period of interest; and circumferential surface tension forces were ignored due to the relatively large diameter of the basal ring at the start of the ring acceleration process. Other assumptions will be discussed as they are introduced. Considering the radial acceleration of the basal ring tube, conservation of momentum yields:

$$\rho_L(\pi^2 d_p d_r^2/4)\, d^2(d_p/2)/dt^2 = C_r(\rho_G u_o^2/2)(\pi d_p d_r) \tag{3}$$

where C_r is an empirical constant, somewhat analogous to a drag coefficient, to account for the fact that the pressure difference across the basal ring is only a fraction of the ideal stagnation pressure increase due to effects of gas motion across the basal ring and the motion of the gas in the bag, particularly as breakup of the bag itself proceeds. In (3) it is also assumed that the aspect ratio of the ring, d_p/d_r is relatively large when approximating the ring volume and cross-sectional area. Adopting d_p/d_o and t/t^* as normalized dependent and independent variables, (3) becomes:

$$d^2(d_p/d_o)/d(t/t^*)^2 = (4C_r/\pi)(d_o/d_r), \quad 2 \leq t/t^* \leq 4 \tag{4}$$

where the time interval of concern is the period when the bag (or at least a portion of it) is present and where the right-hand-side of this equation is taken to be a constant under the assumptions of the present approximate analysis. The initial conditions for (4) were chosen to match the value of d_p/d_o at $t/t^* = 2$ from (2) while adjusting the initial outward velocity of the basal ring to best fit the present measurements, as follows:

$$t/t^* = 2: \quad d_p/d_o = 2.0, \quad d(d_p/d_o)/d(t/t^*) = 0.8. \tag{5}$$

Finally, integrating (4) subject to the initial conditions of (5) and adjusting the value of the constant on the right-hand side of (4) to best fit the present measurements, yields:

$$d_p/d_o = 0.25(t/t^*)^2 - 0.18(t/t^*) + 1.43, \quad 2 \leq t/t^* \leq 4 \tag{6}$$

which is the form that is plotted in Fig. 1. The result implies $C_r \approx 0.04$ in (3), which is reasonable in view of the residual motions of the gas within the bag (particularly toward the end of bag breakup) and the fact that the relative velocity of the parent drop with respect to the gas is only roughly 70–90% of the initial relative velocity during the period of bag growth and breakup.

Proceeding to the basal ring breakup period, it is assumed that the basal ring, and the drops that are formed by breakup of the basal ring, simply coast outward with a constant radial velocity once the bag, and thus the mechanism for a pressure difference across the basal ring, has disappeared. This behavior agrees with the observed variation of d_p in this time period, and involves neglecting the relatively small drag forces on drop liquid elements in the radial

direction. Finally, the value of d_p/d_o at $t/t^* = 4$ is matched to the results of (6) and the outward coasting velocity in the ring breakup period is reoptimized to best fit the measurements. The final variation of d_p/d_o in the ring breakup period then becomes:

$$d_p/d_o = 1.79(t/t^*) - 2.51, \quad 4 \leq t/t^* \leq 6 \tag{7}$$

which is the form that is plotted in Fig. 1.

Taken together, (2), (6) and (7) provide a reasonable correlation of the measured variations of d_p/d_o as a function of t/t^* in Fig. 1. These results suggest that the flow resistance caused by the bag, and the remaining portions of the bag during its breakup period, are mainly responsible for the cross-stream spread of drops formed by breakup of the parent drop, including the large drops resulting from breakup of the basal ring. Stabilization of this motion by surface tension within the deformation period can be important; after all, this mechanism is responsible for controlling drop deformation and for preventing drop breakup in the deformation regime at *We* smaller than the bag breakup regime. Nevertheless, effects of surface tension on the radial dispersion of liquid during bag breakup appear to be relatively small.
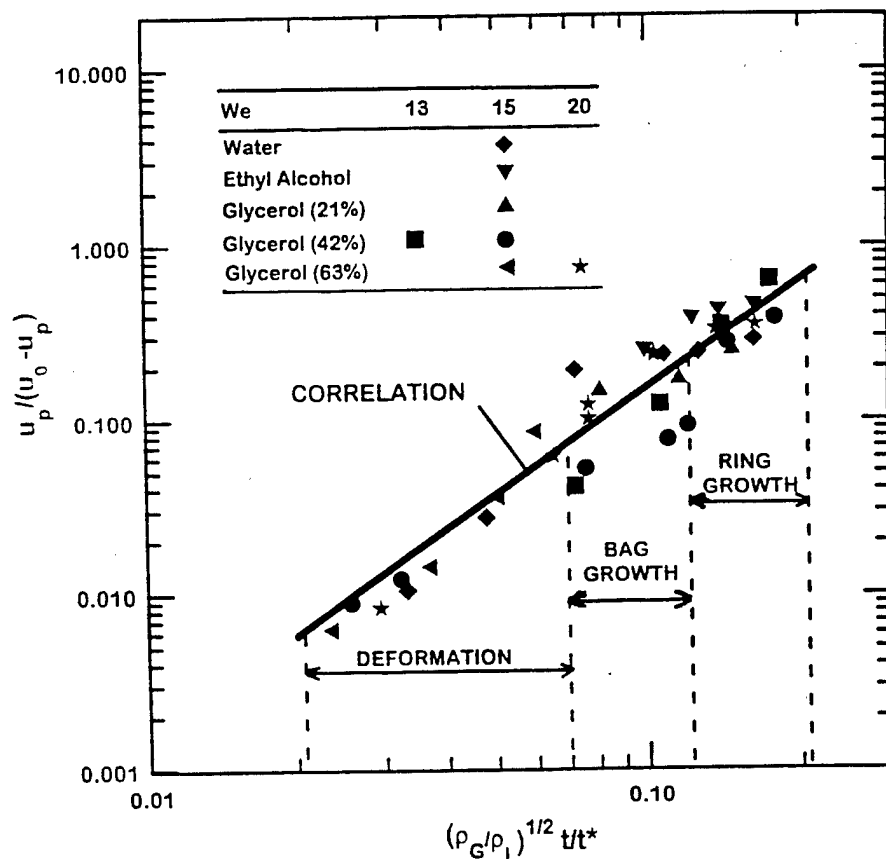

Fig. 2. Parent drop velocity as a function of time during bag breakup.

3.1.2. Parent drop velocities

The velocity of the parent drop, u_p, is plotted as a function of normalized time in Fig. 2. The various breakup periods—deformation, bag growth and basal ring growth (the last combining the bag breakup and ring breakup periods of Fig. 1)—are marked on the plot for reference purposes. The parent drop exhibits considerable acceleration during the breakup period, similar to past observations of the motion of parent drops for shear breakup (Hsiang and Faeth, 1992, 1993, 1995). In fact, the absolute, u_p, and relative, (u_o-u_p), velocities of the parent drop are comparable at the end of the ring growth period, which implies a reduction of the relative velocity of the parent drop of roughly 50% during the time of breakup, which is quite substantial. This behavior comes about due to growth of the cross-stream dimensions of the deformed parent drop, as a result of deformation and bag formation, as well as due to increased drag coefficients of the deformed parent drop, both of which significantly increase the drag forces on the parent drop compared to the original spherical drop.

3.1.3. Drag coefficients

In order to provide a common basis for comparing the drag coefficients of the parent drops during the various breakup periods, they were based on the current (local) cross-sectional area of the drop normal to the flow and relative velocity of the deformed parent drop with respect to the ambient gas. The position of the parent drop was taken to be either the centroid of the deforming drop ($0 \leqslant t/t^* \leqslant 2$) or the axis of the basal ring ($2 \leqslant t/t^* \leqslant 5$). The temporal variation of the temporal drag coefficients are plotted in Fig. 3. The drag coefficients of spheres, $C_D = 0.4$, and thin disks, $C_D = 1.2$, at similar Reynolds numbers are also shown on the plot for reference purposes. In the deformation period ($0 \leqslant t/t^* \leqslant 2$), the drag coefficient increases rapidly as the degree of deformation increases, reaching a maximum value when the bag begins to form. This maximum value approximates the drag coefficient of a thin disk, which is reasonable in view of the shape of the parent drop at this condition. In the bag growth period ($2 \leqslant t/t^* \leqslant 3$), the continuous increase of the cross-stream diameter of the parent drop, along with bag growth (which reduces the transfer of drag forces to the basal ring) causes parent drop drag coefficients to become smaller. The reduced drag of the ring growth and breakup periods ($3 \leqslant t/t^* \leqslant 5$) is then representative of the lost flow resistance of the parent drop once the bag is no longer present.

3.2. Basal ring properties

3.2.1. Basal ring volume

Drop sizes formed from the bag and the basal ring of the bag are substantially different; therefore, it is important to know the relative volumes of the bag and its basal ring in order to estimate drop sizes produced by the bag breakup. Thus, measurements were undertaken to establish the distribution of the parent drop liquid between the bag and the basal ring over the complete range of the present data. These measurements were made by characterizing the ring at the end of bag breakup, including the volume of the nodal drops as well as the cylindrical sections of the ring in the region between the nodal drops. The ratio of the liquid volume in the basal ring, V_r, to the initial volume of the parent drop, V_o, is summarized in Table 2 (other parameters in this table include the Ohnesorge number based on the tube diameter of the ring
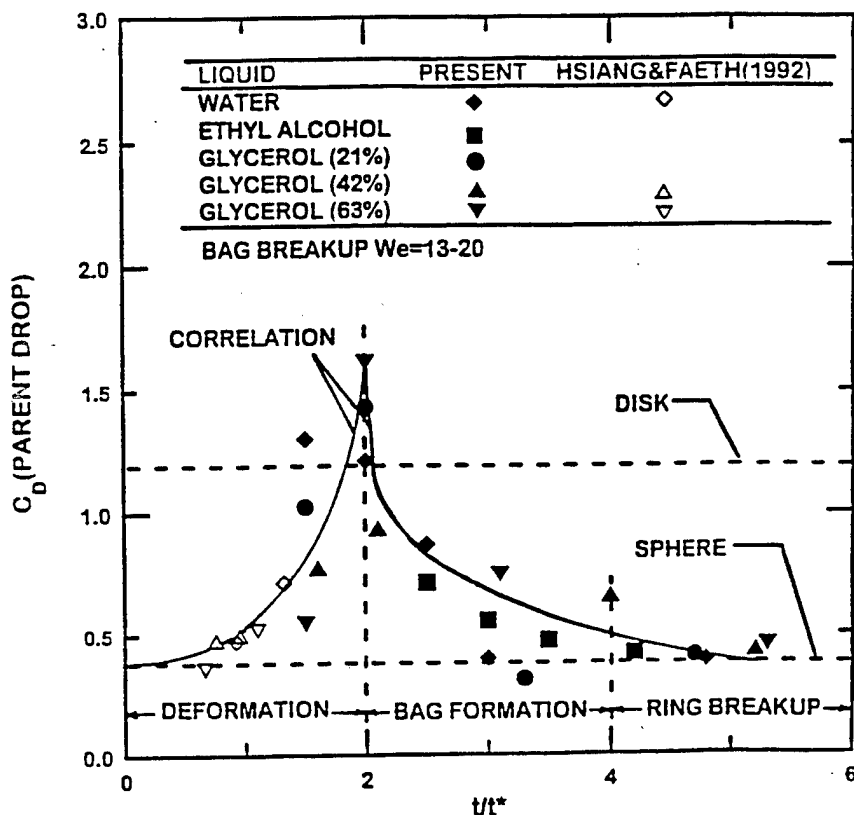
Fig. 3. Parent drop drag coefficient as a function of time during bag breakup.

$Oh_r = \mu_L/(\rho_L d_r \sigma)^{1/2}$, and the diameter of drops formed from the ring, d_{rd}, limited to the properties of the ring between node drops). For present test conditions, each value of Oh corresponds to a particular drop liquid; nevertheless, it can be seen that V_r/V_o is essentially independent of Oh over the present test range, yielding the correlation:

$$V_r/V_o = 0.56 \tag{8}$$

Table 2
Summary of properties of basal ring†

Liquid‡	We	Oh	V_r/V_o	Oh_r	d_{rd}/d_r
Water	15	0.0043	0.57	0.013	2.53
Ethyl Alcohol	15	0.0150	0.52	0.045	2.54
Glycerol (21%)	15	0.0075	0.59	0.021	1.91
Glycerol (42%)	17	0.0161	0.57	0.045	1.87
Glycerol (63%)	15	0.0427	0.54	0.130	2.21

†Result based on the properties of the bag during the bag breakup period for the test conditions summarized in Table 1.

‡Glycerol compositions given in parentheses are percent glycerin (by mass) in water.

with a standard deviation of 0.04. Lane (1951) carried out early measurements of bag breakup and mentions a determination of $V_r/V_o = 0.75$; nevertheless, this earlier value is only mentioned in passing with no information provided about its accuracy and method of determination so that its reliability is uncertain.

3.2.2. Tube axis diameter

Given that the volume of the ring is a fixed fraction of the initial drop volume, it should be possible to determine the diameter of the tube axis of the ring as a function of the ring diameter. In particular, if the presence of node drops along the basal ring is ignored:

$$V_r/V_o = (\pi^2 d_p d_r^2/4)/(\pi d_o^3/6) \tag{9}$$

which implies

$$d_r/d_o = (2V_r/(3\pi V_o))^{1/2}/(d_p/d_o)^{1/2} = 0.35/(d_p/d_o)^{1/2} \tag{10}$$

where d_p/d_o is known as a function of time either from Fig. 1 or from (6) and (7).

Present measurements of d_r/d_o are plotted as a function of t/t^* in Fig. 4. The predictions of d_r/d_o from (10) using (6) and (7) to find d_p/d_o, are also shown on the plot. There is significant
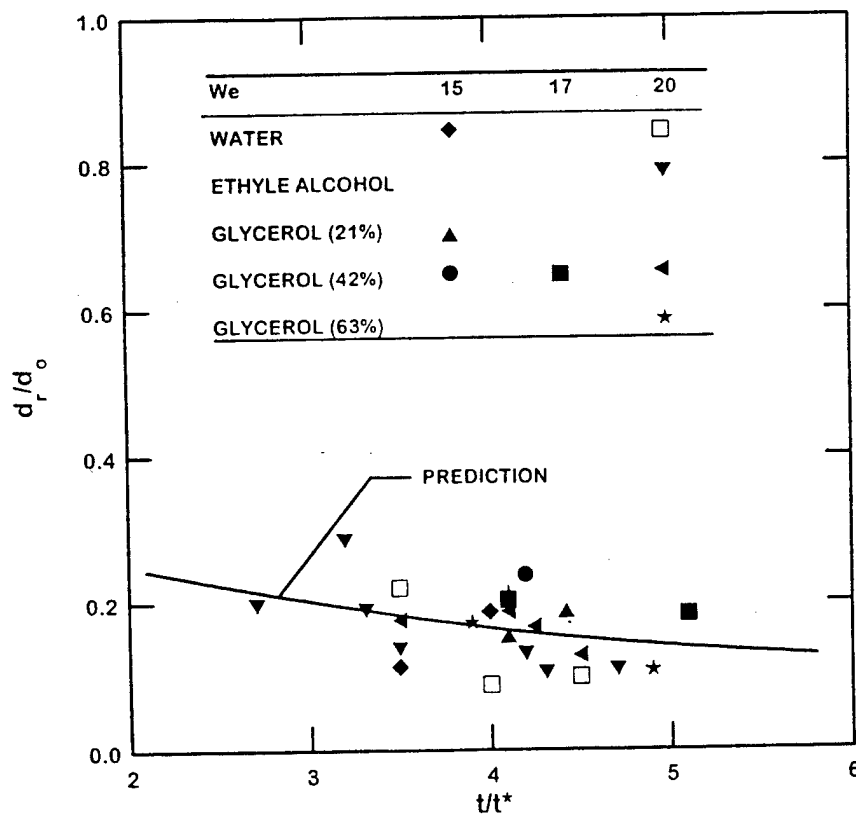
Fig. 4. Ring tube diameter as a function of time during bag breakup.

scatter of the measurements due to problems of observing the basal ring, particularly when the bag is present, and effects of the presence of node drops. Nevertheless, the measurements are in reasonably good agreement with (10), supporting a relatively slow reduction of d_r/d_o with increasing time due to the increased diameter of the tube axis of the basal ring itself.

3.2.3. Basal ring drop diameters

Two types of drops are formed from the basal ring: node drops and drops from the cylindrical portions of the ring between the nodes that are somewhat smaller than the node drops. The drops formed from the cylindrical portion of the basal ring are not subject to strong strain and appear to result from classical Rayleigh breakup of a nearly constant-diameter liquid column. In addition, the Ohnesorge numbers of the rings observed during the present investigation were relatively small ($Oh \leqslant 0.13$ based on values given in Table 2) so that effects of liquid viscosity should be small as well. Under these circumstances, the ratio of the diameter of the drops formed by ring breakup, and the ring diameter, should be a constant, as follows (Dombrowski and Hooper, 1962):

$$d_{rd}/d_r = 1.88, \quad \text{predicted.} \tag{11}$$

The Rayleigh breakup condition of (11) was evaluated using the present measurements. In doing this, the complication of the node drops was ignored (they will be considered later) and only drops formed from the intervening constant-diameter portions of the ring were considered. In addition, d_r was determined for this expression at the time of ring drop breakup, i.e. $t/t^* = 5$ where $d_r/d_o = 0.13$ from Fig. 4 with a 16% uncertainty.

The values of d_{rd}/d_r measured during the present investigation are summarized as a function of Oh in Table 2. As before, the present experiments involved a nearly constant Oh (and Oh_r) for each liquid because the variation of We is small in the bag breakup regime. The measurements do not suggest a significant effect of Oh over the present test range and yield

$$d_{rd}/d_r = 2.2, \quad \text{measured.} \tag{12}$$

Clearly, (12) is in reasonably good agreement with the Rayleigh breakup prediction at small Oh given by (11), supporting Rayleigh breakup as the mechanism producing drops from the ring-like portions of the basal ring. Finally, given $d_r/d_o = 0.13$, as just discussed, implies:

$$d_{rd}/d_o = 0.29. \tag{13}$$

The effect of the node drops on the mean size of drops produced by the ring will be considered next. In general, there were 4–6 node drops, having diameters of $(1.3-1.6)d_{rd}$. Thus, if this contribution is added to that of the drops from the tubular portions of the ring, the final average size of drops formed from the basal ring, d_{trd}, can be correlated as follows:

$$d_{trd}/d_o = 0.30 \tag{14}$$

with the uncertainty of this constant being less than 20%. Finally, the total number of drops produced by the basal ring, N_{trd}, can be found from the mean size of the basal ring drops given by (14) and the volume of the basal ring given by (8), as follows:

$$N_{trd} = 22.1.$$

3.2.4. Basal ring breakup time

As discussed by McCarthy and Molloy (1974), the Rayleigh breakup times, t_{rt} of liquid columns have been shown to be

$$t_{rt} = C(\rho_t d_r/\sigma)^{1/2}(1 + 3Oh_r)d_r \tag{16}$$

where d_r is the column diameter, Oh_r is the Ohnesorge number based on this dimension, and C is a stability constant that must be determined. Smith and Moss (1917) found C to be 13 for different liquids and column diameters. Associating the time required for the Rayleigh breakup with the time required for the basal ring to breakup, by replacing the column diameter with the tube axis diameter in (16), yields:

$$t_{rt} = CC_{rt}(\rho_L d_r/\sigma)^{1/2}(1 + 3Oh_r)d_r \tag{17}$$

where C_{rt} is an unknown constant of proportionality expected to be on the order of unity. For the conditions of the present study, Oh_r is small so that the effect of liquid viscosity represented by the Oh term can be neglected. Then, normalizing (17) by t^* yields:

$$t_{rt}/t^* = 13C_{rt}We^{1/2}(d_r/d_o)^{1/2}. \tag{18}$$

For bag breakup, $We = 13$–25. while $d_r/d_o = 0.17$–0.19 in the region where the basal ring is present (i.e. $2 \leqslant t/t^* \leqslant 5$) as seen in Fig. 4. Substituting averages of these parameters into (18) then yields:

$$t_{rt}/t^* = 3.88C_{rt}. \tag{19}$$

Finally, it is assumed that the Rayleigh breakup process of the basal ring begins when the ring has just formed ($t/t^* \approx 2$) and ends upon ring breakup ($t/t^* \approx 5$), based on the results illustrated in Fig. 1. This implies that the time required from initial basal ring formation to basal ring breakup is $t_{rt} = 3t^*$, so that $C_{rt} = 0.77$. Since C_{rt} is on the order of unity, as expected, this finding provides good support for the idea that basal ring breakup involves a relatively passive Rayleigh breakup process. Thus, given that the time required to reach maximum deformation, where basal ring formation is completed, is $2t^*$, the Rayleigh breakup time of the basal ring of roughly $3t^*$ fixes the entire bag breakup time to be roughly $5t^*$. This breakup time is nearly the same as for shear breakup (Liang et al., 1988) but the previous reasoning suggests that this agreement is fortuitous due to the very different breakup phenomena that comprise the bag and shear breakup processes.

3.2.5. Ring drop velocity distributions

Ring drop velocity distributions were essentially independent of drop size, except for a slight tendency for node drops to move slower than the smaller ring drops formed from portions of the basal ring between the node drops. This effect is evident from the downstream deflection of the basal ring in the region between nodes seen in the inset figure at $t/t^* = 4$ in Fig. 1. This variation, however, is less than present experimental uncertainties for velocity measurements so that initial ring drop velocities can be computed from the results illustrated in Fig. 2 with little error.

3.3. Bag properties

3.3.1. Bag drop diameters

The properties of drops formed by breakup of the bag, along with a few determinations of bag thickness, h, by measurements from holograms, are summarized in Table 3. It should be noted that the values of h given in Table 3 are not very reliable because they approach present limits of spatial resolution and involve additional problems of estimating film thicknesses from the region where the bag breaks up into drops (in particular, later considerations will show that unbalanced surface tension forces in the region where bag drops are forming are important so that these effects probably locally increase bag thicknesses as well). In view of these problems, it is estimated that the values of h in Table 3 might be too large by as much as a factor of two, although the corresponding drop diameter measurements for drops found from bag breakup are felt to be reliable within the uncertainties stated earlier. Entries provided in Table 3 include d_0, the time when drop sizes were measured (except for one condition at $t/t^* = 3$, these results were averaged over the entire breakup period of $t/t^* = 3$–4), the number-averaged bag drop diameter, d_{bda}, and the Sauter mean diameter, SMD_{bd}, of drops formed from the breakup of the bag, several normalizations of these properties and the Ohnesorge number based on the dimension d_{bda}.

Comparing mean drop diameters at the start of bag breakup and averaged over the entire bag breakup period for glycerol (42%) indicates an increase of the drop sizes as the basal ring of the bag is approached. This is not unexpected as some stretch of the bag membrane, and a corresponding reduction of the size of drops formed by breakup of the membrane, is expected as the farthest downstream location is approached. Nevertheless, the variation of drop diameters is not large, with drops formed initially from the bag being only 15% smaller than the mean size of drops formed from the bag.

A second issue of interest about drops formed by breakup of the bag itself is the variation of mean drop sizes with Oh. The results of Table 3 show that both d_{bda}/d_0 and SMD_{bd}/d_0 increase as Oh increases over the test range. Characterizing this behavior by the Ohnesorge number based on the average size of drops formed from the bag, it is seen that d_{bda}/d_0

Table 3
Summary of properties of drops formed from the bag†

Liquid‡	d_0 (μm)	t/t^* (−)	h (μm)	d_{bda} (μm)	SMD_{bd} (μm)	Oh_{bda}	h/d_0 (%)	d_{bda}/h (−)	d_{bda}/d_0 (%)	SMD_{bd}/d_0 (%)
Water	620	3–4	16.4	21.9	23.8	0.023	2.65	1.33	3.5	3.8
Glycerol (21%)	650	3–4	—	22.1	23.9	0.077	—	—	3.8	3.5
Glycerol (42%)	650	3	23.2	25.8	28.9	0.038	3.57	1.12	4.0	4.5
Glycerol (42%)	650	3–4	—	29.6	33.2	0.075	—	—	4.6	5.1
Glycerol (63%)	850	3–4	35.4	42.1	48.8	0.193	4.16	1.17	4.9	5.2
					averages =		3.46	1.21	4.2	4.4

†Results based on the properties of the bag and the properties of drops formed by breakup of the bag during the bag breakup period for the test conditions summarized in Table 1.

‡Glycerol compositions given in parentheses are percent glycerin (by mass) in water.

increases from 3.5* to 4.9* as Oh_{bda} increases from 0.023 to 0.193. This behavior suggests an effect of liquid viscosity on bag properties, and thus on the properties of drops formed from the bag; such behavior is not surprising in view of past observations (Hsiang and Faeth, 1992, 1993, 1995) of strong effects of liquid viscosity on the drop sizes formed by secondary breakup.

Mean drop sizes resulting from breakup of the bag vary somewhat with initial Oh as just noted, but yield an average value of d_{bda}/d_o of 4.2%, over the present test range. Thus, bag drops generally are relatively small and do not have as strong an effect on spray transport properties as the drops produced by breakup of the basal ring. For example, based on the diameter-squared behavior that tends to dominate drop properties in sprays (Faeth 1997), the lifetime of drops formed from the basal ring would be nearly 60 times longer than the lifetime of drops formed from the bag. Another issue concerning mean drop sizes is that SMD_{bd} and d_{bda} are nearly the same, e.g. the average value of the ratio $SMD_{bd}/d_{bda} = 0.89$. This behavior implies a nearly monodisperse size distribution for these drops, a property that will be considered in more detail next. To summarize, the correlation of bag drop sizes becomes:

$$d_{bda}/d_o = 0.042. \tag{20}$$

The size distribution function of drops formed by breakup of the bag is illustrated in Fig. 5. These results are plotted according to the root normal distribution function that has proven to
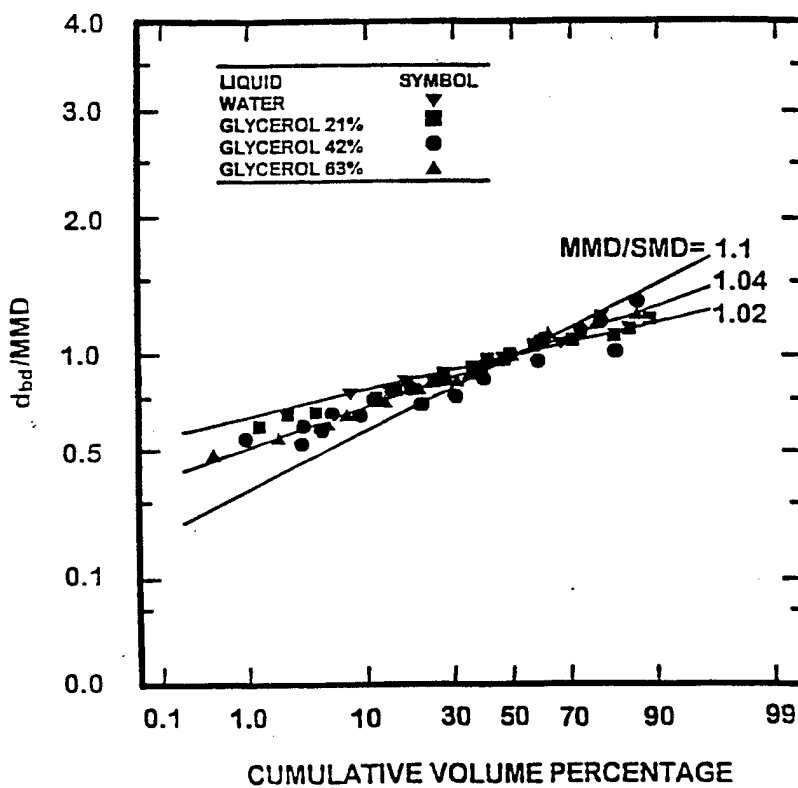

Fig. 5. Drop size distributions of drops formed from breakup of the bag itself during bag breakup.

be successful for a variety of drop and spray breakup processes (Faeth, 1997). Results for various values of MMD/SMD for the bag drops are shown on the plot for comparison with the measurements. In the past, this distribution function with $MMD/SMD = 1.20$ has been successful for correlating drop size distributions in sprays. The bag drops themselves, however, while correlating reasonably well according to the root normal distribution function, do so only with a much smaller value of $MMD/SMD = 1.04$. As discussed earlier, however, this result is not unexpected due to the nearly monodisperse size distribution of drops formed from the bag because the bag membrane itself appears to have a relatively uniform thickness. The behavior of the drop size distribution function changes when drops formed from both the bag and the ring are considered, however, as discussed later in connection with overall breakup properties.

3.3.2. Bag breakup time

The time required for breakup of the bag, t_b, is also an important parameter that must be known. This issue will be considered in the following, assuming a constant bag thickness during bag growth period with an average bag velocity, u_b as shown in Table 4, by relating the bag breakup time to the breakup time of a thin film.

From Dombrowski and Hooper (1962), the time required from breakup of a thin film, t_{fl}, can be correlated as follows:

$$t_{fl}/t^* = 3.73 We^{-1/2}(u_o/u_L)^2(h/d_o)^{1/2} \tag{21}$$

where u_L is the liquid film velocity. For the bag growth period, the liquid film velocity can be approximated by u_b to yield the time required for breakup of bag as follows:

$$t_{bt}/t^* = 3.73 C_{bt} We^{-1/2}(u_o/u_b)^2(h/d_o)^{1/2} \tag{22}$$

where C_{bt} is a constant of proportionality expected to be on the order of unity. Applying (22), using a constant value of $h/d_o = 1\%$, yields the bag breakup times summarized in Table 4. From Fig. 1, the time required for breakup of the bag is typically $t_{bt}/t^* = 1.0$, thus, averaging the results in Table 4 implies that the $C_{bt} = 0.91$ which is on the order of unity, as expected. This finding strongly supports the idea that breakup of the bag itself involves a simple thin film breakup of the membrane-like bag, and that the bag inflation time is controlled by the breakup time of the first part of the bag that is formed, i.e. the tip of the bag.

Table 4
Summary of properties of bag during bag formation period†

Liquid‡	We	t/t^*	h/d_o	u_b/u_o	t_{bt}/t^*
Water	15	2.0–3.5	0.01	0.266	1.36
Glycerol (21%)	15	3.0–3.5	0.01	0.288	1.16
Glycerol (42%)	17	3.0–3.5	0.01	0.324	0.92
Glycerol (63%)	15	3.0–3.5	0.01	0.317	0.96

†Result based on the properties of the bag during the bag breakup period for the test conditions summarized in Table 1.
‡Glycerol compositions given in parentheses are percent glycerin (by mass) in water.

3.3.3. Bag drop velocity distribution

Initial velocities of bag drops exhibit negligible variation with size over the narrow range of sizes of these drops. In addition, even though portions of the bag move at somewhat different velocities than the parent drop (which is taken to be the basal ring for $2 \leqslant t/t^* \leqslant 5$ when parent drop velocities are found) these velocity variations are small compared to the parent drop velocity. Thus, within present experimental uncertainties, initial bag drop velocities can be estimated as the parent drop velocity at the time they are formed from Fig. 2. Present observations indicate that the time of breakup of the bag extends over the range $t/t^* = 3.2$–3.5, thus, in view of the relatively slow variation of parent drop velocities seen in Fig. 2, initial bag drop velocities are essentially monodisperse within present experimental uncertainties.

3.4. Overall breakup properties

3.4.1. Drop size distributions

Past work yielded different observations about overall drop size distributions resulting from bag breakup, for example, Hsiang and Faeth (1992, 1993, 1995) find that drop size distribution functions were represented reasonably well by the universal root normal size distribution function while Gel'fand et al. (1974) report a bimodal drop size distribution function with one nearly monodisperse group associated with drops formed from the ring and a second nearly monodisperse group associated with drops formed from the bag. The overall drop size distribution function properties were studied during the present investigation in order to help resolve these differences. As a practical matter it was found that in spite of the nearly monodisperse drops formed from the bag, no bimodal behavior for the drop size distribution function was evident. Thus, present results concerning the drop size distribution function were correlated in terms of the universal root normal distribution function of Simmons (1977). It will be shown later, however, that this behavior probably is due to undersampling the small drops formed from the bag, tending to support the findings of Gel' fand et al. (1974) at least to the extent that an overall drop size distribution is useful for treating bag breakup processes.

The drop size distribution results for the present measurements of bag breakup properties are plotted in terms of the universal root normal distribution function in Fig. 6. These results emphasize behavior over the entire test range rather than more statistically significant results at a fewer number of conditions. Thus, the measurements illustrated in Fig. 6 are scattered due to inadequate statistics. In particular, bag breakup of individual drops yields a relatively small number of large drops that dominate the size distribution function because they represent a large fraction of the drop volume produced by breakup. In addition, the small drops formed from breakup of the bag itself tend to be undersampled because they are small and poorly resolved and also are rapidly swept downstream due to their rapid acceleration to gas velocities. The results shown in Fig. 6 however, are reasonably represented by the root normal distribution function, with $MMD/SMD = 1.2$, which is similar to earlier findings for other spray breakup processes (Faeth, 1997).

A second issue of interest about the drop size distribution is the SMD after bag breakup. The SMD is mainly dominated by the largest drop sizes in the distribution; thus, by neglecting the small drops from the bag, the present measurements of SMD/d_0 after bag breakup are summarized in Table 5, along with the average ring drop size from (14) and the average bag drop size from Table 3. Clearly, the SMD after bag breakup is dominated by the node drop
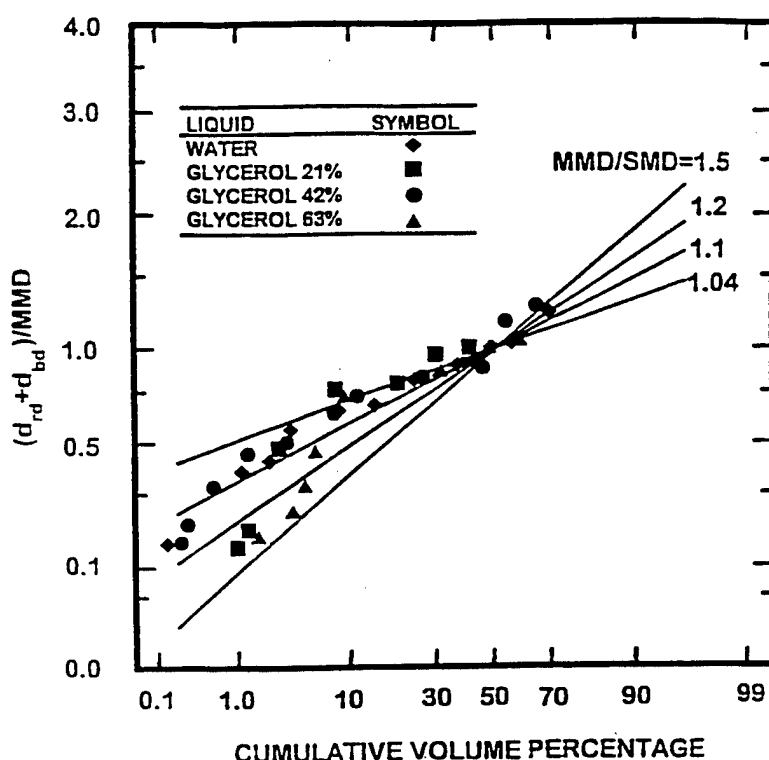
Fig. 6. Drop size distributions of drops formed from both the bag and the basal ring during the entire bag breakup process.

size (the largest drop size of ring drops) and is essentially independent of Oh over the present range to yield:

$$SMD_{total}/d_o = 0.36 \qquad (23)$$

with a standard deviation of 0.05 for (23).

Table 5
Summary of SMD after bag breakup†

Liquid‡	We	Oh	SMD_{total}/d_o	d_{trd}/d_o	d_{bd}/d_o
Water	15	0.0043	0.34	0.30	0.035
Ethyl alcohol	15	0.015	0.32	0.30	—
Glycerol (21%)	15	0.0075	0.41	0.30	0.038
Glycerol (42%)	17	0.016	0.37	0.30	0.040
Glycerol (63%)	15	0.042	0.38	0.30	0.041
		averages =	0.36	0.30	0.041

†Result based on the properties of the bag during the bag breakup period for the test conditions summarized in Table 1.
‡Glycerol compositions given in parentheses are percent glycerin (by mass) in water.

The present correlation of the *SMD* for the entire bag breakup process from (23) differs from the earlier findings of Hsiang and Faeth (1992). The correlating expression for the *SMD* for bag breakup from Hsiang and Faeth (1992) was found as an empirical extension of the boundary layer stripping analysis developed for the shear breakup regime to yield the following expression:

$$\rho SMD u_0^2 / \sigma = 6.2(\rho_L/\rho_G)^{1/4}(\nu_L/d_o u_o)^{1/2} We. \tag{24}$$

The SMD after bag breakup for the present measurements is plotted in Fig. 7 as suggested by (24), along with the data of Hsiang and Faeth (1992) for the bag breakup region. Both sets of measurements roughly agree with each other, however, the results of the present study, characterized by the results of (23), yield a constant value of SMD/d_o for the bag region instead of the correlation of (24). This implies that the *SMD* after bag breakup only fortuitously agreed with the boundary layer analogy, over the narrow range of *We* of the bag breakup regime. Thus, a more rational approach would be to treat bag breakup as dominated by Rayleigh breakup of the basal ring, including the complications due to the presence of node drops to yield (23).
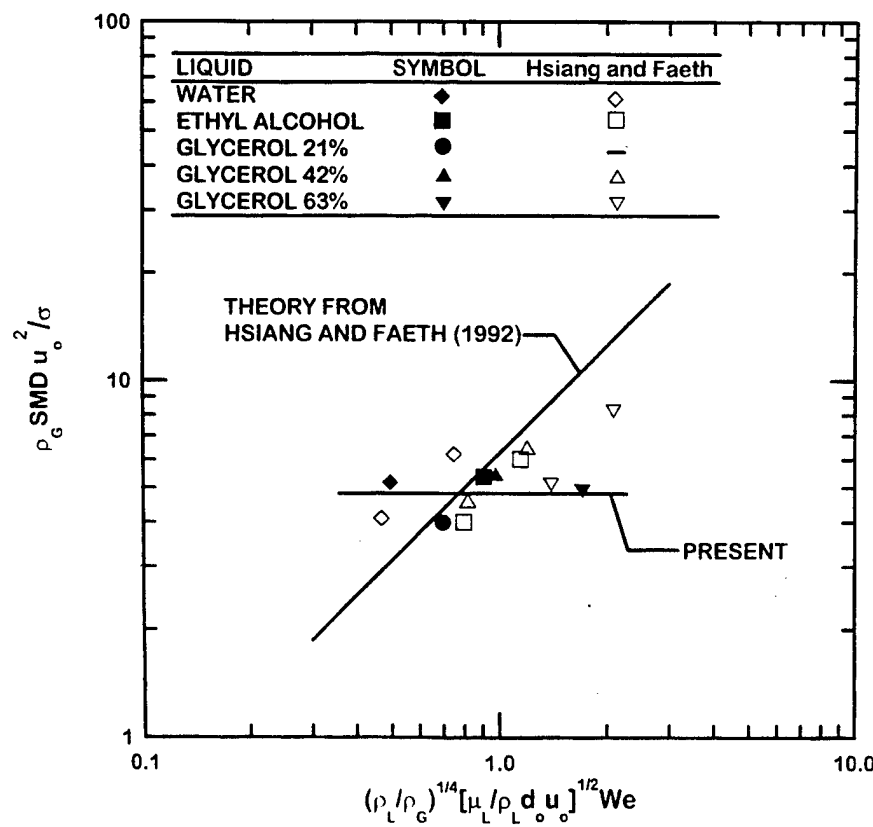

Fig. 7. Correlation of the *SMD* after the entire bag breakup process.

The small drops (which mainly are formed from the bag) can have a large effect on the *SMD*, however, even though they are often ignored, because there are a large number of small drops due to the reasonably large mass fraction and small size of drops formed from the bag. In the same way that the number of drops formed from the ring was estimated in (15), the number of drops formed from the bag can be estimated as follows:

$$\pi/6 d_o^3 (\text{mass fraction of bag drops}) = N_b \pi / 6 d_{bd}^3. \tag{25}$$

Using the mass fraction of the basal ring from (8) and the average bag drop size given by (20), the number of drops formed from the bag can be computed from (25) to yield $N_b = 5940$ bag drops per initial drop. Summarizing the results from (8) and (25), and estimating the number of node drops as 6 per initial drop, then the number distribution involves fixed fractions for the bag, node and ring drops as follows: $f_b = 0.996$, $f_n = 0.001$ and $f_r = 0.003$. It is obvious, that the small drops dominate the number of drops in the distribution.

Given this information, the overall *SMD* including the small drops can be estimated from the fundamental definition of the *SMD* as follows:

$$SMD/d_o = \frac{f_b(d_{bd}/d_o)^3 + f_r(d_{rd}/d_o)^3 + f_n(d_{nd}/d_o)^3}{f_b(d_{bd}/d_o)^2 + f_r(d_{rd}/d_o)^2 + f_n(d_{nd}/d_o)^2}. \tag{26}$$

Substituting the values of f_b, f_r and f_n, and the ratios d_{bd}/d_o, d_{rd}/d_o, d_{nd}/d_o, found earlier, yields $SMD/d_o = 0.11$, which is much smaller than the result given by (23) where the bag drops have been ignored. This implies that the small drops do affect the *SMD* substantially when the overall *SMD* is sought. This behavior suggests that such gross averages for the entire bag breakup process are not very helpful, although the drops formed from the bag are still important in spite of their small size because they amount to 44* of the initial mass of the drop. Taken together, a more effective approach is to use (23) to estimate the size of the ring drops, and (20) to estimate the size of the bag drops, while treating these drops as separate populations.

3.4.2. Drop breakup rate

In order to find drop breakup rates, the fact that the entire bag breakup process involves two separate periods of liquid removal from the parent drop must be considered: one period associated with breakup of the bag itself, and the other period associated with breakup of the basal ring. The first period involves 44% of the original drop mass from (8), with this process approximated by a constant rate of liquid removal over the time period, $t/t^* = 3.2–3.5$, when the bag itself was observed to break up based on present measurements. The second period involves 56% of the original drop mass from (8), with this process assumed to occur by the nearly simultaneous formation of drops from the basal ring at $t/t^* = 5.0$, when the basal ring was observed to break up based on present measurements.

Present measurements of the cumulative volume percentage of liquid removed from the parent drop, based on the assumptions just discussed, are plotted in Fig. 8. Thus, unlike shear breakup, bag breakup involves two relatively short breakup periods, separated by periods of development of the Rayleigh breakup processes. An interesting feature of the results illustrated in Figs. 1 and 8 is that the bag forms for a time period 1.0 t^* with bag formation ending due

98
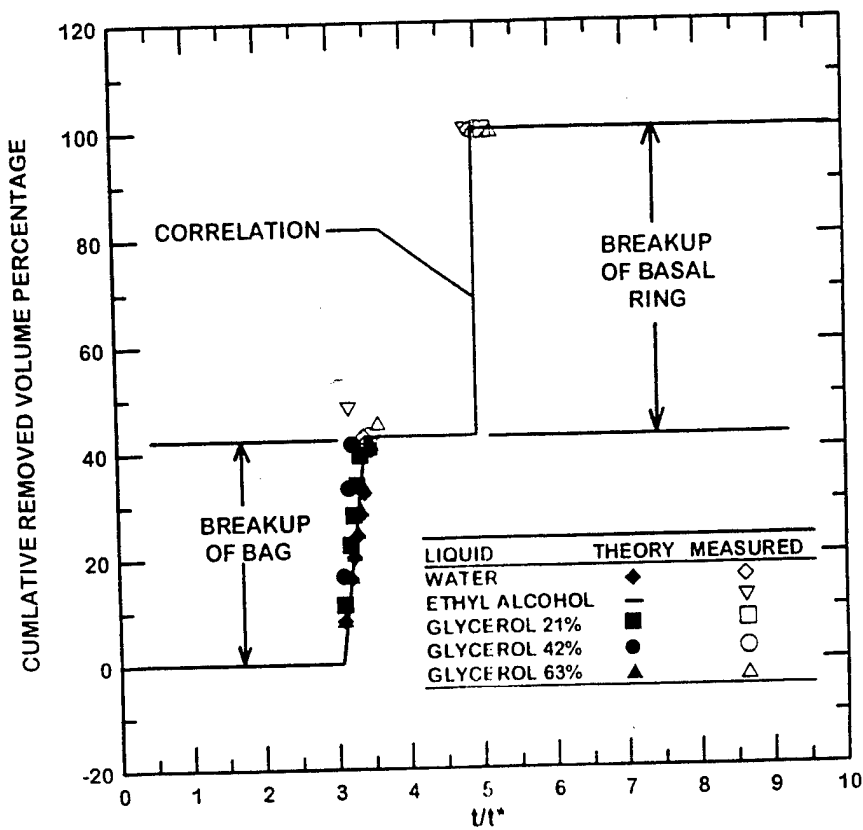
Fig. 8. Cumulative removed volume percentage of liquid from the parent drop as a function of time during bag breakup.

to Rayleigh breakup of the tip of the bag. Thus, if the entire process of breakup of the bag proceeded by passive Rayleigh breakup, a total breakup period of the bag 1.0 t^* might be expected as well. Instead, the bag actually breaks up in a much shorter time, 0.3 t^*. This suggests that once breakup of the bag starts, the unbalanced surface tension forces on the broken bag enhance its motion toward the basal ring so that its time of breakup (or disappearance) is reduced. This behavior also helps to explain the tendency for bag drop sizes to be larger than suggested by estimates of bag thickness, and to increase as the basal ring is approached due to a corresponding increase of the membrane thickness. Finally, the liquid removal properties of bag breakup highlights why separate treatment of drops formed from the bag and from the basal ring is preferable to attempting to treat all the drops as a single population.

3.4.3. Temporal and spatial breakup region

The spatial and temporal properties of bag breakup based on the velocity results of Fig. 2 are illustrated in Fig. 9. These findings involve the streamwise positions of the drops and the tip of the bag, denoted by x, as functions of the time after the start of breakup. The positions of the parent drop (which is the slowest drop to relax toward gas velocities), the tip of the bag
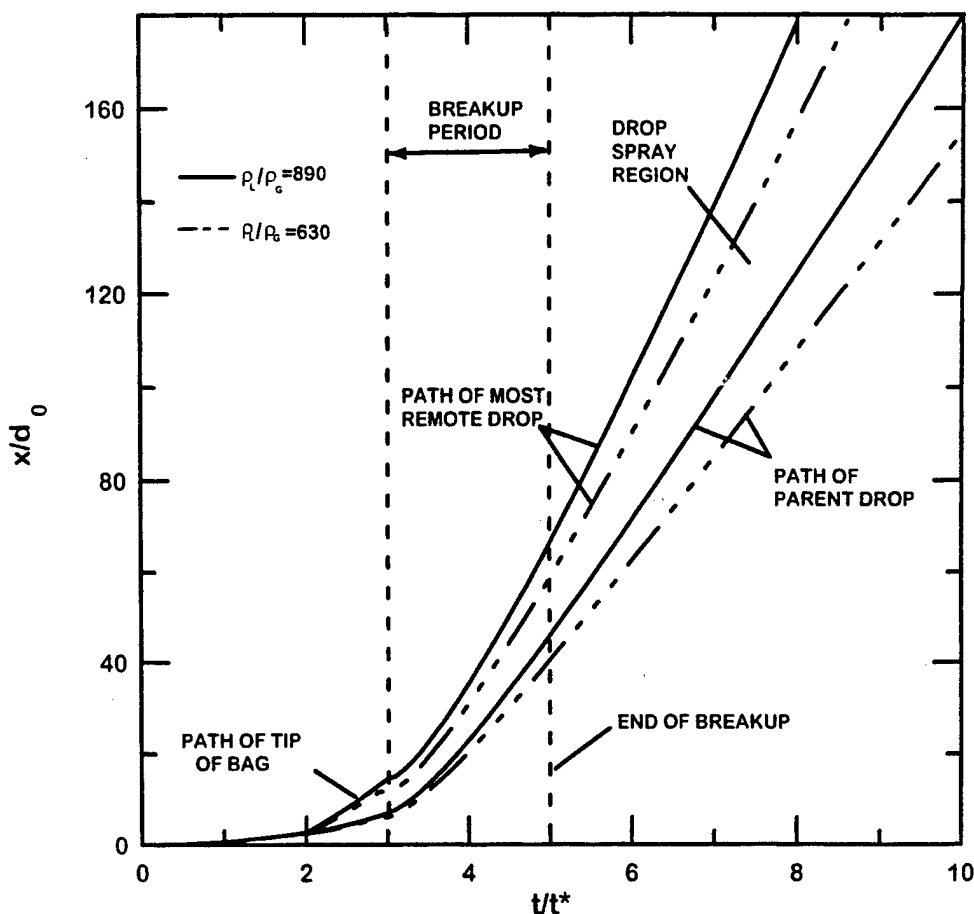
Fig. 9. Streamwise positions of the parent and the most remote drops as a function of time during bag breakup.

(when it is present in the period $2 < t/t^* < 3$) and the most remote drop (which is the first drop formed from breakup of the tip of the bag and which responds relatively rapidly to the gas motion due to its relatively small size) are illustrated in the figure. The most remote drop separates from the parent drop at roughly $t/t^* = 3$ (actually $t/t^* = 3.2$) when the bag begins to break up, and begins its streamwise travel from the tip of the bag. The breakup process itself typically is ended when breakup of the ring is completed, which occurs roughly at $t/t^* = 5$ for present test conditions. In the coordinate system of Fig. 9, there is a small effect of ρ_L/ρ_G on drop motion; therefore, results at the limits of the present test range, $\rho_L/\rho_G = 630$ and 890, have been illustrated on the plot.

The results illustrated in Fig. 9 indicate that the temporal and spatial ranges of bag breakup are comparable to the findings for shear breakup observed by Chou et al. (1997). In particular, the breakup period requires t/t^* in the range 0–5; in this period, the most remote drop moves a streamwise distance of roughly 60 initial drop diameters and the parent drop moves a streamwise distance of roughly 50 initial drop diameters. Finally, the results plotted in Fig. 1 (based on the value of d_p/d_o at the time of breakup of the basal ring) imply that the largest

drops formed by breakup of the ring spread laterally to a diameter of roughly 7 initial drop diameters. These times and distances are comparable to characteristic times and distances associated with the dense region of pressure-atomized sprays (Faeth, 1997); therefore, both bag and shear breakup should be treated as rate processes rather than by jump conditions, in many instances.

4. Conclusions

The objective of the present study was to experimentally investigate the temporal properties of bag breakup for shock-wave initiated disturbances in air at normal temperature and pressure. The test liquids included water, ethyl alcohol and various glycerol mixtures to yield liquid/gas density ratios of 633–893, Weber numbers of 13–20, Ohnesorge numbers of 0.0043–0.0427 and Reynolds numbers of 1550–2150. The major conclusions of the study are as follows:

1. The basal ring formed from the parent drop contains roughly 56% of the initial drop volume (mass) and eventually yields drops having mean diameters of roughly 30% of the initial drop diameter due to a Rayleigh-like breakup process of the basal ring that occurs relatively abruptly near $t/t^* = 5$.
2. The bag formed from the parent drop contains roughly 44% of the initial drop volume (mass) and eventually yields nearly monodisperse drops having mean diameters of roughly 4% of the initial drop diameter due to a breakup process of the membrane-like bag. This breakup process propagates progressively from the tip to the basal ring end of the bag over the period $t/t^* = 3.2$–3.5 and yields a nearly monodisperse drop size distribution; this behavior suggests a relatively uniform bag thickness of roughly 2–3% of the initial drop diameter.
3. The distinct properties of the drops formed from the bag and from the basal ring suggest that they should be treated as separate drop populations rather than merged as in past determinations of bag breakup jump conditions, e.g. the approach developed by Hsiang and Faeth (1992). Thus, the two drop populations should be represented by separate size distribution functions with the bag drops assumed to be formed at a uniform rate over the period $t/t^* = 3.2$–3.5 and the basal ring drops assumed to be formed abruptly at $t/t^* = 5.0$, with initial drop velocities at these conditions relatively independent of drop size and approximated by corresponding parent drop velocities at the time of drop formation.
4. The parent drop experiences large acceleration rates due to the development of both large cross-sectional areas and large drag coefficients caused by drop deformation and bag formation. Phenomenological analyses provided reasonably good correlations of parent drop velocities similar to earlier considerations of jump conditions for drop velocities due to Hsiang and Faeth (1992, 1993, 1995).
5. Bag breakup causes significant temporal and spatial dispersion of drops during the breakup period, as follows: the breakup process requires a total time of $t/t^* = 5$; the cross-stream dispersion, based on the diameter of the ring axis when ring breakup is completed, amounts to roughly 7 initial drop diameters; and the streamwise dispersion when breakup is

completed involves a streamwise motion of the parent drop of roughly 50 initial drop diameters and corresponding motion of the most remote drop of roughly 60 initial diameters. These times and distances are not always small in comparison to the characteristic times and distances of dense spray processes, implying that bag breakup should be treated as a rate process, rather than by jump conditions, in some instances, in agreement with earlier findings for shear breakup due to Chou et al. (1997).

Acknowledgements

References

Chou, W-H., 1997. Temporal variation of drop properties and formation rates during secondary breakup. Ph.D. thesis, The University of Michigan, Ann Arbor, Michigan, U.S.A.

Chou, W.H., Hsiang, L-P., Faeth, G.M. 1997. Temporal properties of secondary drop breakup in the shear breakup regime. Int. J. Multiphase Flow, 23, 651–669.

Dombrowski, H., Hooper, P.C., 1962. The effect of ambient density on drop formation in sprays. Chem. Engr. Sci. 19, 291–305.

Faeth, G.M. 1997. Spray combustion phenomena. In: Twenty-Sixth Symposium (International) on Combustion. The Combustion Institute, Pittsburgh, Pennsylvania, U.S.A., pp. 1593–1612.

Faeth, G.M., Hsiang, L-P., Wu, P-K., 1995. Structure and breakup properties of sprays. Int. J. Multiphase Flow 21 (Suppl.), 99–127.

Gel'fand, B.E., Gubin, S.A., Kogarko, S.M., 1974. Various forms of drop fractionation in shock waves and their special characteristics. Inzhenerno-Fizicheskii Zhurnal 27, 119–126.

Hsiang, L-P., Faeth, G.M., 1992. Near-limit drop deformation and secondary breakup. Int. J. Multiphase Flow 18, 635–652.

Hsiang, L-P., Faeth, G.M., 1993. Drop properties after secondary breakup. Int. J. Multiphase Flow 19, 721–735.

Hsiang, L-P., Faeth, G.M., 1995. Drop deformation and breakup due to shock wave and steady disturbances. Int. J. Multiphase Flow 21, 545–560.

Lane, W.R., 1951. Shatter of drops in streams of air. Ind. Engr. Chem. 43, 1312–1317.

Lange, N.A., 1952. Handbook of Chemistry, 8th ed. Handbook Publishers, Sandusky, Ohio, p. 1134 and 1709.

Liang, P.Y., Eastes, T.W., Gharakhari, A., 1988. Computer simulations of drop deformation and drop breakup. AIAA Paper No. 88-3142.

McCarthy, M.J., Malloy, N.A., 1974. Review of stability of liquid jets and the influence of nozzle design. Chem, Engr. J. 7, 1–20.

Ranger, A.A., Nicholls, J.A., 1969. The aerodynamic shattering of liquid drops. AIAA J. 7, 285–290.

Simmons, H.C., 1977. The correlation of drop-size distributions in fuel nozzle sprays. J. Engr. Power 99, 309–319.

Smith, S.W.J., Moss, H., 1917. Mercury jets. Proc. Roy. Soc. 93, 373–393.

White, F.M., 1974. Viscous Fluid Flow. McGraw–Hill, New York.

Wu, P-K., Ruff, G.A., Faeth, G.M., 1991. Primary breakup in liquid/gas mixing layers for turbulent liquids. Atomization and Sprays 1, 421–440.

Wu, P-K., Hsiang, L-P., Faeth, G.M., 1995. Aerodynamic effects on primary and secondary breakup. Prog. Astro. Aero. 169, 247–279.

Appendix F: Dai, Z. and Faeth, G.M. (2001) Temporal Properties of Secondary Breakup in the Multimode Breakup Regime. *Int. J. Multiphase Flow* 27, 217-236.

Temporal properties of secondary drop breakup in the multimode breakup regime

Z. Dai, G.M. Faeth*

Department of Aerospace Engineering, The University of Michigan, Ann Arbor, MI 48109-2140, USA

Abstract

Secondary drop breakup due to shock wave disturbances was studied for the multimode breakup regime, emphasizing the temporal evolution of breakup for shock wave disturbances. Measurements were carried out in a shock tube using pulsed shadowgraphy and holography to observe the mechanism and outcome of breakup. Test conditions involved water and ethanol drops, liquid/gas density ratios greater than 500, Ohnesorge numbers less than 0.1 and Weber numbers of 15–150. The evolution of properties in the multimode breakup regime with increasing Weber number begins at the end of the bag breakup regime with the appearance of a plume drop at the apex of the bag at a Weber number of roughly 15, continues in a bag/plume breakup regime which involves the presence of both bag-like structures and plume drops and transitions when bags are no longer present at a Weber number of roughly 40, and ends with a plume/shear breakup regime which involves development of plume-like structures that progressively evolve into a parent drop and ligament system as the shear breakup regime is approached at a Weber number of roughly 80. Measurements over the test range provide breakup times, drop deformation properties and drag coefficients before the onset of breakup, distributions of drop liquid and resulting drop sizes for various breakup structures, drop velocities after breakup, and liquid removal rates during breakup; all these properties are provided as a function of Weber number in the multimode breakup regime. © 2001 Elsevier Science Ltd. All rights reserved.

Keywords: Drop breakup; Drop dynamics; Pulsed holography; Sprays; Atomization

---

* Corresponding author. Tel.: + 1-734-764-7202; fax: + 1-734-936-0106.

E-mail address: gmfaeth@umich.edu (G.M. Faeth).

1. Introduction

The secondary breakup of drops is an important fundamental process of sprays. For example, drops formed by primary breakup are intrinsically unstable to secondary breakup whereas secondary breakup can be the rate controlling process within dense sprays in much the same way as drop vaporization can be the rate controlling process within dilute sprays (Faeth, 1990; Wu et al., 1995). Motivated by these observations, Chou et al. (1997) and Chou and Faeth (1998) extended earlier studies of the regimes and outcomes of secondary breakup caused by shock-wave disturbances due to Hsiang and Faeth (1992, 1993, 1995) to consider the properties and the formation rates of drops resulting from secondary breakup as a function of time in the bag and shear breakup regimes. The present study seeks to extend this work to the more complex multimode breakup regime that is bounded by these regimes.

Earlier studies of secondary breakup are discussed by Giffen and Muraszew (1953), Hinze (1955), Clift et al. (1978), Krzeczkowski (1980), Wierzba and Takayama (1987, 1988), Faeth (1990), Wu et al. (1995) and Gel'fand (1996), among others. Shock-wave disturbances were considered during most earlier studies, providing a step change of the drop environment, similar to conditions experienced by drops at the end of primary breakup. The main findings of early works included the conditions required for particular deformation and breakup regimes, time required for the onset and end of primary breakup, the drag properties of deformed drops in the period before breakup begins, and the drop size and velocity distributions that resulted from the breakup process (i.e., the jump conditions). This behavior can be illustrated in terms of the characteristic shear breakup time of Ranger and Nicholls (1969), t^*, defined as follows:

$$t* = d_0 (\rho_L / \rho_G)^{1/2} / u_0 \tag{1}$$

In Eq. (1) d_0 and u_0 are the initial drop diameter and relative velocity, ρ denotes density, and the subscripts L and G denote liquid and gas properties, respectively. Liang et al. (1988) show that the average breakup time for a wide range of drop conditions is roughly $5.5t*$, which is comparable to flow residence times within the dense spray region where secondary breakup is a dominant process (Faeth, 1990; Wu et al., 1995). Put another way, the original (or parent) drop moves roughly $50d_0$ and the smallest drops formed by secondary breakup move roughly $100d_0$ during the breakup time for typical shear breakup processes (Hsiang and Faeth, 1993, 1995) which can be a significant fraction of the dense spray region. This implies that secondary breakup should be treated as a rate process rather than by jump conditions in some instances. Work to provide the temporal properties of breakup in the bag and shear breakup regimes for drop breakup in gases at standard temperature and pressure (STP), and for conditions where effects of liquid viscosity are small, was completed by Chou et al. (1997) and Chou and Faeth (1998). The present investigation continues the study of the temporal properties of secondary breakup when effects of liquid viscosity are small, by considering the multimode breakup regime. The objective is to provide a way to estimate the temporal properties of secondary drop breakup that can be used within contemporary models of sprays, see Faeth (1990, 1996) and references cited therein for descriptions of typical spray models.

The present measurements were carried out using a shock tube facility with the drop

environment during secondary breakup approximating air at STP. Single- and double-pulse shadowgraphy and holography were used to find the degree of deformation and drag coefficients prior to the onset of breakup, the size and velocity properties of drops produced by secondary breakup and the rate of liquid removal from the parent drop as a function of time. Multimode breakup is more complex than the bag and shear breakup regimes; therefore, visualization of breakup within this regime was emphasized in order to establish subregimes involving particular breakup mechanisms. Finally, earlier information about the onset and end of multimode breakup was limited so that additional measurements of this type were carried out as well. Similar to the earlier studies of the temporal properties of bag and shear breakup regimes (Chou et al., 1997; Chou and Faeth, 1998), test conditions were most representative of drop breakup within sprays having modest liquid viscosities at STP.

2. Experimental methods

2.1. Apparatus and instrumentation

The test apparatus and instrumentation will be described only briefly because it was similar to earlier work (Hsiang and Faeth, 1992, 1993, 1995; Chou et al., 1997; Chou and Faeth, 1998). The tests were carried out in a rectangular shock tube with the driven section open to the atmosphere and the side walls windowed to provide optical access. A vibrating capillary tube drop generator similar to Dabora (1967) and an electrostatic drop selection system similar to Sangiovanni and Kestin (1977) provided a stream of drops having sufficient spacing so that there was negligible drop–drop interactions within the multimode breakup regime.

Single- and double-pulse shadowgraphy and holography were used to visualize the secondary breakup process, and to measure the properties of the parent drop and the drops produced by secondary breakup as a function of time. Laser pulse times were only 7 ns, which stopped drop motion; a weaker second laser pulse allowed directional ambiguity to be resolved during velocity measurements. Objects as small as 6 μm could be observed and as small as 10 μm could be measured with 10% accuracy. Results at each test condition were averaged over no less than four realizations, considering 100–200 liquid elements, in order to find drop diameter and velocity properties. Estimated experimental uncertainties (95% confidence) are less than 15% for drop diameters and less than 20% for streamwise velocities.

2.2. Test conditions

The test conditions are summarized in Table 1. Liquid properties were obtained from Lange (1952). Parameters given in the table include the Weber number, $We = \rho_G u_0^2 d_0 / \sigma$, the Reynolds number, $Re = \rho_G u_0 d_0 / \mu_G$, and the Ohnesorge number, $Oh = \mu_L / (\rho_L d_0 \sigma)^{1/2}$ where σ is the surface tension and μ is the molecular viscosity. Earlier work has shown that dimensionless properties such as the Weber number, Ohnesorge number, density ratio, etc., provide an adequate treatment of different liquid properties for secondary breakup effects (Chou and Faeth, 1998; Chou et al., 1997; Hsiang and Faeth, 1992, 1993, 1995). As a result, only water and ethanol were used as the drop liquids in order to check effects of liquid properties. The

Weber number range was prescribed to cover the multimode breakup regime and to extend results to overlap portions of both the bag and shear breakup regimes. The Reynolds number range of the experiments is larger than the conditions where gas viscosity has a significant effect on drop drag properties, e.g., the drag coefficient, C_D, for spheres varies only in the range 0.4–0.5 for this Reynolds number range (White 1974). Shock wave Mach numbers were relatively small, less than 1.24; therefore, the physical properties of the gas surrounding the drops during breakup was nearly the same as air at STP.

3. Results and discussion

3.1. Flow visualization

Pulsed shadowgraphy flow visualization was used to help resolve the rich variation of behavior seen in the multimode breakup regime. Typical visualizations are presented in Figs. 1–7 for drops having We = 15, 20, 25, 32, 40, 50 and 81, respectively, with Oh < 0.1, which places these results at conditions where effects of liquid viscosity are negligible. Shadowgraphs are shown for each condition at various values of t/t^* during the breakup process, where t denotes time after the shock wave passes the drop. The shock wave and flow velocities behind the shock wave are directed from the top to the bottom of the shadowgraphs.

Fig. 1 is an illustration of typical shadowgraphs of behavior in the bag breakup regime with We = 15, as a baseline for behavior in the multimode breakup regime. Similar to the observations of Chou and Faeth (1998), various conditions during bag breakup can be defined as follows: the deformation period where the drop deforms from a spherical to a disk-like shape for t/t^* = 0–2.0, the bag growth period where the center of the disk deforms into a thin membrane-like bag with a much thicker basal ring surrounding its open (upstream) end for t/t^* of 2.0–3.0, the bag breakup period where the bag progressively breaks up from its closed

Table 1
Summary of test conditions[a]

Parameter	Range
Liquid	Water,[b] ethanol[c]
Initial drop diameter	0.50–0.80 mm
Liquid/gas density ratio (ρ_L/ρ_G)	680–850
Weber number (We)	15–150
Reynolds number (Re)	1500–3300
Ohnesorge number (Oh)	0.0045–0.013

[a] Air initially at 98.8 kPa and 298 ± 2 K in the driven section of the shock tube. Shock Mach numbers of 1.01–1.24. Properties of air taken at standard temperature and pressure: ρ_G = 1.18 kg/m³. μ_G = 18.5 × 10⁻⁴ kg/ms.

[b] Properties of water taken at standard temperature and pressure: ρ_L = 997 kg/m³. μ_L = 8.94 × 10⁻⁴ kg/ms, σ = 70.8 mN/m.

[c] Properties of ethanol taken at standard temperature and pressure: : ρ_L = 800 kg/m³. μ_L = 16.0 × 10⁻⁴ kg/ms, σ = 24.0 mN/m.

downstream end toward the basal ring for t/t^* of 3.0–3.5, and the ring breakup period where a series of relatively large node drops form along the ring followed by breakup of the ring into a circular array of relatively large drops to end the breakup process for t/t^* of 3.5–4.5.

Fig. 2 shows typical pictures of breakup in a portion of the multimode regime, that will be called the bag/plume breakup regime, for a water drop having $We = 20$. Similar to $We = 15$, the drop deforms to disk-like shape for t/t^* of 0–2.0 and then the bag grows with the basal ring surrounding its open end. However, as the bag grows, a so-called plume drop also grows from the center of the bag; this plume drop can be seen clearly from the picture at $t/t^* = 2.7$. The plume drop is not connected to the basal ring. The existence of plume drop is characteristic of multimode (bag/plume) drop breakup. Measurements reveal that bag/plume breakup starts at roughly $We = 18$. At this condition, the bag breaks up from $t/t^* = 2.7$–3.5. The plume drop separates from the bag at $t/t^* = 3.0$ due to bag breakup. Also note that at $t/t^* = 3.5$, a large drop detaches from the plume drop, which will be called core drop. The basal ring breakup period is $t/t^* = 3.5$–3.8. Then the plume drop breaks up which ends the breakup process.

Fig. 3 shows typical pictures of multimode (bag/plume) breakup for a water drop having $We = 25$. Similar to $We = 20$, the drop deforms to a disk-like shape for $t/t^* = 0$–2.0. At $t/t^* = 2.3$, the bag, basal ring and plume drop can be seen clearly. However the sizes of the bag and

| INITIAL STATE
t/t*=0.0 | DROP DEFORMED
0.5 | DROP FLATTENED
1.5 | BAG FORMING
2.0 |

| BAG
t/t*=2.5 | BAG BREAKUP
3.0 | RING BREAKUP
3.5 | END OF BREAKUP
4.1 |
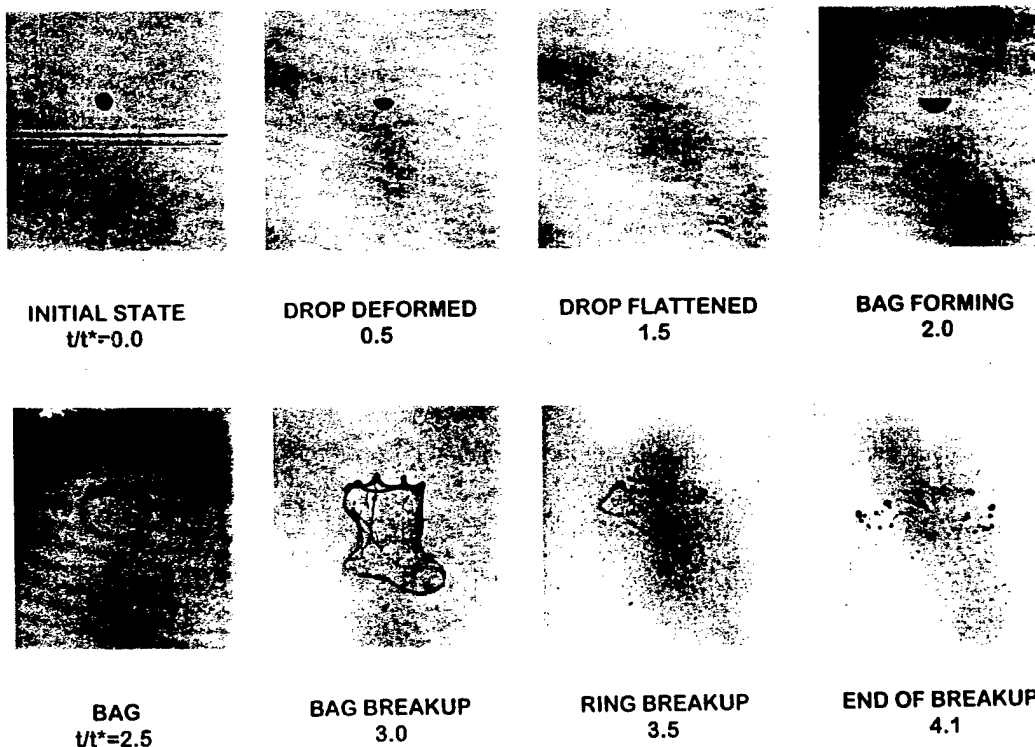
Fig. 1. Pulse shadowgraphs of secondary breakup in the bag breakup regime (water, $We = 15$, $Oh = 0.0045$).

basal ring are much smaller, while the size of plume drop has increased, compared to conditions seen in Fig. 2. The bag begins to break up at $t/t^* = 2.5$ and ends breakup before $t/t^* = 3.0$, which is sooner than observations at smaller We. The basal ring subsequently breaks up and leaves the plume drop at $t/t^* = 3.5$. The plume then undergoes Rayleigh breakup which is finished at $t/t^* = 5.7$. Note that the core drop forms at $t/t^* = 5.0$ and its shape is variable but more or less spherical.

Fig. 4 shows pictures of multimode (bag/plume) breakup at $We = 32$. The bag finishes breakup sooner than at smaller We, before $t/t^* = 2.3$. The ring and bag size continue to become smaller and the liquid volume inside the plume drop increases dramatically. The core drop forms after the plume finishes breakup, which is different from $We = 20$ and 25, where the core drop forms before the plume finishes breakup. The core drop is not spherical. Contrary to the expectation of deforming into a spherical core drop without any further breakup, the core drop undergoes Rayleigh breakup and finishes breakup at $t/t^* = 7.3$; therefore, the total breakup time is increased by roughly 60% compared to the breakup times in the bag and shear breakup regimes.

Fig. 5 shows pictures of breakup in a portion of the multimode regime, that will be called the plume/shear breakup regime, for a water drop having $We = 40$. At this condition, the bag

|				
INITIAL STATE	DROP DEFORMED	DROP FLATTENED	BAG FORMING	BAG
t/t*=0.0	0.5	1.5	2.0	2.5
PLUME INSIDE BAG	BAG BREAKUP	RING BREAKUP	PLUME BREAKUP	END OF BREAKUP
t/t*=2.7	3.0	3.5	3.8	4.2
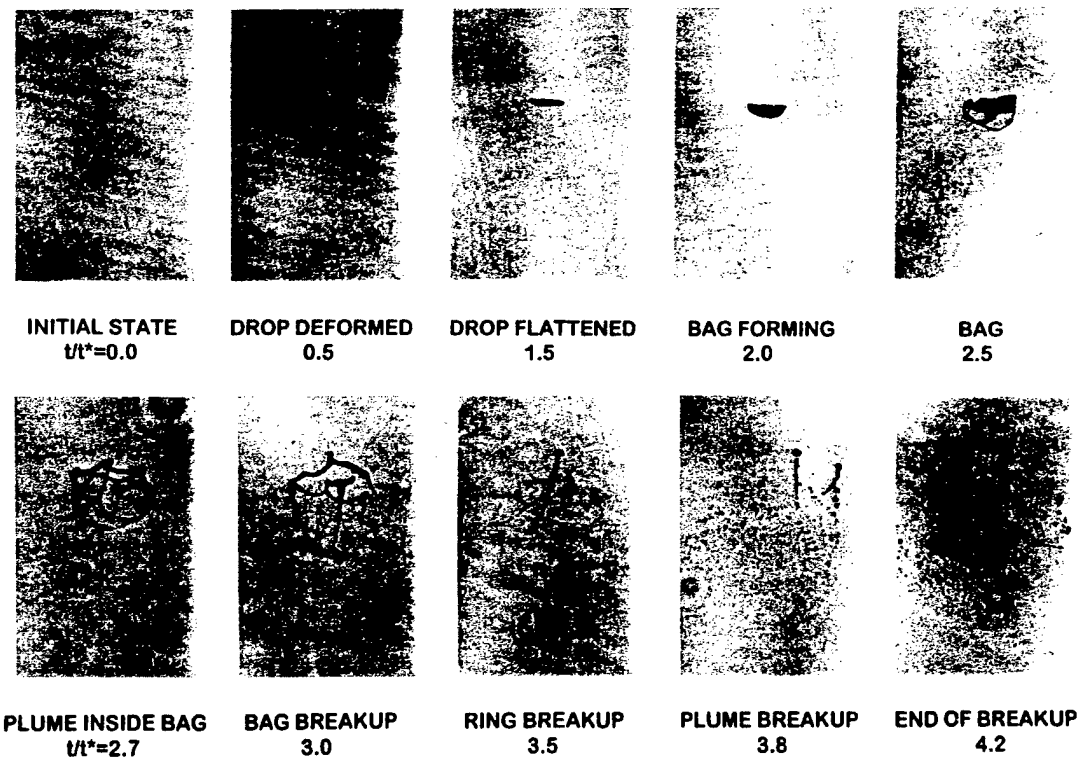
Fig. 2. Pulse shadowgraphs of secondary breakup in the bag/plume breakup regime (water, $We = 20$, $Oh = 0.0045$).

and ring do not appear any longer. The plume breakup process also differs from behavior at smaller *We* in the bag/plume breakup regime because the core drop does not detach from the plume; instead, the plume becomes simply an appendage of the core drop and drops are continuously removed from the core-drop/plume complex in a manner resembling the stripping mechanism of the shear breakup regime. Thus, while these conditions involve the presence of a plume, they have many of the characteristics of shear breakup, suggesting the plume/shear breakup regime designation. Finally, breakup of the core-drop/plume complex is relatively slow at this condition with the entire breakup process not complete until $t/t^* = 7.5$, which is the longest breakup time in the multimode breakup regime. This associated maximum breakup time, along with the disappearance of the bag and a detached plume, provide other reasons to designate the conditions of Fig. 5 as the onset of a new plume/shear breakup regime.

Fig. 6 shows typical pictures of multimode (plume/shear) breakup of a water drop having $We = 50$. The main difference between Figs. 5 and 6 as We increases in the plume/shear breakup regime is that the plume becomes less prominent. This trend continues with increasing We throughout the remainder of the plume/shear breakup regime. Another trend in this regime is a progressive reduction of t/t^* at the end of breakup with increasing We, as the size of the core-drop/plume complex continues to decrease.

Fig. 7 shows typical pictures at the onset of the shear breakup regime for an ethanol drop

INITIAL STATE	DROP DEFORMED	DROP FLATTENED	BAG/PLUME FORMING	BAG BREAKUP
t/t^*=0.0	0.5	1.5	2.3	2.5

| RING BREAKUP	END OF RING BREAKUP	ONSET OF PLUME BREAKUP	PLUME BREAKUP	END OF BREAKUP
t/t^*=3.0	3.5	4.0	5.0	5.7
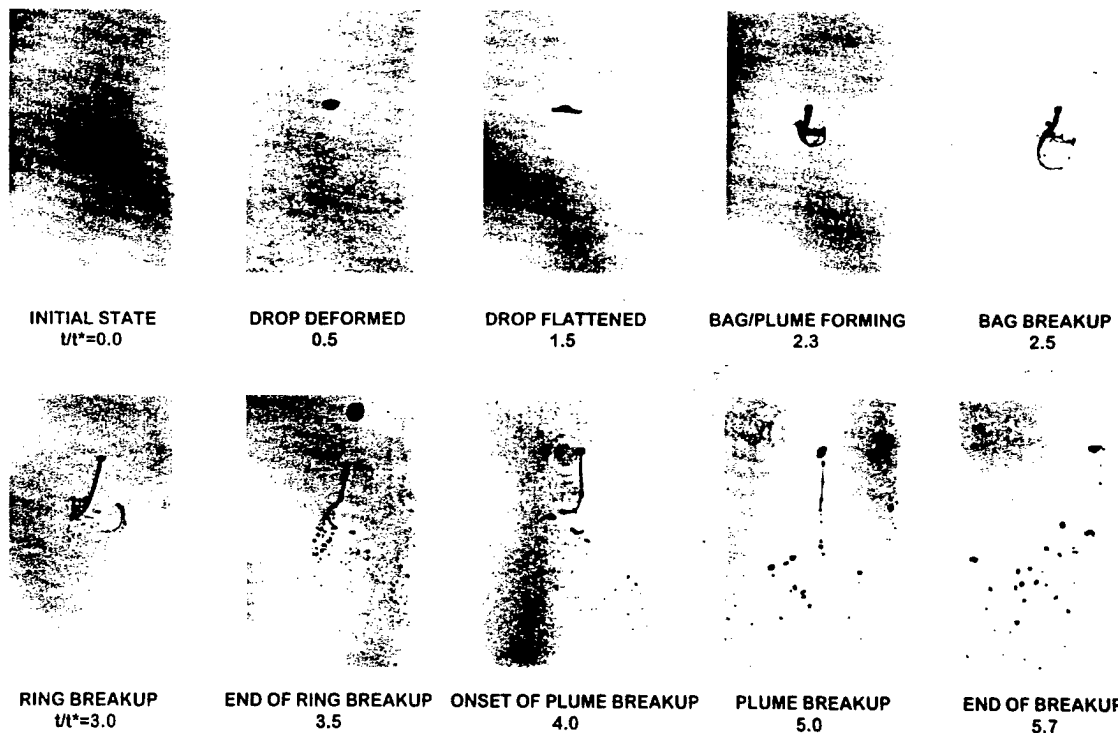
Fig. 3. Pulse shadowgraphs of secondary breakup in the bag/plume breakup regime (water, $We = 25$, $Oh = 0.0045$).

with $We = 80$. At this condition, a plume is no longer present with drops simply being stripped from the periphery of the flattened core drop. In addition, the increased breakup time due to the relatively slow breakup of the core-drop/plume complex has ended, and t/t^* has returned to values associated with the bag and shear breakup regimes, providing another reason to designate a transition to shear breakup at this condition.

3.2. Breakup times

Times of the onset and end of breakup are plotted as a function of We, for $Oh < 0.1$, in Fig. 8. These results include measurements of Hsiang and Faeth (1992), Chou et al. (1997), Chou and Faeth (1998) and the present investigation for $We = 15$–150, which spans the range from bag to well into the shear breakup regime. The breakup regimes that were described based on Figs. 1–7 are also marked on the plots with bag breakup observed for $We = 13$–18, multimode breakup for $We = 18$–80 and shear breakup for We greater than 80. In addition, the multimode breakup regime is divided into two subregimes as just discussed: bag/plume breakup for $We = 18$–40 and plume/shear breakup for $We = 40$–80. The agreement among the various measurements illustrated in Fig. 8 is seen to be very good.

The onset of breakup at small We in the bag breakup regime occurs for t/t^* of roughly 3.0.

| INITIAL STATE $t/t^*=0.0$ | DROP DEFORMED 1.0 | DROP FLATTENED 1.5 | BAG/PLUME 2.0 | ONSET OF BREAKUP 2.3 | RING BREAKUP 2.8 |

| PLUME BREAKUP $t/t^*=3.3$ | BREAKUP 3.8 | BREAKUP 4.5 | BREAKUP 5.5 | BREAKUP 6.0 | END OF BREAKUP 7.3 |
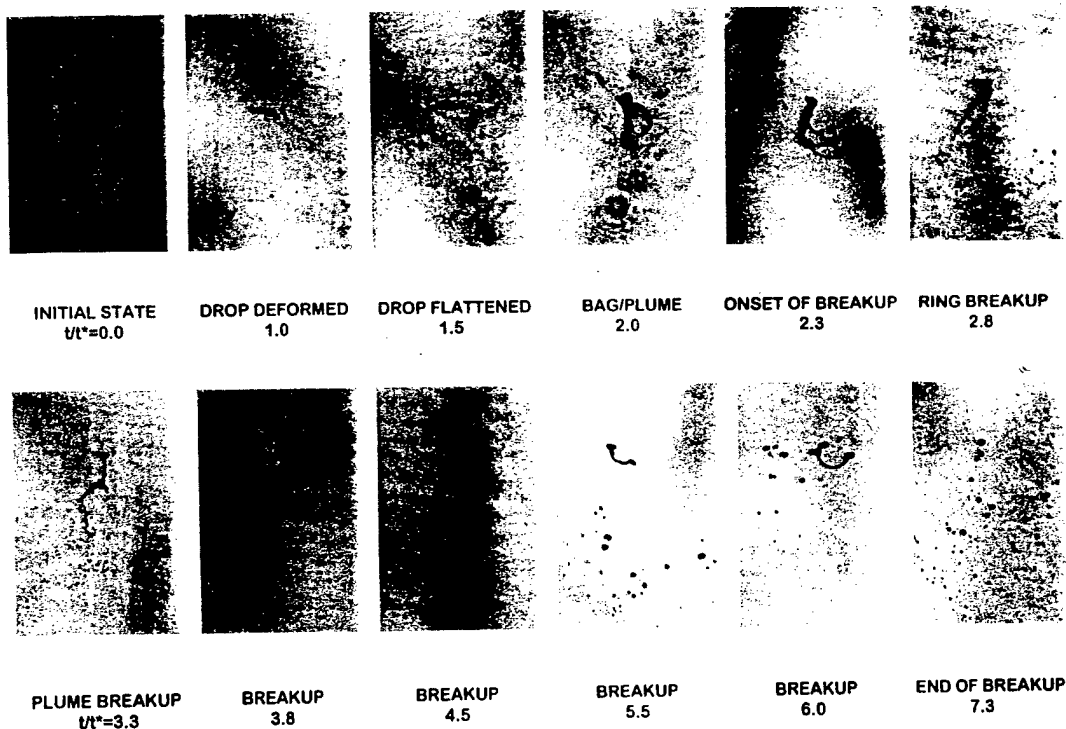
Fig. 4. Pulse shadowgraphs of secondary breakup in the bag/plume breakup regime (water, $We = 32$, $Oh = 0.0045$).

Onset times progressively decrease throughout the bag/plume breakup regime, however, before reaching values of t/t^* = 2.0 at larger values of We in the plume/shear and shear breakup regimes.

The end of breakup in the bag breakup regime occurs for t/t^* of roughly 4.0. Then, t/t^* at the end of breakup progressively increases with increasing We within the bag/plume breakup regime, reaching a maximum of t/t^* of roughly 7.5 at We = 40 where breakup makes the transition to the plume/shear breakup regime. Finally, t/t^* at the end of breakup progressively decreases with increasing We within the plume/shear breakup regime, reaching t/t^* at the end of breakup of roughly 5.0 at the onset of the shear breakup regime at We = 80. Hassler (1970) has reported similar behavior for the end of breakup over this Weber number range. It appears that the main reason for the local maximum of t/t^* at the end of breakup is the development of the large core-drop/plume complex and the relatively slow breakup of this complex by what appears to be a mainly relatively passive Rayleigh breakup process because the plume is sheltered to some extent by the core drop.

3.3. Drop deformation properties

The properties of drops in the period prior to the onset of breakup — drop deformation and drag coefficient properties — will be considered next. These properties are of interest because
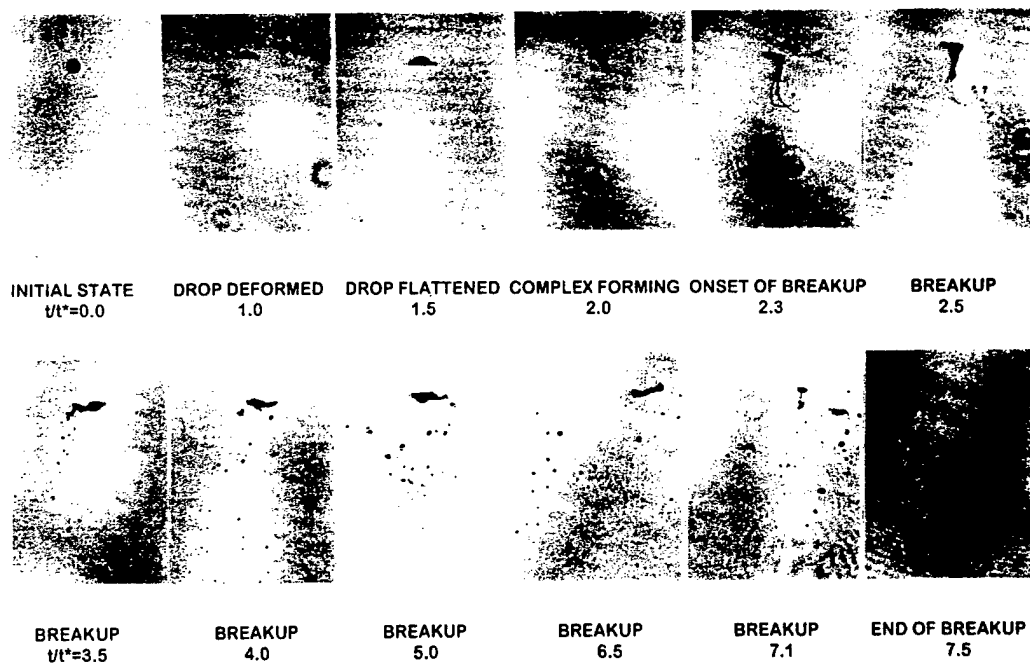

Fig. 5. Pulse shadowgraphs of secondary breakup in the plume/shear breakup regime (water, We = 40, Oh = 0.0045).

they can be used to evaluate numerical simulations of drop dynamics and as a crucial first step toward gaining a better understanding of secondary drop breakup.

Present measurements of maximum cross stream diameters of drops at the onset of secondary drop breakup, D_{Lmax}, are plotted as a function of the Weber number in Fig. 9. Earlier measurements of this property due to Hsiang and Faeth (1992) are also illustrated on the plot. Present measurements yield little variation of the maximum cross stream drop diameter as the Weber number is varied, yielding an average value of $D_{Lmax}/d_0 = 2.15$ in the multimode breakup regime. The results of Hsiang and Faeth (1992) agree with present measurements within experimental uncertainties but exhibit a consistent trend toward increasing D_{Lmax}/d_0 with increasing Weber number. Much of the increase in the Hsiang and Faeth (1992) correlation comes about, however, by fitting data extending from the bag breakup until well into shear breakup regime, e.g., $We < 100$.

The present measurements of the cross stream and streamwise dimensions of the deformed drop, D_L and D_H, are plotted as a function of normalized time, t/t^*, in Fig. 10. This plot is arranged as the normalized cross stream and streamwise distortions, $D_L - d_0$ and $d_0 - D_H$, as suggested by Hsiang and Faeth (1992). The correlation of cross stream distortion due to Hsiang and Faeth (1992) is also shown in the plot. This expression involves their measurements

| INITIAL STATE | DROP DEFORMED | DROP FLATTENED | COMPLEX FORMED | ONSET OF BREAKUP |
| t/t*=0.00 | 0.75 | 1.50 | 2.25 | 2.50 |

| BREAKUP | BREAKUP | BREAKUP | BREAKUP | END OF BREAKUP |
| t/t*=3.00 | 4.00 | 5.00 | 6.40 | 7.40 |
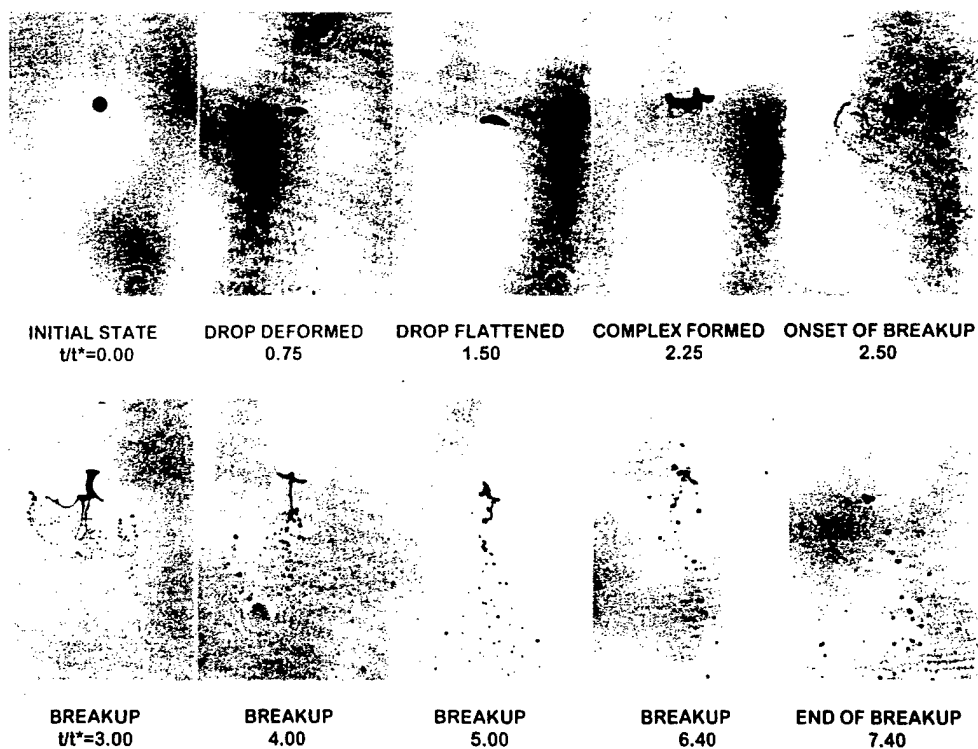
Fig. 6. Pulse shadowgraphs of secondary breakup in the plume/shear breakup regime (water, $We = 50$, $Oh = 0.0045$).

| INITIAL STATE | DROP DEFORMED | LIGAMENT FORMING | ONSET OF BREAKUP |
| t/t*=0.00 | 0.75 | 1.40 | 1.75 |

| BREAKUP | BREAKUP | BREAKUP | END OF BREAKUP |
| t/t*=2.75 | 3.75 | 4.75 | 5.75 |
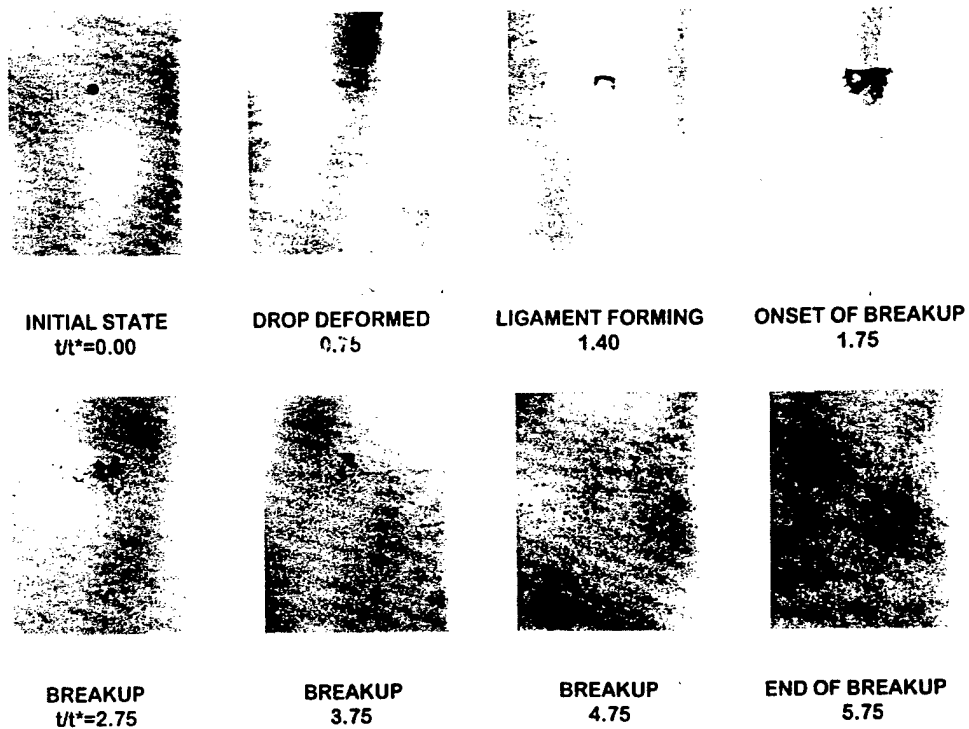
Fig. 7. Pulse shadowgraphs of secondary breakup in the shear breakup regime (ethyl alcohol, $We = 81$, $Oh = 0.0126$).
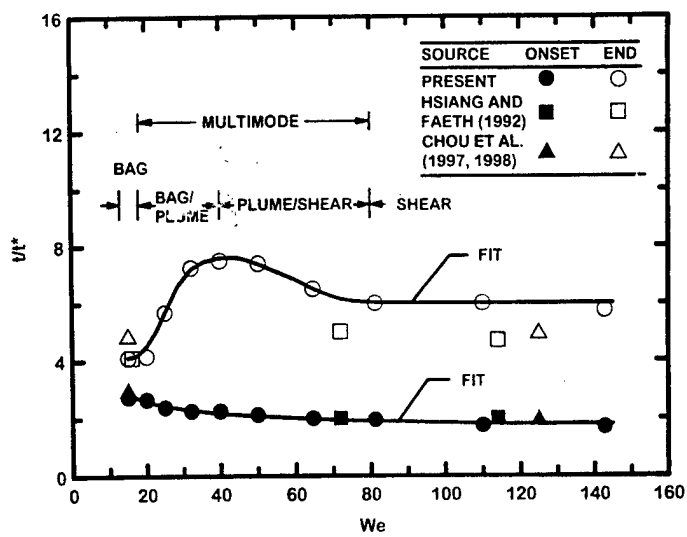

Fig. 8. Times of onset and end of breakup as a function of We. Measurements of Hsiang and Faeth (1992), Chou et al. (1997), Chou and Faeth (1998) and the present investigation.
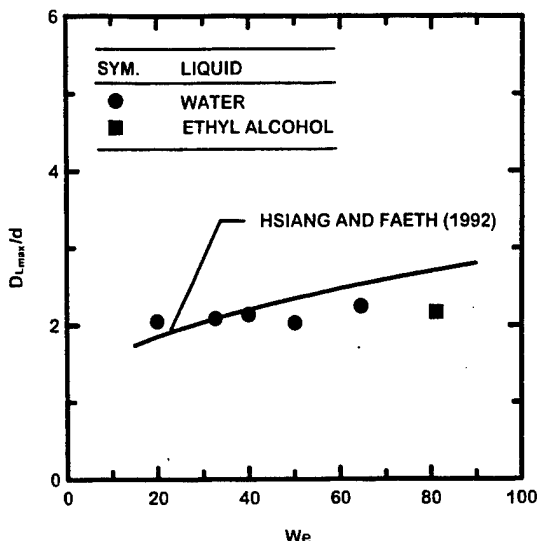
Fig. 9. Maximum cross stream dimension of the drop at the onset of breakup. Measurements of Hsiang and Faeth (1992) and the present investigation.
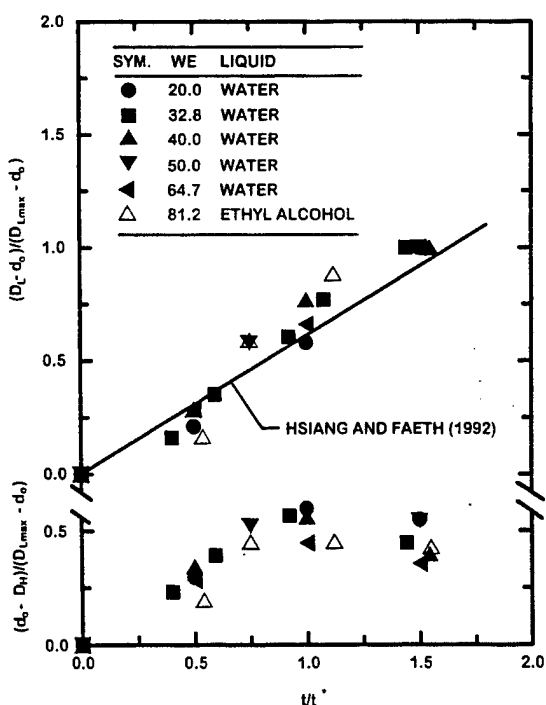

Fig. 10. Evolution of drop deformation as a function of time prior to the onset of breakup. Measurements of Hsiang and Faeth (1992) and the present investigation.

115

for We of 4–21, those of Engel (1958) for We of 10^3–10^4, those of Ranger and Nicholls (1969) for We of 10^3–10^5, and those of Wierzba and Takayama (1988) for We of 10^2–10^4. There is a tendency for the measurements at large Weber numbers, $We > 10^2$, to be consistently above the correlation of Hsiang and Faeth (1992) and another expression probably should be used for these results. Present measurements, however, are in good agreement with those of Hsiang and Faeth (1992) at comparable Weber numbers and can be correlated quite well by their expression.

3.4. Drop drag coefficient

Similar to past work by Hsiang and Faeth (1992), the drop/drag coefficient is defined in terms of the local relative velocity, $u_\infty - u_p$, where u_∞ is the local gas velocity and u_p is the local drop velocity, and the cross stream dimensions of the drop, as follows:

$$C_D = D / \left(\pi \rho_G D_L^2 (u_\infty - u_p)^2 / 8 \right) \qquad (2)$$

where D is the local drag force on the drop. Drop/drag properties were found by measuring the motion of the centroid of the drop in the uniform flow field behind the shock wave. This approach is only approximate because it neglects redistribution of drop mass due to deformation but the error is small because liquid velocities are small, of the order of 1% of the initial relative velocity. In addition, pressure gradient forces were neglected because the flow behind the shock wave was uniform and virtual mass and Basset history forces were neglected because $\rho_L/\rho_G \gg 1$. The final formulation used to compute C_D under these assumptions can be found in Hsiang and Faeth (1992); the experimental uncertainties (95% confidence) in present
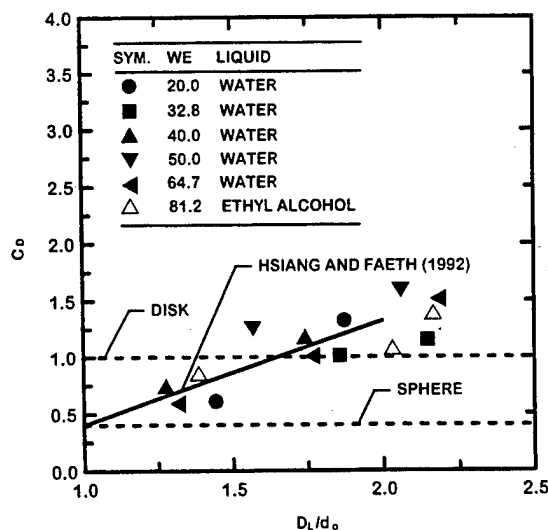

Fig. 11. Evolution of drop/drag coefficient as a function of time period prior to the onset of breakup. Measurements of Hsiang and Faeth (1992) and the present investigation.

determinations of C_D are less than 30%, mainly governed by uncertainties in locating the centroid of the deforming drops.

The experiments to find C_D involved the deformation period of the drops prior to the onset of breakup, $Oh < 0.1$ and Re of 1000–3300 (counting data drawn from earlier studies) where effects of Re on drop drag are expected to be small (White, 1974). Thus, C_D was largely a function of degree of deformation of the drop, D_L/d_0, and is correlated in this manner following Hsiang and Faeth (1992), as illustrated in Fig. 11. Measurements of C_D for solid spheres and thin disks, drawn from White (1974) at comparable Re, as well as an earlier correlation of measurements of Hsiang and Faeth (1992) for similar conditions as the present investigation, are also shown in the plot. Present measurements agree very well with the results of Hsiang and Faeth (1992). Quite plausibly, the results exhibit transition from findings similar to round spheres for $D_L/d_0 \approx 1$ to results typical of thin disks for $D_L/d_f \approx 2$. Combined with the increase of the cross stream diameter of the drop, the results of Figs. 9 and 11 indicate that drop/drag forces increase by a factor of roughly 16 between the start and end of the drop deformation period, with the corresponding rapid increase of drop acceleration providing ample reason for the onset of drop breakup.

3.5. Volume fractions of bag, ring, plume and core drops

The volume fractions of the bag, ring, plume and core drops are plotted as a function of the Weber number in Fig. 12, for $Oh < 0.1$. The volume of the ring was determined similarly to Chou and Faeth (1998) for bag breakup, from the dimensions of the ring at the end of breakup of the bag. The plume also had a reasonably regular shape so that its volume was
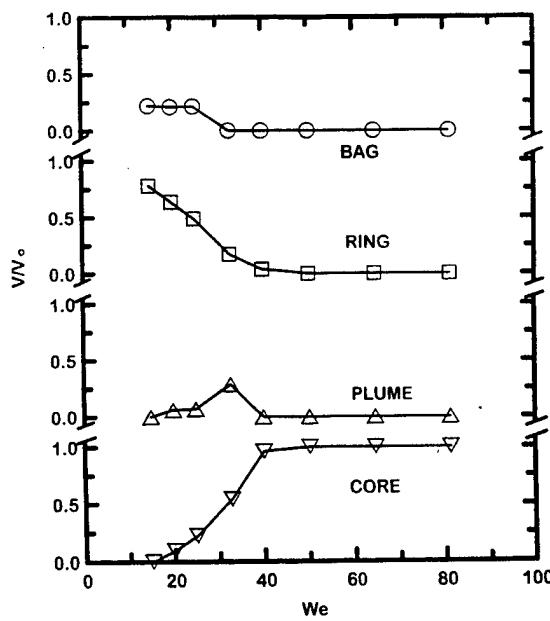

Fig. 12. Volumes of the bag, ring, plume and core drops as a function of We.

computed from its projected image assuming that it had a round cross section. The volume of the core drop was found by measuring the sizes of all drops formed from the core drop and summing their volumes; this approach was required because the core drop was rather irregular in shape for $We > 33$. Finally, the volume of the bag drops was found by difference, given the initial drop volume and the volume of the ring, plume and core drops. Experimental uncertainties in the maximum volumes of the ring and plume drops (95% confidence) are less than 10% at their maximum volume conditions, increasing inversely proportional to volume for smaller volumes. The uncertainties for the core drop at volume fractions less than 80% are comparable to the ring and plume drops with this uncertainty becoming negligible for $We > 40$, where all the drops originate from the core drop, similar to the shear breakup regime.

The results plotted in Fig. 12 at a value of $We = 15$ imply 75% of the drop volume in the ring, 25% in the bag and negligible volumes associated with the plume and the core. This finding is in good agreement with an early determination of ring volume due to Lane (1951) who also finds 75% of the volume associated with the ring at this condition. On the other hand, Chou and Faeth (1998) find 56% of the drop volume associated with the ring and 44% with the bag at this condition; unfortunately, repeated testing was unable to resolve the discrepancy. The volume of the bag and the ring progressively decrease with increasing We; with both elements finally disappearing at $We = 40$, where the bag/plume breakup regime ends. Over the same We range, the liquid volume fraction in the plume increases at first to reach a maximum of 25% at $We = 33$ and then decreases to zero once again at $We = 40$. The volume fraction of the core drop also progressively increases with increasing We within the bag/plume regime and then remains constant at 100% in the plume/shear breakup regime for $We > 40$.
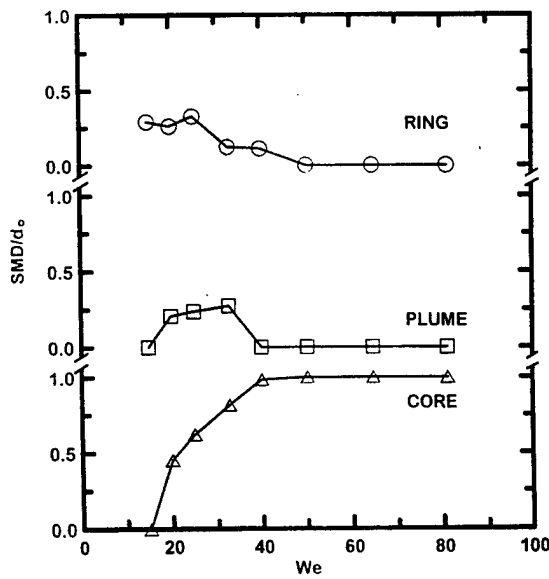

Fig. 13. SMD of the ring, plume and core drops as a function of We.

3.6. Sizes of ring, plume and core drops

The sizes of the ring, plume and core drops are plotted as a function of *We* in Fig. 13 for *Oh* < 0.1. These sizes are given by SMD/d_0, with each of these drop groups best treated as being approximately monodisperse. The sizes of bag drops were small and were not resolved during the present measurements; the results of Chou and Faeth (1998) for bag breakup suggest SMD/d_0 of 3–5% and the present bag drops were either comparable to or smaller than these sizes. At *We* = 15 in the bag breakup regime, $SMD/d_0 \approx 0.27$ which agrees with the measurements of Chou and Faeth (1998) at these conditions. The size of the ring drops progressively decreases with increasing *We*, however, reaching zero at *We* = 40 which corresponds to the end of the bag/plume breakup regime. The SMD of plume drops increases with increasing *We* in the bag/plume region for a time, reaching a maximum of SMD/d_0 = 0.30 at *We* = 33 where the volume of the plume reaches a maximum as well. Plume drop sizes subsequently decrease, reaching zero at *We* = 40 which corresponds to the end of the bag/ plume regime. Thus, the maximum sizes of the ring and the plume drops are roughly the same. However, the number of ring drops is much larger than the number of plume drops (which is typically near ten for a single drop breakup) due to the larger volume fractions of the ring at small *We* (see Fig. 12). The core drop first appears at the onset of the bag/plume breakup regime and progressively increases in size with increasing *We* in this regime; by definition, however, SMD/d_0 = 1 for the core drop in the plume-shear breakup regime for *We* > 40.

3.7. Velocities of parent and post breakup drops

The velocities of parent and post breakup drops, u_p and u, are plotted as a function of normalized time in Fig. 14. Chou and Faeth (1998) present simplified analysis that proves to be
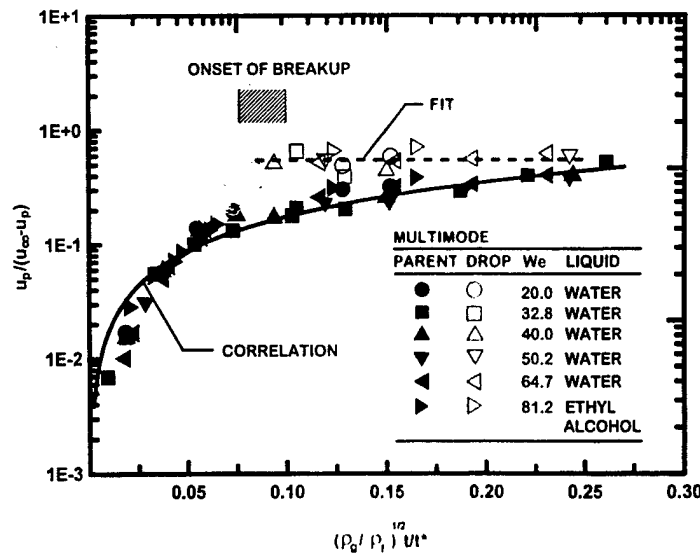

Fig. 14. Velocities of parent and post breakup drops as a function of time during breakup.

helpful in correlating drop velocities. The parent drop velocities for bag breakup from Chou and Faeth (1998) and the present times of onset of breakup, are plotted in Fig. 14 for reference purposes, based on the Chou and Faeth (1998) analysis. For this figure, the parent drop is defined as all the liquid that will continue to break up as time increases. Before the onset of breakup, the parent drop velocity is taken to be the velocity of the centroid of the entire drop. After the onset of breakup, the parent drop velocity is taken to be the velocity of the leading edge of the parent drop. Similar to past observations of bag and shear breakup (Chou and Faeth 1998; Hsiang and Faeth 1992, 1993, 1995), the parent drop exhibits considerable acceleration during the breakup period, due to the growth of the cross stream dimensions of the deformed parent drop as a result of deformation and bag formation. The acceleration decreases during the latter stages of breakup because cross stream dimensions decrease once again. Near the onset of breakup, however, the velocities of post breakup drops are larger than the parent drop because these drops are small and tend to accommodate to the gas velocity sooner than the parent drop. Similar to the observations of Chou and Faeth (1998) in the bag breakup regime, the absolute and relative velocities of the parent drop, u_p and $u_\infty - u_p$, tend to be comparable, which implies a reduction in the relative velocity of the parent drop by roughly 50% during the time of breakup, which is quite substantial.

3.8. Volume removal rates from the parent drop

Present measurements of the cumulative volume percentage of liquid removed from the parent drop are plotted in Fig. 15 as a function of normalized time. Correlations also shown in the plot include results for shear breakup due to Chou et al. (1997); results for bag breakup due to Chou and Faeth (1998) and a correlation taken as the mean of present measurements of multimode breakup. The results for bag breakup exhibit step-like changes due to rapid
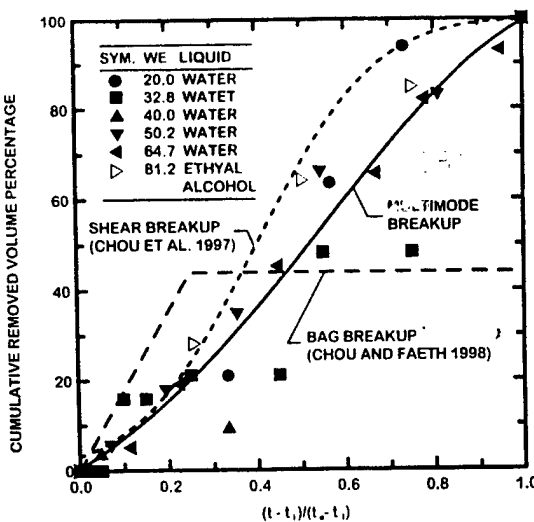

Fig. 15. Cumulative volume removed from the parent drop as a function of time during breakup. Measurements of Chou et al. (1997), Chou and Faeth (1998) and the present investigation.

breakup of bag drops and nearly simultaneous breakup of ring drops, see Chou and Faeth (1998). Results for shear breakup are more continuous due to the stripping of drops from the parent drop, see Chou et al. (1997). Present results for multimode breakup are intermediate between the behaviors of the bag and shear breakup processes, which is quite reasonable. The differences between these limits, however, show that it is impossible for behavior during the multimode breakup to collapse to a single curve. Nevertheless, the correlation shown in the figure should still be useful for modeling and simulating spray structure.

4. Conclusions

The present investigation considered the temporal properties of secondary drop breakup due to shock-wave disturbances in the multimode breakup regime for $Oh < 0.1$; see Table 1 for a detailed specification of the present test range. The major conclusions of the study are as follows:

1. With increasing Weber numbers, the multimode breakup regime begins at the end of the bag breakup regime at $We = 18$ and ends at the start of the shear breakup regime at $We = 80$. The multimode breakup regime can be subdivided into a bag/plume breakup regime for $We = 18$–40 and a plume/shear breakup regime for $We = 40$–80 with the transition between these regimes fixed by the disappearance of bag and ring structures and the attainment of a maximum breakup time.
2. With increasing We in the range 18–80, t/t^* at the onset of breakup decreases from a value of 3.0 to a value of 2.0 at the onset of shear breakup. The end of breakup has values of $t/t^* = 4.0$ and 5.0 at the end of bag breakup and the beginning of shear breakup but reaches a maximum value of t/t^* of 7.5 at the transition between the bag/plume and plume/shear regimes at $We = 40$ because Rayleigh breakup of the plume is slow.
3. Drop deformation and drag properties prior to the onset of breakup appear to be relatively universal for We of 13–150. The drop/drag coefficient transitions from values similar to spheres to values similar to thin disks as the cross stream dimension of the drop D_{Lmax}/d_0 varies in the range 1.0–2.0 and the onset of breakup is approached. These two effects cause drop/drag forces to increase 16:1 in the deformation period for present test conditions, with associated drop accelerations leading to breakup onset.
4. Liquid volume fractions associated with the bag, ring, plume and core drops have been found for We of 18–80, and the sizes of ring, plume, and core drops have been found for the same range of conditions. The sizes of drops formed by breakup of the bag and the core drops were not found but should approximate the known behavior in the bag and shear breakup regimes until specific information becomes available. The velocities of the parent drop were similar to behavior observed by Chou and Faeth (1998) for bag breakup, whereas, the velocities of post breakup drops exhibited continuous variations with increasing t/t^* and did not indicate any sudden changes at transitions to new breakup regimes.
5. The mass removal rates of liquid from the parent drop resembles behavior in the bag breakup regime at small We and behavior in the shear breakup regime at large We. The differences between these behaviors are not large compared to experimental uncertainties,

however, yielding a reasonable correlation of liquid removal rates for spray modeling purposes.

Acknowledgements

References

Chou, W.-H., Faeth, G.M., 1998. Temporal properties of secondary drop breakup in the bag breakup regime. Int. J. Multiphase Flow 24, 889–912.

Chou, W.-H., Hsiang, L.-P., Faeth, G.M., 1998. Temporal properties of drop breakup in the shear breakup regime. Int. J. Multiphase Flow 23, 651–669.

Clift, R., Grace, J.R., Weber, M.E., 1978. Bubbles, Drops and Particles, 26. Academic Press, New York, pp. 339–347.

Dabora, E.K., 1967. Production of monodisperse sprays. Rev. Sci. Instru 38, 502 506.

Engel, O.G., 1958. Fragmentation of waterdrops in the zone behind an air shock. J. Res. Natl. Bur. Stds 60, 245–280.

Faeth, G.M., 1990. Structure and atomization properties of dense turbulent sprays. In: Twenty-Third Symposium (International) on Combustion. The Combustion Institute, Pittsburgh, 1345 1352.

Faeth, G.M., 1996. Spray combustion phenomena. In: Twenty-Sixth Symposium (International) on Combustion. The Combustion Institute, Pittsburgh, 1593–1612.

Gel'fand, B.E., 1996. Droplet breakup phenomena in flows with velocity lag. Prog. Energy Combust. Sci. 22, 201–265.

Giffen, E., Muraszew, A., 1953. The Atomization of Liquid Fuels. Chapman & Hall, London.

Hassler, G., 1970. Breakup of large water drops under the influence of aerodynamic forces in a steady stream of steam at subsonic velocity. In: Third International Conference on Rain Erosion and Related Phenomena, Hampshire, England.

Hinze, J.O., 1955. Fundamentals of the hydrodynamic mechanism of splitting in dispersion processes. AIChE. J. 1, 289–295.

Hsiang, L.-P., Faeth, G.M., 1992. Near-limit drop deformation and secondary breakup. Int. J. Multiphase Flow 18, 635–652.

Hsiang, L.-P., Faeth, G.M., 1993. Drop properties after secondary breakup. Int. J. Multiphase Flow 19, 721–735.

Hsiang, L.-P., Faeth, G.M., 1995. Drop deformation and breakup due to shock wave and steady disturbances. Int. J. Multiphase Flow 21, 545–560.

Krzeczkowski, S.A., 1980. Measurements of liquid droplet disintegration mechanism. Int. J. Multiphase Flow 6, 227–239.

Lane, W.R., 1951. Shatter of drops in streams of air. Ind. Engr. Chem. 43, 1312 and 1317.

Lange, N.A., 1952. Handbook of Chemistry. 8th ed. Handbook Publishers, Sandusky, OH. pp. 1134 and 1709.

Liang, P.Y., Eastes, T.W., Gharakhari, A. 1988. Computer simulations of drop deformation and drop breakup. AIAA Paper No. 88-3142.

Ranger, A.A., Nicholls, J.A., 1969. The aerodynamic shattering of liquid drops. AIAA J. 7, 285–290.

Sangiovanni, J., Kestin, A.S., 1977. A theoretical and experimental investigation of the ignition of fuel droplets. Combust. Sci. Tech. 6, 59–70.

White, F.M., 1974. Viscous Fluid Flow. McGraw-Hill, New York.

Wierzba, A., Takayama, K., 1987. Experimental investigation on liquid droplet breakup in a gas stream. Rept. Inst. High Speed Mech. (Tohoku Univ.) 53 (382), 1–99.

Wierzba, A., Takayama, K., 1988. Experimental investigation of the aerodynamic breakup of liquid drops. AIAA J. 26, 1329–1335.

Wu, P.-K., Hsiang, L.-P., Faeth, G.M., 1995. Aerodynamic effects on primary and secondary breakup. Prog. Astro. Aero. 169, 247–279.

Appendix G: Mazallon, J., Dai, Z. and Faeth, G.M. (1999) Primary Breakup of Nonturbulent Round Liquid Jets in Gas Crossflows. *Atom. Sprays* 9, 291-312.

PRIMARY BREAKUP OF NONTURBULENT ROUND LIQUID JETS IN GAS CROSSFLOWS

J. Mazallon, Z. Dai, and G. M. Faeth
Department of Aerospace Engineering, The University of Michigan, Ann Arbor, Michigan, USA

An experimental investigation of primary breakup of nonturbulent round liquid jets in gas crossflows is described. Pulsed shadowgraph measurements of jet primary breakup regimes, jet deformation properties, time of onset of primary breakup, and liquid column and liquid surface disturbance wavelengths were obtained for air crossflows at normal temperature and pressure. The test range included crossflow Weber numbers of 0–200, liquid jet Weber numbers of 0–1,600,000, liquid jet Reynolds numbers of 0–800,000, liquid/gas momentum ratios of 100–8000, liquid/gas density ratios of 700–1100, and Ohnesorge numbers of 0.00006–0.3. The results suggest qualitative similarities between the primary breakup of nonturbulent round liquid jets in crossflows and the secondary breakup of drops, with relatively little effect of the liquid/gas momentum ratio over the present test range. Effects of liquid viscosity were also small for Ohnesorge numbers less than 0.1, but larger Ohnesorge numbers modified primary breakup because unusually long ligaments developed that also are seen during the secondary breakup of drops.

INTRODUCTION

The deformation and primary breakup of nonturbulent round liquid jets in subsonic gaseous crossflows were studied experimentally. The investigation was motivated by applications of spray breakup in crossflow to air-breathing propulsion systems, liquid rocket engines, diesel engines, spark ignition engines, and agricultural sprays, among others. Methods of injector design and experimental observations were similar to past work in this laboratory; see Dai et al. [1] and references cited therein.

Earlier studies of round liquid jets in gaseous crossflows were recently reviewed by Wu et al. [2] and Vich and Ledoux [3]; therefore, the present discussion of earlier work is brief. Past research on liquid jets in crossflows has focused mainly on penetration lengths and jet/spray plume trajectories for various liquid properties, liquid jet properties, and crossflow properties [2–15]. The primary liquid breakup properties of liquid jets in crossflow have recently received more attention, however, with both Wu et al. [2] and Vich and Ledoux [3] reporting similarities between the breakup properties of round liquid jets in gas crossflows and the secondary breakup of drops. Wu et al. [2] mention bag, multimode, and shear breakup along the liquid column in addition to breakup of the entire liquid column

NOMENCLATURE

d_f	frontal dimension of the liquid jet	u	streamwise velocity
d_{inj}	injector diameter	We	crossflow Weber number (= $\rho_\infty d_n u_\infty^2/\sigma$)
d_n	initial liquid jet diameter	We_j	jet Weber number (= $\rho_j d_n u_j^2/\sigma$)
d_{eqt}	equivalent jet diameter (= $d_f d_s$)$^{1/2}$	y	cross-stream distance from edge of air jet
d_s	cross-stream dimension of the liquid jet	λ_c, λ_s	column and surface wavelength
e	ellipticity (= d_f/d_s)	μ	molecular viscosity
Oh	Ohnesorge number [= $\mu/(\rho_j d_n \sigma)^{1/2}$]	ρ	density
q	momentum ratio [= $\rho_j u_j^2/(\rho_\infty u_\infty^2)$]	σ	surface tension
Re_j	jet Reynolds number (= $\rho_j u_j d_j/\mu_j$)		
t	time		**Subscripts**
t_i	time of onset of breakup		
t^*	characteristic breakup time	j	liquid jet property
	[= $d_n(\rho/\rho_\infty)^{1/2}/u_\infty$]	∞	air jet property

itself; they also define breakup regimes for liquid surface and liquid column breakup. Vich and Ledoux [3], however, find breakup regimes for bag and liquid column breakup (they call the latter arcade breakup) that are somewhat different from [2]. In addition, both studies indicate the presence of liquid jet distortions [2] or effects of turbulent transitions on jet breakup behavior [3] that probably are caused by disturbances within the liquid jet passage. Other earlier studies of round liquid jets in gas crossflows [4–15] also involve considerable uncertainties about flow disturbance levels at the jet exit.

The objectives of the present investigation were to extend the studies of Wu et al. [2] and Vich and Ledoux [3] by observing the properties of uniform nonturbulent round liquid jets in uniform gas crossflows, seeking to quantify the effect of parameters known to influence both the properties of primary breakup of liquid jets in gas crossflows and the secondary breakup of drops. Present observations included pulsed shadowgraphs of nonturbulent round liquid jets of various liquids (water, ethyl alcohol, and glycerol mixtures) in air crossflows at normal temperature and pressure. The shadowgraphs were used for flow visualization and to determine jet primary breakup regimes, jet deformation properties, time of onset of primary breakup, and the properties of waves observed along the liquid column and the liquid surface.

The article begins with a description of experimental methods. Results are then discussed considering flow visualization, primary breakup regimes, liquid column deformation properties, the properties of the onset of primary breakup, and the properties of liquid column and liquid surface waves associated with the primary breakup process, in turn. The article ends with a summary of the major conclusions of the investigation.

EXPERIMENTAL METHODS

Apparatus

The apparatus consisted of liquid pressure feed, liquid nozzle, air crossflow, and liquid collection assemblies. The configuration involved injection of uniform nonturbulent round liquid jets vertically downward by the action of the pressure feed system. The air

126

crossflow was horizontal, with the liquid jet directed along a vertical plane through the air jet axis. After passing through the region where observations were made, the liquid jet was deflected downward into a collecting tank using a baffle. The test liquid was discarded after use in order to maintain liquid cleanliness. The experiments were carried out within a 2100 mm long × 1100 mm high × 660 mm wide plastic enclosure, with windows to provide optical access, in order to control liquid splashing.

A sketch of the liquid nozzle assembly appears in Fig. 1. The test liquid was contained within a cylindrical chamber having a diameter of 100 mm and a length of 230 mm, constructed of type 304 stainless steel. The nozzle was located along the axis at the bottom of the chamber. The nozzles consisted either of round sharp-edged (Borda) nozzles or a round supercavitating nozzle (having a sharp-edged inlet and exit with a length-to-diameter ratio less than 3), both of which yield uniform nonturbulent round liquid jets, as discussed by Wu et al. [16] and Lienhard [17]. Several different Borda nozzles (2, 4, and 16 mm diameter) and a supercavitating nozzle (1 mm diameter) were used to provide liquid jets having various diameters (note that actual liquid jet diameters are only 50–70% of the geometric diameters of Borda and supercavitating nozzles; see Dai et al. [1] and Lienhard [17]).

The test liquid was placed within the cylindrical chamber using the liquid fill line. A cork in the nozzle passage was used to prevent premature outflow of the liquid. Pressurized air was admitted to the top of the chamber upon activation of a solenoid valve; this air was stored in a large (1.3 m³ volume) air reservoir set to the desired injection pressure by filling from the laboratory high-pressure air supply system (pressures up to 1500 kPa with a dew point less than 240 K). The increased pressure in the cylindrical chamber due to air inflow caused liquid outflow once the cork was forced out of the nozzle.
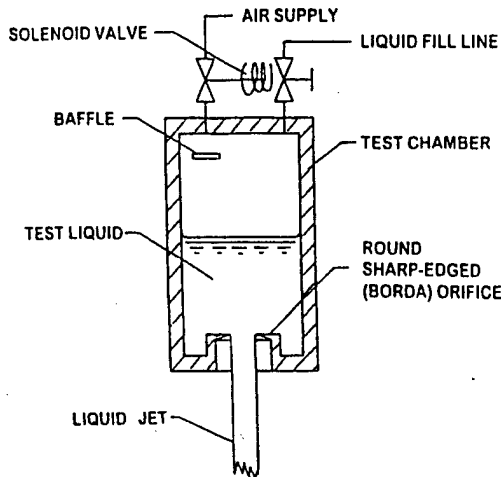

Fig. 1   Sketch of the liquid injector system.

Excessive aeration of the test liquid during injection was prevented by a baffle across the
air inlet of the cylindrical chamber. Once all the liquid was forced out of the liquid chamber,
the solenoid valve was closed and the chamber was allowed to vent to the surrounding
atmosphere. The cork was then replaced and the chamber was refilled for the next test. The
pressure of the air in the air reservoir was varied to provide liquid velocities at the nozzle
exit in the range 0–50 m/s. The corresponding liquid injection times were as small as 200
ms, but this was not a problem because flow development times (taken as the time required
for a given liquid sample to cross the air jet) were less than 10% of the liquid injection times
whereas data acquisition times using pulsed shadowgraph photography were even shorter
(requiring less than 10 µs).

The air crossflow was provided by a blower drawing air at normal temperature and
pressure from the laboratory. The blower flow was regulated using a gate valve to provide
mean crossflow velocities in the range 0–24 m/s; these velocities were measured using a vane
anemometer (Omega model HH-31). The flow leaving the blower passed through a honey-
comb flow straightener section (hexagonal cells 8 mm wide having a length of 50 mm) and
three screens (wire diameters of 0.3 mm in a square pattern on 1 mm centers) spaced 100 mm
apart to yield a relatively uniform nonturbulent and nonswirling horizontal flow having a
nominal diameter of 200 mm. Distributions of streamwise mean and fluctuating crossflow
velocities were measured using a hot-wire probe (TSI digital monitor and power supply,
model 1051-1; constant-temperature linearized anemometer, model 1054A; variable decade
probe resistance, model 1056; and sensor probe, model 1210-60). These observations
showed that the shear layer at the edge of the air jet extended ± 20 mm from the nominal
jet diameter at the location of the liquid injector. The remainder of the jet had relatively
uniform mean streamwise velocities (within 5%) and root-mean-square (rms) streamwise
turbulence intensities less than 2%. The outlets of the liquid nozzles (e.g., the bottom edge
of test chamber illustrated in Fig. 1) were placed 20 mm above the upper edge of the
nominal diameter of the air crossflow, right at the upper edge of the shear layer. It should
be noted that for present test conditions, velocity variations of the liquid jet due to effects
of gravity and drag were negligible over the air jet crossection in the absence of crossflow.

The nozzle and crossflow assemblies were connected to form a single rigid unit. This
unit was then placed on a mounting frame so that the assembly could be positioned in the
vertical direction to accommodate rigidly mounted optical instrumentation.

Earlier experiments using Borda nozzles to create nonturbulent liquid jets showed
that the velocity coefficients of these designs were greater than 95%; see [1] and references
cited therein. In addition, present results did not indicate strong effects of liquid jet
velocities on the flow properties of interest. Thus, liquid jet velocities were simply com-
puted from the nozzle pressure drop, assuming ideal flow, for the present experiments.

Instrumentation

The measurements were limited to pulsed shadowgraphy. Light sources consisted of
either a xenon arc lamp (Xenon Corp., model 437B, nanopulser) that generated a light pulse
having an optical energy up to 10 mJ and a duration of 20 ns, or a frequency-doubled YAG
laser (Spectra Physics, model GCR-130) yielding a light pulse having an optical energy up
to 300 mJ and a pulse duration of 7 ns. The light pulses from both these sources were short
enough to stop the motion of the flow. The light beams were expanded to provide
collimated beams having diameters of 30–60 mm through the flow.

The shadowgraph images were recorded using a 100 × 125 mm (4 × 5 in.) Graphlex still camera. The camera was focused at the plane of symmetry of the deflecting liquid jet with the image magnified 2–7:1 on the film. The camera was operated with an open shutter within a darkened room so that exposure times were controlled by the duration of the light pulses. The images were recorded using Polaroid type 55–57 black-and-white film.

One property of interest was the crosstream (frontal) and streamwise dimensions of the liquid jets. Unfortunately, the present test arrangement could not provide simple projections of both these images; instead, two cameras were used to record images of the liquid jets along optical axes that were horizontal and were directed at angles of 48° and 90° to the direction of the crossflow. The resulting images were then analyzed assuming that the liquid column had an elliptical cross section, similar to the approach used by Nguyen and Karagozian [13].

Test Conditions

The test liquids included water, ethyl alcohol, and glycerol mixtures (66%, 79%, and 84% glycerin by mass in water). The properties of the test liquids are summarized in Table 1. The liquid properties summarized in Table 1 were measured as follows: liquid density using a set of hydrometers (Fisher model 11-582, 0.1% accuracy), liquid viscosity using a Cannon-Fenske viscosimeter (Fisher model 13-617, 3% accuracy), and surface tension using a ring tensiometer (Fisher model 20, 1% accuracy). The present results for pure liquids agreed with the values given by Lange [18] within the accuracy of the instruments.

Test conditions were varied by considering the various liquids, liquid jet diameters of 0.8–13 mm, liquid jet velocities of 0–50 m/s, and air crossflow velocities of 0–24 m/s at normal temperature and pressure. This yielded the following ranges of normalized test variables: the ratio of drag-to-surface tension forces, characterized by the crossflow Weber number, We, of 0–200; liquid jet Weber numbers, We_j, of 0–1,600,000; liquid jet Reynolds numbers, Re_j, of 0–800,000; the ratio of liquid/gas momentum fluxes, q, of 100–8000; the ratio of liquid/gas densities, ρ_f/ρ_g, of 700–1100; and the ratio of liquid-viscous/surface-tension forces, characterized by the Ohnesorge number, Oh, of 0.00006–0.3. Crossflow Mach numbers were less than 0.07; therefore, effects of compressibility were negligible.

Table 1 Properties of the Test Fluids[a]

Liquids[b]	Density (kg/m³)	Viscosity (g/m s)	Surface tension (mN/m)
Water	996	0.82	70.9
Ethyl alcohol	806	1.23	22.2
Glycerol (66%)	1172	16.4	60.7
Glycerol (79%)	1205	37.3	59.8
Glycerol (84%)	1219	80.4	63.0

[a] Measured at normal temperature and pressure: 297 ± 3K and 97 kPa. Ambient air properties: density of 1.14 kg/m³ and viscosity of 0.01846 g/m s.
[b] Numbers in parentheses denote concentration of glycerin by mass.

RESULTS AND DISCUSSION

Flow Visualization

The presentation of the results will begin with pulsed shadowgraph photography for flow visualization of various liquid jet primary breakup conditions. The properties of the injection process of the present nonturbulent round liquid jets in still air are illustrated by the photograph of Fig. 2. These test conditions involved a water jet with a liquid jet diameter of 3.2 mm, using a Borda nozzle having a diameter of 4 mm, but the appearance of this jet is typical of the present liquid jets in the absence of crossflow. It is evident that the surface of the liquid column is smooth and that no disturbances or protrusions are observable over the 30 mm vertical height of the image even though the jet Reynolds number at this condition is relatively large, i.e., $Re_j = 45,900$. In fact, this behavior persisted over the observable length of the liquid jet, which was up to 300 mm long. Thus, present behavior for uniform nonturbulent jet exit conditions was very similar to a liquid cutting jet, which is consistent with past observations of the behavior of uniform nonturbulent round liquid jets for injection into still gases with liquid/gas density ratios greater than 500 [16, 17]. All liquid jet operating conditions considered during the present investigation had smooth round liquid surfaces with no significant deformation or variation of the cross-stream diameter over the cross section of the air jet, similar to the jet appearance of Fig. 2, and in this sense are referred to as liquid jets in the following. These results also provide direct proof that all primary breakup processes observed during the present investigation were caused by the air crossflow rather than by liquid vorticity or turbulence, which leads to other breakup processes such as turbulent primary breakup [16].

For conditions where effects of liquid viscosity were small ($Oh < 0.1$), five kinds of flow were observed as the crossflow velocity (characterized by the Weber number) was
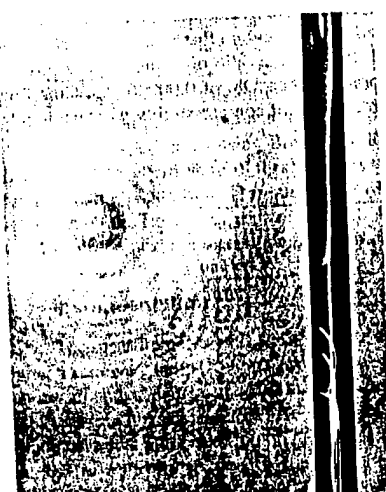

Fig. 2 Pulsed shadowgraph of a nonturbulent round liquid jet in still air (water, $d_o = 3.2$ mm, $u_\infty = 0$ m/s, $u_j = 11.8$ m/s, We $= 0$, $q = \infty$, $Re_j = 45,900$, and Oh $= 0.0029$).

increased: simple deformation of the shape and trajectory of the liquid jet with no primary breakup, followed by several primary breakup regimes, as follows: breakup of the liquid column as a whole, bag breakup, bag/shear breakup, and shear breakup. The appearance of the four liquid jet primary breakup regimes at Oh < 0.1 will now be considered in the order of progressively increasing We.

The primary breakup mechanism observed at the smallest crossflow velocities used during the present experiments was liquid column breakup as a whole. A pulsed shadowgraph of typical breakup behavior in this regime is illustrated in Fig. 3. Typical of all conditions where primary breakup of the liquid occurred, the column first deforms in the direction normal to the crossflow, to yield an ellipsoidal cross section. This behavior is caused by the reduced gas pressure near the side of the jet as the gas accelerates over the liquid column, with the resulting lateral motion of the liquid stabilized to some extent by surface tension, somewhat analogous to the behavior of individual drops subjected to shock wave disturbances in the deformation regime [19–23]. The increased drag forces due to the flattened shape of the column also enhance the tendency of the liquid column to be deflected downstream with respect to the gas motion. As the liquid column deflects in the streamwise direction, in addition to the flattened shape, somewhat thickened regions (nodes) appear along the column. The nodes subsequently develop into droplike structures with thinner interconnecting liquid column regions that deflect in the streamwise direction compared to the slower-moving node drops. Breakup of the liquid column then finally occurs by breakup of the thin liquid column regions, due to Rayleigh-like breakup, or Rayleigh-like breakup supplemented by stretching of the thin liquid columns. Vich and Ledoux [3] observe similar column breakup at small We, which they define as arcade breakup. Naturally, very low crossflow velocities would lead eventually to transition from this breakup regime to a stable liquid jet similar to Fig. 2. It was not possible to find the
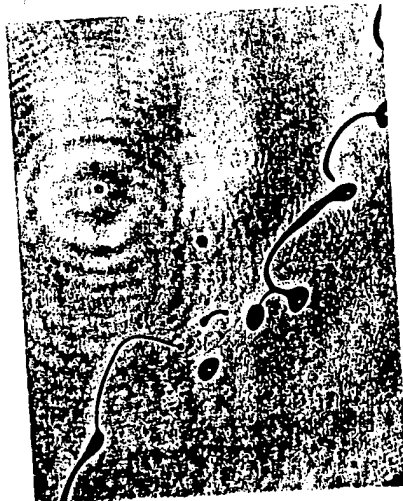

Fig. 3   Pulsed shadowgraph of a nonturbulent round liquid jet in crossflowing air within the liquid column breakup regime [glycerol (79%), $d_n = 0.8$ mm, $u_\infty = 15.9$ m/s, $u_j = 11.8$ m/s, We $= 4$, $q = 562$, $Re_j = 305$, and Oh $= 0.155$].

transition to the liquid column breakup regime, however, due to the limited dimensions of the present crossflow.

As crossflow velocities increase, the next breakup regime observed is the bag-breakup regime. An illustration of the bag-breakup regime appears in Fig. 4. In this case, after the liquid column flatten sufficiently and started to deflect in the downstream direction, baglike structures appear which are very similar to the bag breakup regime observed during the secondary breakup of drops [19–21]. This behavior involves the formation of bags as a result of the deformation of the central portion of the liquid column downstream due to the higher pressure of the stagnating gas flow on the upstream side of the flattened liquid column. The development of bags is not a two-dimensional phenomenon, however, due to the appearance of nodes along the liquid column, characterized by a wavelength of separation between the nodes of λ_r, somewhat analogous to the node drops discussed in connection with liquid column breakup. With increasing distance along the liquid column, the bags at first progressively grow in the downstream direction. As the bags approach their maximum size, however, they begin progressively to break up, beginning at their tip. This process appears to be the result of Rayleigh-like breakup of the thin liquid sheet, augmented by motion of the liquid/gas edge of the bag due to unbalanced surface tension forces, very similar to the bag breakup process of drops [19–21]. Upon completion of the breakup of the bags themselves, there remain two strings of node drops, connected by thinner liquid columns that deflect downstream due to the drag forces caused by the crossflow. The connecting liquid columns then break up, probably due to Rayleigh breakup, in a manner similar to the basal ring of secondary drop breakup in the bag breakup regime [19, 23]. The final result is a polydisperse array of large drops associated with the presence of nodes and the breakup of their connecting liquid columns, along with a large number of much smaller drops associated with breakup of the bags themselves. This behavior tends to separate

Fig. 4   Pulsed shadowgraph of a nonturbulent round liquid jet in crossflowing air within the bag breakup regime [glycerol (84%), $d_r = 0.8$ mm, $u_\infty = 21.6$ m/s, $u_j = 11.8$ m/s, We = 7, $q =$ 308, $Re_j = 143$, and Oh = 0.320].

132

drops according to size along the deforming liquid column, with the smallest drops appearing near the onset of breakup and drop sizes progressively increasing with increasing distance along the liquid jets, very much the way bag breakup during the secondary breakup of drops progressively separates drop sizes as a function of time [23]. As noted earlier, both Wu et al. [2] and Vich and Ledoux [3] observe similar bag breakup regimes for their round jets in crossflow.

Further increases of crossflow velocities cause transition to a complex breakup regime that is a combination of bag breakup as just discussed and shear breakup that was observed at the largest crossflow velocities considered during the present investigation. An illustration of typical behavior in this bag/shear breakup regime appears in Fig. 5. In this case, both baglike structures, due to penetration of the liquid column, and liquid ligaments, due to the shearing of liquid from the periphery of the liquid column, appear at roughly the same time. Breakup then involves breakup of the baglike structures as discussed in connection with Fig. 4 as well as breakup of the ligaments in a manner that appears to be very similar to the secondary breakup of drops in the shear breakup regime; see [19–23] and references cited therein.

The largest crossflow velocities considered during the present investigation caused transition to the shear-breakup regime. A pulsed shadowgraph of typical behavior in this regime is illustrated in Fig. 6. Similar to the bag and bag/shear breakup regimes, the process begins by deflection of the liquid column in the streamwise direction of the crossflow, followed by distortion of the column into a somewhat flattened shape. Wavelike disturbances also appear in the upstream side of the liquid column, but the wavelengths of these disturbances are smaller than the diameter of the liquid column and they do not develop into the nodes observed in the liquid-column and bag-breakup regimes. Instead, ligaments are stripped from the periphery of the liquid column, very similar to the behavior of secondary

Fig. 5 Pulsed shadowgraph of a nonturbulent round liquid jet in crossflowing air within the bag/shear breakup regime (water, $d_n = 6.4$ mm, $u_\infty = 23.9$ m/s, $u_j = 8.32$ m/s, We = 61, $q = 102$, $Re_j = 64,700$, and Oh = 0.0012).

Fig. 6   Pulsed shadowgraph of a nonturbulent round liquid jet in crossflowing air within the shear breakup regime (ethyl alcohol. d_n = 7.0 mm. u_n = 23.7 m/s, u_j = 11.8 m/s. We = 209. q = 169, Re_j = 54,100. and Oh = 0.0035).

drop breakup in the shear breakup regime; see [19–23] and references cited therein. Within the ligament structures, occasional sheetlike regions are observed, i.e., they are enclosed at the sides by ligaments, bag shapes are convex rather than concave as seen in Fig. 4, and the base of the sheets is thick, comparable to the column diameter, rather than the small-diameter liquid columns associated with bags.

As discussed subsequently, effects of liquid viscosity, characterized by the Ohnesorge number, were not very significant for Oh < 0.1. Within the shear breakup regime, however, the length of the ligaments being stripped from the sides of the liquid column increased progressively with increasing Ohnesorge number. Thus, similar to the secondary breakup of drops in the shear breakup regime [19–21], a long-ligament shear breakup regime was defined for Oh > 0.1. A pulsed shadowgraph of the typical appearance of the region near the liquid column as the long-ligament regime is approached appears in Fig. 7. The long ligaments are clearly evident; in addition, there are thin liquid sheets between the ligaments similar to the appearance of the flow in Fig. 6. The long-ligament regime presents significant experimental difficulties due to the problem of tracking flow behavior when ligaments are long; therefore, the present measurements generally were limited to Ohnesorge numbers smaller than the long-ligament regime.

Primary Breakup Regimes

Exploiting the similarities between the primary breakup regimes of nonturbulent round liquid jets (denoted liquid jets in the following) in crossflow and the secondary breakup of drops, the liquid jet primary breakup regimes were correlated in terms of the Weber and Ohnesorge numbers as first proposed by Hinze [24] for the secondary breakup of drops exposed to shock-wave disturbances and used subsequently by most investigators

of secondary drop breakup; see [19–23] and references cited therein. The resulting breakup regime map is plotted in Fig. 8. In this figure, the present regime boundaries are located where roughly half the observations corresponded to conditions similar to each of the two bounding regimes, similar to past work for secondary breakup of drops, e.g., [19, 22]. Experimental uncertainties (95% confidence) of these boundaries are less than 25% for We and are less than 5% for Oh (which has negligible effect for the test range of Fig. 8), set largely by problems of identifying particular breakup behavior in a consistent way. For present conditions (We of 0–200 and Oh of 0.00006–0.3) the liquid jet breakup regimes are relatively independent of Oh, with four breakup regimes identified, as discussed in connection with the flow visualization study, as follows: liquid-column breakup ($We < 5$), bag breakup ($5 < We < 60$), bag/shear breakup ($60 < We < 110$), and shear breakup ($110 < We$). Finally, it should be noted that variations of liquid/gas momentum and density ratios did not have a significant effect on these breakup regime transitions over the present test range, i.e., q in the range 100–8000 and ρ/ρ_∞ in the range 700–1100.

The four liquid jet breakup regimes plotted in Fig. 8 are somewhat analogous to the secondary breakup regimes of drops subjected to shock-wave disturbances. In order to show this relationship, the secondary breakup regime map for drops from Hsiang and Faeth [19–21] is plotted in Fig. 8 for comparison with the present liquid jet breakup results. The main differences between liquid column and drop breakup are that secondary breakup of drops does not exhibit behavior analogous to liquid column breakup and is characterized only by a drop deformation regime prior to transition to the bag-breakup regime, and that secondary drop breakup responds to a greater degree to increasing Oh than liquid jet breakup, with progressively increasing We with increasing Oh at the transitions to various breakup regimes for Oh > 0.01. At small Oh < 0.01, however, the transitions to secondary

Fig. 7   Pulsed shadowgraph of a nonturbulent round liquid jet in crossflowing air approaching the long-ligament bag breakup regime [glycerol (79%), $d_o = 6.4$ mm, $u_\infty = 17.8$ m/s, $u_j = 8.3$ m/s, We $= 44$, $q = 220$, $Re_j = 1720$, and Oh $= 0.055$].
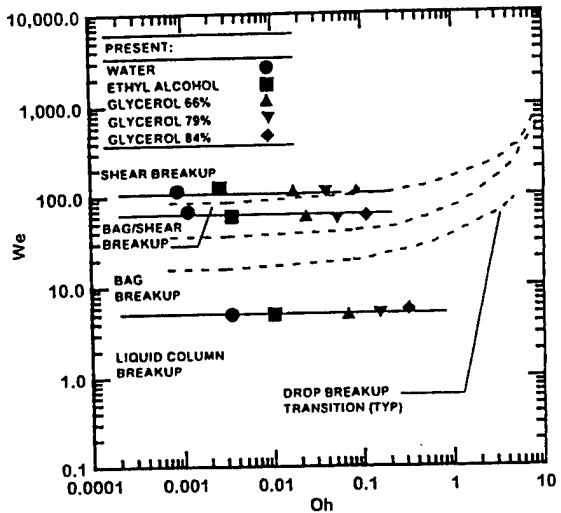
Fig. 8 Breakup regime maps for primary breakup of round nonturbulent liquid jets in crossflows (ρ/ρ_s = 580–1020, We < 200, q < 8000, and Oh < 0.4) and for secondary breakup of drops (ρ/ρ_s = 580–1020, We < 1000, and Oh < 10). Results for secondary breakup of drops from Hsiang and Faeth [19–21].

drop breakup regimes become relatively independent of Oh, similar to liquid jet primary breakup, and have the following values at the transitions: deformation (We < 13), bag breakup (13 < We < 35), multimode breakup (35 < We < 80), and shear breakup (80 < We). With respect to these transitions, it should be noted that bag/shear breakup of liquid jets is analogous to multimode breakup of drops, and the original diameters of the liquid jets and the drops should be used in the corresponding expressions for We and Oh.

Effects of Oh on breakup regime transitions are not considered explicitly by Wu et al. [2] and Vich and Ledoux [3]; nevertheless, it is interesting to compare their other observations with the present findings. During both these studies it was observed that column breakup would occur before other forms of breakup as q becomes small. This behavior is quite plausible, because column breakup seems to be associated with Rayleigh breakup and can occur close to the jet exit when liquid velocities are small; in this manner, column breakup can supersede other breakup mechanisms. Sufficiently small liquid velocities were not considered during the present investigation (in order to avoid significant gravitational acceleration of the liquid jet) for this behavior to be observed. Otherwise, effects of q on breakup regime transitions were small in [2, 3]. For conditions where q does not affect breakup regime transitions, Wu et al. [2] quote the same breakup regimes and transition Weber numbers as those given by Hsiang and Faeth [19–21] for the secondary breakup of drops; these values are somewhat different than the present assessment of breakup regimes for nonturbulent liquid jets in crossflow as just discussed, with the onset

of bag breakup deferred significantly from present observations. In contrast. Vich and Ledoux [3] find transition to bag breakup beginning at $We = 1.5$ and ending at $We = 8$. which yields an average value of $We = 5$ for this transition, which exactly agrees with present observations.

Liquid Column Deformation

The first stage of liquid jet breakup involves deformation of the liquid column: this behavior is similar to the secondary breakup of drops. where distortion of the drop into a flattened shape invariably precedes drop breakup. The important properties of liquid jet deformation are as follows: the frontal dimension of the liquid jet, d_f which is the local width of the jet in the direction normal to the motion of the air crossflow; the streamwise dimension of the liquid jet. d_s, which is the local projected length of a jet normal to the frontal dimension in a plane normal to the jet axis (which is roughly in the streamwise direction for the modest levels of deflection of the present jets in the air flow crossection): the equivalent jet diameter, d_{ref} which is the geometric mean of these two dimensions; and the ellipticity, which is defined as the ratio of the frontal and streamwise dimensions of the jet.

Typical measurements of the deformation properties of a nonturbulent round liquid jet in crossflow are plotted in Fig. 9. This test condition involves relatively small Weber and Ohnesorge numbers, $We = 7.8$ and $Oh = 0.0012$, with liquid column properties, d_f/d_{ref}, d_s/d_{ref}, d_{ref}/d_o, d_f/d_o ,and e, plotted as a function of normalized cross-stream distance, y/d_{inj},
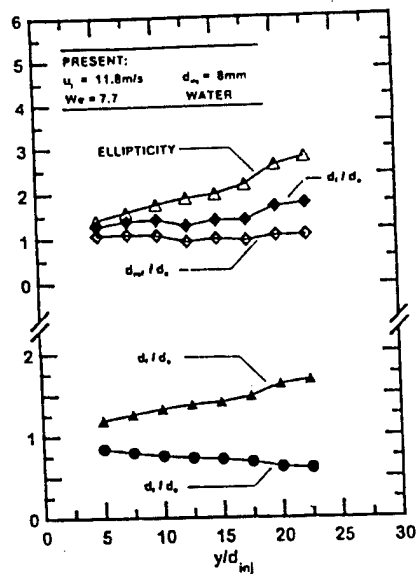

Fig. 9 Deformation of a nonturbulent round liquid jet in crossflowing air prior to the onset of bag breakup (water, $d_o = 6.4$ mm. $u_\infty = 8.6$ m/s. $u_j = 11.8$ m/s, $We = 7.7$, $q = 1590$, $Re_j = 91.700$, and $Oh = 0.0012$).

where y is measured from the nominal boundary of the air jet (the midpoint of the shear layer). The first thing to note is that d_{ref}/d_o approximates unity throughout the deformation process, which implies that the cross-sectional area of the liquid jet is conserved. Such behavior is reasonable because liquid jet velocities do not vary significantly prior to breakup for the condition shown here, so the cross-sectional area of the liquid jet must be conserved (this is not always the case when jet deflections are large). In contrast, d_f/d_{ref} and d_s/d_{ref} exhibit strong distortion of the jet, with the lateral dimension increasing by roughly 40%. This distortion is also reflected by the large values of ellipticity reached during the process, reaching $e \approx 3$ for the range of conditions considered in Fig. 9. This large degree of distortion is responsible for the large increases of drag forces and drag coefficients of liquid jets as they break up, seen by Wu et al. [2], analogous to effects of drop deformation during secondary drop breakup [19–23].

Another feature of liquid jet breakup in crossflow that is similar to the secondary breakup of drops subject to shock-wave disturbances is the relative universality of liquid column deformation at the onset of breakup. This behavior is illustrated in Fig. 10, where d_f/d_o at the onset of breakup is plotted as a function of We for We > 5. It is evident that $d_f/d_o \approx 1.8$ for We in the range 5–200 for various liquids and values of liquid jet velocity (or q). For comparison, $d_f/d_o \approx 2.0$ at the onset of secondary drop breakup for shock-wave
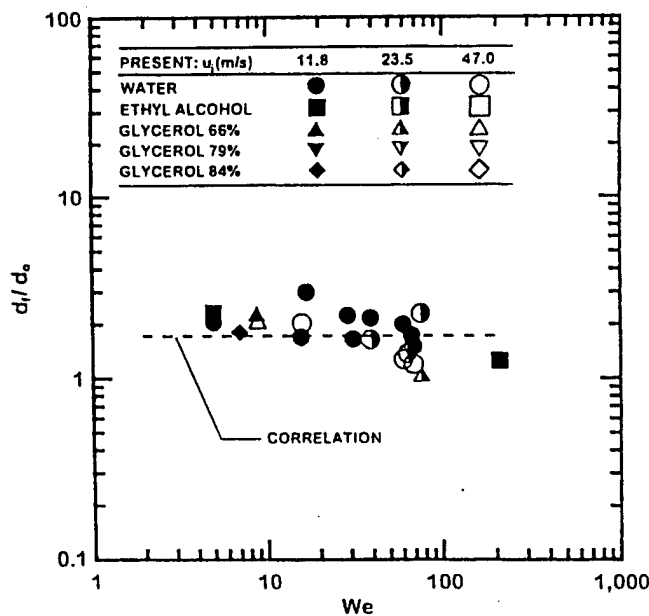

Fig. 10   Maximum deformation at the onset of primary breakup as a function of Weber number for nonturbulent round liquid jets in crossflows.

disturbances over a very broad range of Weber numbers, We in the range 13–6000, at small Oh (i.e., Oh < 0.1) [19, 20].

Onset of Breakup

Opposing all the similarities between liquid jet breakup in crossflow and secondary breakup of drops subjected to shock-wave disturbances, however, is the striking differences between the correlation for the time of onset of breakup (taken as the condition where drops just begin to form due to breakup at the liquid surface). For the secondary breakup of drops, the time of onset of secondary breakup, normalized by the characteristic secondary breakup time of Ranger and Nicholls [25], is $t_i/t^* \approx 2$ for We ranging over the bag, multimode, and shear breakup regimes [22, 23]. This behavior can be rationalized by noting that the characteristic velocity within the liquid phase, based on conservation of momentum principles, is $(\rho_\infty/\rho_j)^{1/2}u_\infty$, while it is reasonable to assume that liquid motion must cause deformation of the drop involving a fixed fraction of the initial drop diameter at the time of onset of breakup (since d_i/d_n is a constant at the onset of breakup for a wide range of We). Then, assuming that the time required to reach the onset of breakup is proportional to the time required to move a distance equal to the drop diameter, at the characteristic liquid-phase velocity, implies that $t_i \propto t^* = d_n(\rho/\rho_\infty)^{1/2}/u_\infty$ or $t_i/t^* =$ constant as observed for the secondary breakup of drops.

Based on the previous discussion, it seems plausible that t_i/t^* should also be a constant for the onset of breakup of liquid jets, because the characteristic liquid phase velocity is similar to the value for drops while the degree of deformation at the onset of breakup for liquid jets is a constant from the results of Fig. 10, which is also similar to the behavior of drops during secondary breakup. This idea is evaluated based on the results plotted in Fig. 11, where t_i is found from the position where the onset of breakup is observed given the known liquid jet velocity. For comparison, past measurements of the times of onset and end of secondary drop breakup are also shown on the plot, based on the results of [19–23] and references cited therein. The values of t_i/t^* for the two types of breakup are of the same order of magnitude, but t_i/t^* for the onset of liquid jet breakup clearly decreases with increasing We, rather than being independent of We similar to the behavior of the secondary breakup of drops. In fact, correlation of the present measurements for Oh < 0.1 yields

$$\frac{t_i}{t^*} = 8.76\,\text{We}^{-0.62} \qquad (1)$$

with a correlation coefficient of the fit of 0.93. The corresponding powers of Oh (−0.01) and q(−0.18) for a three-variable correlation are relatively small, so it is concluded that Weber number mainly influences t_i/t^* over the present test range. At the present stage of understanding liquid jet breakup, however, the reasons for the difference between the behavior of the time of onset of breakup of liquid jets in crossflow and the secondary breakup of drops are not known.

Column and Surface Waves

Another feature of liquid jet breakup in crossflow is the appearance of waves in the streamwise direction along the liquid column. Two kinds of waves are observed: the
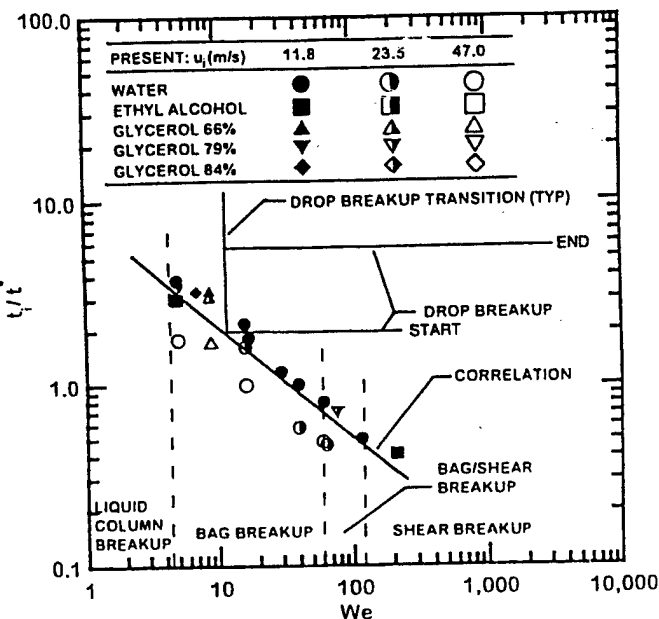
Fig. 11 Time of the onset of primary breakup as a function of Weber number for nonturbulent round liquid jets in crossflows and times of onset and end of secondary breakup of drops. Results for the secondary breakup of drops from Chou et al. [22, 23] and Hsiang and Facth [19–21].

wavelengths between nodes, λ_r, involving deflection of the entire liquid column, that have already been discussed in connection with Figs. 3–5; and the smaller wavelength, λ_s, associated with periodic disturbances of liquid stripping along the sides of the liquid column during shear breakup, that have been mentioned in connection with Figs. 5 and 6.

The appearance of liquid column waves can be seen from the pulsed shadowgraph photograph of Fig. 12. This condition involves a liquid jet having small liquid viscous effects, Oh = 0.0103 in the liquid column breakup regime close to the transition to the bag-breakup regime at We = 4.0. The region shown corresponds to the onset of growing liquid column waves. It is seen that the amplitude of these waves grows with increasing distance along the liquid column but that the wavelength does not change significantly, i.e., the disturbance appears to convect along the liquid jet. The cusps of these waves eventually are associated with the nodes along the liquid column that are a dominant feature of the bag and bag/shear breakup regimes. It seems likely that these waves are caused by Rayleigh/ Taylor instability due to the acceleration of the dense liquid column by the low-density gas; in particular, the node structures tend to lag the motion of the rest of the column.

The wavelengths of liquid column disturbances decrease progressively with increasing Weber number as discussed later; in addition, liquid surface waves appear along the
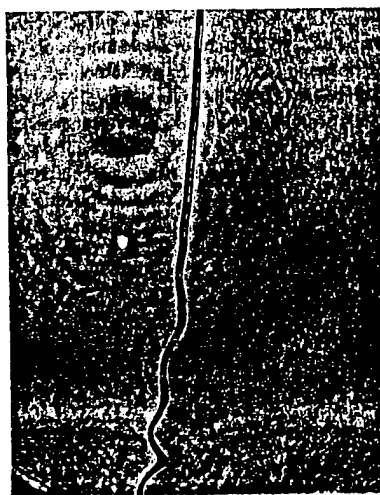
Fig. 12   Pulsed shadowgraph of liquid column waves for a nonturbulent round liquid jet in an air crossflow (ethyl alcohol, d_o = 0.8 mm, u_- = 10.8 m/s, u_j = 11.8 m/s, We = 4.0, q = 815, Re_j = 6,190, and Oh = 0.0103).

liquid column at larger values of We. The appearance of combined liquid column and liquid surface waves can be seen from the pulsed shadowgraph photograph of Fig. 13. This condition involves a liquid jet having small liquid viscous effects, Oh = 0.0687 in the bag breakup regime, We = 8.8. The region shown corresponds to the onset of growing liquid
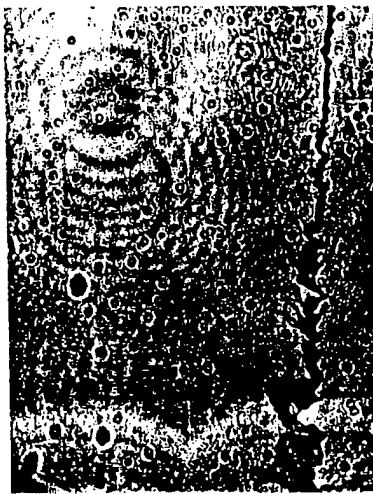

Fig. 13   Pulsed shadowgraph of liquid surface and liquid column waves for a nonturbulent round liquid jet in an air crossflow [glycerol (66%), d_o = 0.8 mm, u_- = 17.9 m/s, u_j = 9.7 m/s, We = 8.8, q = 292, Re_j = 554, and Oh = 0.0687].

column and surface waves as well as the onset of bag breakup. The liquid surface waves appear first, they have relatively short wavelengths, and they are most prominent on the upstream side of the liquid column. This behavior suggests that they are associated with Rayleigh/Taylor instability similar to the liquid column waves but involve a local phenomenon that is not affected by the dimensions of the liquid column itself. With increasing distance along the liquid jet, however, longer-wavelength liquid column disturbances appear which eventually dominate the breakup process for these bag breakup conditions

Normalized liquid column and liquid surface wavelengths, λ_c/d_o and λ_s/d_o, are plotted as a function of the Weber number in Fig. 14. The experimental uncertainties (95% confidence) of these parameters are estimated to be less than 25%, due largely to wavelength irregularities similar to those seen in Figs. 12 and 13. For reference purposes, present
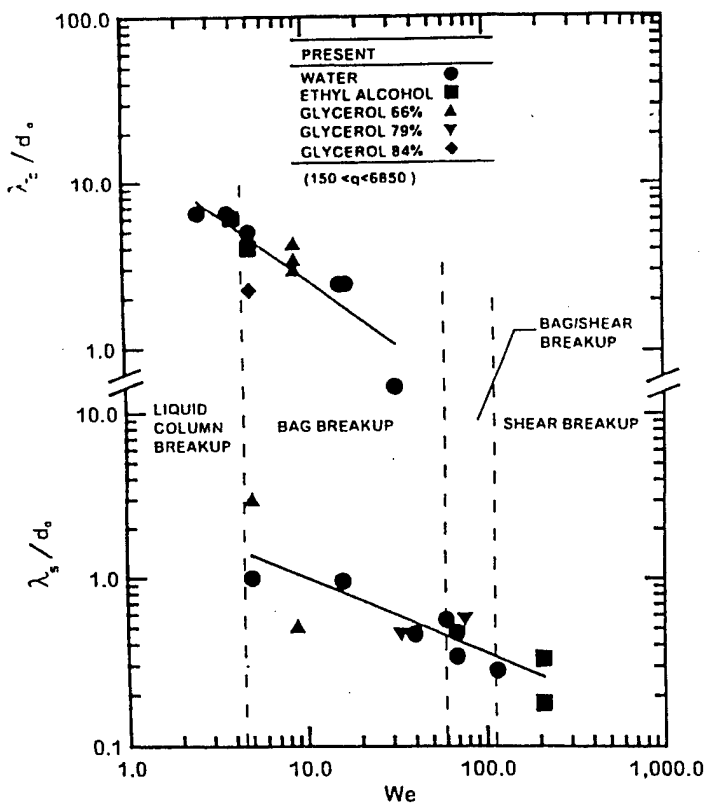

Fig. 14   Liquid column and surface wavelengths of nonturbulent round liquid jets in air crossflows.

values of We at transitions to various breakup regimes are also marked on the plots. As noted earlier, liquid column waves first appear in the liquid column breakup regime and eventually are associated with the disturbances that lead to breakup of the liquid column itself as illustrated in Fig. 3. These disturbances begin with $\lambda_c/d_n \approx 10$ at We ≈ 1 and then decrease to $\lambda_c/d_n \approx 1$ at We = 60, which represents the onset of the bag/shear breakup regime. These disturbances decrease at larger We, where the breakup process becomes dominated by shear breakup along the sides of the jet, which involves more rapidly developing surface waves. The surface disturbance wavelengths are smaller than the liquid column waves, with λ_s/d_n generally less than unity. The wavelength of the surface waves also decreases as We increases and they are still visible in the shear breakup regime, where they are associated with the distance between ligaments being stripped from the sides of the liquid columns.

Correlations of λ_c/d_n and λ_s/d_n were sought in terms of We, Oh, and q. The best-fit correlations were achievable as a function of We alone, as follows:

$$\frac{\lambda_c}{d_n} = 16.3\,\text{We}^{-0.79}$$

(2)

with a correlation coefficient of this fit of 0.86, and

$$\frac{\lambda_s}{d_n} = 2.82\,\text{We}^{-0.45}$$

(3)

with a correlation coefficient of this fit of 0.82. The effect of Oh on λ_c/d_n and λ_s/d_n could not be resolved within experimental uncertainties, while the corresponding powers of q in combined We, q correlations were -0.13 and -0.09, respectively. Thus, it is concluded that these wavelengths are mainly functions of We over the present test range. Due to the obvious relationships between λ_c and λ_s and the properties of bag, bag/shear, and shear breakup of liquid jets in crossflow, this primary dependence of breakup properties on We helps strengthen the analogy between the breakup properties of liquid jets in crossflow and the secondary breakup properties of drops subjected to shock-wave disturbances.

CONCLUSIONS

Results of an investigation of nonturbulent round liquid jets in air crossflows at normal temperature and pressure have been described. Test liquids included water, ethyl alcohol, and glycerol mixtures; liquid jet diameters in the range 0.8–13 mm; liquid jet velocities in the range 0–50 m/s; and air crossflow velocities in the range 0–24 m/s. The corresponding test range involved crossflow Weber numbers of 0–200, jet Weber numbers of 0–1,600,000, jet Reynolds numbers of 0–800,000, liquid/gas momentum ratios of 100–8000, liquid/gas density ratios of 700–1100, and Ohnesorge numbers of 0.00006–0.3. The major conclusions of the study are as follows:

1. There is a useful general analogy between the surface primary breakup of nonturbulent round liquid jets in crossflow and the secondary breakup of individual drops which suggests modest streamwise interactions between cross sec-

J. MAZALLON ET AL.

tions in the jets; i.e., liquid surface deformation and breakup properties are not strongly affected by the liquid/gas momentum ratio for values less than 8000, the largest value considered during the present study.

2. Transitions to various breakup regimes are not influenced significantly by liquid viscosities for Oh < 0.1. For these conditions, the onset of breakup occurs as bag breakup at We = 5; there is a transition to bag/shear breakup at We = 60 and another transition to shear breakup at We = 110. These properties are similar to earlier observations of Wu et al. [2] and Vich and Ledoux [3]. A long-ligament shear breakup regime also appears for Oh > 0.1.

3. The deformation of the liquid jet prior to the onset of breakup also is somewhat analogous to drop deformation prior to secondary breakup of drops, with the liquid column attaining a frontal diameter roughly twice the initial jet diameter at the onset of breakup, relatively independent of the breakup regime, We, Oh, and q.

4. An interesting difference between breakup of nonturbulent round liquid jets in crossflow and the secondary breakup of drops is that the normalized time at the onset of breakup, t/t^*, is proportional to $We^{-0.62}$ instead of being relatively independent of We similar to the secondary breakup of drops. Values of t/t^* were relatively independent of Oh and q, however, for the present test range.

5. The primary breakup process involved the formation of two kinds of waves: waves involving deformation of the entire liquid column and waves associated with disturbances of the liquid surface. The wavelengths of both types of waves decreased with increasing We but were relatively independent of Oh and q. The bag and bag/shear breakup regimes involved the presence of both types of waves, but the liquid column breakup regime involved only the presence of column waves and the shear breakup regime involved only surface waves. An interesting feature of the present observations is that the wavelengths of the column waves are roughly equal to the initial diameter of the jet when the onset of shear-breakup regime is reached.

It should be noted that the present results are limited to nonturbulent liquid jets at relatively large liquid/gas density ratios ($\rho/\rho_\infty > 500$). Smaller liquid/gas density ratios and the presence of liquid turbulence are likely to change liquid breakup behavior significantly, based on past observations of both primary breakup of liquid jets and the secondary breakup of drops.

REFERENCES

1. Z. Dai, W.-H. Chou, and G. M. Faeth, Drop Formation due to Turbulent Primary Breakup at the Free Surface of Plane Liquid Wall Jets, *Phys. Fluids*, vol. 10, pp. 1147–1157, 1998.

2. P.-K. Wu, K. A. Kirkendall, R. P. Fuller, and A. S. Nejad, Breakup Processes of Liquid Jets in Subsonic Crossflows, *J. Prop. Power*, vol. 13, pp. 64–73, 1997.

3. G. Vich and M. Ledoux, Investigation of a Liquid Jet in a Subsonic Cross-Flow, *Proc. Int. Conf. Liquid Atomization and Spray Systems*, Seoul, Korea, pp. 23–30, 1997.

4. E. L. Geary and M. J. Margettes, Penetration of a High Velocity Gas Stream by a Water Jet, *J. Spacecraft*, vol. 6, pp. 79–81, 1969.

5. P. R. Reichenbach and K. P. Horn, Investigation of Injectant Properties in Jet Penetration in a Supersonic Stream, *AIAA J.*, vol. 9, pp. 469–471, 1971.

6. E. A. Kush and J. A. Schetz, Liquid Jet Injection into a Supersonic Flow, *AIAA J.*, vol. 11, pp. 1223–1224, 1979.
7. J. A. Schetz and A. Paddye, Penetration of a Liquid Jet at Subsonic Airstreams, *AIAA J.*, vol. 15, pp. 1385–1390, 1977.
8. J. A. Schetz, E. A. Kush, and P. B. Joshi, Wave Phenomena in Liquid Jet Breakup in a Supersonic Crossflow, *AIAA J.*, vol. 15, pp. 774–778, 1979.
9. A. S. Nejad and J. A. Schetz, Effects of Properties and Locations in the Plume or Droplet Diameter for Injection in a Supersonic Stream, *AIAA J.*, vol. 21, pp. 956–961, 1983.
10. A. S. Nejad and J. A. Schetz, Effects of Viscosity and Surface Tension on a Jet Plume in Supersonic Cross-Flow, *AIAA J.*, vol. 22, pp. 458–459, 1984.
11. D. M. Less and J. A. Schetz, Transient Behavior of Liquid Jets Injected Normal to a High-Velocity Gas Stream, *AIAA J.*, vol. 24, pp. 1979–1985, 1986.
12. Y. Kitamura and T. Takahashi, Stability of a Liquid Jet in Air Flow Normal to the Jet Axis, *J. Chem. Eng. Jpn.*, vol. 9, pp. 282–286, 1976.
13. T. T. Nguyen and A. R. Karagozian, Liquid Fuel Jet in a Subsonic Crossflow, *J. Propulsion Power*, vol. 8, pp. 21–29, 1992.
14. A. R. Karagozian, An Analytical Model for the Vorticity Associated with a Transverse Jet, *AIAA J.*, vol. 24, pp. 429–436, 1986.
15. F. J. Higuera and M. Martinez, An Incompressible Jet in a Weak Crossflow, *J. Fluid Mech.*, vol. 249, pp. 73–97, 1993.
16. P.-K. Wu, R. F.Miranda, and G. M. Faeth, Effects of Initial Flow Conditions on Primary Breakup of Nonturbulent and Turbulent Round Liquid Jets, *Atomization and Sprays*, vol. 5, pp. 175–196, 1995.
17. J. H. Lienhard, Velocity Coefficients for Free Jets from Sharp-Edged Orifices, *J. Fluids Eng.*, vol. 106, pp. 13–17, 1984.
18. N. A. Lange, *Handbook of Chemistry*, 8th ed., pp. 1134 and 1709, Handbook Publishers, Sandusky, Ohio, 1952.
19. L.-P. Hsiang and G. M. Faeth, Near-Limit Drop Deformation and Secondary Breakup, *Int. J. Multiphase Flow*, vol. 18, pp. 635–652, 1992.
20. L.-P. Hsiang and G. M. Faeth, Drop Properties after Secondary Breakup, *Int. J. Multiphase Flow*, vol. 19, pp. 721–735, 1993.
21. L.-P. Hsiang and G. M. Faeth, Drop Deformation and Breakup due to Shock Wave and Steady Disturbances, *Int. J. Multiphase Flow*, vol. 21, pp. 545–560, 1995.
22. W.-H. Chou, L.-P. Hsiang, and G. M. Faeth, Temporal Properties of Secondary Drop Breakup in the Shear Breakup Regime, *Int. J. Multiphase Flow*, vol. 23, pp. 651–669, 1997.
23. W.-H. Chou and G. M. Faeth, Temporal Properties of Secondary Drop Breakup in the Bag Breakup Regime, *Int. J. Multiphase Flow*, vol. 24, pp. 889–912, 1999.
24. J. O. Hinze, Fundamentals of the Hydrodynamic Mechanism of Splitting in Dispersion Processes, *AIChE J.*, vol. 1, pp. 289–295, 1955.
25. A. A. Ranger and J. A. Nicholls, The Aerodynamic Shattering of Liquid Drops, *AIAA J.*, vol. 7, pp. 285–290, 1969.